DYNAMIC MODELLING AND ANALYSIS OF SPLIT-TORQUE FACE-GEAR SYSTEMS

A THESIS SUBMITTED TO
THE GRADUATE SCHOOL OF NATURAL AND APPLIED SCIENCES
OF
MIDDLE EAST TECHNICAL UNIVERSITY

BY

MUSTAFA ÖZGÜR AYDOĞAN

IN PARTIAL FULFILLMENT OF THE REQUIREMENTS
FOR
THE DEGREE OF DOCTOR OF PHILOSOPHY
IN
MECHANICAL ENGINEERING

AUGUST 2022

Approval of the thesis:

DYNAMIC MODELLING AND ANALYSIS OF SPLIT-TORQUE FACE-GEAR SYSTEMS

submitted by **MUSTAFA ÖZGÜR AYDOĞAN** in partial fulfillment of the requirements for the degree of **Doctor of Philosophy** in **Mechanical Engineering, Middle East Technical University** by,

Prof. Dr. Halil Kalıpçılar
Dean, Graduate School of **Natural and Applied Sciences**

Prof. Dr. M. A. Sahir Arıkan
Head of the Department, **Mechanical Engineering**

Prof. Dr. H. Nevzat Özgüven
Supervisor, **Mechanical Engineering, METU**

Assoc. Prof. Dr. Zihni B. Sarıbay
Co-Supervisor, **Transmission Systems, Togg**

Examining Committee Members:

Prof. Dr. Ender Ciğeroğlu
Mechanical Engineering, METU

Prof. Dr. H. Nevzat Özgüven
Mechanical Engineering, METU

Prof. Dr. Yavuz Yaman
Aerospace Engineering, METU

Prof. Dr. S. Çağlar Başlamışlı
Mechanical Engineering, Hacettepe University

Assoc. Prof. Dr. Can U. Doğruer
Mechanical Engineering, Hacettepe University

Date: 29.08.2022

I hereby declare that all information in this document has been obtained and presented in accordance with academic rules and ethical conduct. I also declare that, as required by these rules and conduct, I have fully cited and referenced all material and results that are not original to this work.

Name Last name : Mustafa Özgür Aydoğan

Signature :

ABSTRACT

DYNAMIC MODELLING AND ANALYSIS OF SPLIT-TORQUE FACE-GEAR SYSTEMS

Aydoğan, Mustafa Özgür
Doctor of Philosophy, Mechanical Engineering
Supervisor : Prof. Dr. H. Nevzat Özgüven
Co-Supervisor: Assoc. Prof. Dr. Zihni B. Sarıbay

August 2022, 229 pages

In this study it is aimed to develop a dynamic model for a face-gear drive system that accounts for all important physical parameters related to the operation to achieve an optimized split-torque face-gear based transmission system. With this new model, nonlinear dynamic response of a face-gear drive system is sought and dynamic stability and limit states of this structure are investigated. The main motivation for the current study is the recent development and utilization of face-gear drive systems in the helicopter industry. Face-gear drive systems are subject of many research studies for the past 30 years. However, mesh stiffness of the face-gear is not modelled accurately. In this study, a nonlinear dynamic model of a multi-mesh involute spur pinion driven face-gear split-torque drive system is developed. A lumped mass system consisting of five pinions and two face gears is constructed. The system has seven rotational degrees of freedom. All pinion and gear blanks are assumed to be rigid disks. The constructed split-torque model includes two input, two output and three idler gears. The mesh parameters, i.e., mesh stiffness and mesh damping, have time varying characteristics. The model includes clearance-type nonlinearity for backlash. The proposed model calculates the time varying mesh stiffness of the gear pair from the generated point clouds of the face-gear and spur-gear pair by using the finite strip method (FSM). The nonlinear equations of motion are solved with Harmonic Balance Method (HBM) for periodic steady state response of the system. The accuracy of the results is compared with direct numerical integration solutions. The stability is checked with Floquet Theory and bifurcation diagrams from Poincare Sections. The effects of mesh phasing between each pinion and face-gear engagement, the effect of static torque and the effects of backlash variations to the response of the system are sought. The effect of subharmonic motion on the dynamic response is demonstrated. Also, torque-split characteristics of the system has been sought.

Keywords: Nonlinear Dynamics of Face-Gear Drive Systems, Nonlinear Gear Dynamics, Split-Torque, Helicopter Rotor Drive System, Finite Strip Method

ÖZ

TORK-AYRIMLI ALIN-DİŞLİ SİSTEMİNİN DİNAMİK MODELLENMESİ VE ANALİZİ

Aydoğan, Mustafa Özgür
Doktora, Makina Mühendisliği
Tez Yöneticisi: Prof. Dr. H. Nevzat Özgüven
Ortak Tez Yöneticisi: Doç. Dr. Zihni B. Sarıbay

Ağustos 2022, 229 sayfa

Bu çalışmada, alın-dişli sistemi yapıları için, operasyonda fiziksel olarak önemli olan tüm etkileri göz önüne alan, tork-ayrımlı sistemlerde kullanılacak gelişmiş bir dinamik analiz modeli geliştirilmesi amaçlanmıştır. Bu yeni model ile alın-dişli sisteminin, maruz kaldığı yüklemeler altındaki doğrusal olmayan tepkileri araştırılmış ve bu yapıların dinamik kararlılığını ve sınır durumlarını tahmin etmeye yönelik yeni ve etkili bir metot geliştirilmiştir. Bu çalışmadaki ana motivasyon kaynağı, alın-dişli ihtiva eden aktarma sistemlerinde son dönemlerde gözlenen gelişmeler ve bu sistemlerin helikopter sanayisindeki kullanımıdır. Son otuz yılda, alın-dişli aktarma sistemleri birçok araştırmanın konusu olmuştur. Ama, alın-dişli kavrama direngenliği tam olarak modellenememiştir. Bu çalışma için, çok yerden kavramalı evolvent düz-dişliler tarafından sürülen tork-ayrımlı alın-dişli sistemi için doğrusal olmayan bir dinamik analiz modeli geliştirilmiştir. Bunun için, beş düz-dişli ve iki alın-dişli içeren bir toplu kütleli sistem kurulmuştur. Sistem, yedi dönme serbestlik derecesine sahiptir. Tüm dişli çarkların rijit disk olduğu varsayılmıştır. Kurulan tork-ayrımlı model, iki giriş, iki çıkış ve üç avare dişlisinden oluşmaktadır. Tüm kavrama parametreleri (kavrama direngenliği, kavrama sönümlemesi vs), zamanla değişen özelliğe sahiptir. Diş boşlukları modele, açıklık-tipi doğrusal olmayan bir eleman olarak dahil edilmiştir. Önerilen metot, dişli çiftine ait zaman değişimli kavrama direngenliğini, alın-dişli ve düz-dişli geometrisinden türetilen nokta bulutlarını kullanarak, Sonlu Şerit Metodu ile hesaplamaktadır. Doğrusal olmayan hareket denklemleri, Harmonik Denge Metodu ile kararlı hal cevapları için çözülmüştür. Sonuçların doğruluğu, nümerik integral çözümleri ile karşılaştırılmıştır. Kararlılık, Floquet Teorisi ve Poincare kesitlerinden elde edilen çatallanma diyagramları ile gözden geçirilmiştir. Her bir düz-dişli ve alın-dişlinin birbirine geçmesi sırasındaki kavrama fazı, etki eden statik tork miktarı ve diş boşluk değişimlerinin, sistem tepkisine etkisi araştırılmıştır. Altharmonik hareketin sistem cevabına etkisi gösterilmiştir. Ayrıca, sistemin tork-ayrım karakteristiği incelenmiştir.

Anahtar Kelimeler: Alın-Dişli Sistemlerinin Doğrusal Olmayan Dinamiği, Doğrusal Olmayan Dişli Dinamiği, Tork-Ayrımı, Helikopter Güç Aktarma Sistemleri, Sonlu şerit metodu

To My Dear Wife,

Gülhan

&

To Our Little Cats,

Bis and Köpük

ACKNOWLEDGMENTS

The author wishes to express his heartfelt gratitude to his supervisor Prof. Dr. H. Nevzat Özgüven, for his continuous guidance, encouragements, invaluable patience throughout the preparation of this thesis. This endeavor would not have been possible without his continuous support.

The author would also like to take this opportunity to extend his deepest gratitude to Prof. Dr. Yavuz Yaman for his existence, wisdom and valuable suggestions.

The author would also like to thank Prof. Dr. Ender Ciğeroğlu for his valuable suggestions and comments.

The author would also like to express his sincere gratitude to his co-supervisor and close friend Assoc. Prof. Dr. Zihni B. Sarıbay for his initiatives and valuable guidance, advice, criticism, encouragements and insight throughout the research. The author could not have undertaken this journey without his existence.

The author is extremely grateful to his Thesis Monitoring Committee members, for attending nine years lasted meetings that he will miss and will never forget.

The author would like to send his very special thanks to Mr. Okan Yıldırım, for long hours/years of discussion on finite strip and quasi prism elements, Mr. Fatih Yılmaz, for his guidance and help during the submission period of the thesis.

The author would also extend his thanks to everyone, in particular to Mr. Fatih Mutlu Karadal, for the last five years who continuously asked whether this thesis study was completed or not.

The author is greatly indepted to his parents, his sister and his brother for their love and sacrifice.

This work is dedicated to author’s dear wife Gülhan, and their little cats Bis and Köpük.

TABLE OF CONTENTS

ABSTRACT v

ÖZ vii

ACKNOWLEDGMENTS x

TABLE OF CONTENTS xi

LIST OF TABLES xv

LIST OF FIGURES xvi

CHAPTERS

1 INTRODUCTION 1
  1.1 Introduction 3
  1.2 Literature Review 3
    1.2.1 Face-Gear Geometry 3
    1.2.2 Mesh Stiffness and Dynamic Modelling 4
    1.2.3 Split-Torque Systems 6
  1.3 Motivation, Scope and Objectives 17
  1.4 Organization of the Thesis 19
2 FACE-GEAR AND PINION TOOTH SURFACE GENERATION 21
  2.1 Introduction 21
  2.2 Surface Generation 22
    2.2.1 Transformation of the Spur-Shaper Surface to the Face-Gear 26
    2.2.2 Face-Gear Surface Equations 29

2.2.3 Limiting Conditions of Surface Generations 30
2.3 Derivation of analytical formulas 43
2.3.1 Inner Radius Formulation 44
2.3.2 Outer Radius Formulation 45
2.3.3 Face Width Formula 46
2.4 Unloaded Tooth Contact Analysis 47
2.4.1 Procedure for the Unloaded Tooth Contact Analysis 48
2.4.2 The Obtained Results and Discussion 50
2.5 Model for The Face-Gear Thickness Variation 55
3 MESH STIFFNESS CALCULATIONS 59
3.1 Stiffness Calculations for One-Tooth 60
3.1.1 Bending Stiffness Contribution 60
3.1.2 Contact Stiffness Contribution 96
3.2 Mesh Stiffness Calculations for a Face-Gear and Spur-Pinion 99
3.2.1 Introduction 99
3.2.2 Application of Finite Strip Method to Mindlin Plate Theory with Cubic B-Splines 103
3.2.3 Combining the stiffnesses of the meshing pairs 109
3.2.4 Determining the Appropriate Strip Elements 115
4 MATHEMATICAL MODELS AND DYNAMIC ANALYSIS OF FACE-GEARS 121
4.1 Non-linear Dynamic Model for a Split-Torque Face-Gear Drive System 121
4.1.1 Mathematical Model 123
4.1.2 Mesh Phasing 129

4.1.3 Effect of Directional Rotational Radius 133
4.1.4 Solution Method 135
4.2 Non-linear Dynamic Model For A Face-Gear and Spur Pinion Pair 136
5 PARAMETRIC STUDIES 139
5.1 Case Studies for a Pair of Face-Gear and Pinion 139
5.1.1 Effect of Backlash 140
5.1.2 Effect of Static Torque 145
5.1.3 Effect of Damping and Static Torque on Subharmonic Response . 147
5.2 Case Studies for Split-Torque Face-Gear Drive System 149
5.2.1 Effect of Orientation Angle Pattern 149
5.2.2 Effect of Time-Variant Parameters 160
5.2.3 Effect of Power Values and Torque-Split Amounts 160
6 CONCLUSION AND FUTURE WORK 169
6.1 Summary & Conclusion 169
6.2 Future Work 172
REFERENCES 175

APPENDICES

A. NURBS Approximation 191
B. Thin Slice Method 194
C. Rayleigh-Ritz Approximation 196
D. Finite Prism Method and Quasi-Prism Method 203
E. Contact Stiffness Methods 213
F. Mathematica Symbolic Code for The Directional Rotational Radius 221
G. Dynamic Modelling of Split-Torque Face-Gear Drive Systems 225

CURRICULUM VITAE 229

LIST OF TABLES

TABLES

Table 2-1 Comparison to selected literature 42

Table 2-2 Input parameters 57

Table 3-1 Comparison of FE and FSM deflection results for Case-1, Case-2, and Case-3 78

Table 3-2 Comparison of FE and FSM deflection results for Case-4.................... 79

Table 3-3 Input values 96

Table 3-4 Input parameters 110

Table 3-5 Rotation angles and corresponding time instants for TP1.................. 114

Table 3-6 Instants when the tooth pairs mesh or lose contact 115

Table 3-7 Comparison of FSM results with 3D FEM ABAQUS results, Case-1 117

Table 3-8 Comparison of FSM results with 3D FEM ABAQUS results, Case-2 118

Table 4-1 Phase differences between the meshes 132

Table 5-1 Parameters of the gear pair 139

Table 5-2 Parameters of the system 149

Table 5-3 Orientation angles of the pinions.. 155

LIST OF FIGURES

FIGURES

Figure 1-1 A face-gear and a spur pinion mesh 1
Figure 1-2 Face-Gear and spur pinion assemblies at different shaft angles 2
Figure 1-3 Application of face-gear drive in helicopter transmission [25] 2
Figure 1-4 Sikorksy CH-53 type helicopter split-torque main transmission, a) Helicopter full view, b) Motor and main transmission configuration, c) main transmission showing three motor input, d) the main transmission showing only one motor input 7
Figure 1-5 MI- 26 type helicopter split-torque main transmission, a) Helicopter full view, b) main transmission showing two motor input, c) Closer view for main transmission showing two motor input, d) Torque distribution sketch as a circuit diagram 9
Figure 1-6 Epicyclic torque splitter 10
Figure 1-7 Split-torque helicopter transmission with two power-branches utilizes a self-adjusting system 11
Figure 1-8 Conventional quill shaft [35] 12
Figure 1-9 Sikorsky CH-53K One Motor Input Stage 13
Figure 1-10 Torque-split design with a dual power concept and clocking angle measurement [42] 14
Figure 1-11 The split-torque system and the corresponding FE model in ABAQUS 15
Figure 1-12 The RDS-21 demonstrator gearbox 15
Figure 1-13 Load-sharing quill shafts 16
Figure 1-14 Split-torque face-gear drive system 17
Figure 1-15 a) Example 3D model b) Produced tooth geometries 18
Figure 2-1 Face-gear and spur shaper dimensions 23
Figure 2-2 a) Spur shaper parameters [15]; b) Shaper from side view with contact lines; c) face-gear tooth 25

Figure 2-3 Flow diagram of face-gear modeling process 26
Figure 2-4 Spur-shaper and face-gear assembly 27
Figure 2-5 Undercut regions on face-gear tooth surface and pointing 30
Figure 2-6 The undercut definition, [62] 31
Figure 2-7 One point of interest at the contact line of the meshing teeth [63], [56]32
Figure 2-8 Surface normal and the directional derivatives over the specified surface 33
Figure 2-9 Cross section of tooth profiles of spur-shaper and the face-gear at the pointing cross section, cross section Π_2 depicted in Figure 2-11 [13] 36
Figure 2-10 Cross section of tooth profiles of spur-shaper and the face-gear at any cross section before the pointing, cross section Π_1 depicted in Figure 2-11 [13]... 38
Figure 2-11 Cross sections Π_1 and Π_2, [13] 39
Figure 2-12 Enveloped u_s , θ_s and ϕ_s parameters with N_s = 20, N_2 = 120, γ = 90˚, m_o = 5.08 mm 41
Figure 2-13 a) Shaper tooth space, b) Face-gear tooth flank in their local coordinate frames.. 41
Figure 2-14 Face-gear tooth forms from viewed on y_2-z_2 plane 43
Figure 2-15 a) Face-gear & spur shaper relations and b) shaper tooth dimensions 43
Figure 2-16 Assembly of a face-gear drive, mating surfaces of spur-pinion.......... 50
Figure 2-17 Unloaded Static Transmission Error, Case-1 51
Figure 2-18 Unloaded Static Transmission Error, Case-2 52
Figure 2-19 Unloaded Static Transmission Error, Case-3 53
Figure 2-20 Unloaded Static Transmission Error, Case-1, 2 and 3 54
Figure 2-21 Contact points on face-gear, for all three cases, 3D view 54
Figure 2-22 Contact points on face-gear, for all three cases, view along yz-axis .. 55
Figure 2-23 a) Point cloud extracted for a typical face-gear and b) the assigned finite strip elements 56
Figure 2-24 Original spur-gear involute profile and the data generated via NURBS curves, with p=3 and 101 control points along the x axis...................................... 57

Figure 2-25 The point cloud for the original face-gear surface and the fillet, and data generated via NURBS curves with p=3, discretizing face-width direction by 9 grids and profile direction by 8 grids 58
Figure 3-1 Uniform cantilever beam assumption for the mesh stiffness........ 59
Figure 3-2 A face-gear tooth with several slices along its face width [91]........ 61
Figure 3-3 a) Uncoupled and b) coupled thin slices of a gear [91]........ 62
Figure 3-4 Spur Gear straight loading on the tip........ 64
Figure 3-5 Comparison of thin slice method results with the FE results for straight loading........ 64
Figure 3-6 a) Spur gear oblique loading on the conjugate surface, b) FE displacement results........ 65
Figure 3-7 Comparison of thin slice method results with the FE results for oblique loading........ 66
Figure 3-8 Utilized plate types a) a uniform plate, b) one-axis trapezoidal plate, .. 67
Figure 3-9 FEM results for uniform bending plate, uniform pressure loading........ 68
Figure 3-10 FEM results for uniform plate, loading along a line........ 69
Figure 3-11 FEM results for uniform plate, point load........ 69
Figure 3-12 FEM results for one-axis tapered plate model, pressure loading........ 71
Figure 3-13 FEM results for two-axis tapered plate model, uniform pressure loading 72
Figure 3-14 A plate discretized with n finite strip elements........ 73
Figure 3-15 Sine functions for seven harmonics for SFMS........ 73
Figure 3-16 Cosine functions for seven harmonics for SFSM........ 74
Figure 3-17 B3 spline functions, for NFSM, specified for a free variable at the boundary of the problem........ 74
Figure 3-18 Spline functions for NFSM, specified for a fixed variable at the boundary of the problem........ 75
Figure 3-19 A finite strip element........ 75
Figure 3-20 a) 2-noded, b) 3-noded, c) 4-noded Finite Strip Element with the appropriate polynomials, [97]........ 77

Figure 3-21 Comparison for deflection Case-4, a) MSC Nastran FE Model with 50 CQUAD elements, b) 2-noded FSM Model with four strip elements, c) 3-noded FSM Model with four strip elements, d) 4-noded FSM Model with four strip elements 79

Figure 3-22 Comparison for deflection Case-4, a) MSC Nastran FE Model with 50 CQUAD elements, b) 2-noded FSM Model with four strip elements 80

Figure 3-23 Prismatic solids discretized in two dimensions a) with FPM and b) with QPM [99] 81

Figure 3-24 A typical QPM element with axodes, [108]....................................... 82

Figure 3-25 a) The element numbering and b) the node numbers for the 2D discretization 83

Figure 3-26 a) The prism with a constant cross-section along the longitudinal axis (FPM), b) the prism with a variable cross-section along the longitudinal axis (QPM) 84

Figure 3-27 Application of point load, constant cross-section 84

Figure 3-28 FPM comparison with 3D FEM, element 1, location [1,-1] (location is depicted in Figure D-1).. 85

Figure 3-29 FPM comparison with 3D FEM, element 3, location [1,-1]] (location is depicted in Figure D-1).. 86

Figure 3-30 FPM comparison with 3D FEM, element 1, location [1,-1], number of utilized harmonics is 8, number of gauss points varies.. 87

Figure 3-31 FPM comparison with 3D FEM, element 1, location [1,-1], gauss point is 6, number of the utilized harmonics varies 87

Figure 3-32 FPM comparison with 3D FEM, element 7, location [-1,1], number of gauss points, and number of utilized harmonics vary.. 88

Figure 3-33 FPM comparison with 3D FEM, element 5, location [-1,1], number of gauss points, and number of utilized harmonics vary.. 88

Figure 3-34 Application of line load, constant cross-section; stress distribution, and deformation results.. 89

Figure 3-35 FPM comparison with 3D FEM, constant cross-section, line load application, element 1, location [-1,-1], gauss point is 4, harmonics 6 89

Figure 3-36 FPM comparison with 3D FEM, constant cross-section, line load application, element 3, location [-1,-1], gauss point is 4, harmonics 6 90
Figure 3-37 FPM comparison with 3D FEM, constant cross-section, line load application, element 1, location [1,-1], gauss point is 5, harmonics 6 90
Figure 3-38 a) 3D FE model and application of line load, b) ABAQUS results..... 91
Figure 3-39 Comparison with 3D FEM, variable cross-section, line load application, element 1, location [1,-1], gauss point is 4, with harmonics 5 or 6........................ 92
Figure 3-40 Comparison with 3D FEM, variable cross-section, line load application, element 3, location [1,-1], gauss point is 4, with harmonics 5 or 6........................ 92
Figure 3-41 Comparison with 3D FEM, variable cross-section, line load application, element 5, location [1,-1], gauss point is 4, with harmonics 5 or 6........................ 93
Figure 3-42 Comparison with 3D FEM, variable cross-section, line load application, element 7, location [1,-1], gauss point is 4, with harmonics 5 or 6........................ 93
Figure 3-43 a) Double axis-trapezoidal tapered plate b) Face-gear 94
Figure 3-44 Contact stiffness a) at the first contact line, by b) Weber/Banascheck, c) Palmgren, d) Brewe&Hamrock, for various load levels 97
Figure 3-45 Contact stiffness a) at the fifth contact line, by b) Weber/Banascheck, c) Palmgren, d) Brewe&Hamrock, for various load levels 98
Figure 3-46 Contact stiffness a) at the sixth contact line, by b) Weber/Banascheck, c) Palmgren, d) Brewe&Hamrock, for various load levels 98
Figure 3-47 Contact stiffness a) at the twenty fifth (last) contact line, by b) Weber/Banascheck, c) Palmgren, d) Brewe&Hamrock, for various load levels 99
Figure 3-48 a) Generated point cloud for the face-gear tooth profile and its fillet surface, b) the boundaries of the tooth with the point cloud, c) the boundaries of the tooth d) the discretized tooth into eight strip elements, e) the resulted finite strip elements 101
Figure 3-49 a) A typical curved finite strip discretization, isometric view, b) view in yz plane, c) the grids, six nodes along the profile direction (utilizing 7 cubic B3-spline functions) and four-noded element formulation along the face-width direction 102

Figure 3-50 The four-noded polynomial shape functions of the finite strip element for the face-width direction of the tooth 106
Figure 3-51 The cubic B3-spline functions for equally spaced sections along the length *a* 107
Figure 3-52 The utilized cubic B3-spline functions for the strip element along the cantilevered side to free side of the toot (profile direction) 108
Figure 3-53 Meshed surfaces of a face-gear and its shaper at a time along a contact line a) at the meshing position b) a separated view of the case in a) 109
Figure 3-54 Averaged stiffness along the contact line 109
Figure 3-55 Face-gear tooth pairs in contact 110
Figure 3-56 Tooth pairs -1, 0 and 1 are in contact, *Case [-1 0 1]* 111
Figure 3-57 Tooth pairs 0 and 1 are in contact, *Case [0 1]* 111
Figure 3-58 Tooth pairs 0, 1 and 2 are in contact, *Case [0 1 2]* 112
Figure 3-59 Tooth pairs 1 and 2 are in contact, *Case [1 2]* 112
Figure 3-60 Tooth pairs 1, 2 and 3 are in contact, *Case [1 2 3]* 113
Figure 3-61 Tooth pairs 1 and 2 are in contact, *Case [1 2]* 113
Figure 3-62 Total Mesh stiffness 115
Figure 3-63 a) Generated tooth geometry, b) 3D FE model in ABAQUS 116
Figure 3-64 Averaged deformation vs number of finite strip elements, Case-1 ... 118
Figure 3-65 Averaged deformation vs number of finite strip elements, Case-2 ... 119
Figure 4-1 a) Example 3D model b) Produced tooth geometries 121
Figure 4-2 Flow diagram for the dynamic analysis of the drive system 122
Figure 4-3 Split-torque face-gear drive system 122
Figure 4-4 Power flow of the split-torque system 123
Figure 4-5 Dynamic model for the split-torque system 124
Figure 4-6 Split-torque and idler arrangements 130
Figure 4-7 Orientation of the pinions on the face-gear 131
Figure 4-8 Involute profile of the shaper 134
Figure 4-9 Dynamic model for a pair of face-gear and a spur-pinion 137

Figure 5-1 Comparison of the RMS values of the response (gear mesh displacement between face-gear and the pinion) for Case-1, increasing backlash from b_c =5 μm to 200 μm, frequency range ω=0.01ω_c to ω=1.4ω_c 140

Figure 5-2 Comparison of the RMS values of the response (gear mesh displacement between face-gear and the pinion) for Case-1, for the backlash values b_c =5, 15, 25, 33 μm and 34 μm, frequency range ω=0.01ω_c to ω=2.5ω_c 141

Figure 5-3 Comparison of the RMS values of the response (gear mesh displacement between face-gear and the pinion) for Case-2, for the backlash values b_c =10, 15, 20, 25, 33 μm and for all values between 34 μm and 200 μm, frequency range ω=0.01ω_c to ω=2.5ω_c 142

Figure 5-4 Comparison of the RMS values of the response (gear mesh displacement between face-gear and the pinion) for Case-3, for the backlash values b_c =10, 15, 25, 35, 45, 50, 55 μm and for all values between and 60 μm and 200 μm, frequency range ω=0.01ω_c to ω=2.5ω_c 143

Figure 5-5 Comparison of the RMS values of the response (gear mesh displacement between face-gear and the pinion) for Case-4, for the backlash values b_c =5 μm, 7 μm, 13 μm, 17 μm, 23 μm, and for all values between and 24 μm and 200 μm, frequency range ω=0.01ω_c to ω=2.5ω_c 144

Figure 5-6 Comparison of the RMS values of the response (gear mesh displacement between face-gear and the pinion) for Case-4, increasing reference torque values for b_c =20 μm, frequency range ω=0.01ω_c to ω=2.5ω_c 146

Figure 5-7 Comparison of the RMS values of the response (gear mesh displacement between face-gear and the pinion) for Case-4, increasing reference torque values from 1.00 T to 100 T, for b_c =20 μm, frequency range ω=0.01ω_c to ω=2.5ω_c 146

Figure 5-8 Comparison of the RMS values of the response (gear mesh displacement between face-gear and the pinion) for the damping values, 1600 N.s/m time simulation (o), 1600 N.s/m HBM solution (–), 1800 N.s/m HBM solution (–), 2400 N.s/m HBM solution (–), 2500 N.s/m HBM solution (–), 3000 N.s/m HBM solution (–), 3250 N.s/m HBM solution (–),for the frequency range ω=0.1ω_c to ω=2.5ω_c148

Figure 5-9 Comparison of the RMS values of the response (gear mesh displacement between face-gear and the pinion) for the torque values, T_g=1.00T (–), T_g=1.05T (–), T_g=1.10T (–), T_g=1.15T (–), T_g=1.18T (–), T_g=1.20(–), for the frequency range $\omega=0.1\omega_c$ to $\omega=2.5\omega_c$ 148

Figure 5-10 Comparison of RMS value of the gear mesh displacements at ten meshing locations, 3-harmonic HBM (—), and time simulation (o) 151

Figure 5-11 Comparison of the RMS values of the response (gear mesh displacement between lower face gear and one of the idler pinions), 3-harmonic HBM (—), 1-harmonic HBM with ½ sub-harmonic solution (—) between 1.00 ω_c and 1.92 ω_c, and the time simulation results (o) 152

Figure 5-12 (a) Time series (b) power spectrum, (c) Phase projection, (d) Poincare section, at $\omega=1.65\ \omega_c$ 153

Figure 5-13 (a) Time series (b) power spectrum, (c) Phase projection, (d) Poincare section, at $\omega=1.16\ \omega_c$ 154

Figure 5-14 Visual representation of the Case Study Sets, a) Set-1 of the parametric study, b) Set-2 of the parametric study 155

Figure 5-15 The RMS values of the gear mesh displacement between LFG and P5 for Set-1; (—) Case-1, (---) Case-2, (−·−) Case-3 156

Figure 5-16 The RMS values of the gear mesh displacement between LFG and P5 for Set-2; (—) Case-4, (---) Case-5, (−·−) Case-6 157

Figure 5-17 The RMS values of gear mesh displacement between LFG and P_5 for Set-2, the regions of unstable points between $\omega=1.0\omega_c$ and $\omega=2.4\omega_c$; Case-4, (—) 3-harmonic HBM, (···) 1-harmonic HBM with ½ sub-harmonic; Case-5 (—) 3-harmonic HBM, (···) 1-harmonic HBM with ½ sub-harmonic; Case-6 (—) 3-harmonic HBM, (···) 1-harmonic HBM with ½ sub-harmonic, (·) stable solution, (*) unstable solution 158

Figure 5-18 Bifurcation diagrams for the RMS values of gear mesh displacement between LFG and P_5 for Set-2, a) Case-4, b) Case-5, c) Case-6 159

Figure 5-19 Modified dynamic model of the split-torque face-gear drive system 161

Figure 5-20 W_{tpu}^i and W_{tpl}^i at the ith pinion 163

Figure 5-21 Torque split ratios for the pinions in the face-gear drive system 164
Figure 5-22 Torque split ratios for the input pinion P_1 165
Figure 5-23 Torque split ratios for the input pinion P_3 166
Figure 5-24 Torque split ratio for the output pinion P_2 167
Figure 5-25 Torque split ratios for the idler pinion P_4 and P_5 167
Figure 5-26 Achieved torque split ratios for the specified system 168
Figure B-1 A slice for an involute profile 194
Figure C-1 A slice for an involute profile 196
Figure D-1 8-noded isoparametric element 203
Figure D-2 A general prism to be modelled with FPM 205
Figure D-3 Mapping from pyhsical system to element in natural coordinate system 209
Figure D-4 Chebyshev functions 210
Figure D-5 Modified Chebyshev functions 210
Figure E-1 Two gears in contact [75] 218
Figure E-2 two elliptically shaped elastic solids in contact, [137–142] 220

CHAPTER 1

INTRODUCTION

A face-gear drive system comprises an involute spur or a helical pinion meshing with a face-gear. This gear drive system is generally utilized to transform the torque between intersected and crossed shafts. An example of a face-gear drive meshing with a spur pinion is shown in Figure 1-1. A set of face gear drive systems with different shaft angles is shown in Figure 1-2.

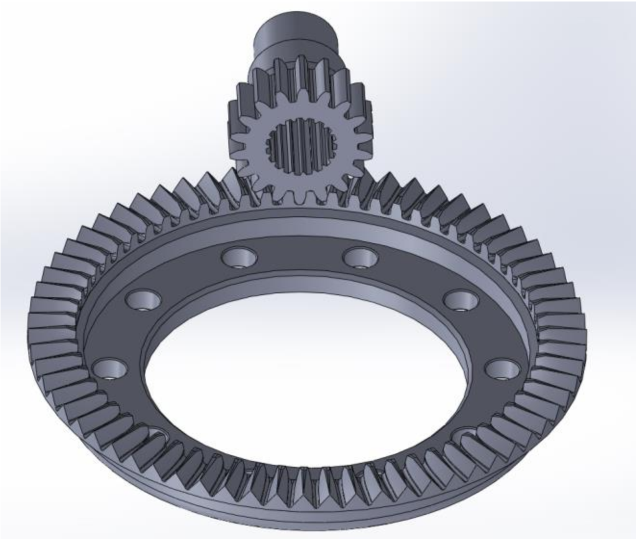

Figure 1-1 A face-gear and a spur pinion mesh

The face-gear drive system enables weight reduction and volume saving by load sharing or torque-splitting capabilities [6-8]. Therefore, such drive systems are generally found in the helicopter or marine transmissions. An example of a helicopter's main gearbox incorporating a torque split among two face-gears at the engine input is given in Figure 1-3.

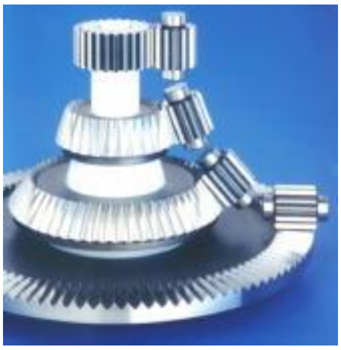

Figure 1-2 Face-Gear and spur pinion assemblies at different shaft angles

Before 1990's, face-gear drive systems were known to be used for low-power applications. By then, helicopter companies started several researches for a light and reliable main rotor drive system having advanced capabilities of torque-split. Hence, face-gear drives become popular due to their several advantages [1–3].

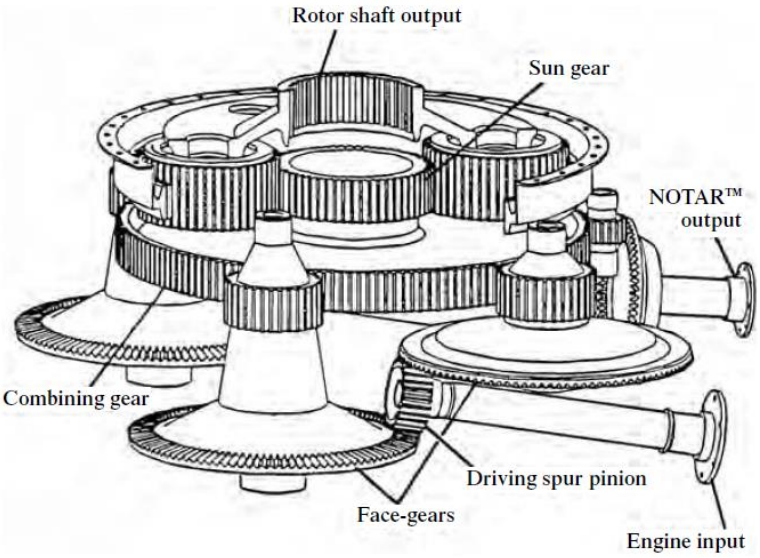
Rotor shaft output
Sun gear
NOTAR™ output
Combining gear
Driving spur pinion
Face-gears
Engine input

Figure 1-3 Application of face-gear drive in helicopter transmission [25]

1.1 Introduction

Split torque face-gear drive systems are typically driven by spur or helical pinions meshing with one or two face-gears, which are utilized to deliver power between intersecting shafts and reduce transmission weight by introducing torque sharing and torque splitting capabilities [4,5].

The face-gear drives have been investigated for helicopter transmission systems due to potential weight savings [2,3]. This drive train consists of an involute spur pinion meshing with a face gear, as shown in Figure 1-1. One of the first high-power face gear designs is named Cylkro Angular Face Gear Transmission [6,7].

Different methods to generate the spur shaper and the face-gear tooth are presented in [8] and [9]. The design aspects and validation of face gears are presented in [10] and [11]. The benefits of the face gears are (i) reduced sensitivity to the bearing contact to gear misalignment, (ii) reduced level of noise due to a very low level of transmission error, (iii) more favorable power transfer from one tooth to another and (iv) tolerance to the assembly inaccuracies compared to the spiral bevel gears [12,13].

1.2 Literature Review

1.2.1 Face-Gear Geometry

The theory of face gears was not sufficiently developed for high-power applications until the first mathematical tooth modeling and the computational tooth contact analysis (TCA) work performed by Litvin et al. [14,15]. The tooth geometries of a spur pinion and a conjugate face-gear are defined using the gearing theory and differential geometry principles. The surface of the face gear is derived from the simulation of meshing with the spur shaper. The critical dimensions of the produced face gear are identified from the limiting conditions of the geometry. These are tooth undercutting at the inner diameter and tooth pointing at the outer diameter. Hence, an exact tooth surface equation and tooth enveloping parameters are generated for mathematical modeling, contact analysis, and machine settings.

Face gears are studied by several researchers. Litvin et al. [14] generated the surface of a face-gear by simulating the machine tool motions. He also studied tooth contact and bending stress analyses using the finite element method (FEM) [8,16]. Heath et al. performed experiments on tooth contact performances and failure modes of face-gears [17], conducted split torque tests on a 250 hp face gear transmission with two inputs, two idlers system [4,5], and also performed tests to seek face-gear surface fatigue characteristics [18].

1.2.2 Mesh Stiffness and Dynamic Modelling

There are a limited number of studies on dynamic analysis of the face-gear drive systems. These studies may be collected under two titles, namely, quasi-static or dynamic analysis of face-gear meshing with spur-pinion pair, and quasi-static or dynamic analysis of split-torque face-gear drive systems.

Guingand et al. [19] presented a quasi-static analysis procedure for the load distribution among the face-gear pairs with experimental validation. The tooth root stresses and the resulting load sharing among the pairs are obtained with reasonable accuracy. The related deformations are calculated using FEA tools and the contact mechanics. Wang et al. [20] proposed a method for loaded tooth contact analysis of a face-gear pair, where bending and contact deformations are determined by FEA and Hertz theory. Load distribution under an applied torque among the tooth pairs is sought.

Peng et al. [21] investigated the parametric instability characteristics of a face-gear pair. An annular Kirchhoff plate with a moving spring is utilized to model the drive system. Floquet theory is used to calculate the stability of the system. The mesh stiffness is obtained through the contact ratio calculated by Tregold's approximation.

The spur pinion is assumed to be rigid, and the mesh stiffness is taken as the face-gear tooth stiffness. Later, this study (dynamic stability) was improved for a split-torque multi-pinion face-gear drive system [22].

Hu et al. [23] studied the effect of the mesh stiffness variation on the dynamic behavior of a 6 DOF (degree of freedom) face-gear pair. The bifurcation diagrams of the pair's response according to the pinion speed are presented. Chen et al. [24] investigated the effect of profile modification on the dynamic behavior of a 6 DOF face-gear pair where support stiffness is also considered. They demonstrated the effect of the static load on the input pinion through bifurcation diagrams, which are plotted according to the input speed of the pinion. In [21–24], the instantaneous contact ratio is calculated via Tregold's approximation, and with these calculated values, the time-varying mesh stiffness is obtained by assuming it to be rectangular.

Tang et al. [25] studied the effect of directional rotational radius variation on a face-gear pair's dynamic response. A single degree of freedom time-varying rotational model is proposed using finite element method tools to obtain mesh stiffness. Hu et al. [26] proposed a fourteen degree-of-freedom (DOF) coupled translational and rotational dynamic model of a face-gear pair. The effects of backlash and the applied torque on the system's dynamic response are sought. The mesh stiffness of the pair is calculated by the finite element method as in the previous references.

Aydogan et al. [27] proposed a nonlinear dynamic model for a multi-mesh face-gear split-torque system focusing on the effects of several mesh parameters (i.e., phasing, stiffness, backlash, and power values) on the system response.

Zhao et al. [28] studied quasi-static analysis of a torque-split face-gear drive system by a hybrid 3D finite element and lumped parameter model. The mesh stiffness of a pair is calculated by commercial software (ANSYS). The load sharing among the pinions is investigated by changing the support stiffness, the backlash, and the tooth number.

Feng et al. [29] proposed a geometric study of a face gear system with an involute helical pinion. The study does not give any mesh stiffness calculations. However, it refers to Ambarisha and Parker [30], which utilizes a 2D finite element model for a planetary set developed from a unique finite element-contact analysis solver specialized for gear dynamics, the Calyx package program.

Liu and Zhang [31] performed a quasi-static analysis to investigate the effect of shaft angle for a face-gear pair. Loaded Tooth Contact Analysis (LTCA) is performed by commercial software (ABAQUS). Dong et al. [32] presented a quasi-static analysis of a split-torque face-gear drive system. The effect of the pinions' orientations, the number of idlers, and the load sharing among them are discussed. ABAQUS is utilized for TCA and mesh stiffness calculations. Later, Dong et al. [33] presented a semi-analytical method for the calculation of mesh stiffness of the face gear.

Li and Zhao [34] studied the effects of rotational speed and a pinion's support stiffness on a face-gear pair's dynamic response. They presented the bifurcation characteristics of the pair's response concerning the change in the pinion's support stiffness and the rotational speed of the pinion.

1.2.3 Split-Torque Systems

Torque splitting is an important phenomenon in the helicopter industry due to its weight and volume saving advantage for a given reduction ratio. When torque is transmitted through several paths, the contact force between teeth becomes smaller, allowing smaller and lighter gears. In addition to weight saving, torque splitting allows redundancy; when any of the designed branches fails during operation, the required torque is transmitted through the intact paths [35].

The first reduction stage splits the main torque into more than one parallel branch. Each branch may also be split into several branches at different reduction stages. Generally, before the last stage, the split torques are collected through a collector gear, which drives the main rotor mast. Figure 1-4 shows the main transmission system for a typical Sikorsky CH-53 Helicopter [36,37], [37].

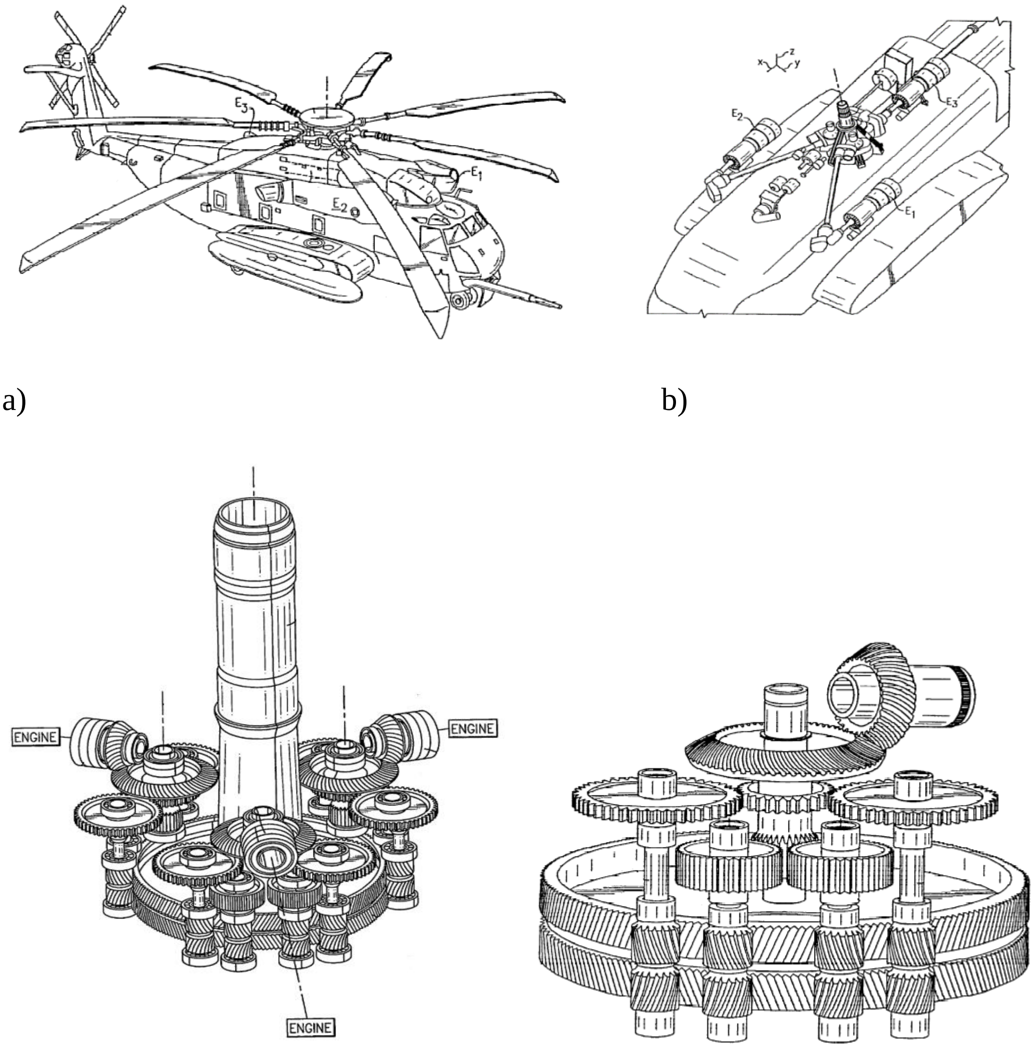

a) b)

c) d)

Figure 1-4 Sikorksy CH-53 type helicopter split-torque main transmission, **a)** Helicopter full view, **b)** Motor and main transmission configuration, **c)** main transmission showing three motor input, **d)** the main transmission showing only one motor input

As seen from Figure 1-4 (d), torque coming from one engine is splitted into four branches at the second stage of reduction and then each of these branches are further split into two branches. Finally, they are collected on double herringbone that rotates the main rotor mast.

As another example, the main transmission model of MI- 26 helicopter is given in Figure 1-5. Similar to the previous example, torque provided by one engine is split into four and then into two branches and collected at two bull gears to turn the main rotor mast of the helicopter. In Figure 1-5-c, the power or torque distribution is drawn as a circuit diagram.

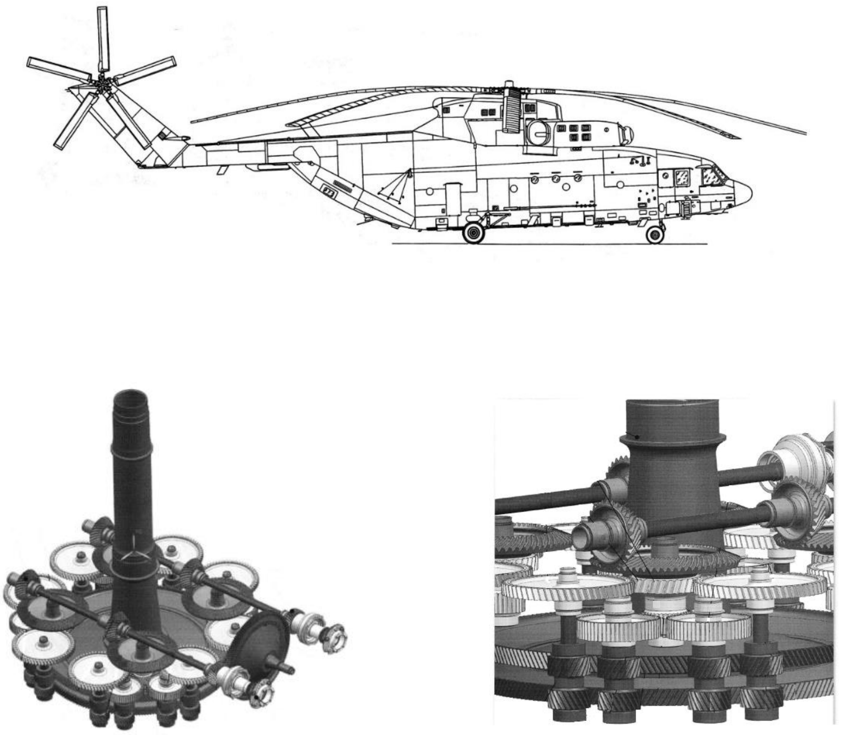

a)

b)

c)

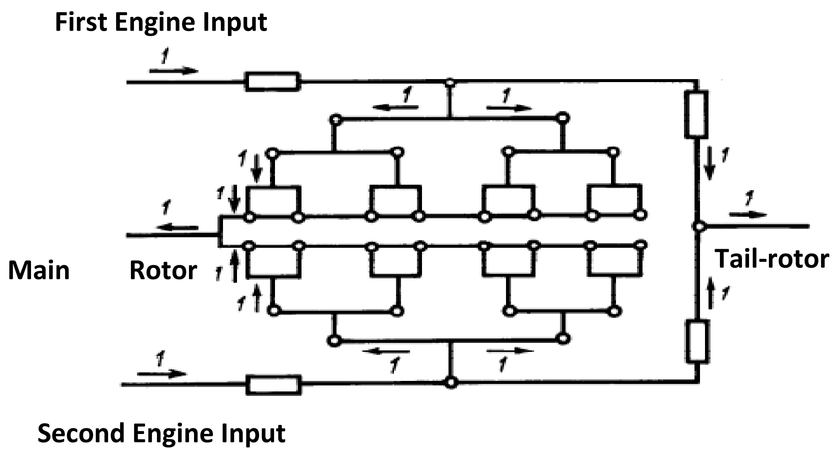

d)

Figure 1-5 MI- 26 type helicopter split-torque main transmission, **a)** Helicopter full view, **b)** main transmission showing two motor input, **c)** Closer view for main transmission showing two motor input, **d)** Torque distribution sketch as a circuit diagram

The disadvantage of this design is that the torque must be distributed equally between the parallel branches. In other words, if it is not an intended design feature, the torque at every parallel split-torque stage should be split evenly. Uneven load sharing at any parallel branch leads to excessive load at that branch, which causes the related components at that load path (gear, shaft, spline, bearing etc.) to wear earlier than the components located at the lesser load carrying branch.

In order to provide an even torque split, several methods have been proposed [35], such as,

a) **Geared differentials:** This method uses a differential mechanism similar to utilization in the automotive industry. A typical example of a planetary gear system is shown in Figure 1-6 [4], in which carrier rotates one branch and the ring gear drives the other branch, both of which drive a collector gear. The deviations from the intended geometry may lead to uneven load distribution.

This deviation is compensated by a small relative rotation of the sun gear and the ring gear [38].

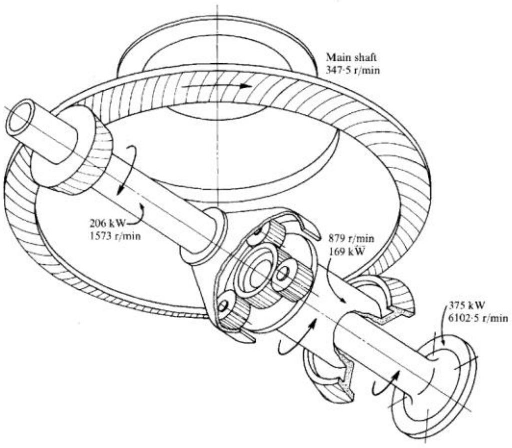

Figure 1-6 Epicyclic torque splitter

b) **Pivoted systems:** This method utilizes a floating pinion that finds a position to provide equal load share by seeking a position where tooth loads are equal. Irrespective of gear teeth errors or gearbox shaft misalignments, the input pinion will float and split torque between the two gears by a self-adjusting (or thrust-balancing) mechanism that moves the gears axially in response to excessive loads [38]. Figure 1-7 gives an example of a system in which axial thrust difference passes to a balance beam whose pivot motion induces sufficient angular motion to equalize the tooth loads [39].

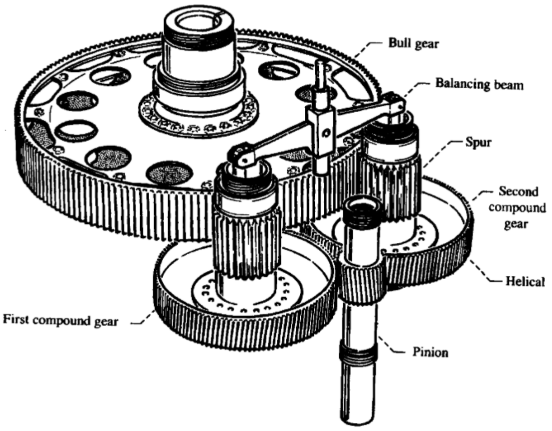

Figure 1-7 Split-torque helicopter transmission with two power-branches utilizes a self-adjusting system

c) **Quill shafts:** This method utilizes an assembly, allowing torsional flexibility between the connected gears. A torsion divider with a separate gear and pinion, each supported on its bearings, are connected through the quill shaft, which allows torsional flexibility.

   Achieving an even torque split between the two paths requires the gear train to have an adequate amount of torsional compliance. Cumulative tooth spacing errors, housing deformations, and assembly backlash values are the main obstacles to achieving an equal percent torque split.

   Figure 1-8 shows a conventional quill shaft. Due to lower torsional compliance of the quill shaft, when one load path transmits more torque than the other one, the angular deviation between the input shaft and the output shaft increases, and this increase leads the shaft that transmits less torque to increase its load. Apart from conventional quill shafts, quill shafts based on elastomeric elements and spring elements also exit [35].

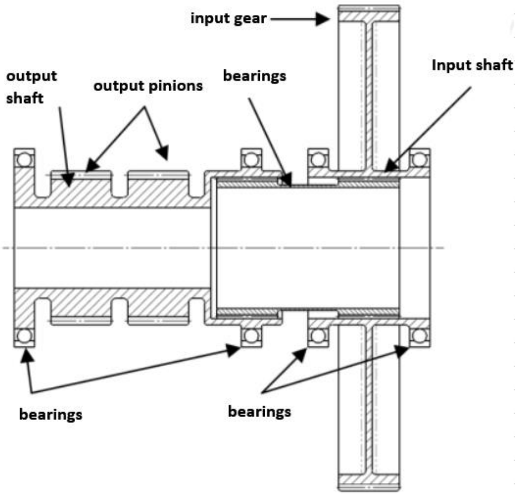

Figure 1-8 Conventional quill shaft [35]

Figure 1-9, as another quill shaft example, demonstrates the CH-53K helicopter one motor input stage mentioned above. The power from the engine at the 1st stage bevel pinion is split into two branches by the 2nd stage spur pinions, one of them is large, and the other is small. Each 2nd stage spur pinion further meshes with two 2nd stage spur gears. Since the torsional stiffness of the 1st stage gear shaft is very high, the torque split between the two 2nd stage spur pinions (large and small ones on the same shaft) becomes even. However, torque split between the 2nd stage spur gears that are in contact with the corresponding 1st stage spur pinions may not be even due to manufacturing errors, assembly tolerances, housing deformations, etc. By utilizing a torsionally soft quill shaft between each 3rd stage double herringbone pinions and 2nd stage spur gear, even torque split is achieved. Quill shafts have two spline meshes at both ends. The torsional windup angle of the quill shaft under a specified load level provides the required shaft flexibility for equal torque split [3,40,41].

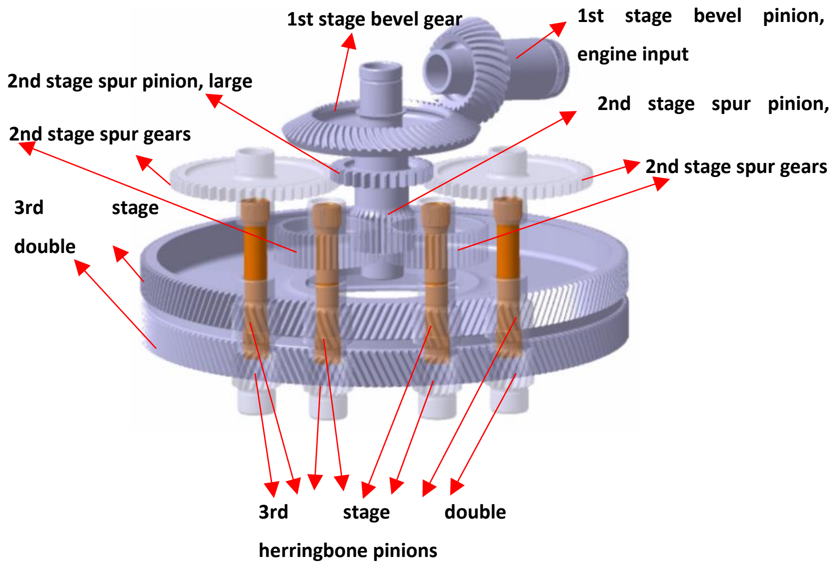
1st stage bevel gear
1st stage bevel pinion, engine input
2nd stage spur pinion, large
2nd stage spur gears
2nd stage spur pinion,
2nd stage spur gears
3rd stage double
3rd stage double herringbone pinions

Figure 1-9 Sikorsky CH-53K One Motor Input Stage

d) **Indexing or clocking:** There is no special component in this method. It requires the component to be manufactured according to strict tolerances and is correctly assembled. The clocking angle is utilized as a design parameter to provide an equal torque split among the parallel paths. The gears are clocked to eliminate any cumulative tooth spacing errors and assembly backlash values in order to provide that all gears are in contact [42–44].

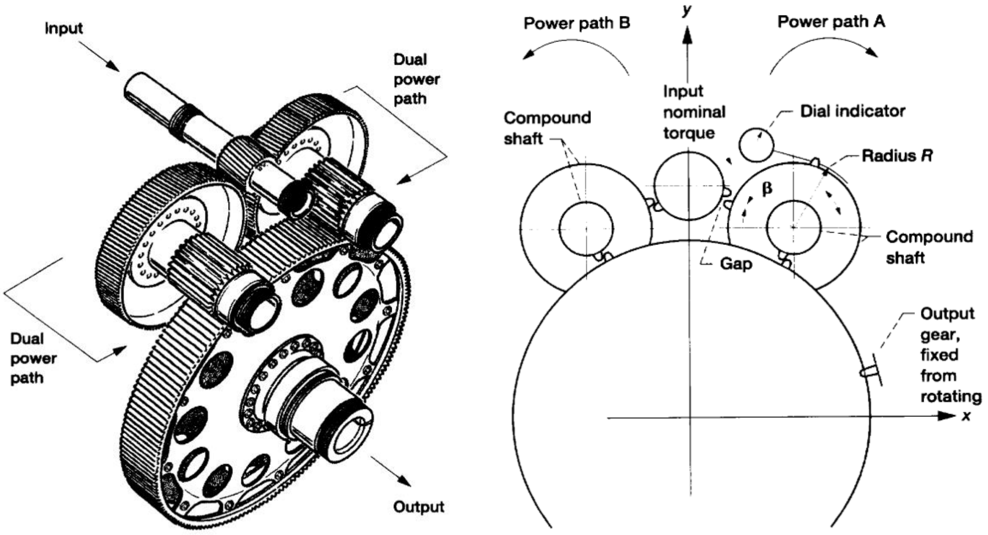
Input
Dual power path
Dual power path
Output
Power path B
y
Power path A
Input nominal torque
Compound shaft
Dial indicator
Radius R
β
Compound shaft
Gap
Output gear, fixed from rotating
x

Figure 1-10 Torque-split design with a dual power concept and clocking angle measurement [42]

Face-gear related studies in the literature utilize the floating pinion and quill shaft concepts. References [45] and [46] give test results for dual input, single output split-torque face-gear drive system with two idlers. The input pinion shafts utilize a cantilevered bearing mount arrangement. This component allows the pinions to float between the two face-gears and achieve a center of torque equilibrium. The test results show that using floating pinions in the face-gear system leads to a closely even torque split.

Boeing Company studied a split-torque face-gear drive system. In order to impose the effect of the quill shaft, they assumed the input pinions to float freely [47]. To simulate this, a 2D ABAQUS model is developed that comprises very soft springs in "1" and "2" directions (0.5 lb/in) for the input pinions where the idlers are fixed in those directions, Figure 1-11.

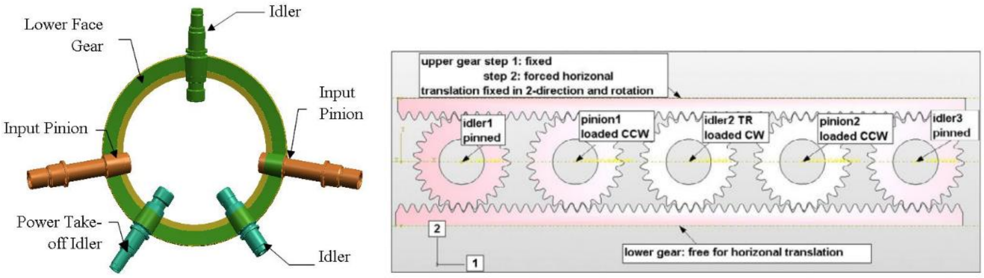
Lower Face Gear
Idler
Input Pinion
Input Pinion
Power Take-off Idler
Idler
upper gear step 1: fixed
step 2: forced horizonal
translation fixed in 2-direction and rotation
idler1 pinned
pinion1 loaded CCW
idler2 TR loaded CW
pinion2 loaded CCW
idler3 pinned
2
1
lower gear: free for horizonal translation

Figure 1-11 The split-torque system and the corresponding FE model in ABAQUS

The RDS-21 demonstrator gearbox of Sikorsky company employs two-stage face-gear meshes, given in Figure 1-12. It splits input torque in the 1st stage through one spur pinion meshing with a 90° face-gear and a 52.85° face-gear simultaneously [48,49]. The output torque from each 1st stage face-gear is further split into two branches before they are collected on a 90° 2nd stage large collector face-gear through helical gears and quill shafts. The difference between the torque split ratios for this design is less than 1%. Precision grinding of the gear tooth (eliminating the associated errors on teeth) yielded a 6% difference [48]. The utilized quill shafts are depicted in Figure 1-13.

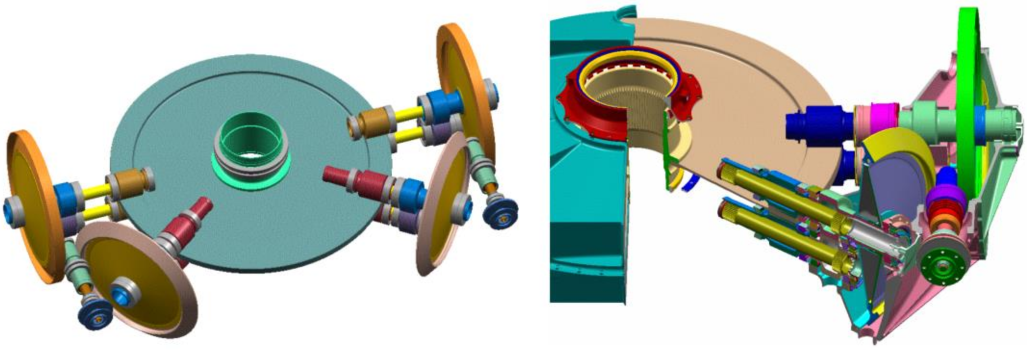

Figure 1-12 The RDS-21 demonstrator gearbox

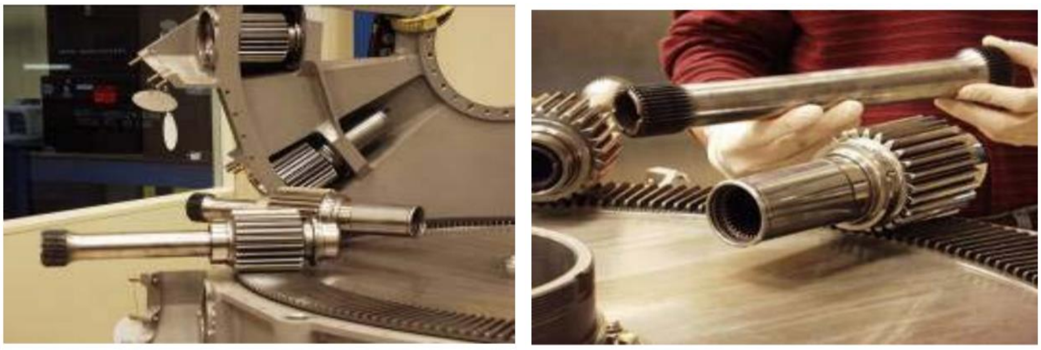

Figure 1-13 Load-sharing quill shafts

Reference [50] utilizes a floating pinion (drive pinion, labeled as 12, in Figure 1-14) carried by the power input shaft that meshes with two coaxial counter-rotating ring gears (upper and lower face gears, labeled as 15, 16 in Figure 1-14). The ability of the floating pinion to move in a direction parallel to the axis of the two ring gears (labeled as 15, 16 in Figure 1-14) enables the torque transmitted by the pinion (labeled as 12 in Figure 1-14) to be distributed equally between the two ring gears regardless of inevitable dimensional tolerances of the gearing, where at least one transmission pinion (idler pinion, labeled as 23 in Figure 1-14) is supported by elements flexible in a circumferential direction with respect to the ring gears.

However, this solve the issue for a single-input system. For multiple input systems, having more than one idler pinion makes it challenging to split even torque with the fixed axes of rotation. Several factors such as the tooth thickness, the position of the pinions, operating conditions may affect the equal load distribution [50]. This is the mesh phasing during the operation.

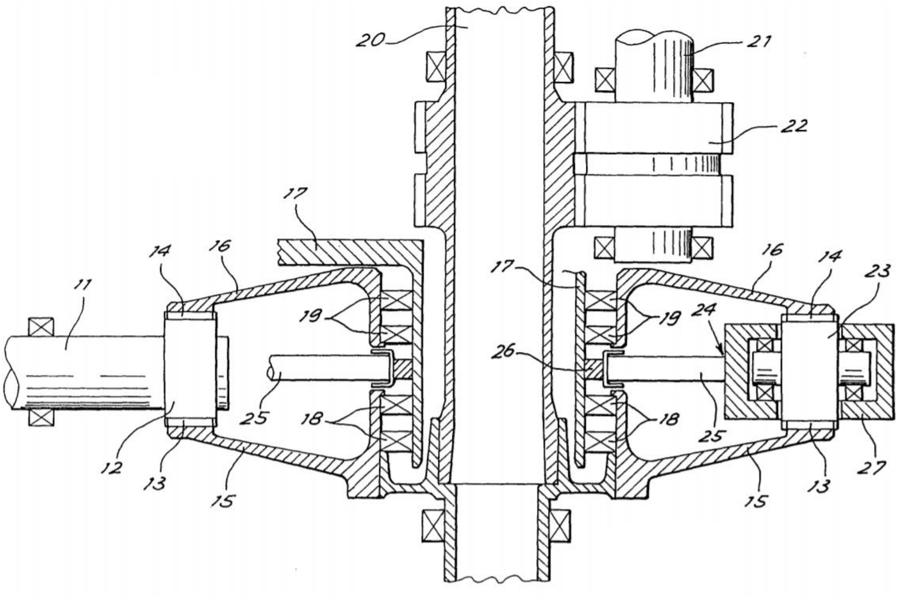

Figure 1-14 Split-torque face-gear drive system

The floating pinion, in fact, makes the pinion shaft a two-force member. The transmitted forces on the two force diametrically opposite meshing points on the pinion are forced to balance each other in order to accomplish even torque-split [51].

1.3 Motivation, Scope and Objectives

In the last three decades, there has been a significant increase in interest about research on main rotor drive systems in the helicopter industry to reduce the weight, to save volume while improving the efficiency and reliability.

The application of face-gear drive become popular among some new helicopters mainly due to its advantage to split torque between multiple drives more efficiently. In addition, when compared to existing drive systems, the application has several advantages, as listed in Chapter 1.1.

Face-gear dynamics is an emerging topic, and the current trend of the investigations relies on commercial tools for stiffness calculations. Although using these models for a frozen design is advantageous, it is not easy to make parametric studies and evaluations of the gear train several times. Therefore, in this thesis, a novel nonlinear dynamic model of a multi-mesh spur pinion-driven face gear split-torque drive system is developed and adapted to be used in complex parametric studies.

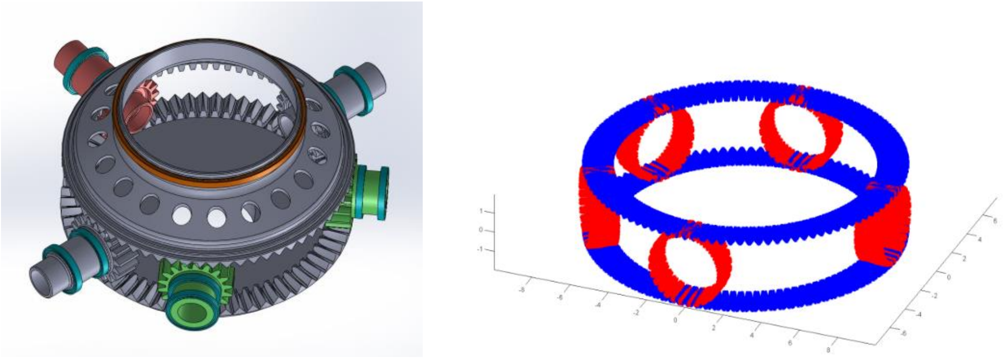

Figure 1-15 a) Example 3D model **b)** Produced tooth geometries

The nonlinear dynamic model of a split-torque face-gear drive system is composed of two face-gears (one output, one idler) and five pinions (two idlers, two inputs, one output). One of the face-gears is considered connected to the main rotor mast of a typical helicopter, while the output pinion emulates the tail rotor shaft of the helicopter. Two input pinions are the power input locations to the system from motors. The mesh stiffness and damping have time-varying characteristics. The model includes clearance type nonlinearity as a backlash at all meshing locations. Each backlash value at these meshing locations will also be set separately.

The dynamic model will utilize mesh stiffness values calculated through the exact face-gear tooth profile, which is based on the detailed theory of gearing and differential geometry of the face-gear. The bending contribution of the mesh stiffness will be calculated from the generated surface of the face gear and spur gear tooth.

The contact contribution will be calculated through the available analytical methods cited in the literature. The tooth will be modeled with Mindlin Plate Theory. In order to extract the compliance matrix at each meshing instant, the tooth surface will be discretized via Finite Strip Method.

The nonlinear differential equations will be solved with Harmonic Balance Method (HBM) in conjunction with the Arc-Length Continuation Method to obtain the system's dynamic response and to capture the stiffening and the softening regions within the specified frequency range. All time-variant parameters will be expressed in discrete Fourier Series.

Finally, several parametric studies will be performed to seek the effects of critical system parameters on the dynamic response of the proposed system. The potential design parameters will be proposed to be utilized in the system's preliminary and detailed design phases.

1.4 Organization of the Thesis

Chapter 1 presents a brief introduction to face-gear drive systems. A literature review is given in which the studies are grouped under the following titles, face-gear geometry, mesh stiffness, and dynamic modeling of face gears and split-torque systems. The motivation, scope, and objectives of this study are described. Finally, the organization of the thesis is portrayed.

Chapter 2 describes tooth surface generation for a typical face gear and a spur-shaper from a point cloud by the theory of gearing. Then, the surface fitting procedure, which uses Non-Uniform Rational B-Splines (NURBS) curves to approximate the thickness at any location on the tooth surface, is presented. Unloaded Tooth Contact Analysis for a face-gear and spur-pinion is presented with some special case studies.

Chapter 3 presents the stiffness calculations for a single gear tooth. Thin-Slice Method, Plate Models for Rayleigh-Ritz Approximation, Finite Strip Method (FSM), and Quasi-Prism Method (QPM) are investigated. For the bending contribution of the mesh stiffness calculations, FSM is chosen for its advantages, and discretization is performed by this method. The tooth is assumed to possess the properties of a Mindlin Plate. For the contact contribution of the mesh stiffness, several analytical methods given in the literature are presented and compared with each other, i.e., Hertz's, Conry's, Cornell's, Palmgren's, Weber’s and Brewe&Hamrock’s method.

Chapter 4 proposes a torsional mathematical model for multi-mesh split-torque face-gear drive systems. The model has 7 degrees of freedom. The system parameters, i.e. mesh stiffness, and damping, have time-varying characteristics. Clearance type nonlinearity is imposed into the model to represent backlash.

Chapter 5 demonstrates several parametric studies which investigate the effect of the orientation angle patterns of the pinions of a split-torque system, the effect of time-variant parameters, and the effect of power values on the system's dynamic response. The resulted mesh phasing effects and the resulted torque-split characteristics are demonstrated.

Finally, Chapter 6 summarizes the main findings of this study and discusses their applications for the design of split-torque face-gear drive systems. The potential critical design parameters for such systems in the preliminary and the detailed design phases are discussed. Currently, there is not any AGMA standard available for such systems. A discussion is performed here with the highlight of available AGMA standard for epicyclic gears and the results obtained with this thesis study.

CHAPTER 2

FACE-GEAR AND PINION TOOTH SURFACE GENERATION

2.1 Introduction

Face-gear geometry is generated as a point cloud by transforming the spur gear (shaper) tooth profile into face-gear tooth profile by simulating the machine tool motions. The position vectors resulted from the equation of the shaper surface is transformed into the face-gear position vector by simple and well-defined three rotation around appropriate axes [8,13,15,16,52–56]. The first transformation is defined as the rotation of spur-gear around its own rotation axis. Second transformation is defined as the rotation between the spur shaper and face-gear rotation axes. Finally, the third transformation is defined as the rotation of face-gear around its own rotation axis. For the conjugate action of tooth profiles, the equation of meshing equation is satisfied. At all-time instants, surface normal at the point of contact must be perpendicular to the sliding velocity between the two meshing surfaces. On the other hand, two limiting criteria exist for surface generation of a face-gear; namely undercutting condition and pointing condition. The first criterion (limiting point for the surface generation) denotes the cutting region of the involute spur-gear shaper that is beyond the active conjugate region and should be avoided. Since undercutting point is a singular point, normal vector for the face-gear surface should be equal to zero at the prescribed singular point. The second criterion, pointing, denotes the location where the thickness of the tooth on the top surface becomes zero. Whole procedure for the surface generation is well-defined in [8,13,15,16,52–56].

2.2 Surface Generation

The cross-sectional view of face-gear spur shaper mesh is schematically illustrated in Figure 2-1. Here, y_s-z_s frame is a body fixed coordinate frame of the shaper, and z_2 axis is the rotation axis of the face-gear. Symbols r_{as} , r_{bs} and r_{ps} are the addendum circle radius, pitch radius and base circle radius of the shaper, respectively. R_{in} , R_p and R_{out} are inner radius, mean pitch radius and outer radius of the face-gear, respectively. Furthermore, L_1, L_p and L_2 are the inner radius, mean pitch radius and outer radius to the pitch cone apex, respectively. O is the pitch cone apex and OI line is the pitch cone line. In this figure, γ is the shaft angle and calculated as $\gamma = \gamma_1 + \gamma_2$, where γ_1 is the pitch cone angle of the spur shaper and formulated as:

$$\gamma_1 = \cot^{-1}\left(\frac{m_{2/s} + \cos\gamma}{\sin\gamma}\right) \tag{2-1}$$

and γ_2 is the face-gear pitch cone angle and formulated as:

$$\gamma_2 = \cot^{-1}\left(\frac{1 + m_{2/s}\cos\gamma}{m_{2/s}\sin\gamma}\right) \tag{2-2}$$

where $m_{2/s}$ is the ratio of face-gear number of tooth (N_2) to shaper number of tooth (N_s) and shown as $m_{2/s} = N_2 / N_s$ [14,15,57–61].

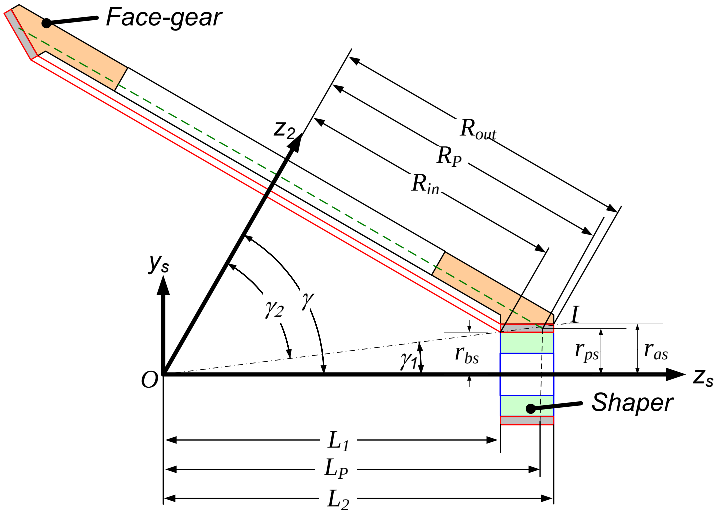

Figure 2-1 Face-gear and spur shaper dimensions

The geometric properties of a spur shaper are represented in Figure 2-2-a. The symbols θ_s and u_s are the shaper surface parameters. They are the surface coordinates in the curvilinear coordinate system. The parameter θ_s is an angle and u_s is a length. The parameter u_s is parallel to the z_s direction in Figure 2-2. In this figure, θ_{0s} is the half space width on the base cylinder [13,14]. The parametric surface equation of the spur shaper tooth surface as a function of θ_s and u_s is:

$$r_s(u_s,\theta_s)=\begin{Bmatrix} \pm r_{bs}[\sin(\theta_s+\theta_{0s})-\theta_s\cdot\cos(\theta_s+\theta_{0s})] \\ -r_{bs}[\cos(\theta_s+\theta_{0s})+\theta_s\cdot\sin(\theta_s+\theta_{0s})] \\ u_s \end{Bmatrix} \tag{2-3}$$

where r_{bs} is formulated as a function of pitch radius and pressure angle at the pitch point (α_0) as:

$$r_{bs}=r_{ps}\cos(\alpha_0) \tag{2-4}$$

The upper and lower (plus and minus) signs in the first row of Equation (2-3) correspond to left and right profiles, respectively. In addition to shaper surface equation, a mathematical coupling between the shaper parameters needs to be derived and used in the face-gear tooth dimension calculations. The equation of meshing is a scalar function of two shaper surface parameters (u_s, θ_s) and one shaper generalized motion parameter (ϕ_s). Formulated as:

$$
\begin{aligned}
f_i(u_s,\theta_s,\varphi_s) = r_{bs}\cdot(1-m_{s/g}\cdot\cos\gamma_m) - \\
u_s\cdot m_{s/g}\cdot\sin\gamma_m\cdot\cos(\varphi_s+\theta_{0s}+\theta_s) = 0
\end{aligned}
\qquad (2\text{-}5)
$$

where, $\gamma_m = \pi - \gamma$ in radians and $m_{s/g} = 1/m_{g/s}$. The equation of meshing is a mathematical coupling between the shaper parameters (u_s, θ_s) and motion parameter (ϕ_s). To obtain the actual tooth form, critical dimensions of the face-gear must be identified. The critical dimensions dictates the value of the shaper parameters u_s, θ_s and ϕ_s. The simultaneous solution of surface equations and equation of meshing with the satisfying parameters produce the actual tooth geometry. This procedure is called enveloping the surface contact lines. The face-gear tooth surface is called the envelope of the family of contact lines [13,15]. In Figure 2-3, the enveloping process is summarized. Here, $\phi_{s\min}$ and $\phi_{s\max}$ are the angles of rotation of shaper that correspond to the start and end of the meshing cycle for single pair of teeth, respectively. These angles are calculated from simulation of meshing and enveloping process as explained in [13] and [15]. Calculated undercut and pointing dimensions of the face-gear identify u_{smin} and u_{smax} values. The equation of meshing is then solved numerically to establish curvilinear coordinates of each contact line at each instant of meshing cycle. The calculated curvilinear coordinates are substituted in shaper and face-gear surface equations to produce the face-gear tooth form. These enveloped contact lines between shaper and the face-gear are numerically generated from simulation of meshing and presented in Figure 2-2-b, viewed at y_s-z_s plane. In this simulation the mesh cycle starts from the base-circle-radius (r_{bs}) of the shaper (point B) and ends at the addendum of the shaper (point A). The shaper tooth geometry is bounded with the rectangle A-A**-B-B**. The face-gear tooth is presented in Figure 2-2-c, where, the tooth-face-width is symbolized as f_w.

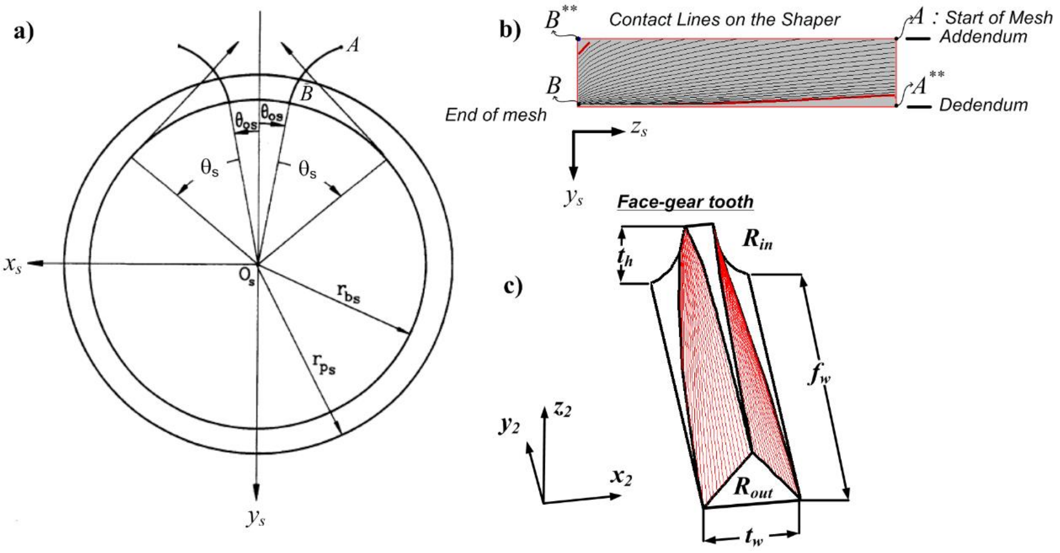
a)
A
B
θos
θos
θs
θs
xs
Os
rbs
rps
ys
b)
B**
Contact Lines on the Shaper
A : Start of Mesh
Addendum
B
End of mesh
A**
Dedendum
zs
ys
Face-gear tooth
th
Rin
c)
fw
y2
z2
x2
Rout
tw

Figure 2-2 a) Spur shaper parameters [15]; **b)** Shaper from side view with contact lines; **c)** face-gear tooth

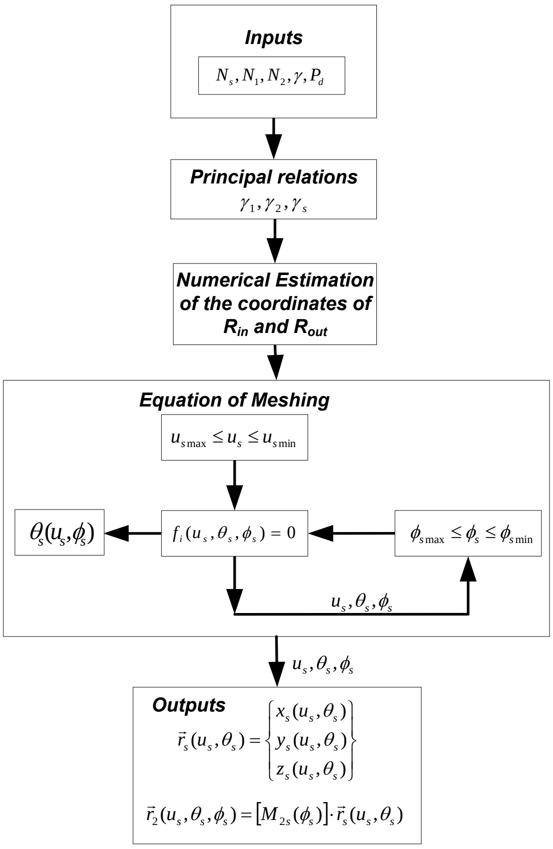
Inputs
$N_s, N_1, N_2, \gamma, P_d$
Principal relations
$\gamma_1, \gamma_2, \gamma_s$
Numerical Estimation of the coordinates of R_{in} and R_{out}
Equation of Meshing
$u_{s\max} \le u_s \le u_{s\min}$
$\theta_s(u_s,\phi_s)$
$f_i(u_s,\theta_s,\phi_s) = 0$
$\phi_{s\max} \le \phi_s \le \phi_{s\min}$
u_s,θ_s,ϕ_s
u_s,θ_s,ϕ_s
Outputs
$\vec{r}_s(u_s,\theta_s) = \begin{Bmatrix} x_s(u_s,\theta_s) \\ y_s(u_s,\theta_s) \\ z_s(u_s,\theta_s) \end{Bmatrix}$
$\vec{r}_2(u_s,\theta_s,\phi_s) = [M_{2s}(\phi_s)] \cdot \vec{r}_s(u_s,\theta_s)$

Figure 2-3 Flow diagram of face-gear modeling process

Reorganizing the meshing Equation (2-5) after solving, the parameter u_s can be calculated as,

$$u_s = -r_{bs} \frac{(-1 + m_{s/g} \cdot \cos\gamma_m)}{m_{s/g} \cdot \sin(\gamma_m) \cdot \cos(\phi_s + \theta_{0s} + \theta_s)} \qquad (2\text{-}6)$$

2.2.1 Transformation of the Spur-Shaper Surface to the Face-Gear

The position vector for the spur-shaper is transformed to the face-gear position vector through three rotations around appropriate axes. As mentioned above, this is defined as the process of simulating the machine tool motions, as depicted in Figure 2-4. ϕ_s and ϕ_2 are the rotational motion parameters of the spur-gear and the face-gear, respectively.

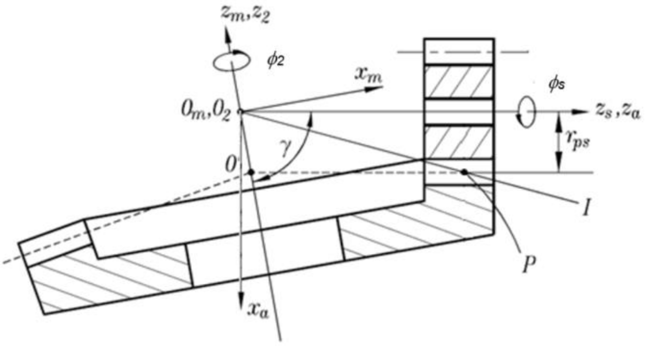

Figure 2-4 Spur-shaper and face-gear assembly

The first transformation is defined as the rotation of spur-gear around its own rotation axis and determined by the following expression,

$$M_{fs} = \begin{pmatrix} \cos(-\phi_s) & \sin(-\phi_s) & 0 \\ -\sin(-\phi_s) & \cos(-\phi_s) & 0 \\ 0 & 0 & 1 \end{pmatrix} \tag{2-7}$$

The second transformation is defined as the rotation between the shaper and face-gear rotation axes and determined by the following expression,

$$M_{af} = \begin{pmatrix} 1 & 0 & 0 \\ 0 & \cos(\gamma) & \sin(\gamma) \\ 0 & -\sin(\gamma) & \cos(\gamma) \end{pmatrix} \tag{2-8}$$

The third transformation is defined as the rotation of face-gear around its own rotation axis, and the corresponding transformation matrix is written as,

$$M_{2a} = \begin{pmatrix} \cos(\phi_2) & \sin(\phi_2) & 0 \\ -sin(\phi_2) & \cos(\phi_2) & 0 \\ 0 & 0 & 1 \end{pmatrix} \tag{2-9}$$

The resulting transformation matrix is written as the product of all three matrices as,

$$M_{2s}(\phi_2, \phi_s) = M_{2a} M_{af} M_{fs} \tag{2-10}$$

As it is seen from the equation above, the total transformation matrix is a function of the rotational motion parameters ϕ_s and ϕ_2, where the angle between spur and face-gears γ is a constant parameter. Also, between two motion parameters, the following relation may be written,

$$\phi_2 = \phi_s \frac{N_s}{N_2} \tag{2-11}$$

where N_s and N_2 are the teeth numbers of the shaper and the face-gear, respectively. Then, after appropriate substitutions, the transformation matrix can be written as a function of ϕ_s only as;

$$M_{2s}(\phi_2,\phi_s) = M_{2s}(\phi_s) \tag{2-12}$$

2.2.2 Face-Gear Surface Equations

The spur-shaper surface given in Equation (2-3) may also be written as,

$$r_s(u_s,\theta_s) = \begin{Bmatrix} \mathrm{x}_s(\mathrm{u}_s,\theta_s) \\ y_s(\mathrm{u}_s,\theta_s) \\ z_s(\mathrm{u}_s,\theta_s) \end{Bmatrix} \tag{2-13}$$

Similarly, the face-gear's surface equation may be expressed as,

$$r_2(u_s,\theta_s,\phi_s) = \begin{Bmatrix} \mathrm{x}_2(u_s,\theta_s,\phi_s) \\ y_2(u_s,\theta_s,\phi_s) \\ z_2(u_s,\theta_s,\phi_s) \end{Bmatrix} \tag{2-14}$$

Different from the surface equation of the spur-gear, the rotation parameter is added to the equation due to the transformation. In terms of spur-shaper parameters and the total transformation matrix, Equation (2-46) may also be expressed as,

$$r_2(u_s,\theta_s,\phi_s) = M_{2s}(\phi_s) r_s(u_s,\theta_s) \tag{2-15}$$

2.2.3 Limiting Conditions of Surface Generations

The undercutting condition and the pointing condition are the two limiting factors for surface generation of a face-gear, as mentioned in the introduction of this chapter. The undercutting criteria constructs a region at the bottom of the tooth, beyond which conjugate action does not work (the blue region in Figure 2-5). And the pointing criteria determines the location where the thickness of the top surface becomes zero. This also fixes the outer radius of the face-gear.

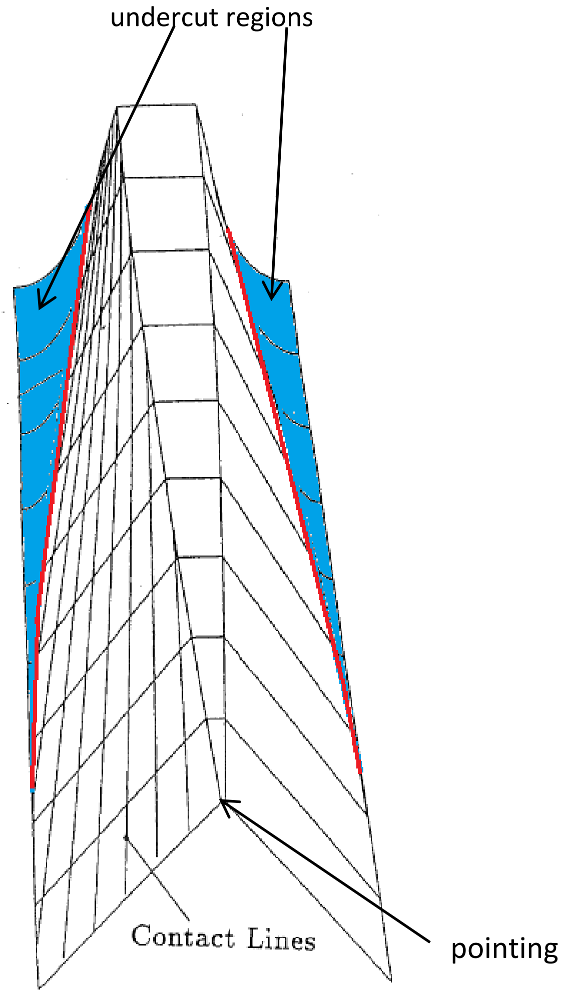

Figure 2-5 Undercut regions on face-gear tooth surface and pointing

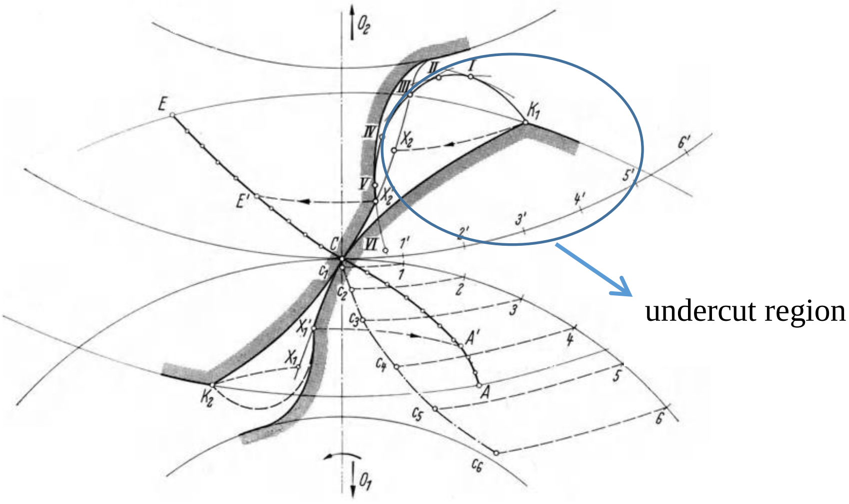

O_2
E
II
I
III
K_1
IV
X_2
6'
V
X_2
5'
E'
4'
3'
2'
C'
VI
1'
C_1
1
C_2
2
3
C_3
X_1'
A'
4
X_1
C_4
5
K_2
A
C_5
6
C_6
O_1
undercut region

Figure 2-6 The undercut definition, [62]

Sliding Velocity:

The meshing teeth of a gear-pair at a contact point is given in Figure 2-7. v_1 and v_2 are the peripheral velocities, v_{1n} and v_{2n} are the normal velocities, v_{1t} and v_{2t} are the tangential velocities of the driven and the driver gears. v_s is called as the sliding velocity which plays an important role in generating the surface profiles of the teeth and may be expressed as,

$$\overrightarrow{v_s}^{\langle 12\rangle} = \overrightarrow{v_1} - \overrightarrow{v_2} \tag{2-16}$$

where, the peripheral velocities are calculated as,

$$\begin{aligned} \overrightarrow{v_1} &= \overrightarrow{\dot{\phi}_1} \times \overrightarrow{r_1} \\ \overrightarrow{v_2} &= \overrightarrow{\dot{\phi}_2} \times \overrightarrow{r_2} \end{aligned} \tag{2-17}$$

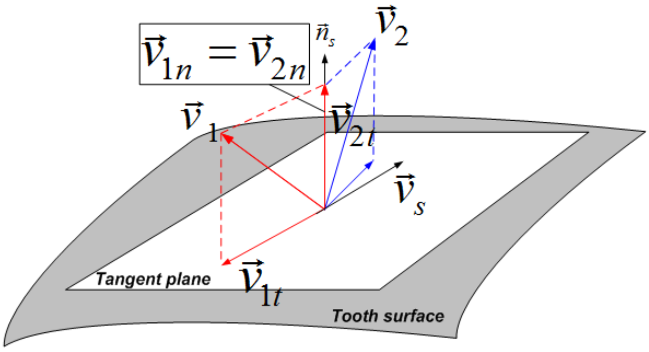
$\vec{v}_{1n} = \vec{v}_{2n}$
$\vec{n}_s$
$\vec{v}_2$
$\vec{v}_1$
$\vec{v}_{2t}$
$\vec{v}_s$
Tangent plane
$\vec{v}_{1t}$
Tooth surface

Figure 2-7 One point of interest at the contact line of the meshing teeth [63], [56]

Surface Normal:

The term $\overrightarrow{n_s}$ is the unit normal vector of the surface, and it may be defined as the cross product of the directional derivatives over a surface in space, as given in Figure 2-8. It can be calculated as,

$$\overrightarrow{n_s} = \frac{\dfrac{\partial \vec{r}_s(u_s,\theta_s)}{\partial u_s} \times \dfrac{\partial \vec{r}_s(u_s,\theta_s)}{\partial \theta_s}}{\left| \dfrac{\partial \vec{r}_s(u_s,\theta_s)}{\partial u_s} \times \dfrac{\partial \vec{r}_s(u_s,\theta_s)}{\partial \theta_s} \right|} \tag{2-18}$$

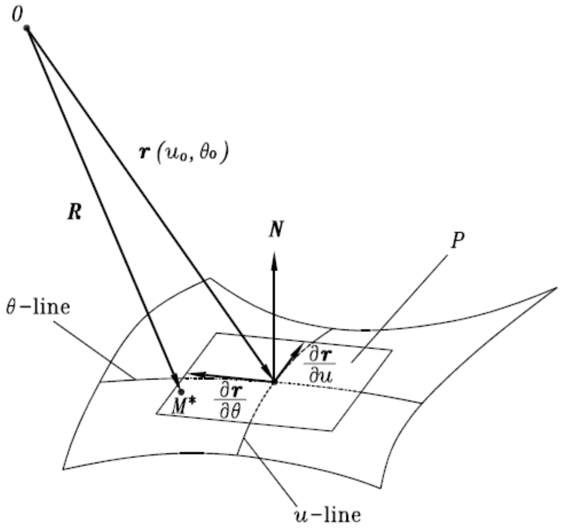
O
$\boldsymbol{r}(u_0, \theta_0)$
$\boldsymbol{R}$
$\boldsymbol{N}$
P
θ-line
$\frac{\partial \boldsymbol{r}}{\partial u}$
M^*
$\frac{\partial \boldsymbol{r}}{\partial \theta}$
u-line

Figure 2-8 Surface normal and the directional derivatives over the specified surface

Equation of Meshing:

For the conjugate action of tooth profiles, the following equation should be satisfied,

$$f(u_s, \theta_s, \phi_s) = \overrightarrow{n_s} \cdot \overrightarrow{v_s}^{\langle s2 \rangle} = 0 \tag{2-19}$$

which is therefore called as the “*equation of meshing*”. At all-time instants, surface normal at the point of contact must be perpendicular to the sliding velocity between the two meshing surfaces. As mentioned above, sliding velocity is the difference between the peripheral velocities. Since the normal velocities of the two surfaces must be equal both in direction and magnitude, the sliding velocity may also be defined as the difference between rolling velocities.

2.2.3.1 Calculations for Undercutting

This criterion (limiting point for the surface generation) denotes the cutting region of the involute spur-gear shaper that is beyond the active conjugate region, and this region is to be avoided. Since the undercutting point is a singular point, normal vector for the face-gear surface should be equal to zero at the prescribed singular point,

$$\vec{n_2} = \frac{\partial \vec{r_2}}{\partial u_s} \times \frac{\partial \vec{r_2}}{\partial \theta_s} = 0 \tag{2-20}$$

Therefore, the points of undercut region may be detected with the above equation. Litvin [8,13–15,52,53], proposes another method for detecting the undercutting points which can be expressed with the following formula,

$$\vec{v_r}^{\langle 1\rangle} + \vec{v_s}^{\langle s2\rangle} = 0 \tag{2-21}$$

where first term is the velocity of the contact point in its relative motion over the generating surface (spur-shaper) and the second term is the sliding velocity. Both vectors are defined with components of coordinate system that is rigidly connected to the generating surface. Equation (2-21) may also be written as in the following form;

$$\frac{\partial \vec{r_2}}{\partial u_s}\frac{du_s}{dt} \times \frac{\partial \vec{r_2}}{\partial \theta_s}\frac{d\theta_s}{dt} = -\vec{v_s}^{\langle s2\rangle} \tag{2-22}$$

For detecting the undercut region, differentiated form of Equation (2-19) and equation (2-22) should be satisfied simultaneously. Therefore, the time-differentiated form of equation of meshing given in (2-19) may be written as,

$$\frac{df(u_s,\theta_s,\phi_s)}{dt}=\frac{\partial f}{\partial u_s}\frac{du_s}{dt}+\frac{\partial f}{\partial \theta_s}\frac{d\theta_s}{dt}+\frac{\partial f}{\partial \phi_s}\frac{d\phi_s}{dt}=0 \tag{2-23}$$

Writing equations (2-22) and (2-23) in matrix form yields,

$$\begin{Bmatrix} \frac{\partial \vec{r_2}}{\partial u_s} & \frac{\partial \vec{r_2}}{\partial \theta_s} \\ \frac{\partial f}{\partial u_s} & \frac{\partial f}{\partial \theta_s} \end{Bmatrix} \begin{Bmatrix} \dot{u}_s \\ \dot{\theta}_s \end{Bmatrix} = \begin{Bmatrix} -\vec{v}_s^{\langle s2\rangle} \\ -\frac{\partial f}{\partial \phi_s}\dot{\phi}_s \end{Bmatrix} \tag{2-24}$$

By solving the Equation (2-24), the undercut region is determined.

2.2.3.2 Calculations for Pointing

Pointing denotes the location where the thickness of the tooth on the top surface becomes zero, as depicted in Figure 2-5. For this, the two tooth surfaces of the face-gear and the spur-pinion may intersect at a point A, as shown in Figure 2-9.

For determining the location where the pointing occurs, firstly, the pressure angle α of the pointed teeth is determined. From Figure 2-9, the following expression can be written,

$$\overrightarrow{O_a^{*}N}+\overrightarrow{NM}+\overrightarrow{MA}=\overrightarrow{O_a^{*}A} \tag{2-25}$$

where

$$\left|\overrightarrow{MA}\right|=\lambda_s \tag{2-26}$$

$$\left|\overrightarrow{NM}\right| = r_{bs}\theta_s \tag{2-27}$$

$$\left|\overrightarrow{O_a^{\,*}N}\right| = r_{bs} \tag{2-28}$$

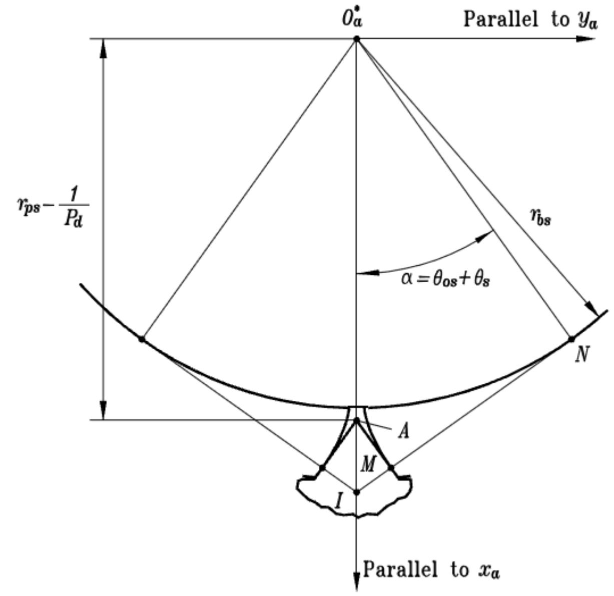

O_a^*
Parallel to y_a
$r_{ps}-\frac{1}{P_d}$
r_{bs}
$\alpha=\theta_{os}+\theta_s$
N
A
M
I
Parallel to x_a

Figure 2-9 Cross section of tooth profiles of spur-shaper and the face-gear at the pointing cross section, cross section Π2 depicted in Figure 2-11 [13]

Substituting Equations (2-26), (2-27) and (2-28) into Equation (2-25) yields,

$$r_{bs}\cdot e^{\left(\alpha+\frac{3\pi}{2}\right)} + r_{bs}\cdot\theta_s e^{(\pi+\alpha)} + \lambda_s\cdot e^{\left(\frac{\pi}{2}+\alpha\right)} = \left|\overrightarrow{O_a^{\,*}A}\right|\cdot e^{-i\pi} \tag{2-29}$$

where . Then, separating the vector equation into two scalar equations yields,

$$r_{bs}\cos\left(\alpha+\frac{3\pi}{2}\right)+r_{bs}\theta_s\cos(\pi+\alpha)+\lambda_s\cos\left(\frac{\pi}{2}+\alpha\right)=-\left|\overrightarrow{O_a^{*}A}\right| \tag{2-30}$$

$$r_{bs}\sin\left(\alpha+\frac{3\pi}{2}\right)+r_{bs}\theta_s\sin(\pi+\alpha)+\lambda_s\sin\left(\frac{\pi}{2}+\alpha\right)=0 \tag{2-31}$$

The following expressions may be derived from Figure 2-9 and Figure 2-10,

$$\begin{aligned} r_{bs} &= r_{ps}\cos(\alpha_{\mathrm{o}}) \\ \alpha_{\mathrm{o}} &= a\cos\left(\frac{r_{bs}}{r_{ps}}\right) \\ \theta_s &= \alpha-\theta_{os} \end{aligned} \tag{2-32}$$

where r_{ps} and θ_{os} are expressed as,

$$\begin{aligned} r_{ps} &= \frac{N_s}{2P_d} \\ \theta_{os} &= \frac{\pi}{2N_s}-inv(\alpha_{\mathrm{o}}) \end{aligned} \tag{2-33}$$

Substituting Equations (2-32) and (2-33) into Equations (2-30) and (2-31), and eliminating yields,

$$\alpha-\sin\left(\frac{N_s}{N_s\cos(\alpha_{\mathrm{o}})}\right)=\frac{\pi}{2N_s}-inv(\alpha_{\mathrm{o}}) \tag{2-34}$$

where denotes the pressure angle at the pointing location.

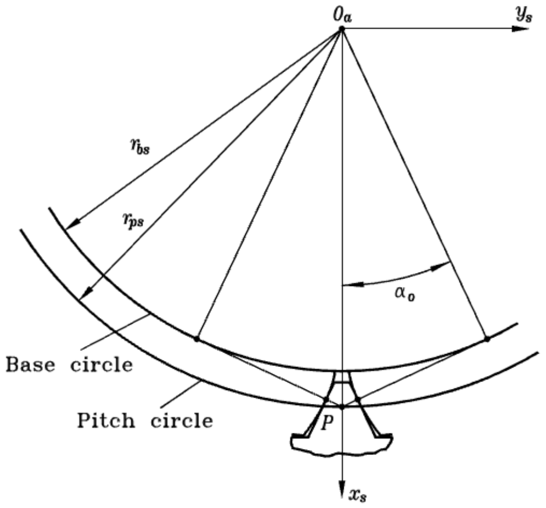

Figure 2-10 Cross section of tooth profiles of spur-shaper and the face-gear at any cross section before the pointing, cross section Π_1 depicted in Figure 2-11 [13]

Secondly, L_2 is calculated by using the value of the pressure angle at the pointing location. Using the Equation ((2-47), the length, given in Figure 2-9, may be expressed as,

$$\left|\overrightarrow{O_a^* I}\right| = \frac{r_{bs}}{\cos(\alpha)} = \frac{N_s \cos(\alpha_o)}{2P_d \cos(\alpha)} \tag{2-35}$$

From Figure 2-11, L_2 is written as,

$$L_2 = \frac{\left|\overrightarrow{O_a^* I}\right|}{\tan(\gamma_s)} \tag{2-36}$$

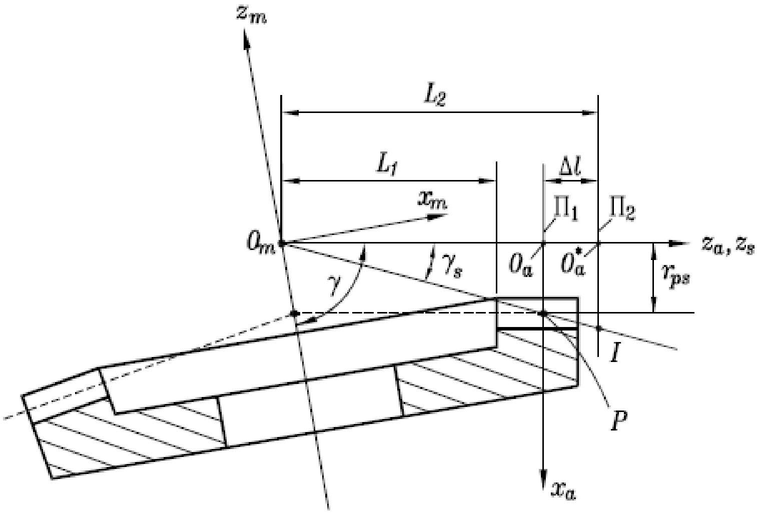

Figure 2-11 Cross sections Π1 and Π2, [13]

Substituting Equation (2-35) into Equation (2-36) yields,

$$L_2 = \frac{N_s}{2P_d \cos(\alpha) \tan(\gamma_s)} \tag{2-37}$$

Assuming $\theta_s{}^p$, $\phi_s{}^p$ and $u_s{}^p$ are the corresponding values of the parameters θ_s, ϕ_s and u_s where the pointing is achieved, then the parameter L2 may be formulated as the z component of the spur-shaper, as depicted in Equation (2-3), (2-6) and (2-50), and can be written as,

$$L_2 = u_s{}^p(\theta_s{}^p, \phi_s{}^p) \tag{2-38}$$

is also the outer radius of the face-gear. Rewriting Equation (2-13) for only the x and y components of the face-gear at the location of pointing yields,

$$\begin{Bmatrix} x_2^{p}(u_s^{p},\theta_s^{p},\phi_s^{p}) \\ y_2^{p}(u_s^{p},\theta_s^{p},\phi_s^{p}) \end{Bmatrix} = \begin{Bmatrix} 0 \\ L_2 \end{Bmatrix} \qquad (2\text{-}39)$$

Therefore, solving the two equations simultaneously for $\theta_s{}^p$ and $\phi_s{}^p$ gives the pointing location.

An example is shown in Figure 2-12. Here, spur shaper number of teeth (N_s) is 20, gear module (m_o) is 5.08 mm or diametral pitch (P_d) is 5 (1/inch). Face-gear number of teeth (N_2) is 120, and the shaft angle (γ) is 90˚. The resulting face-gear tooth form is presented in Figure 2-13.

The critical dimensions of the face-gear drives can be assessed by two approaches. The first approach is based on the conversion of u_{smin} and u_{smax} values into face-gear coordinates as presented in [15]. The second approach is reading the coordinates of the minimum and maximum values in y_2 direction, specified in Figure 2-13. This approach requires further coordinate transformations and more computation time. Hence, the first approach is more convenient for parametric studies and repetitive calculations; however, the method still requires complex numerical calculations and computer time. Depending on gear parameters these two methods may show up to 5% difference both in inner and outer radii.

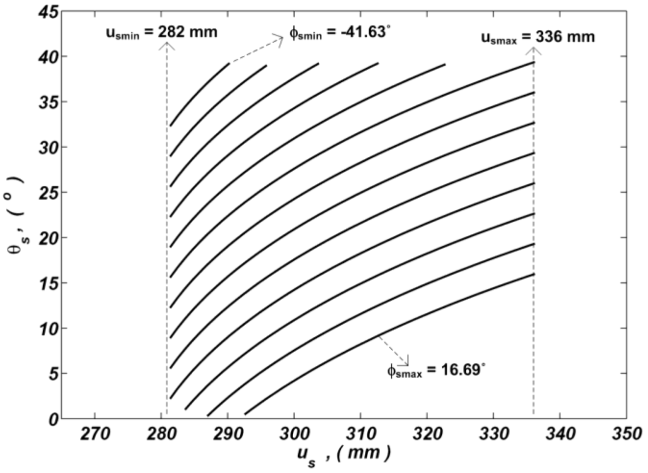

Figure 2-12 Enveloped u_s , θ_s and ϕ_s parameters with $N_s = 20$, $N_2 = 120$, $\gamma = 90^\circ$, $m_o = 5.08$ mm

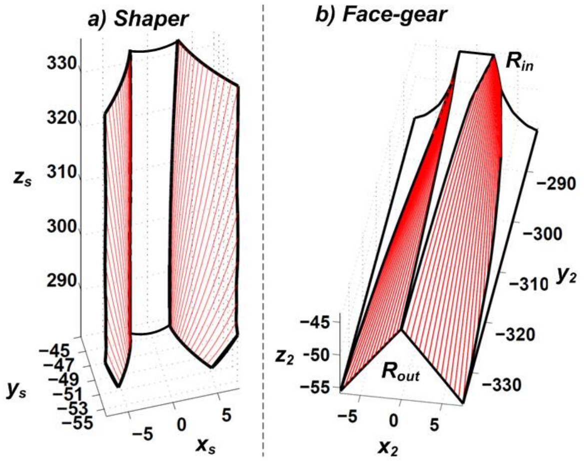
a) Shaper
b) Face-gear
z_s
330
320
310
300
290
y_s
-45
-47
-49
-51
-53
-55
-5
0
5
x_s
R_in
R_out
z_2
-45
-50
-55
-5
0
5
x_2
y_2
-290
-300
-310
-320
-330

Figure 2-13 a) Shaper tooth space, **b)** Face-gear tooth flank in their local coordinate frames

The numerical method used in this chapter is compared to the published face-gear data to estimate the accuracy of the model. The references are listed at the last column of Table 2-1. The numbers of teeth, shaft angle and gear module are presented in the first four columns of Table 2-1, respectively. Here, the critical dimensions are extracted from the minimum and maximum values of the respective y_2 coordinates of the tooth forms shown in Figure 2-14. In this table, the shaper pressure angle (α_0) is 25˚ for Case-1, and 20˚ for the rest. Shaper is positioned at 90˚ shaft angle (γ) in Cases from 1 to 4. Case 5 has 80˚ shaft angle. Calculated inner and outer radii and their percentile difference (ε_{in} and ε_{out}) from the references are also listed in Table 2-1. Both inner and outer radii are in a good correlation (less than 5% difference) with the published data. The inner radius results vary from 0.4% to 4% for $\gamma = 90˚$, and -1.7% for $\gamma = 80˚$. The outer radius varies from 0.2% to 1.5% for $\gamma = 90˚$, and 4.6% for $\gamma = 80˚$. These variations can be caused due to using different numerical techniques, different initial value assumptions, or different step sizes used in the numerical calculations in each reference and this study.

Table 2-1 Comparison to selected literature

Case	N_s	N_2	γ (˚)	m_o (mm)	R_{in} (mm)	R_{out} (mm)	ε_{in} %	ε_{out} %	Ref.
1	28	160	90	6.35	469	558.1	0.4	0.2	[13]
2	20	100	90	2.54	117.6	140.2	-4.0	1.5	[15]
3	19	71	90	4.00	131.2	157	-2.0	-1.1	[64]
4	28	107	80	3.175	161	182.2	-1.7	4.6	[65]

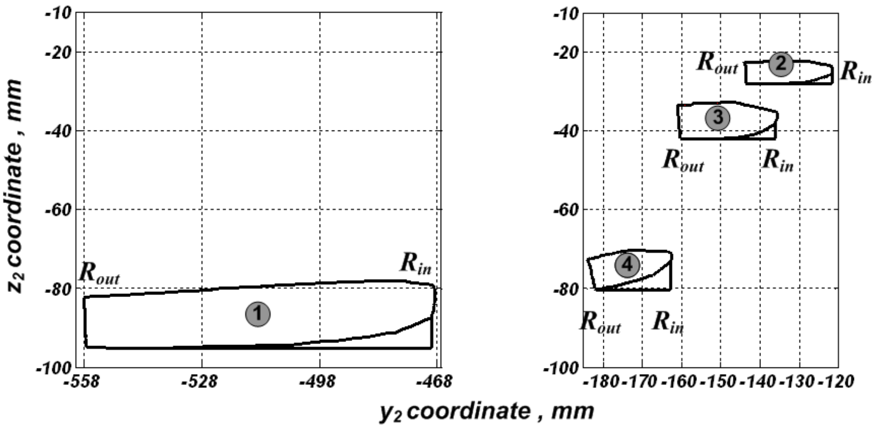

Figure 2-14 Face-gear tooth forms from viewed on y_2-z_2 plane

2.3 Derivation of analytical formulas

In this section, the dimensions L_1, L_2, R_{in}, R_{out}, f_w are derived using geometric relations presented in Figure 2-1 and Figure 2-2. The dimensions of the shaper and the face-gear are shown in Figure 2-1. The important coordinates of the shaper and the face-gear are labeled in Figure 2-15-a and b. Figure 2-15-b is the illustration of the shaper tooth from the side view.

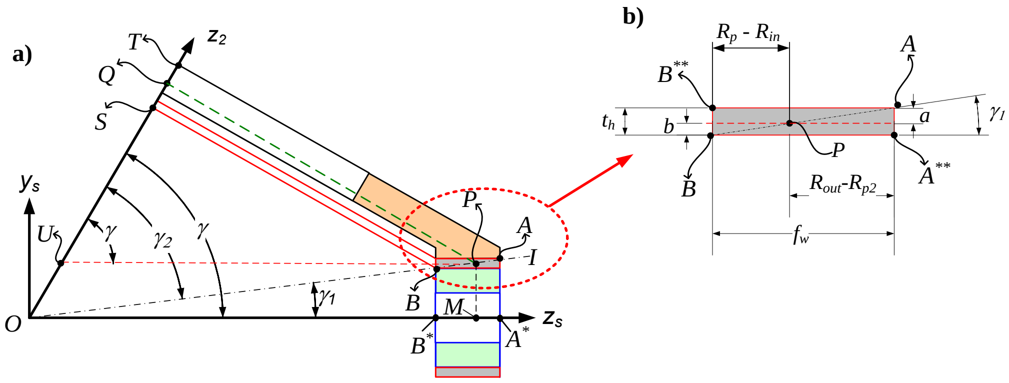
a)
T
Q
S
z_2
y_s
U
γ
γ_2
γ
O
γ_1
P
A
I
B
M
z_s
B^*
A^*
b)
R_p - R_{in}
B^{**}
A
t_h
b
a
γ_1
P
B
A^{**}
R_{out}-R_{p2}
f_w

Figure 2-15 a) Face-gear & spur shaper relations and **b)** shaper tooth dimensions

2.3.1 Inner Radius Formulation

In Figure 2-15-a, $\overline{QP}$ line is perpendicular to $\overline{OT}$ line and parallel to $\overline{SB}$, $\overline{TA}$ lines. Also, $\overline{UB}$ line is parallel to z_s axis and perpendicular to $\overline{PM}$ line. Triangles *OSB* and *OB*B* share a common hypotenuse which is $\overline{OB}$ line and its length is:

$$\overline{OB} = r_{bs} / \sin(\gamma_1) \tag{2-40}$$

Here, r_{bs} is the length of $\overline{BB^*}$ line. Hence, the relationship for the length L_1 (Figure 2-1) is:

$$L_1 = (r_{bs} / \sin(\gamma_1)) \cdot \cos(\gamma_1) \tag{2-41}$$

where, L_1 is the length of OB^* line in Figure 2-15. The face-gear inner radius (R_{in}) is derived from *OBS* triangle where the length of $\overline{SB}$ line is the corresponding dimension. Equation (2-41) is rearranged as $r_{bs}\cot(\gamma_1)$ and reformulated by using Equation (2-1) as:

$$L_1 = \frac{N_s \cos(\alpha_0)}{2P_d} \cdot \left(\frac{m_{2/s} + \cos\gamma}{\sin\gamma} \right) \tag{2-42}$$

Consecutively, the inner radius length is $\overline{SB} = L_1 \sin(\gamma_2)$ and rearranged as to give the radius as:

$$R_{in} = r_{bs} \cot(\gamma_1) \cdot \sin(\gamma_2) \tag{2-43}$$

where, γ_2 is calculated from Equation (2-2). The face-gear inner radius is then reformulated as a function of shaper number of tooth (N_s), pressure angle at the pitch circle (α_0), diametral pitch (P_d) and pitch cone angles (γ_1 and γ_2) as:

$$R_{in} = \frac{N_s \cos(\alpha_0)}{2P_d} \cdot \cot(\gamma_1) \cdot \sin(\gamma_2) \tag{2-44}$$

and redefined with Equations (2-1) and (2-2) in its final form as:

$$R_{in} = \frac{N_s \cos(\alpha_0)}{2P_d} \cdot \left(\frac{m_{2/s} + \cos\gamma}{\sin\gamma} \right) \cdot \sin\left(\cot^{-1}\left(\frac{1 + m_{2/s} \cos\gamma}{m_{2/s} \sin\gamma} \right)\right) \tag{2-45}$$

2.3.2 Outer Radius Formulation

Similar to inner radius formulation, the outer radius of the face-gear is calculated from OTA and OA*A triangles. Here, the common hypotenuse is $\overline{OA}$ line and its length is

$$\overline{OA} = \overline{AA^*} / \sin(\gamma_1) \tag{2-46}$$

Here, r_{as} is the addendum radius and is equal to the length of $\overline{AA^*}$ line. Limiting length for outer radius is:

$$L_2 = r_{as} \cdot \cot(\gamma_1) \tag{2-47}$$

where, the addendum radius is calculated from $r_{as} = r_{ps} + a$, and $a = 1/P_d$. Hence:

$$L_2 = \left(\frac{N_s}{2P_d} + \frac{1}{P_d}\right) \cdot \cot(\gamma_1) \tag{2-48}$$

The term cot(γ_1) is already formulated in Equation (2-1). By substituting this term into Equation (2-48), L_2 can be expressed in terms of N_s, P_d, $m_{2/s}$, and γ as:

$$L_2 = \left(\frac{N_s}{2P_d} + \frac{1}{P_d}\right) \cdot \left(\frac{m_{2/s} + \cos\gamma}{\sin\gamma}\right) \tag{2-49}$$

Finally, the outer radius is calculated from OTA triangle as:

$$R_{out} = L_2 \sin(\gamma_2) \tag{2-50}$$

By replacing γ_2 with Equation (2-2), the outer diameter formula as a function of N_s, P_d, $m_{2/s}$, and γ is presented in its final form as:

$$R_{out} = \left(\frac{N_s}{2P_d} + \frac{1}{P_d}\right) \cdot \left(\frac{m_{2/s} + \cos\gamma}{\sin\gamma}\right) \cdot \sin\left(\cot^{-1}\left(\frac{1 + m_{2/s}\cos\gamma}{m_{2/s}\sin\gamma}\right)\right) \tag{2-51}$$

2.3.3 Face Width Formula

Finally, the face width of a face-gear generated by a spur shaper is the difference between limiting dimensions L_1 and L_2. Simply, formulated from L_2 - L_1 as:

$$f_w = \frac{\left(N_s + 2 - N_s \cos(\alpha_0)\right)}{2P_d}\left(\frac{m_{2/s} + \cos\gamma}{\sin\gamma}\right) \tag{2-52}$$

As a specific case, the face width of the face-gears with 90° shaft angle is calculated from:

$$f_w = \frac{m_{2/s}\left(N_s + 2 - N_s \cos(\alpha_0)\right)}{2P_d} \tag{2-53}$$

2.4 Unloaded Tooth Contact Analysis

Unloaded Tooth Contact Analysis (UTCA) is performed over meshing teeth in order to obtain the contact paths on the gear surfaces and calculate the transmission error. Besides manufacturing errors, using pinion other than shaper with different tooth number, shaft angle misalignment, axial displacement of the pinion, micro modifications (i.e. profile and face-width modifications) can also lead to transmission errors in the drive systems [65,66].

For the face-gear drives, except the micro modifications over the surface of the tooth, misalignments along any axis and also shaft angle does not lead to any significant transmission errors, which is considered to be an advantage of the face-gear drives.

For the localization of the bearing contact, two approaches are generally suggested [67,68] one is double crowning of the pinion and the other is using a pinion having less teeth number than the shaper-pinion of the face-gear.

In this chapter, the second approach is utilized, and coupled with shaft and pinion position misalignments. Three case studies have been performed in order to validate the developed surface generation code and calculate the resulted unloaded static transmission errors. The cases studies are taken from [67], [68]. For all three cases, face-gear generated by an involute shaper with a tooth number of N_s=28 and a diametral pitch of P_d=8, driven by an involute spur-pinion with a tooth number of N_1=25. The tooth number of the face-gear is N_2=108,

In Case-1, no axial and shaft misalignments are imposed ($q=0$ *mm*, $\Delta\gamma=0$ º). The shaper-pinion and the utilized spur-pinion tooth number difference is taken as 3 (N_s-N_1=3).

In Case-2, a misalignment along rotational axis of the spur-pinion has been imposed ($q=0.1$ *mm*). No shaft misalignment is imposed ($\Delta\gamma=0$ º). The shaper-pinion and the utilized spur-pinion tooth difference is taken as 3 (N_s-N_1=3).

In Case 3, a shaft misalignment is imposed ($\Delta\gamma$ =0.04 º). Along rotational axis of the spur-pinion an axial misalignment has been imposed ($q=0.1$ *mm*). The shaper-pinion and the utilized spur-pinion tooth number difference is taken as 3 (N_s-N_1=3).

2.4.1 Procedure for the Unloaded Tooth Contact Analysis

are the spur-pinion's surface geometry parameters and are the spur-shaper's surface geometry parameters. If the parameters ϕ_1 and ϕ_2' represent the rotational degree of freedom of the spur-pinion and the face-gear, respectively, then the following relations exists between them

$$\Delta\phi_2 = \phi_2' - \phi_1 \frac{N_1}{N_2} \tag{2-54}$$

where $\Delta\phi_2$ defines the static transmission error, N_1 and N_2 are the tooth numbers of pinion and the face-gear, respectively. If, on the other hand, the parameters ϕ_s and ϕ_2 represent the rotational degree of freedom of the spur-shaper and the face-gear, respectively, then the following relation exists between them

$$0 = \phi_2 - \phi_s \frac{N_s}{N_2} \tag{2-55}$$

where and are the tooth numbers of pinion and the face-gear respectively. Note that, due to perfect conjugate action, the resulting transmission error is zero.

For the unloaded tooth contact analysis, generally, the perfect conjugate tooth geometry (which is the shaper pinion here) and the modified tooth geometry (which is the driving spur-pinion here) are compared by equating the surface geometries and the surface normal of both pinions to each other. Equation (2-56) represents the tooth surfaces and their surface normals.

$$\begin{aligned} \overrightarrow{r_{f1}}\left(u_1, \theta_1, \phi_1'\right) &= \overrightarrow{r_{f2}}\left(\phi_s, \theta_s, \phi_2'\right) \\ \overrightarrow{n_{f1}}\left(\theta_1, \phi_1'\right) &= \overrightarrow{n_{f2}}\left(\phi_s, \theta_s, \phi_2'\right) \end{aligned} \tag{2-56}$$

$\overrightarrow{r_{f1}}$ and $\overrightarrow{n_{f1}}$ belong to the driving spur-pinion and $\overrightarrow{r_{f2}}$ and $\overrightarrow{n_{f2}}$ belong to the generated face-gear geometry. Equation (2-56) gives 6 nonlinear equations, but only 5 of them are independent due to the fact that $\overrightarrow{n_{f1}}$ and $\overrightarrow{n_{f2}}$ are unit vectors.

By the help to the surface formulations given by Equation (2-3) and (2-15), and the transformation matrices given in Equation (2-7), (2-8) and (2-9), Equation (2-56) is reformulated as,

$$r_{f2}\left(\phi_s', \theta_s, \phi_s\right) = \begin{Bmatrix} E \\ B \\ q \end{Bmatrix} + M_{af}\left(\gamma_m + \Delta\gamma\right) \cdot M_{2a}\left(-\phi_s'\right) \cdot r_2(u_s, \theta_s, \phi_s) \tag{2-57}$$

$$n_{f2}\left(\phi_s',\theta_s,\phi_s\right)=M_{af}\left(\gamma_m+\Delta\gamma\right)\cdot M_{2a}\left(-\phi_s'\right)\cdot n_2(\theta_s,\phi_s) \tag{2-58}$$

where *E* is the shortest distance between pinion-gear axes, *q* is the axial displacement of the face-gear, is the change of the shaft angle, *B* is the center distance defined as,

$$B=\left(r_{bs}-r_b\right)\cos\left(\alpha_0\right) \tag{2-59}$$

The five unknowns u_1, θ_1, ϕ_1', ϕ_s, and θ_s are solved by increasing ϕ_2' incrementally (rotation degree of freedom of the face-gear), and the unloaded static transmission error $\Delta\phi_2$ is obtained. Matlab® "*fsolve*" function is utilized as a nonlinear solver. The utilized procedure is described in [13,14,55,68–70].

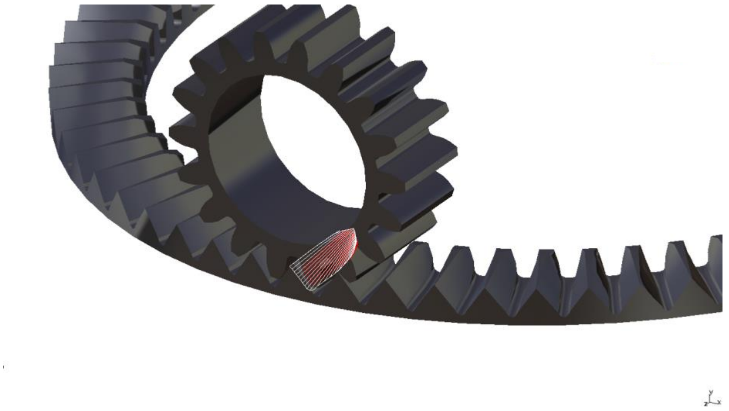

Figure 2-16 Assembly of a face-gear drive, mating surfaces of spur-pinion and face-gear

2.4.2 The Obtained Results and Discussion

The unloaded static transmission error results are displayed in Figure 2-17, Figure 2-18 and Figure 2-19 for Case-1, Case-2 and Case-3, respectively.

As depicted in Figure 2-17, utilization of spur-pinion having different number of tooth from the spur-shaper used to generate the surface geometry of the face-gear, does not create any transmission error. The shaper-pinion and the utilized spur-pinion tooth number difference was taken as 3 (N_s-N_1=3).

Figure 2-18 demonstrates that utilization of spur-pinion having different number of tooth from the spur-shaper, and also addition of an axial misalignment along rotational axis of the spur-pinion (*q=0.1 mm*), again does not create any transmission error.

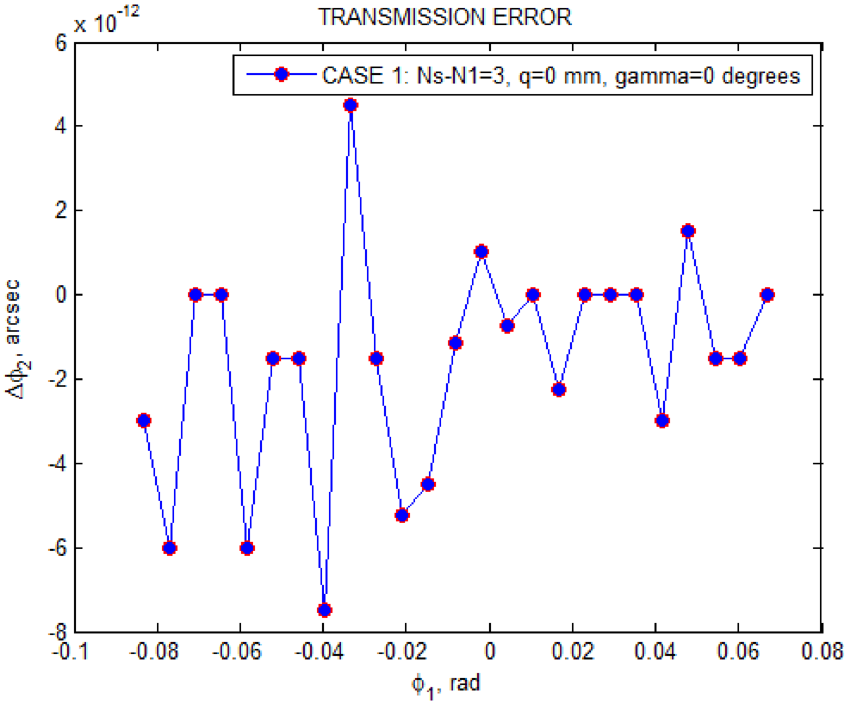

Figure 2-17 Unloaded Static Transmission Error, Case-1

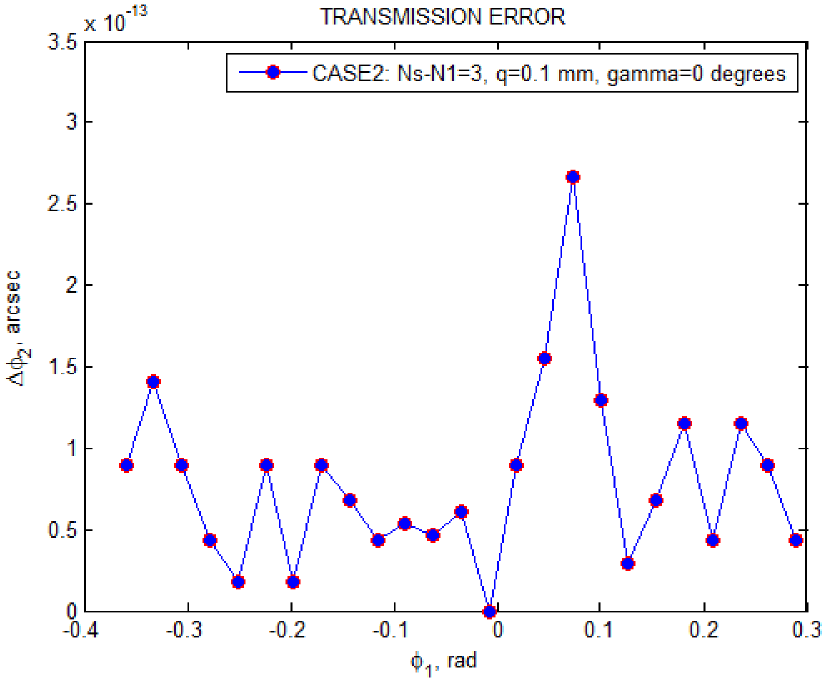

Figure 2-18 Unloaded Static Transmission Error, Case-2

Finally, Figure 2-19 shows that defining a shaft misalignment with $\Delta\gamma = 0.04^o$ to the face-gear system, in addition to the imposed axial misalignment and using different number of tooth for spur-pinion, does not create any transmission error.

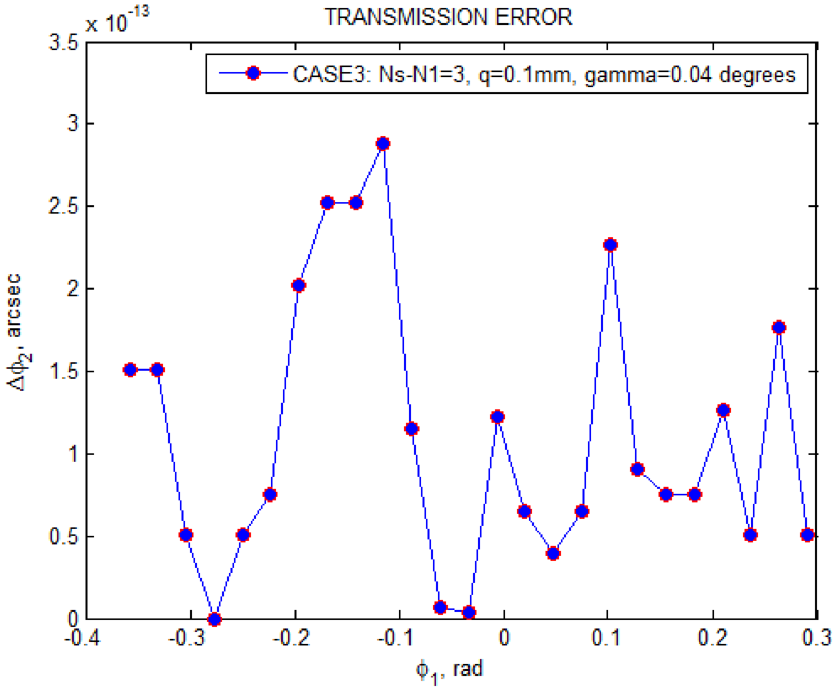

Figure 2-19 Unloaded Static Transmission Error, Case-3

In Figure 2-20, the resulting transmission errors of all cases are plotted together. The face-gear drive system is less sensitive to transmission error caused by imposed misalignments of shaft and pinion position along its axis; the calculated values in arcseconds (1/3600th of a degree) are almost zero.

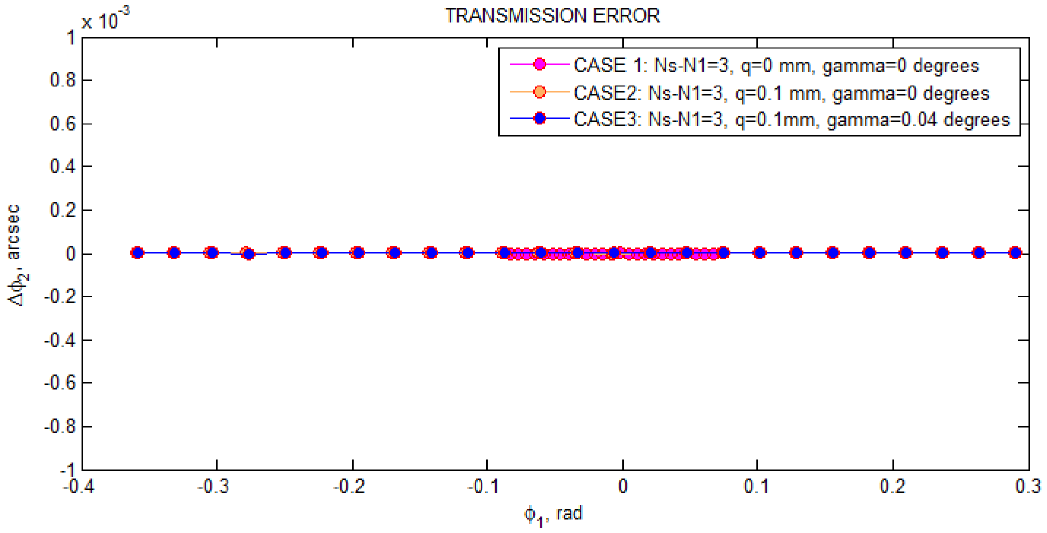

Figure 2-20 Unloaded Static Transmission Error, Case-1, 2 and 3

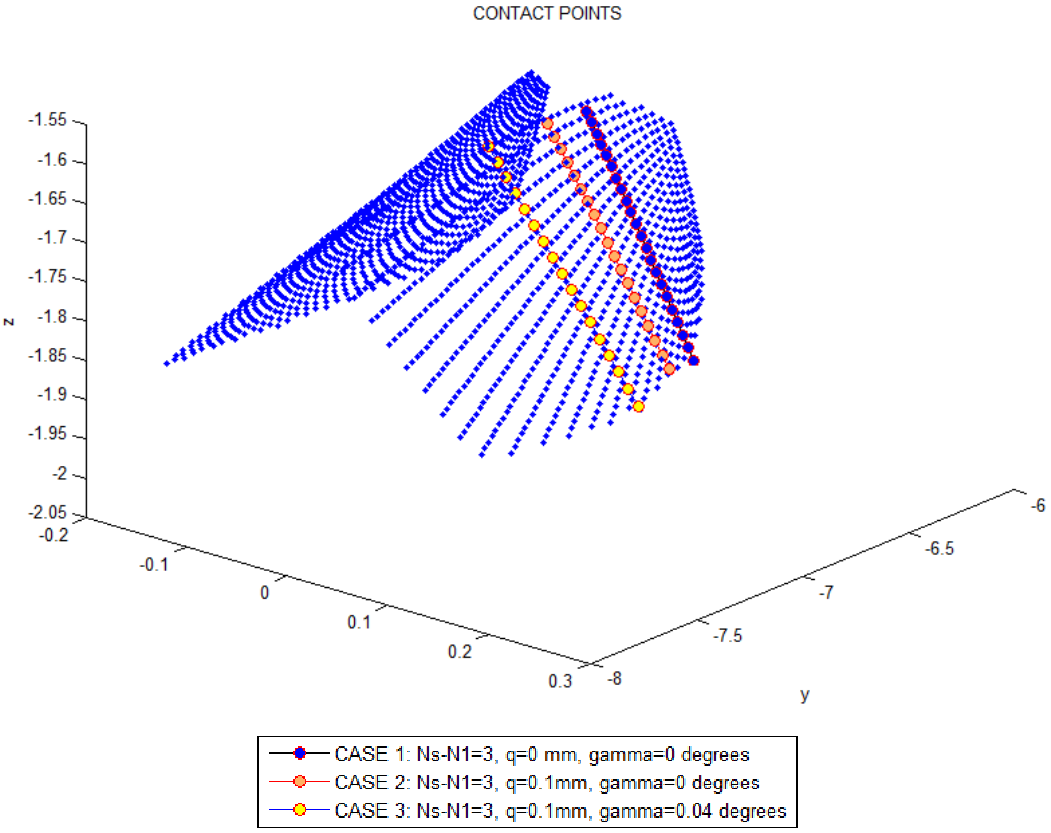

Figure 2-21 Contact points on face-gear, for all three cases, 3D view

Figure 2-21 and Figure 2-22 demonstrate the contact points on the face-gear tooth surface. It is noted that, using a spur-pinion with different number of tooth from the shaper-pinion leads to point contact rather than the line contact, as in the case of shaper-pinion driven face-gear.

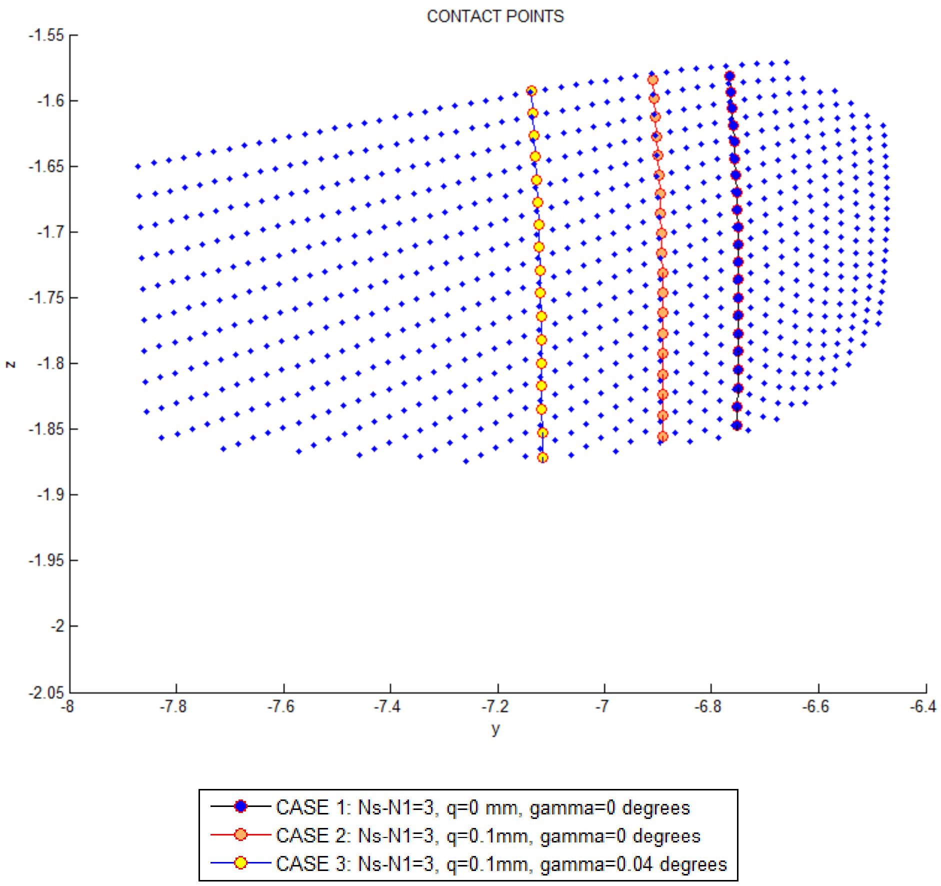

Figure 2-22 Contact points on face-gear, for all three cases, view along yz-axis

2.5 Model for The Face-Gear Thickness Variation

After the surface of the face-gear is generated as a point cloud, whole surface is approximated via NURBS (Non-Uniform Rational B-Splines) functions [71,72].

This is a necessary step to estimate the thickness throughout the generated surface of the face-gear and the spur-pinion. By this approximation, a continuous thickness variation along the face width and along the profile direction of the gears is achieved within the Finite Strip Elements established for the discretization, which is detailed in Chapter 3. A typical generated point cloud and a FSM discretization is shown in Figure 2-23.

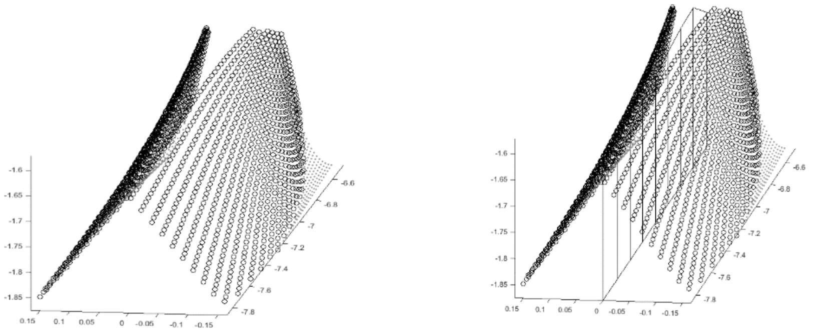

Figure 2-23 a) Point cloud extracted for a typical face-gear and **b)** the assigned finite strip elements

NURBS method is a piecewise parametric approximation for a curve or a surface. To be generated shape is defined by a set of control points, blending functions and knots. The control points are used to define the general shape while the blending functions and the knots are used to control how much each point influences the generated shape. NURBS curves are more popular among the CAD system developers compared to with other parametric and non-parametric curves due its several advantages. They easily represent geometrical shapes in a very compact form. The utilized formulation is given in Appendix A.

Figure 2-24 shows the involute profile of the spur-shaper which has the properties given in

Table **2-2**. The profile is approximated by utilizing NURBS in one dimension. The red dots are taken from the point cloud data, and the continuous line represents the results of the NURBS approximation.

Table 2-2 Input parameters

Parameter	N_s	N_2
Number of teeth	28	108
Diametral pitch 1/inch)	8	
Pressure angle (˚)	20	
Face-width (inch)	1.33	

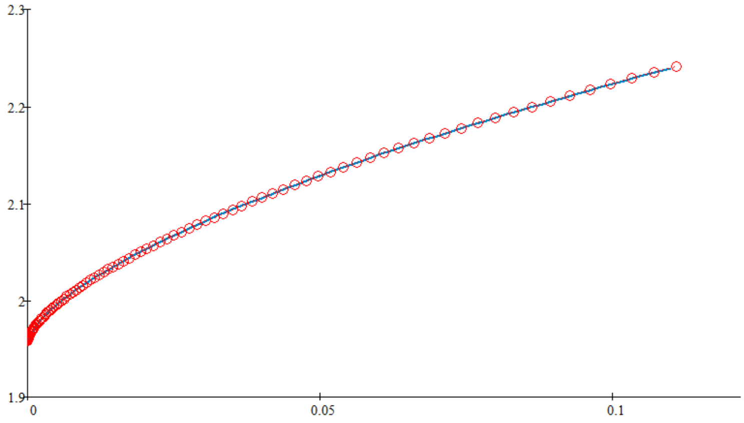

Figure 2-24 Original spur-gear involute profile and the data generated via NURBS curves, with p=3 and 101 control points along the x axis

Figure 2-25, on the other hand, shows the face-gear surface generated with the spur-pinion specified in Table 2-2, and the data generated via NURBS curves. The red dots are taken from the point cloud data where the blue dots are the taken from the NURBS curves. The fillet region is also accurately fit by the NURBS curves.

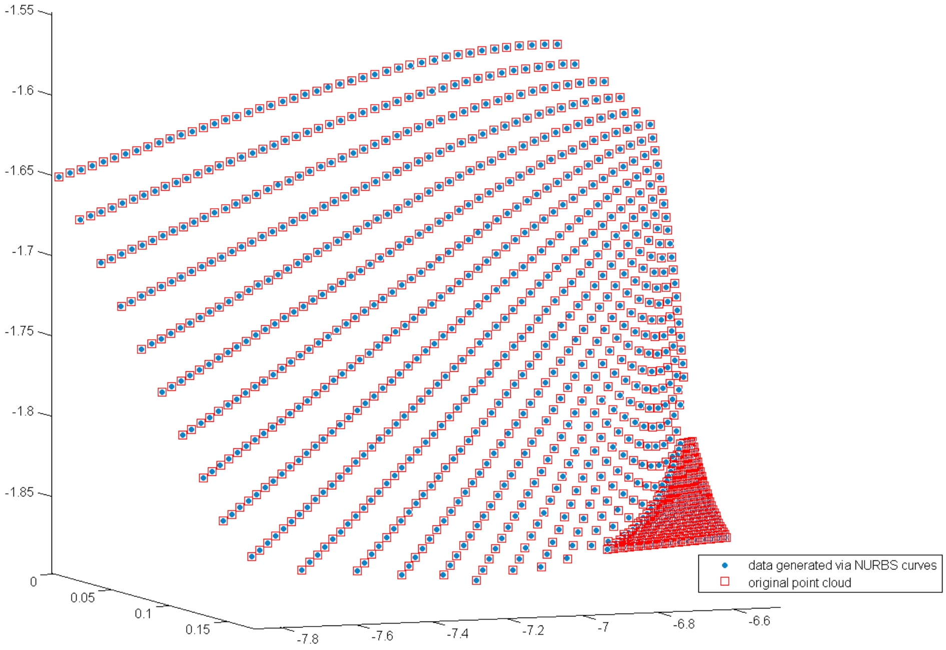

Figure 2-25 The point cloud for the original face-gear surface and the fillet, and data generated via NURBS curves with *p*=3, discretizing face-width direction by 9 grids and profile direction by 8 grids

CHAPTER 3

MESH STIFFNESS CALCULATIONS

Mesh stiffness is an important parameter for the dynamic analysis of the gear drive systems since it varies with the load position and affects the load distribution among the other tooth pairs in contact.

In literature, the mesh stiffness calculations may be classified into three categories: analytical, finite element based, and experimental [25]. Experimental methods give accurate values, but they need repetitive measurements from different kinds of (or from a specific kind of) gear specimen, which costs a lot [73]. Finite element models are generally less expensive and more efficient but require more modelling and computational time than the other methods.

There is no analytical solution to the mesh stiffness for a face-gear because of the tooth surface's complex geometry and the variation of the tooth thickness (and the pressure angle) along the tooth face-width direction. Several studies on the spur, helical, and face gears are based on mesh stiffness calculated from a uniform cross-section cantilevered beam assumption [22,25,74].

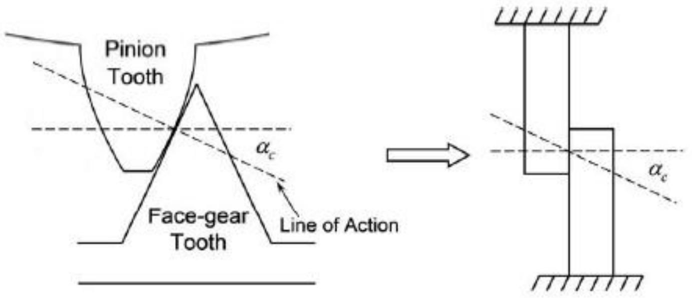

Figure 3-1 Uniform cantilever beam assumption for the mesh stiffness

For analytical calculation of the mesh stiffness of any type of gear, mainly the following contributors are taken into account; bending deformation, shear deformation, axial compression, the flexibility of fillet and foundation, and local compliance due to contact forces [75–85]. Generally, it is assumed that all contact takes place along the line of action, and the rims of the gears are assumed to be solid [86].

In literature, tooth bending and shear deflections of any kind of gear are computed by using a Rayleigh-Ritz solution of a tapered plate model [82], a beam model [73,76–78,86,87], or a finite element solution of a tapered beam model [80].

Load Distribution Program [88] uses a cantilevered tapered plate model using the Rayleigh-Ritz method, first developed by Yakubek [89] and implemented by Yau [90]. This model proves very reliable for use on the pinion, where the geometry is constant across the face width and does not change as a function of the face width.

Hertzian deflections [85] and deflection of the tooth base [82] are the additional tooth deflection components that have to be added to the total stiffness or compliance appropriately.

This chapter investigates several methods for calculating bending and contact contributors of the mesh stiffness.

3.1 Stiffness Calculations for One-Tooth

3.1.1 Bending Stiffness Contribution

The following methods are utilized in the literature for a tooth's bending stiffness. These methods, except the Finite Element Method (2D or 3D), are investigated in this chapter.

- Thin Slice Method (1D)
- Rayleigh-Ritz Approximation (2D)

- Finite Strip Method (2D)
- Finite Prism Method (3D)
- Finite Element Method (2D or 3D)

3.1.1.1 Thin Slice Method (TSM)

In this method, the tooth is divided into several slices, as depicted in Figure 3-2, and their stiffness values are extracted independently. Compliance due to bending, shear, axial load, base rotation, and compliance due to contact deformation is calculated and then added together to obtain one tooth's total stiffness.

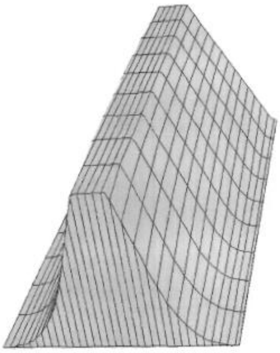

Figure 3-2 A face-gear tooth with several slices along its face width [91]

In order to have the effect of the accurate tooth profile in the stiffness values, especially for the face-gear, the interested tooth has to be sliced into an adequate number of slices. This is because the section profile varies along the face width. For the spur-shaper, on the other hand, the profile remains constant. Figure 3-3-a shows a TSM model of a spur gear with n uncoupled slices, whereas Figure 3-3-b shows the coupled version.

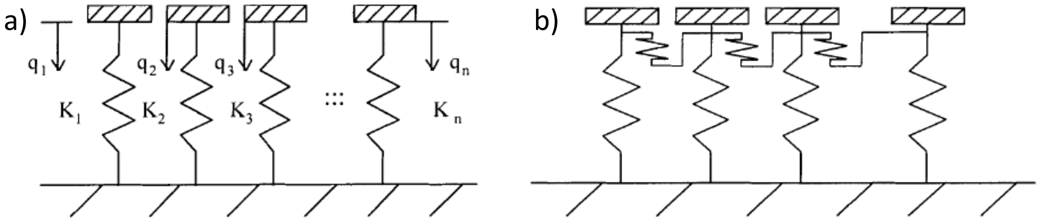

Figure 3-3 a) Uncoupled and b) coupled thin slices of a gear [91]

For instance, for an *n* sliced gear tooth, the uncoupled stiffness matrix due to bending, shear, base rotation, axial load, and contact deformation is written as,

$$K = \begin{bmatrix} k_1 & 0 & \cdots & 0 & 0 \\ 0 & k_2 & \ddots & 0 & 0 \\ \vdots & \ddots & \ddots & \ddots & \vdots \\ 0 & 0 & \ddots & k_{n-1} & 0 \\ 0 & 0 & \cdots & 0 & k_n \end{bmatrix} \tag{3-1}$$

whereas the coupling terms between those slices are formulated as,

$$\mathrm{X} = \begin{bmatrix} \chi_1 & -\chi_1 & 0 & \cdots & 0 & 0 & 0 \\ -\chi_1 & \chi_1+\chi_2 & -\chi_2 & \ddots & 0 & 0 & 0 \\ 0 & -\chi_2 & \chi_2+\chi_3 & \ddots & 0 & 0 & 0 \\ \vdots & \ddots & \ddots & \ddots & \ddots & \ddots & \vdots \\ 0 & 0 & 0 & \ddots & \chi_{n-3}+\chi_{n-2} & -\chi_{n-2} & 0 \\ 0 & 0 & 0 & \ddots & -\chi_{n-2} & \chi_{n-2}+\chi_{n-1} & -\chi_{n-1} \\ 0 & 0 & 0 & \cdots & 0 & -\chi_{n-1} & \chi_n \end{bmatrix} \tag{3-2}$$

and total stiffness matrix is written as,

$$K_T = K + \mathrm{X} \tag{3-3}$$

Börner suggests an empirical formula for the coupling stiffnesses based on measurements and several finite element models for an involute gear [26]. In his formulation, the coupling stiffness between the ith and (i+1)th slice is given as,

$$\chi_i = 2.75 \cdot \left(\frac{m_n}{b_s} \right) \cdot \frac{k_i + k_{i+1}}{2} \tag{3-4}$$

where b_s is the face width of the slice, m_n is the normal module, k_i is the calculated stiffness of the slice, k_{i+1} and is the calculated stiffness of the adjacent slice.

Application of this method to a spur gear geometry for a straight loading and an oblique loading are given in the following sections. The bending stiffness formulation for a slice is given in Appendix B.

3.1.1.1.1 Results and Comparison with FEM for Straight Loading

An example tooth is modelled with 40 slices along the face width. Each slice has ten segments along the profile for an arbitrarily loaded case. The results are compared with the 3D FE model result.

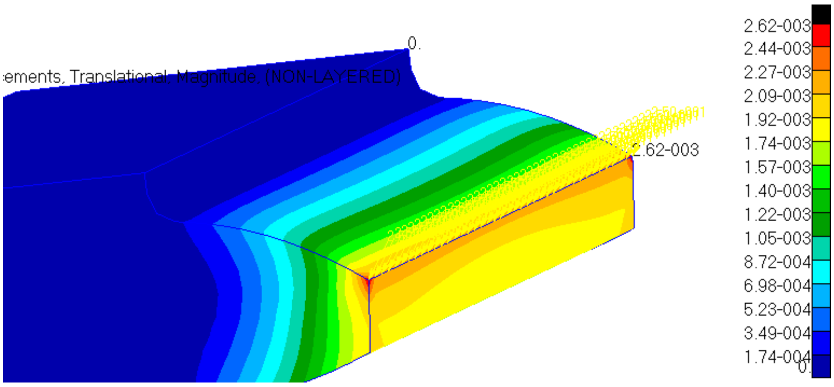
ements, Translational, Magnitude, (NON-LAYERED)
0.
2.62-003
2.62-003
2.44-003
2.27-003
2.09-003
1.92-003
1.74-003
1.57-003
1.40-003
1.22-003
1.05-003
8.72-004
6.98-004
5.23-004
3.49-004
1.74-004
0.

Figure 3-4 Spur Gear straight loading on the tip

The FE result is displayed in Figure 3-4. The deflections of the slices are shown in Figure 3-5. The TSM model approximates the FE results with a maximum error of 4.1%.

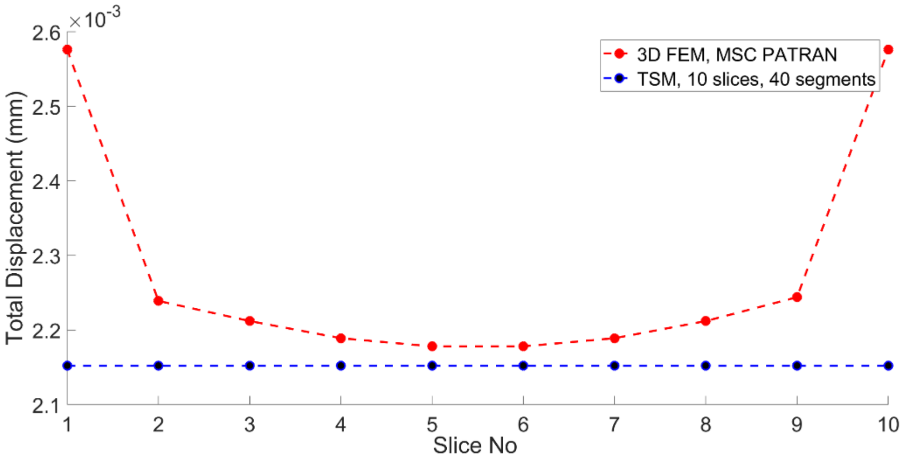

Figure 3-5 Comparison of thin slice method results with the FE results for straight loading

3.1.1.1.2 Results and Comparison with FEM for Oblique Loading

The same FE and TSM models are also used for another arbitrarily loaded case. Here, an oblique loading on the tooth's surface is given in Figure 3-6-a, and the FE result is displayed in Figure 3-6-b.

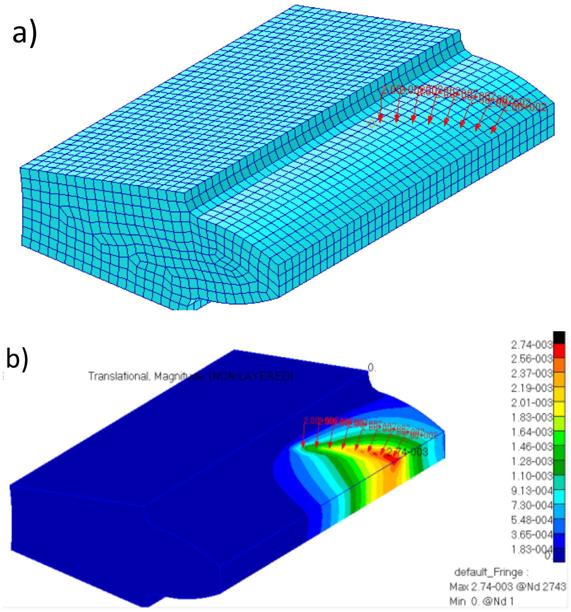
a)
b)
Translational, Magnitude, (NON-LAYERED)
0.
2.74-003
2.74-003
2.56-003
2.37-003
2.19-003
2.01-003
1.83-003
1.64-003
1.46-003
1.28-003
1.10-003
9.13-004
7.30-004
5.48-004
3.65-004
1.83-004
0.
default_Fringe :
Max 2.74-003 @Nd 2743
Min 0. @Nd 1

Figure 3-6 a) Spur gear oblique loading on the conjugate surface, **b)** FE displacement results

The deflections of the points where the load is applied are shown in Figure 3-5. The gear is sliced into 40 slices, but only eight have been loaded; therefore, only the deflections of these loaded slices are depicted in Figure 3-5. The TSM model approximates the FE results with a maximum error of 15.6 %.

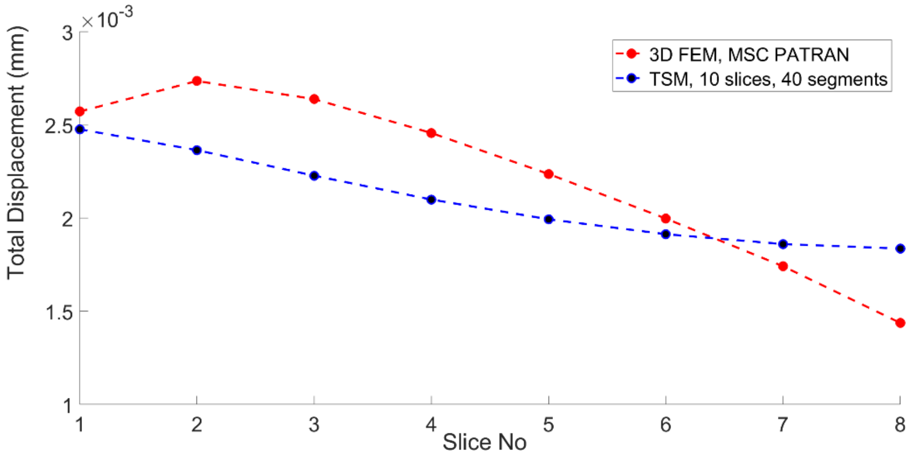

Figure 3-7 Comparison of thin slice method results with the FE results for oblique loading

3.1.1.2 Rayleigh-Ritz Approximation

For the deflection study of a tooth, the Kirchoff plate theory is employed and solved through the Rayleigh-Ritz approximation method. The results have been compared with the values obtained from the FE model run within the Nastran package program. The equation of motion is derived from the energy equations. Eigenfunctions for a cantilever-free beam are utilized as shape functions along the longitudinal axis. Similarly, eigenfunctions for a free-free beam are utilized along the transverse axis. The derived formulations are given in the Appendix C. The generated code is developed in the Mathcad package program.

A uniform plate (Figure 3-8-a), a one-axis trapezoidal plate (Figure 3-8-b), and a two-axes trapezoidal plate (Figure 3-8-c) are constructed.

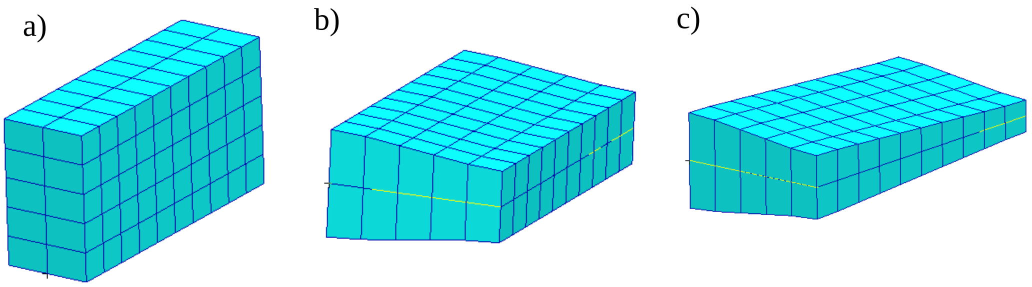

Figure 3-8 Utilized plate types **a)** a uniform plate, **b)** one-axis trapezoidal plate, **c)** two-axes trapezoidal plate

In the energy equations, the plate type is varied through the thickness function specified in Equations (3-5), (3-6), (3-7), and (3-8).

3.1.1.2.1 Uniform Plate

For a uniform plate, as depicted in Figure 3-8-a, the thickness does not vary across the x and y-axes of the plate. The thickness variation is imposed into the energy equation as follows;

$$h(\mathrm{x},\mathrm{y}) = t \tag{3-5}$$

The plate is modelled as a cantilevered Kirchoff plate along one longitudinal side via Rayleigh-Ritz approximation, where the transverse shear effects are neglected. In order to compare the results with those of the FE model, an example case is modelled and solved in MSC Patran/Nastran as a bending plate. The following arbitrarily selected loaded cases are solved;

- Case-1, a uniform pressure loading of 2000 N/mm^2 is applied to the plate

- Case-2, a uniform distributed line loading of 11000 N/mm along the longitudinal axis
- Case-3, a point load line loading of 1000 N at the point (x,y)=(a,b/2)

For Case-1, the FE model gives the maximum deflection as 0.0328 mm, as depicted in Figure 3-9, whereas the Rayleigh-Ritz approximation with seven shape functions in both directions gives 0.0312 mm. The error is calculated as 0.488%.

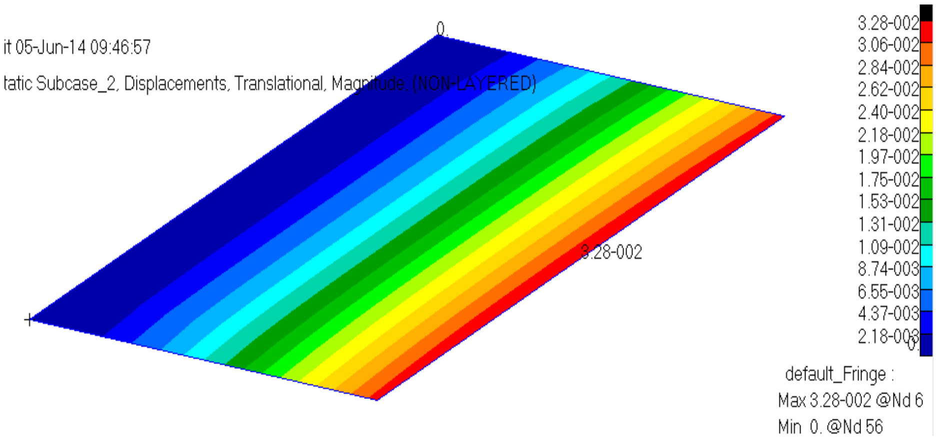

Figure 3-9 FEM results for uniform bending plate, uniform pressure loading

For Case-2, the maximum deflection for a uniform distributed line loading of 11000 N/mm is obtained from the Nastran package program as 0.942 mm, as depicted in Figure 3-10. The Rayleigh-Ritz approximation with eight shape functions in both directions gives the maximum deflection as 0.0924 mm. The error is calculated as 1.91 %.

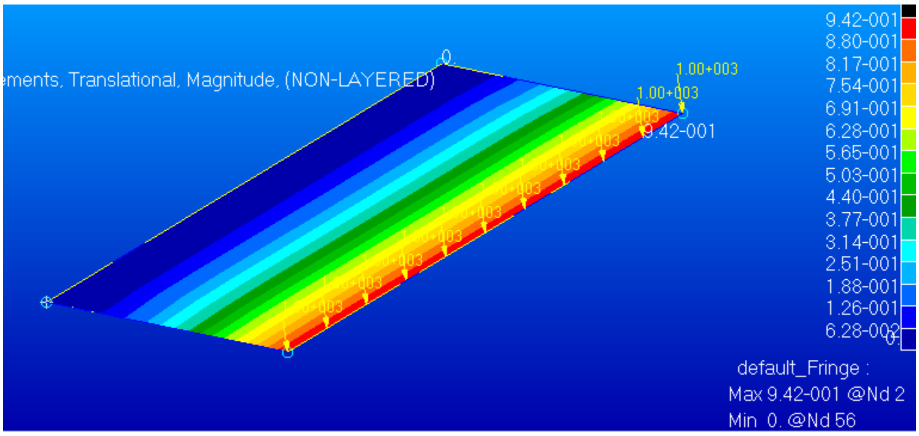
ments, Translational, Magnitude, (NON-LAYERED)
0
1.00+003
1.00+003
9.42-001
9.42-001
8.80-001
8.17-001
7.54-001
6.91-001
6.28-001
5.65-001
5.03-001
4.40-001
3.77-001
3.14-001
2.51-001
1.88-001
1.26-001
6.28-002
0
default_Fringe :
Max 9.42-001 @Nd 2
Min 0. @Nd 56

Figure 3-10 FEM results for uniform plate, loading along a line

For Case-3, the maximum deflection for a point load line loading of 1000 N at the point (x,y)=(a,b/2) is obtained from the FE model as 0.107 mm, as shown in Figure 3-11. The maximum deformation calculated by the Rayleigh-Ritz approximation with seven shape functions in both directions is 0.126 mm. The error is calculated as 17 %.

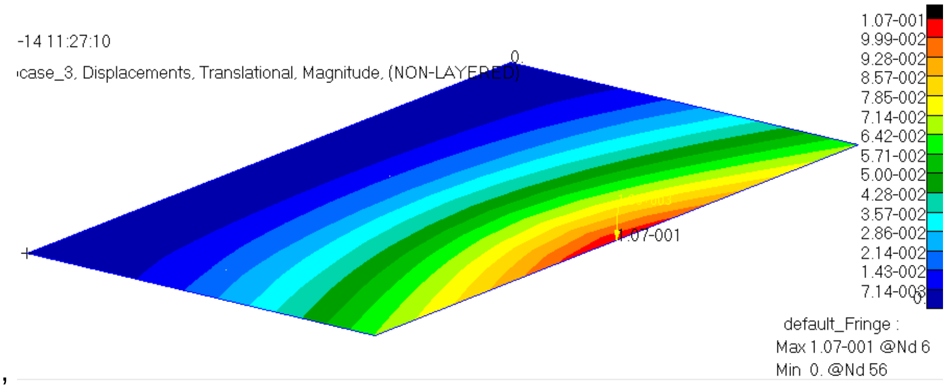
-14 11:27:10
case_3, Displacements, Translational, Magnitude, (NON-LAYERED)
0
1.07-001
1.07-001
9.99-002
9.28-002
8.57-002
7.85-002
7.14-002
6.42-002
5.71-002
5.00-002
4.28-002
3.57-002
2.86-002
2.14-002
1.43-002
7.14-003
0
default_Fringe :
Max 1.07-001 @Nd 6
Min 0. @Nd 56

Figure 3-11 FEM results for uniform plate, point load

3.1.1.2.2 One-axis Trapezoidal Plate:

For a one-axis trapezoidal plate, as shown in Figure 3-8-b, the thickness varies across the x or y-axes of the plate, and this thickness variation is imposed into the energy equation as,

$$h(\mathrm{x}) = \mathrm{t}\left(1 - c_x \frac{x}{a}\right) \tag{3-6}$$

or

$$h(\mathrm{y}) = \mathrm{t}\left(1 - c_y \frac{y}{b}\right) \tag{3-7}$$

where t is the thickness parameter, c_x and c_y are the taper ratio specifying the thickness variation along the plate x-axis or y-axis, respectively, *a* is the length of the longitudinal side and *b* is the length of the transverse side of the plate.

The same plate model given at 3.1.1.2.1 is utilized. The plate is loaded with a uniform pressure of 2000 N/mm^2 for an arbitrarily loading case. As shown in Figure 3-12, the maximum deflection for a uniform pressure loading of 2000 N/mm^2 is obtained as 0.0394 mm at the point (*x*,*y*)=(*a*,*b*/2). On the other hand, the maximum deflection from the Rayleigh-Ritz approximation with five shape functions in both directions is calculated as 0.0399 mm. The error is calculated as 1.2 %.

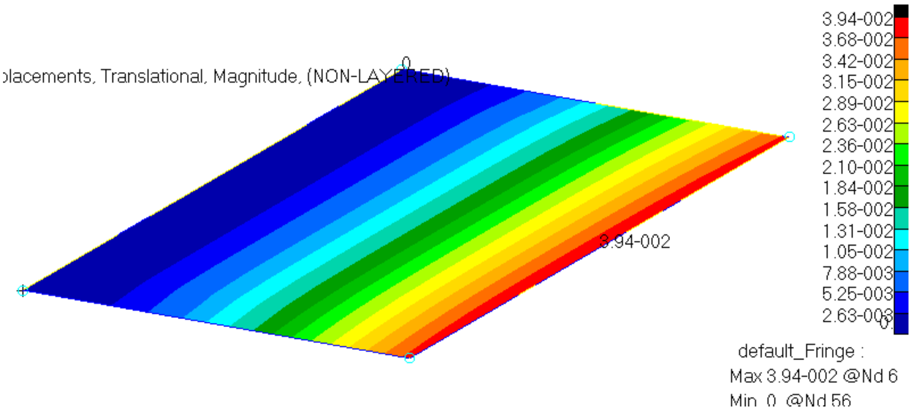

Figure 3-12 FEM results for one-axis tapered plate model, pressure loading

3.1.1.2.3 Two-axis Trapezoidal Plate:

For a two-axes trapezoidal plate, as shown in Figure 3-8-c, the thickness varies along both the x and y axes of the plate, and this variation is imposed into the energy equation as follows;

$$h(\mathrm{x},\mathrm{y}) = \mathrm{t}\left(1 - c_x \frac{x}{a} - c_y \frac{y}{b}\right) \tag{3-8}$$

where and are the taper ratios specifying the thickness variation along the plate x-axis or y-axis, respectively.

The same plate model given at 3.1.1.2.1 is solved with the thickness function given in Equation (3-8). The plate is loaded with a uniform pressure of 2000 N/mm^2 for an arbitrarily loading case.

In Figure 3-13 below, deformation results obtained from Nastran are displayed; the maximum deflection is obtained from Nastran as 0.104 mm. On the other hand, the maximum deformation calculated by the Rayleigh-Ritz approximation is 0.0979 mm, with two shape functions in both directions, and 0.1004 mm, with seven shape functions in both directions. The error is calculated for seven shape functions in both directions as 3.8%.

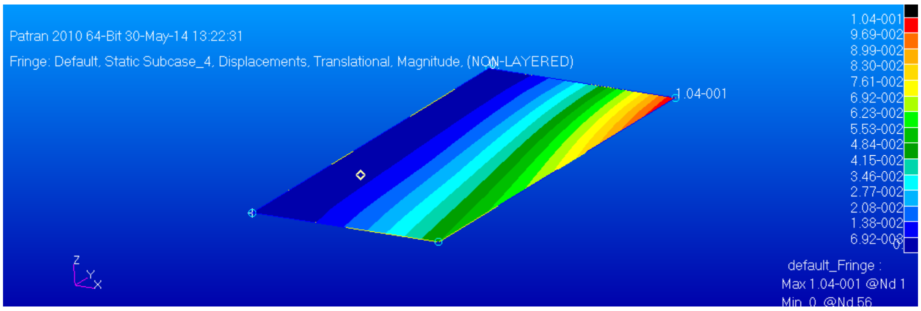
Patran 2010 64-Bit 30-May-14 13:22:31
Fringe: Default, Static Subcase_4, Displacements, Translational, Magnitude, (NON-LAYERED)
1.04-001
1.04-001
9.69-002
8.99-002
8.30-002
7.61-002
6.92-002
6.23-002
5.53-002
4.84-002
4.15-002
3.46-002
2.77-002
2.08-002
1.38-002
6.92-003
0.
default_Fringe :
Max 1.04-001 @Nd 1
Min 0. @Nd 56
Z
Y
X

Figure 3-13 FEM results for two-axis tapered plate model, uniform pressure loading

3.1.1.3 Finite Strip Method

The finite strip method (FSM) is a numerical method that compares favorably with the finite element method (FEM) in terms of run-time, storage of stiffness, load, and resulting output matrices. FSM combines the idea of the analytical Kantorovich-Vlassov's method and the FEM technique [92]. It is a semi-analytical finite element modelling using continuous functions to satisfy the boundary conditions in one direction of the plate and finite element discretization in the other direction. Thus, the two-dimensional plate problem reduces to a one-dimensional problem [93]. A typical plate discretized with n finite strip elements is shown in Figure 3-14.

FSM can be classified into two categories that differ in selecting the shape functions for the longitudinal axis of the plate problem, namely [94],

- Semi-analytical FSM (SFSM)
- Numerical FSM (NFSM).

SFSM uses a function series (beam eigenfunctions, orthogonal polynomial series) that satisfy a finite strip's end conditions in the longitudinal direction. In the orthogonal direction, simple polynomials are utilized. Sample sine and cosine functions defined over the width of a finite strip element are plotted in Figure 3-15 and Figure 3-16, respectively.

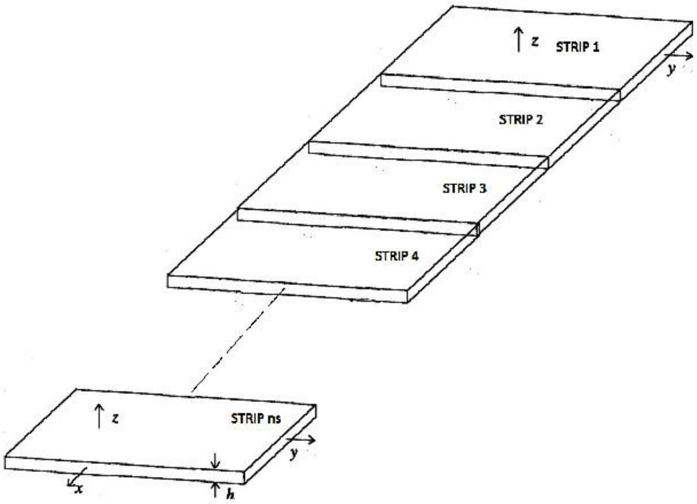
z
STRIP 1
y
STRIP 2
STRIP 3
STRIP 4
z
STRIP ns
y
x
h

Figure 3-14 A plate discretized with n finite strip elements

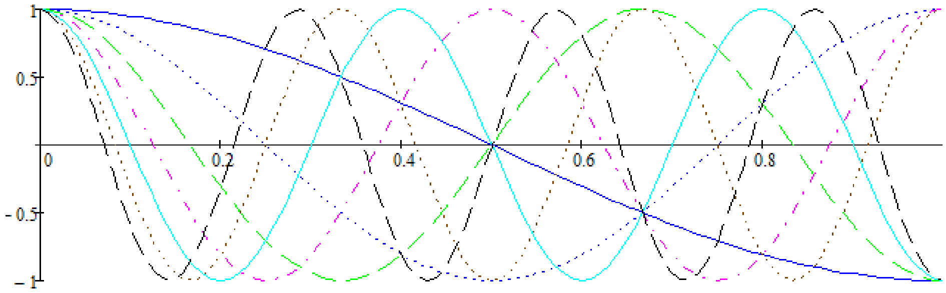

Figure 3-15 Sine functions for seven harmonics for SFMS

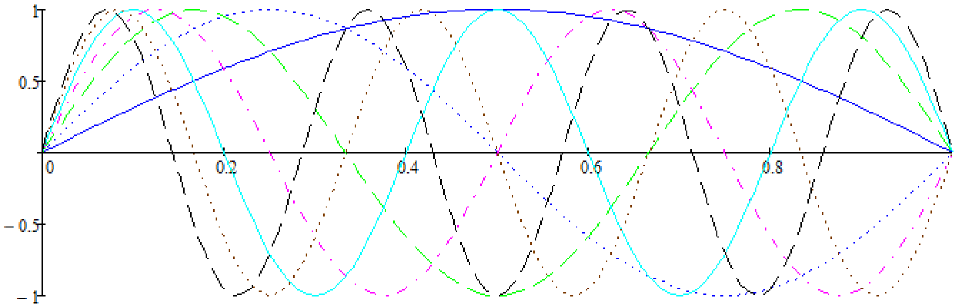

Figure 3-16 Cosine functions for seven harmonics for SFSM

However, SFSM has some disadvantages while defining the concentrated forces, multiple spans, and discrete supports at strip ends [92]. Since sine and cosine series are continuously differentiable everywhere, this property causes problems when there is an abrupt change in any property (i.e., thickness) or the presence of any concentrated loads, or internal supports, because second or third derivatives will be discontinuous [92].

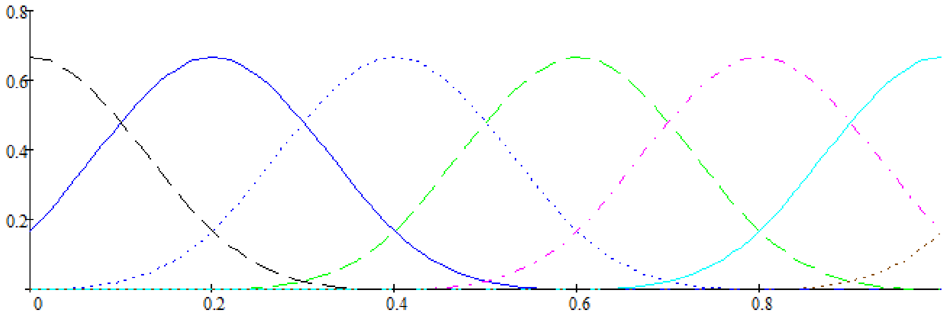

Figure 3-17 B3 spline functions, for NFSM, specified for a free variable at the boundary of the problem

Therefore, to overcome these difficulties, NFSM is proposed by several authors. NFSM utilizes spline functions instead of Fourier series. Sample B3 spline functions defined over the width of a finite strip element are plotted in Figure 3-17 and Figure 3-18 for free and fixed variables at the boundary of the plate, respectively.

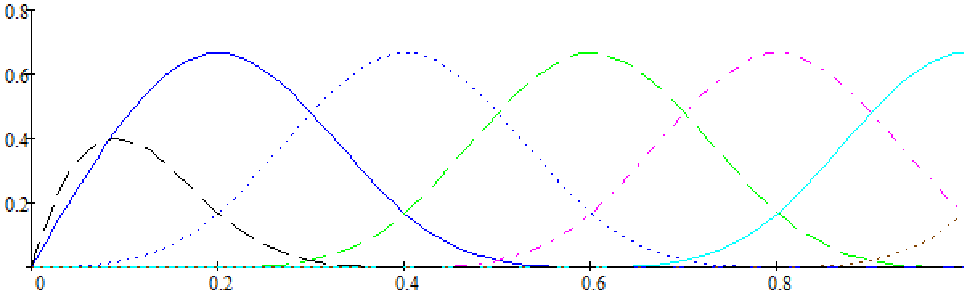

Figure 3-18 Spline functions for NFSM, specified for a fixed variable at the boundary of the problem

FSM become the subject of many researches, several of them are given in the review article [95]. Some of them are directly related to gear tooth modelling by using FSM [96]. For the face-gear and the spur pinion, the utilized strip element formulation is given at Chapter 3.2.

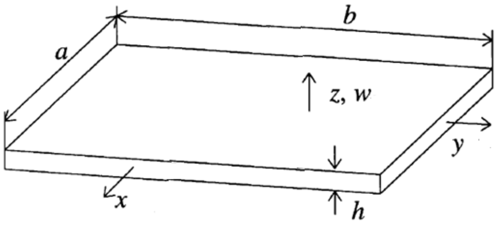

Figure 3-19 A finite strip element

The following cases are solved for a uniform thickness plate. For Case-1, 2, and 3, the plate is loaded with arbitrary uniform pressure, simply supported on both long sides (along x=0 and x=b) and free on the short sides (along y=0 and y=b). SFSM is utilized. Along the long side, appropriate shape functions are imposed by the Fourier series with seven harmonics. The short side of the strip element is taken as,

- 2-noded at Case-1, as depicted in Figure 3-20-a,
- 3-noded at Case-2, as depicted in Figure 3-20-b
- 4-noded at Case-3, as depicted in Figure 3-20-c

For Case-4, NFSM is utilized. Along the long side, appropriate shape functions are imposed with B3 splines. The short side of the strip element is taken as,

- 2-noded at Case-4, as depicted in Figure 3-20-a.

The deflection results for Case-1, 2, and 3 are tabulated in Table 3-1. The deflections are also demonstrated in Figure 3-22. As shown in the table, the results are comparable with the MSC Nastran model of the plate. As node number increases along the plate's short side, the error is reduced for the displacement values at the free edges and the specified arbitrary point on the first strip element.

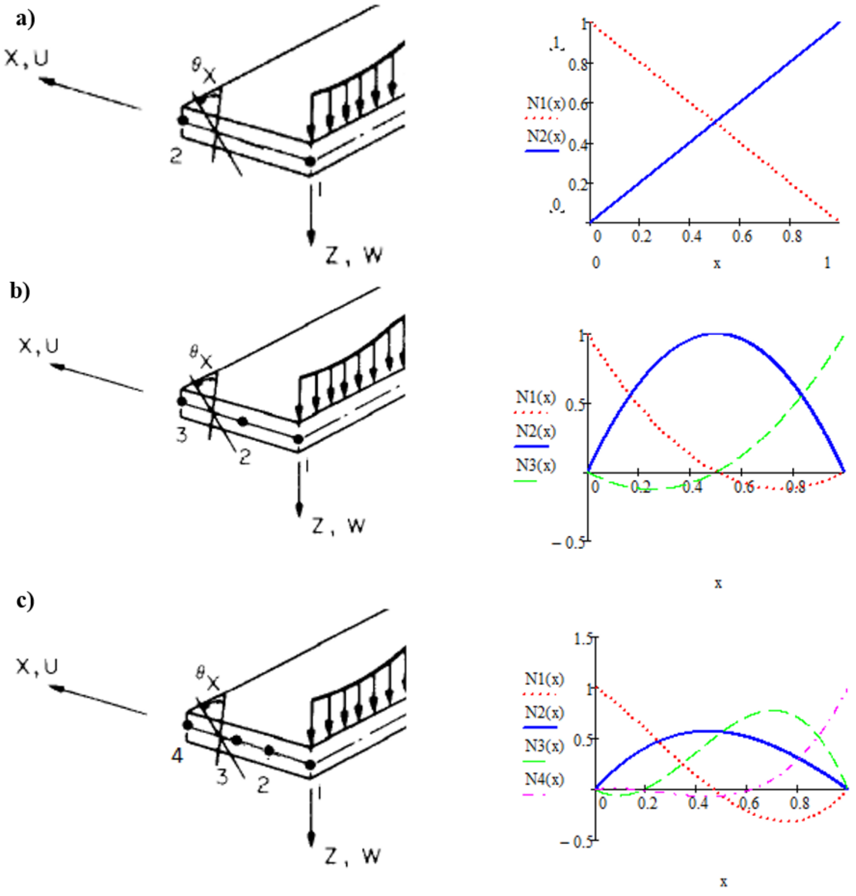
a)
X, U
θX
2
1
Z, W
N1(x)
N2(x)
x
b)
X, U
θX
3
2
1
Z, W
N1(x)
N2(x)
N3(x)
x
c)
X, U
θX
4
3
2
1
Z, W
N1(x)
N2(x)
N3(x)
N4(x)
x

Figure 3-20 a) 2-noded, **b)** 3-noded, **c)** 4-noded Finite Strip Element with the appropriate polynomials, [97]

Table 3-1 Comparison of FE and FSM deflection results for Case-1, Case-2, and Case-3

	At the free edges (mm) (x=0, y=b/2 on 1st strip)			In the middle (mm) (x=a, y=b/2 on 2nd strip)			At an arbitrary point (mm), at the edge of strip 1 (x=a, y=b/2 on 1st strip)		
	SFSM	MSC-Nastran	Error (%)	SFSM	MSC-Nastran	Error (%)	SFSM	MSC-Nastran	Error (%)
Case-1	7.29	7.88	7.4	6.40	6.39	-0.25	6.48	6.63	2.25
Case-2	7.68		2.4	6.48		-1.5	6.57		0.84
Case-3	7.74		1.6	6.48		-1.4	6.58		0.80

The deflection results for Case-4 are tabulated in Table 3-2. The deflections are also demonstrated in Figure 3-22. Even with four strip elements, the error is less than 1%. This demonstration shows the power of the Finite Strip Method for the cases for uniform or slightly varying cross sections.

Table 3-2 Comparison of FE and FSM deflection results for Case-4

	At the free end of the plate (mm) (x=0, y=b on 1st strip)			In the middle (mm) (x=a, y=b/2 on 2nd strip)		
	NFSM	MSC-Nastran	Error (%)	NFSM	MSC-Nastran	Error (%)
Case-4	7.29	7.88	4.0	22.47	22.6	-0.56

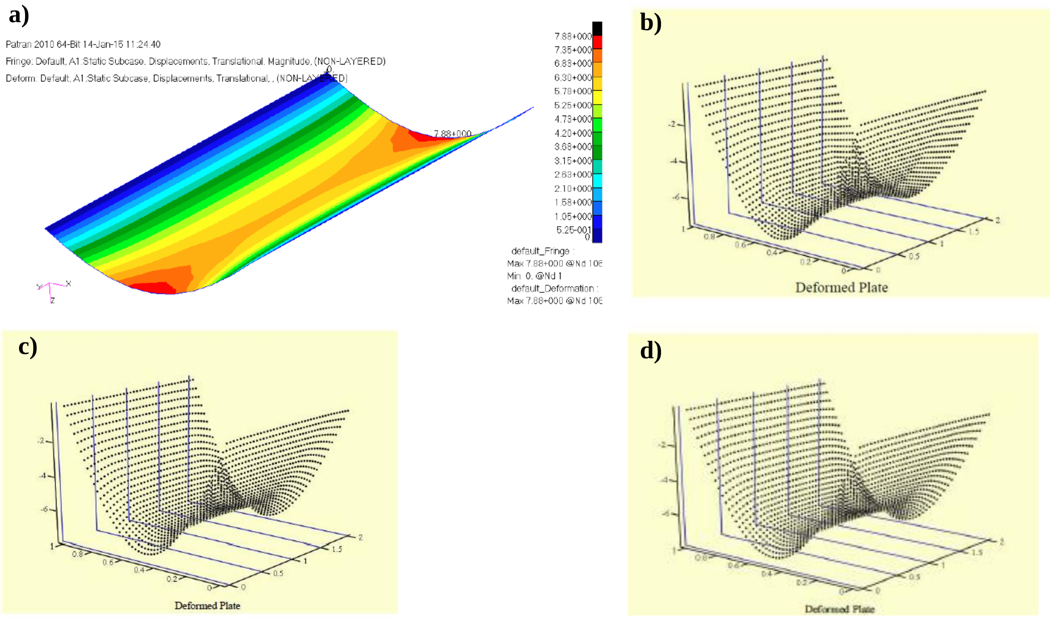

Figure 3-21 Comparison for deflection Case-4, **a)** MSC Nastran FE Model with 50 CQUAD elements, **b)** 2-noded FSM Model with four strip elements, **c)** 3-noded FSM Model with four strip elements, **d)** 4-noded FSM Model with four strip elements

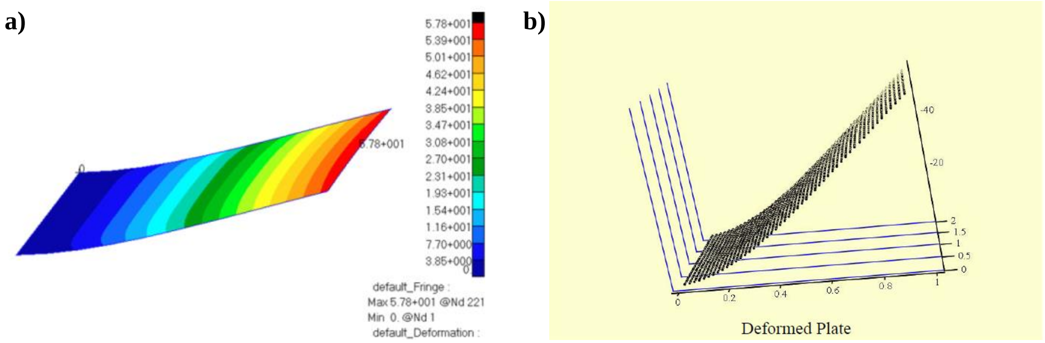

Figure 3-22 Comparison for deflection Case-4, **a)** MSC Nastran FE Model with 50 CQUAD elements, **b)** 2-noded FSM Model with four strip elements

3.1.1.4 Finite Prism and Quasi Prism Method

Analysis of a structure with 3D FEM costs and sometimes is unnecessary for the structures with a constant or a nearly constant shape in one direction, and simple boundary conditions. The Finite Prism Method (FPM) yields good results with a much smaller number of input data and compares favorably with FEM in terms of run time. A typical FPM and QPM elements are depicted in Figure 3-23-a and Figure 3-23-b, respectively.

As Finite Strip Method (FSM), FPM also combines the idea of the analytical Kantorovich-Vlassov's method and the FEM technique [92]. FPM can be considered as a special form of 3D FEM concerning the shape of displacements along a given direction [98]. FPM does not use polynomial displacement functions in all three directions for the elementwise discretization. It incorporates polynomial displacement functions only in two directions. Along the third direction, it uses continuous functions which satisfy the boundary conditions without any elementwise discretization.

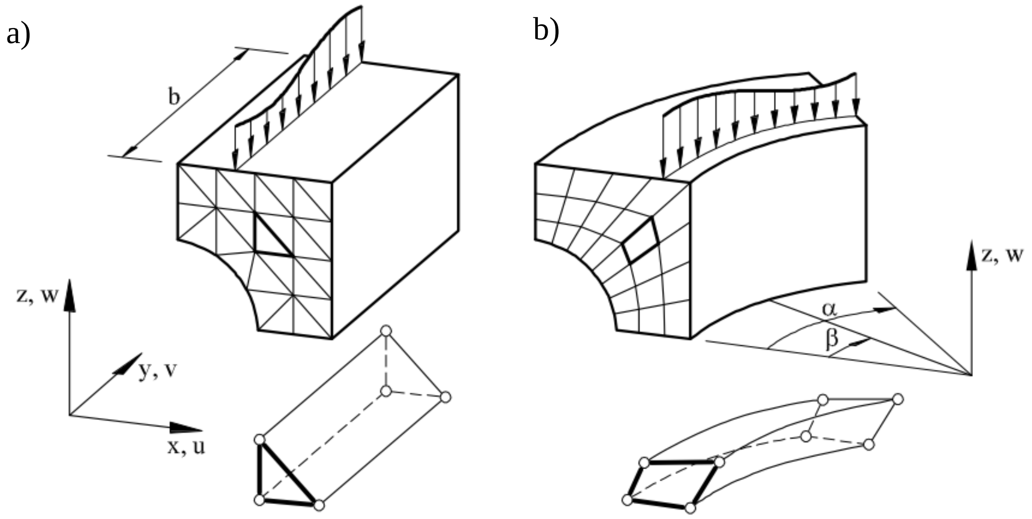

Figure 3-23 Prismatic solids discretized in two dimensions **a)** with FPM and **b)** with QPM [99]

Similar to FSM, FPM can also be classified into two categories that differ in selecting the shape functions for the longitudinal axis of the plate problem.

Semi-analytical FPM uses a function series (beam eigenfunctions, orthogonal polynomial series) which satisfies the end conditions of a prism-like structure a priori in the longitudinal direction and simple polynomials in the remaining orthogonal directions [98]. Numerical FPM combines Fourier expansions along the prismatic direction and 2D solid elements for discretizing the transverse cross-section [100]. The method is suitable for analyzing prismatic solid structures that do not have significant changes in transverse cross sections. The method have been utilized by several authors for the analysis of different structures [101–107].

The finite Quasi-Prism Method (QPM), on the other hand, is a valuable method for modelling structures that are only partially prismatic shapes or which have prismatic shapes within them [108–110]. A quasi-prism element is a three-dimensional element. It is utilized for the analyses of the parts in which the cross-section remains constant or nearly constant for the length of the element. It resembles the FPM element but differs in that, along all axode curves, depicted in Figure 3-24, the geometry is approximated with higher order Chebyshev functions [108] in all three dimensions. Element formulations for both methods have been given in Appendix D.

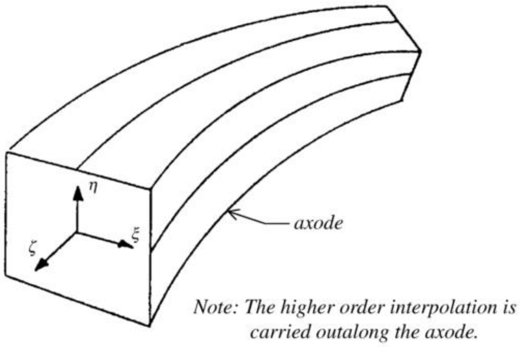

η
ξ
ζ
axode
Note: The higher order interpolation is carried outalong the axode.

Figure 3-24 A typical QPM element with axodes, [108]

The following arbitrarily loading cases are solved.

- Case-1, an arbitrary unit point load is applied to a constant cross-section plate, which is modelled by FPM,
- Case-2, an arbitrary uniformly distributed line load along a straight line applied to a constant cross-section plate, which is modelled by FPM,
- Case-3, an arbitrary uniformly distributed line load along a straight line applied to a variable cross-section plate, which is modelled by QPM.

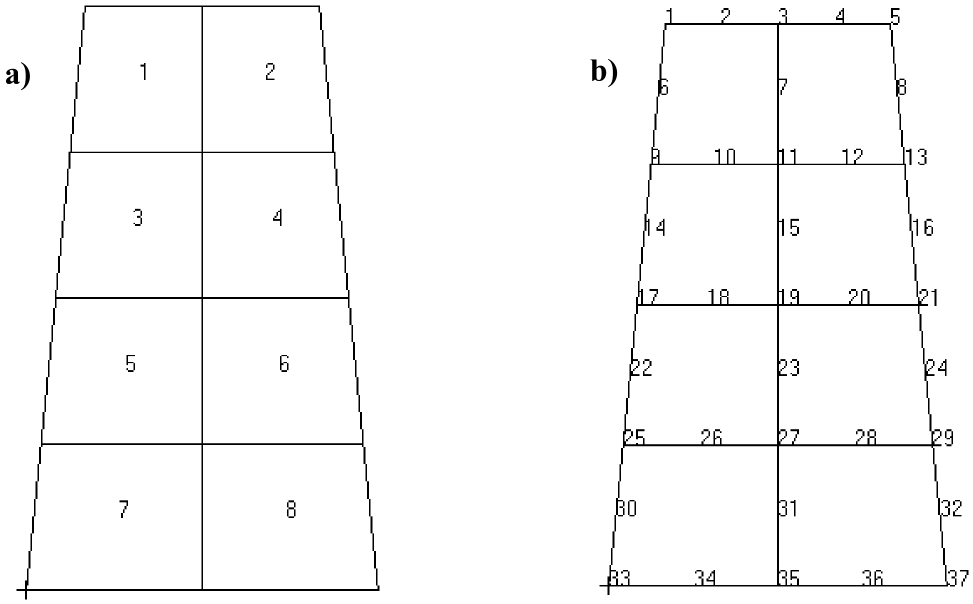
a)
1
2
3
4
5
6
7
8
b)
1 2 3 4 5
6 7 8
9 10 11 12 13
14 15 16
17 18 19 20 21
22 23 24
25 26 27 28 29
30 31 32
33 34 35 36 37

Figure 3-25 a) The element numbering and **b)** the node numbers for the 2D discretization

For all cases, eight 8-noded iso-parametric elements have been utilized for the modelling, which is formulated in Appendix D. The two ends of the plate are simply supported. The following discretization in the *xz* plane is performed. The element numbers and corresponding node numbers and their connectivity information are given in Figure 3-25. Figure 3-26-a and Figure 3-26-b show a plate modelled with finite prism elements and a plate modelled with quasi prism elements, respectively.

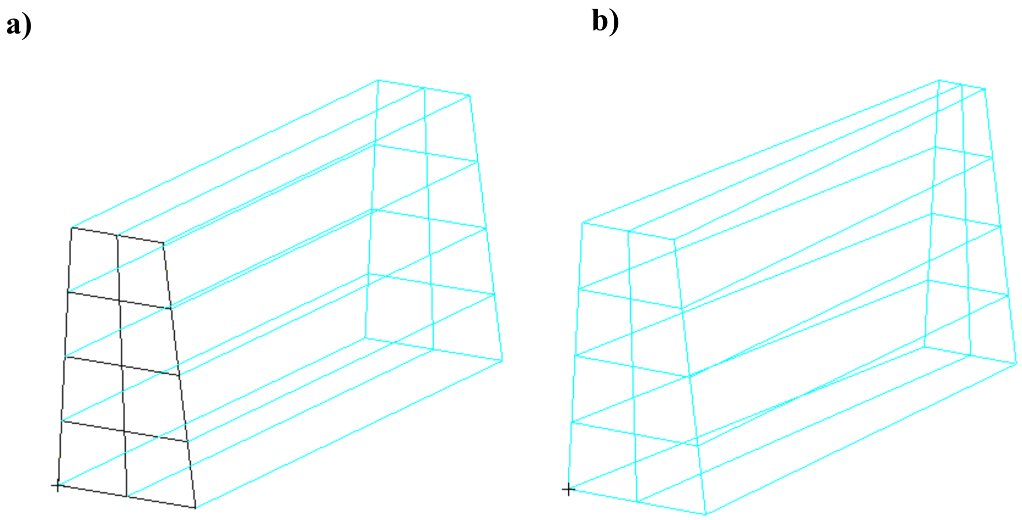

Figure 3-26 a) The prism with a constant cross-section along the longitudinal axis (FPM), **b)** the prism with a variable cross-section along the longitudinal axis (QPM)

Case-1: Constant cross section, ends simply supported, point load is applied, depicted in Figure 3-27

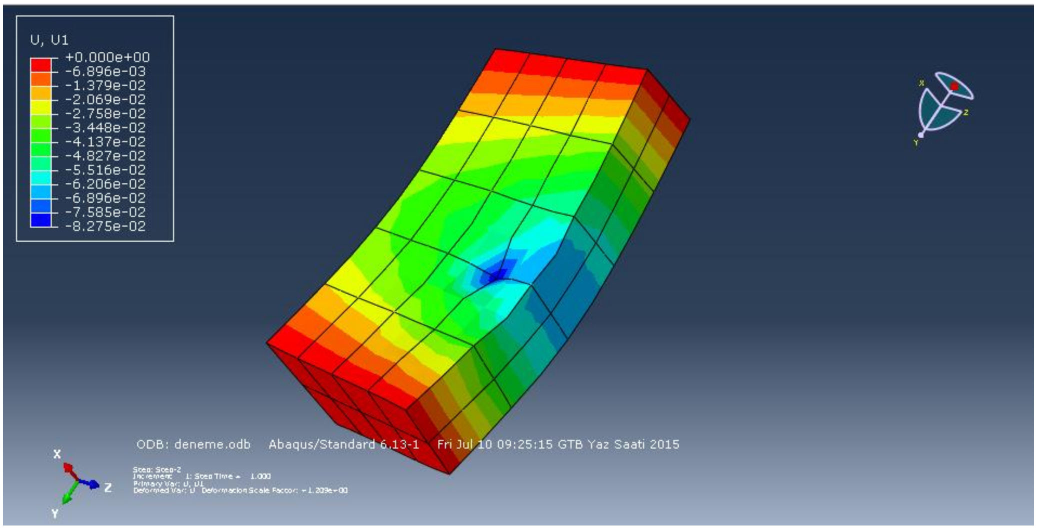
U, U1
+0.000e+00
-6.896e-03
-1.379e-02
-2.069e-02
-2.758e-02
-3.448e-02
-4.137e-02
-4.827e-02
-5.516e-02
-6.206e-02
-6.896e-02
-7.585e-02
-8.275e-02
ODB: deneme.odb Abaqus/Standard 6.13-1 Fri Jul 10 09:25:15 GTB Yaz Saati 2015
Step: Step-2
Increment 1: Step Time = 1.000
Primary Var: U, U1
Deformed Var: U Deformation Scale Factor: +1.209e+00
X
Y
Z

Figure 3-27 Application of point load, constant cross-section

Figure 3-28 shows the FPM results and the Abaqus 3D FEM results at the upper left corner of element 1, varying the number of utilized harmonics and gauss integration points. Note that position 0.6 is the load application point.

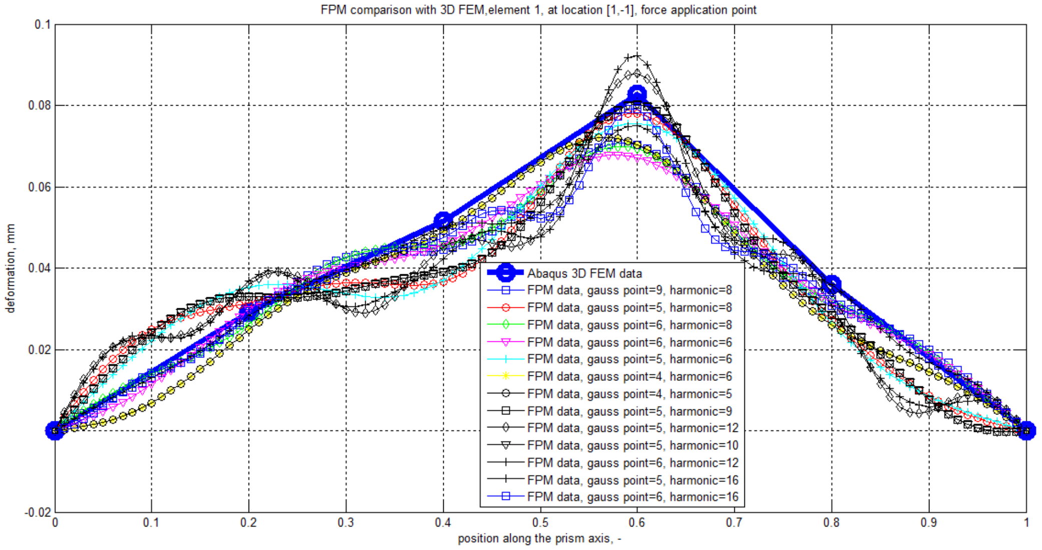

Figure 3-28 FPM comparison with 3D FEM, element 1, location [1,-1] (location is depicted in Figure D-1)

Figure 3-29 shows the FPM results and the Abaqus 3D FEM results at the upper left corner of element 2, varying the number of utilized harmonics and gauss integration points. FPM gives a very good approximation at the specified locations.

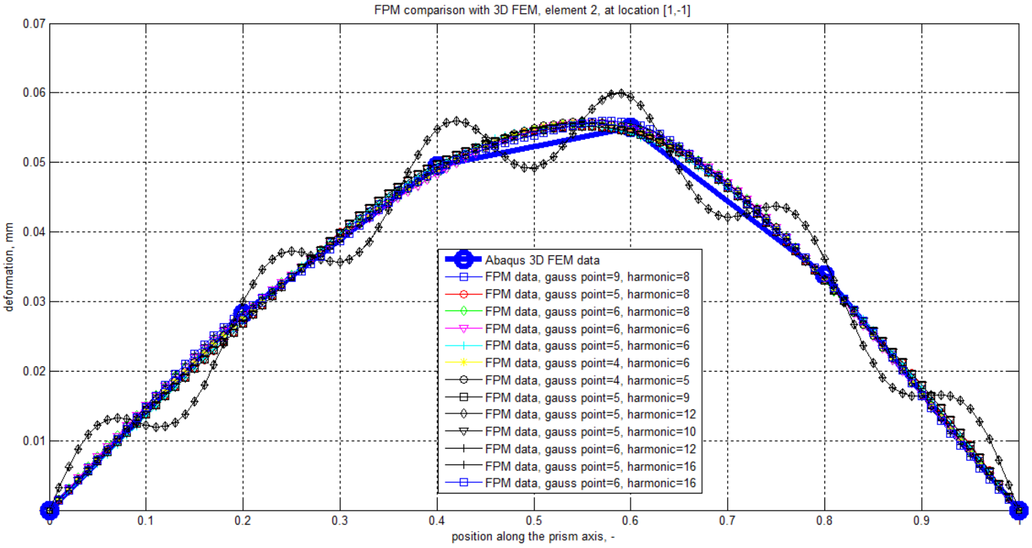

Figure 3-29 FPM comparison with 3D FEM, element 3, location [1,-1]] (location is depicted in Figure D-1)

In Figure 3-30, for a fixed number of harmonics, increasing the gauss points in the integration process yields better results for all positions, except at the load application point. As it can be seen by examining both Figure 3-30 and Figure 3-31 that increasing both utilized harmonics and gauss integration points will decrease the error.

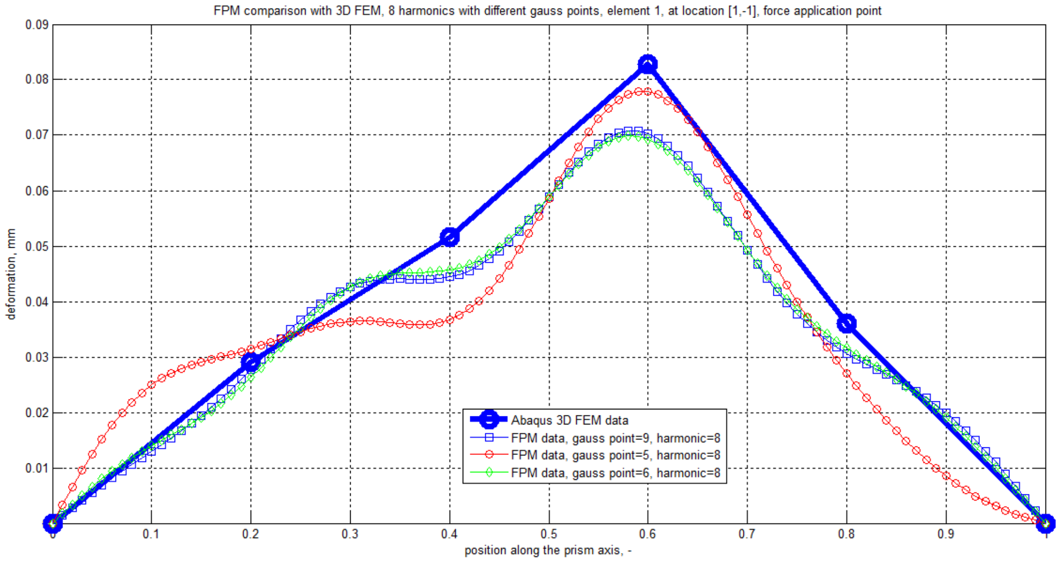

Figure 3-30 FPM comparison with 3D FEM, element 1, location [1,-1], number of utilized harmonics is 8, number of gauss points varies

As seen from Figure 3-31, especially for the load application point, as harmonics are increased, better results are obtained for a fixed number of gauss points.

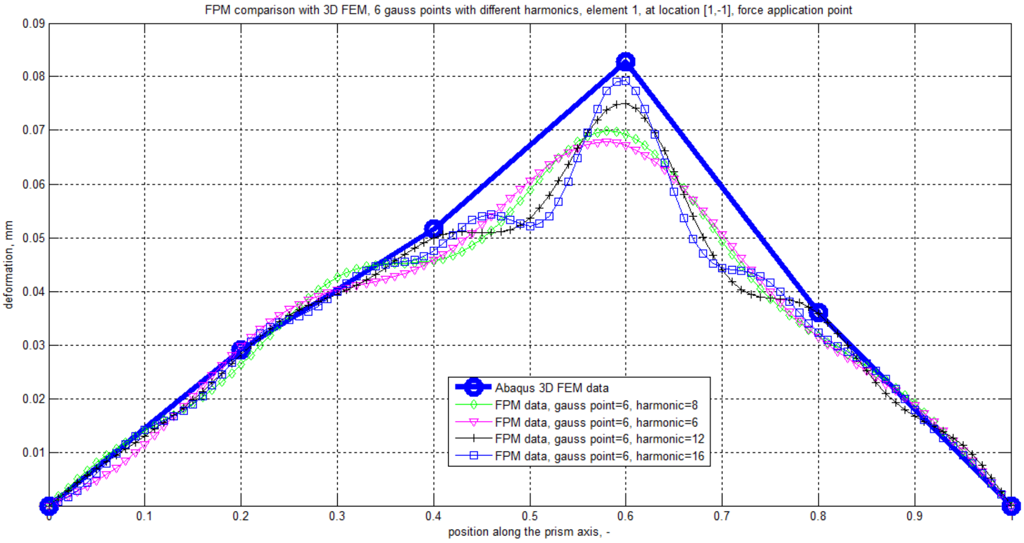

Figure 3-31 FPM comparison with 3D FEM, element 1, location [1,-1], gauss point is 6, number of the utilized harmonics varies

Figure 3-32 and Figure 3-33 compares the results for element 7 and element 5, respectively, for several gauss points and harmonics with the Abaqus 3D FEM data.

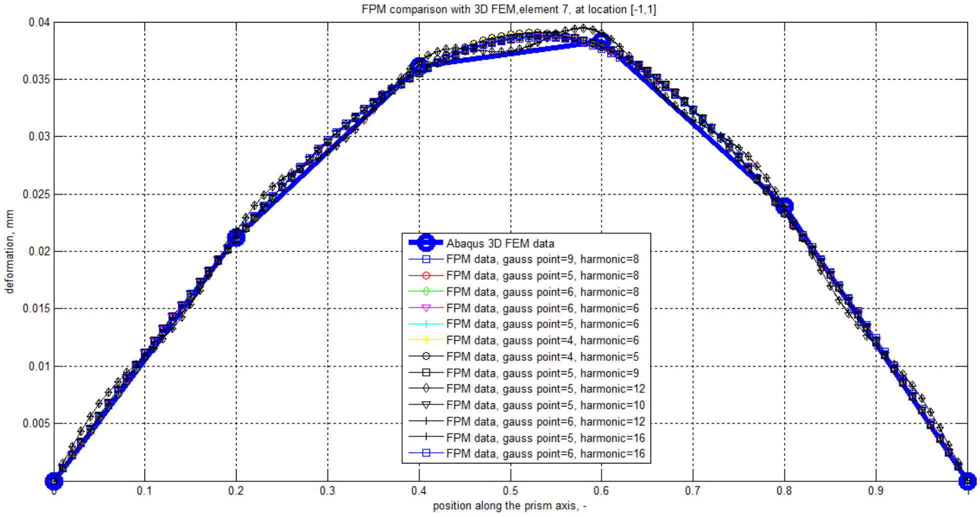

Figure 3-32 FPM comparison with 3D FEM, element 7, location [-1,1], number of gauss points, and number of utilized harmonics vary

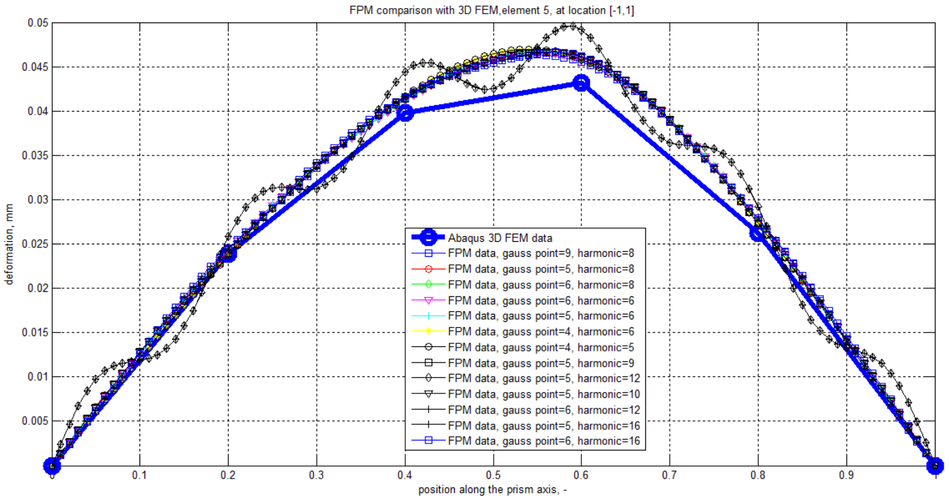

Figure 3-33 FPM comparison with 3D FEM, element 5, location [-1,1], number of gauss points, and number of utilized harmonics vary

Case-2: Constant cross-section, ends simply supported, line load is applied along a straight line, depicted in Figure 3-34.

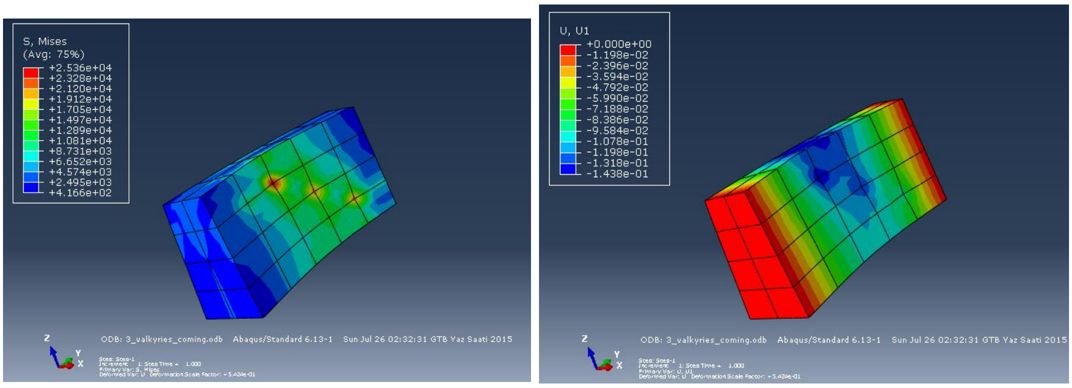
S, Mises
(Avg: 75%)
+2.536e+04
+2.328e+04
+2.120e+04
+1.912e+04
+1.705e+04
+1.497e+04
+1.289e+04
+1.081e+04
+8.731e+03
+6.652e+03
+4.574e+03
+2.495e+03
+4.166e+02
U, U1
+0.000e+00
-1.198e-02
-2.396e-02
-3.594e-02
-4.792e-02
-5.990e-02
-7.188e-02
-8.386e-02
-9.584e-02
-1.078e-01
-1.198e-01
-1.318e-01
-1.438e-01
ODB: 3_valkyries_coming.odb Abaqus/Standard 6.13-1 Sun Jul 26 02:32:31 GTB Yaz Saati 2015
Z
Y
X

Figure 3-34 Application of line load, constant cross-section; stress distribution, and deformation results

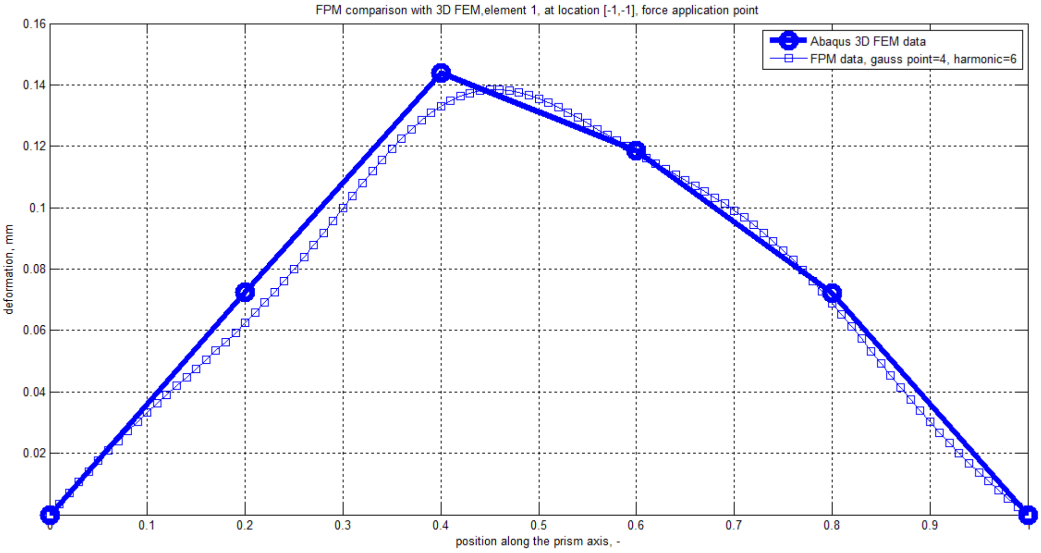

Figure 3-35 FPM comparison with 3D FEM, constant cross-section, line load application, element 1, location [-1,-1], gauss point is 4, harmonics 6

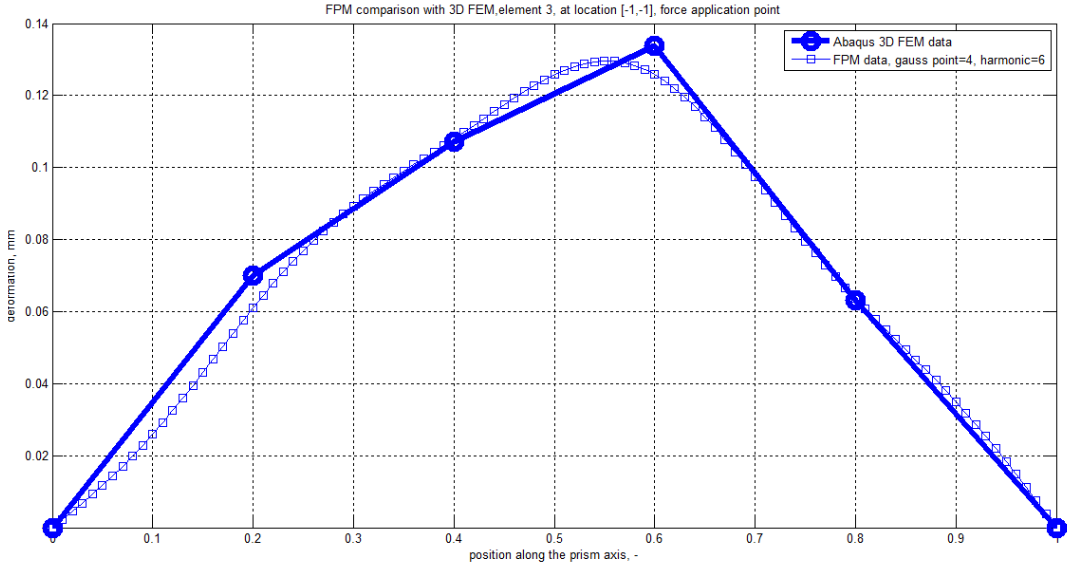

Figure 3-36 FPM comparison with 3D FEM, constant cross-section, line load application, element 3, location [-1,-1], gauss point is 4, harmonic 6

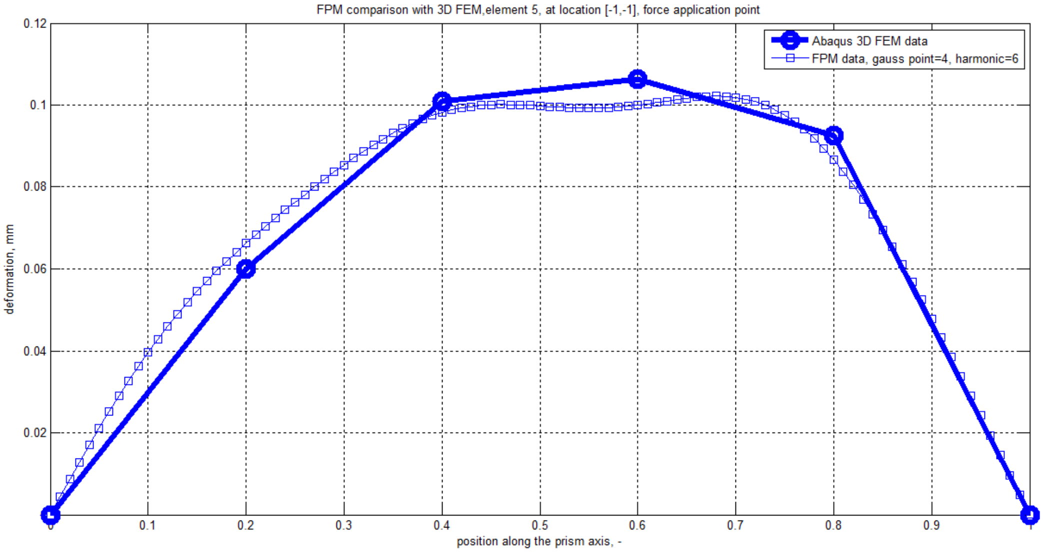

Figure 3-37 FPM comparison with 3D FEM, constant cross-section, line load application, element 1, location [1,-1], gauss point is 5, harmonics 6

Case-3: Variable cross-section, ends simply supported, line load is applied along a straight line

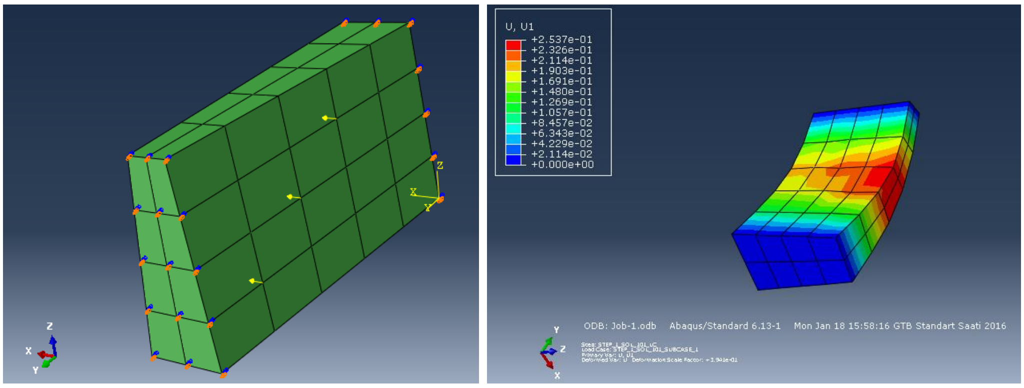
Z
X
Y
Z
X
Y
U, U1
+2.537e-01
+2.326e-01
+2.114e-01
+1.903e-01
+1.691e-01
+1.480e-01
+1.269e-01
+1.057e-01
+8.457e-02
+6.343e-02
+4.229e-02
+2.114e-02
+0.000e+00
ODB: Job-1.odb Abaqus/Standard 6.13-1 Mon Jan 18 15:58:16 GTB Standart Saati 2016
Y
Z
X

Figure 3-38 a) 3D FE model and application of line load, **b)** ABAQUS results

Figure 3-39, Figure 3-40, Figure 3-41, and Figure 3-42 compare the deflections obtained by the Abaqus 3D model and the variable cross-section FPM (QPM) for elements 1, 3, 5, and 7, respectively. The utilized gauss points for the integral calculations are four, and the utilized harmonics along the cross-section are taken as five or six. The figures show that utilizing six harmonics with four gauss points for the variable cross-section case is not enough to get accurate results. Increasing them, on the other hand, will significantly increase the computational time. In Case-1 and Case-2, four gauss points incorporating five or six harmonics were enough to catch accurate plate deflection results.

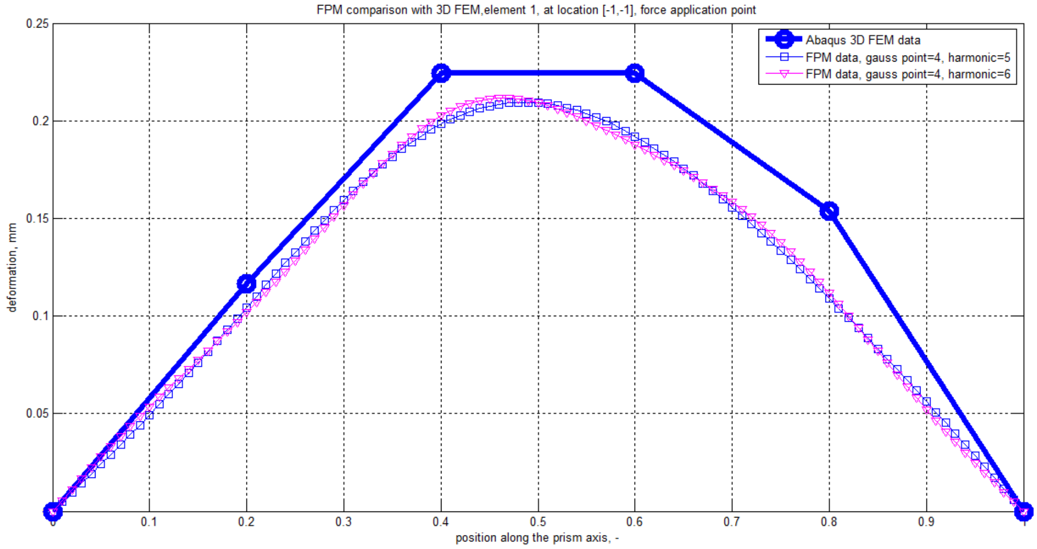

Figure 3-39 Comparison with 3D FEM, variable cross-section, line load application, element 1, location [1,-1], gauss point is 4, with harmonics 5 or 6

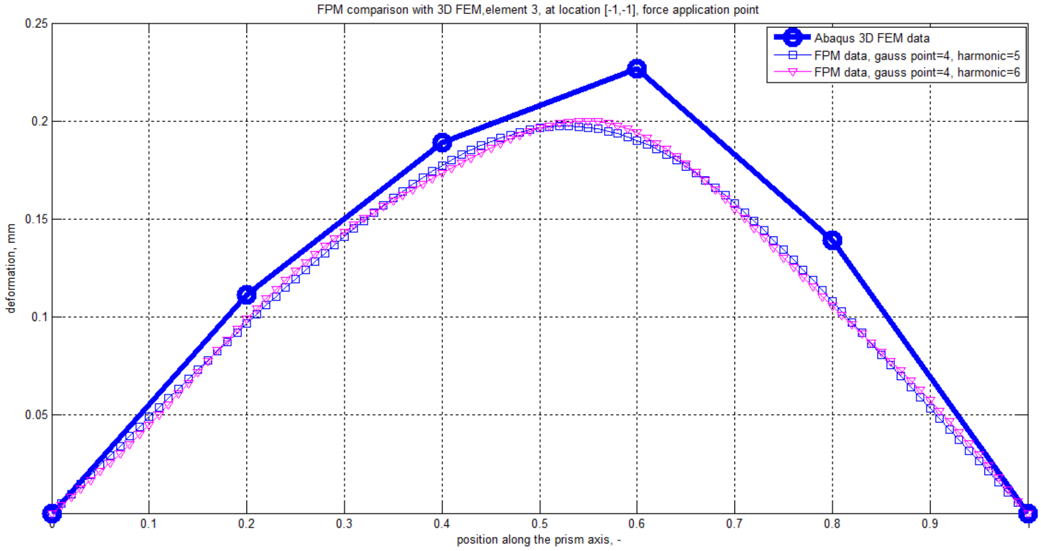

Figure 3-40 Comparison with 3D FEM, variable cross-section, line load application, element 3, location [1,-1], gauss point is 4, with harmonics 5 or 6

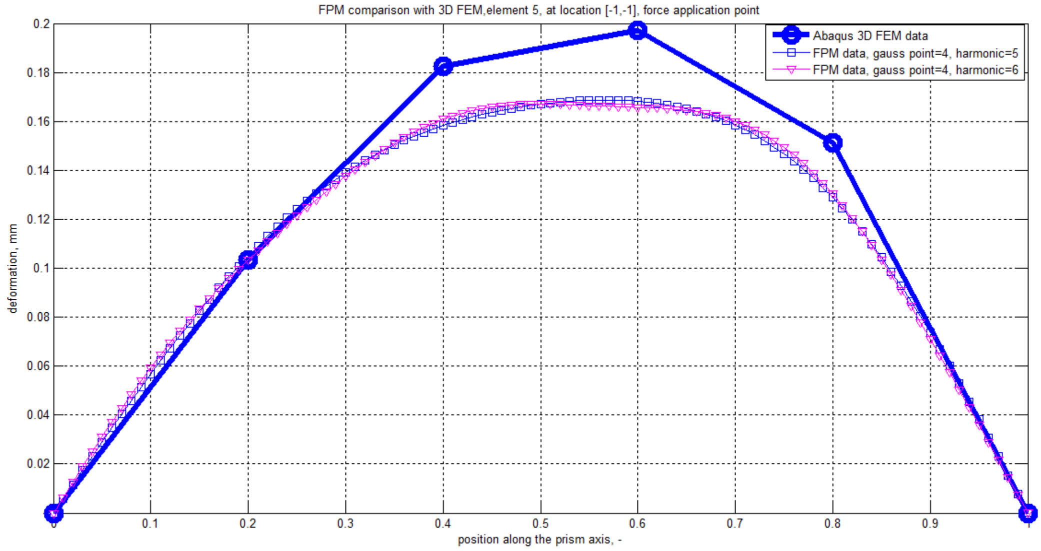

Figure 3-41 Comparison with 3D FEM, variable cross-section, line load application, element 5, location [1,-1], gauss point is 4, with harmonics 5 or 6

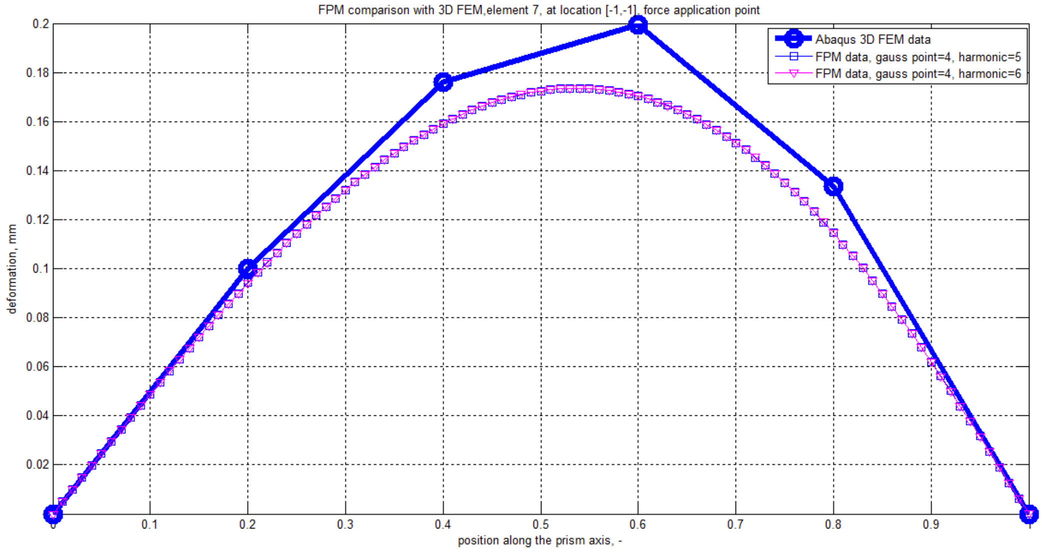

Figure 3-42 Comparison with 3D FEM, variable cross-section, line load application, element 7, location [1,-1], gauss point is 4, with harmonics 5 or 6

3.1.1.5 Discussion on the methods for the bending stiffness

The TSM yields good results compared to models created via the finite element method. It saves considerable computational time and appears to be the most straightforward method. However, since each slice is independent of each other, the main problem is finding the coupling stiffness between those slices. In literature, these stiffness values are generally calculated by several 3D FE runs, by which an empirical formula is generated for the coupling between the adjacent slices, and this coupling term is added to the uncoupled stiffness matrix of the gear, as in the Börner's empirical formula, given in Equation (3-4). This formula will be model dependent and will not apply to a specific geometry.

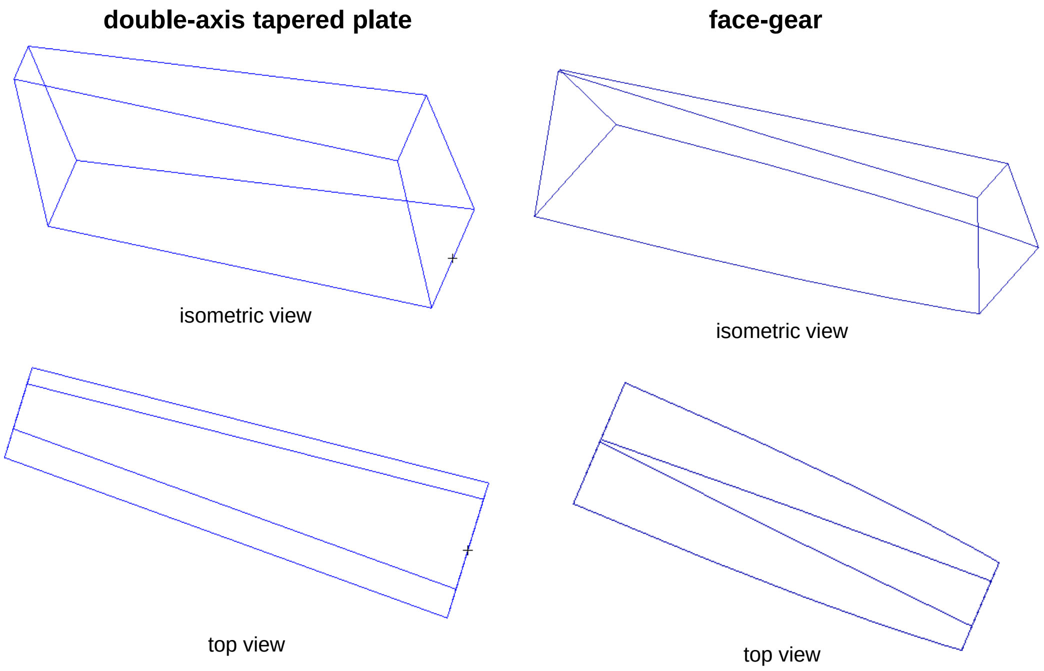

Figure 3-43 a) Double axis-trapezoidal tapered plate **b)** Face-gear

Then, one should calculate the coefficient C of Börner's equation, which will require several FE runs and increase computational time.

The Rayleigh-Ritz approximation for the Kirchoff plate works very well. It has been incorporated for different loading conditions and obtained comparable results with the FE models run within the Nastran package program. Also, with imposing thickness variation along both x and y axes, any geometry may be modelled via this method. Figure 3-43 shows the double-axis trapezoidal tapered plate and face-gear profiles. In order to model the thickness variation on the face-gear's tooth surface, the thickness Equation (3-8) must be derived analytically or numerically for a typical face-gear.

Finite Prism Method gives accurate results obtained via 3D FE model with a favorable number of gauss points for the integrals and five or six harmonic functions along the cross-section. However, the face-gear’s surface geometry varies along the face width and therefore has to be modelled by a varying cross-section prism element, which is, in fact, the Quasi-Prism element. On the other hand, the Quasi-Prism Method does not give accurate results for the same amount of gauss points and harmonics. In order to catch the deflection of the varying cross section, the gauss point and the harmonics incorporated along the face width have to be increased. This will lead to increased computational time. In addition, both FPM and QPM a priori require modelling a 2D finite element model. They, therefore, require the connectivity information of the nodes on this 2D model to be provided, which will increase the computational time.

The study in this chapter is performed to select an efficient, less time-consuming, and the most straightforward stiffness calculation method for parametric studies. The FSM appears to be the most advantageous method among the others. It does not a priori require any 2D or 3D element formulation since it is an extension of a 1D beam element. The second dimension is introduced by B3 splines or the Fourier series, which are appropriately formed according to the plate boundary conditions in the problem. The Mindlin plate theory can easily be applied to finite strip elements. As discussed in Chapter 2, a variable thickness strip element can also be incorporated to increase the method's accuracy with a small number of strip elements.

3.1.2 Contact Stiffness Contribution

Contact deformation between the meshing gear teeth is a contributing deflection to the total deflection. In literature, apart from utilization of sophisticated hybrid FE package programs, the following analytical methods are utilized for calculating this deformation [111]. Except Brewe&Hamrock's method, all equations assume line contact between the meshing gears.

- Hertz's Equation,
- Conry's Equation
- Cornell's Equation
- Palmgren's Equation
- Weber's Equation
- Brewe&Hamrock's Equation

The formulations for the listed methods are given in Appendix E.

3.1.2.1 Comparison of the Methods

For the case tabulated in Table 3-3, the contact stiffness values are calculated for the load levels F=500N, F=1000N, F=1500N, F=2000N according to Palmgren’s, Weber/Banascheck’s and Brewe&Hamrock’s equations.

Table 3-3 Input values

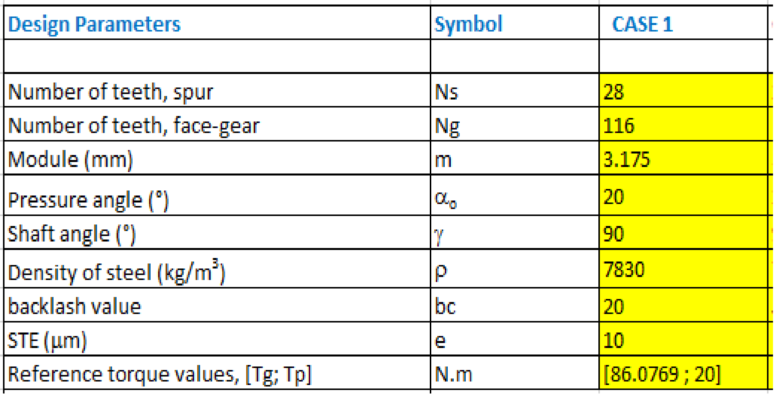

Design Parameters	Symbol	CASE 1
Number of teeth, spur	Ns	28
Number of teeth, face-gear	Ng	116
Module (mm)	m	3.175
Pressure angle (°)	α_o	20
Shaft angle (°)	γ	90
Density of steel (kg/m^3)	ρ	7830
backlash value	bc	20
STE (µm)	e	10
Reference torque values, [Tg; Tp]	N.m	[86.0769 ; 20]

Figure 3-44 to Figure 3-47 show the contact stiffness values of the contact points located on four different contact lines (at four different instants of a mesh cycle) of the conjugate action between the face-gear and the spur-pinion, specified in Table 3-3. The values are comparable for the bottom surface of the face-gear's tooth. But as contact line approaches to top surface of the tooth, Brewe&Hamrock's method gives higher values than the values calculated by Palmgren and Weber/Banascheck Method.

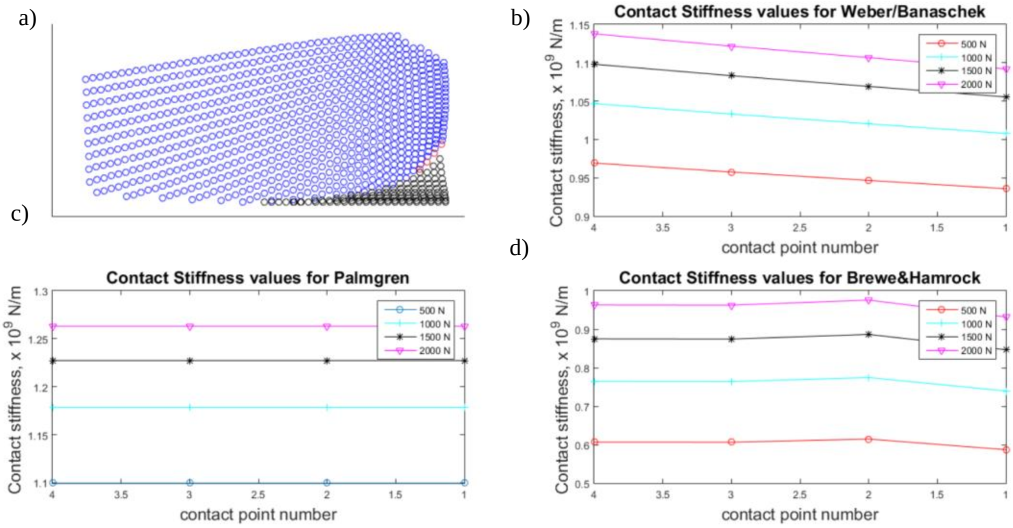

Figure 3-44 Contact stiffness **a)** at the first contact line, by **b)** Weber/Banascheck, **c)** Palmgren, **d)** Brewe&Hamrock, for various load levels

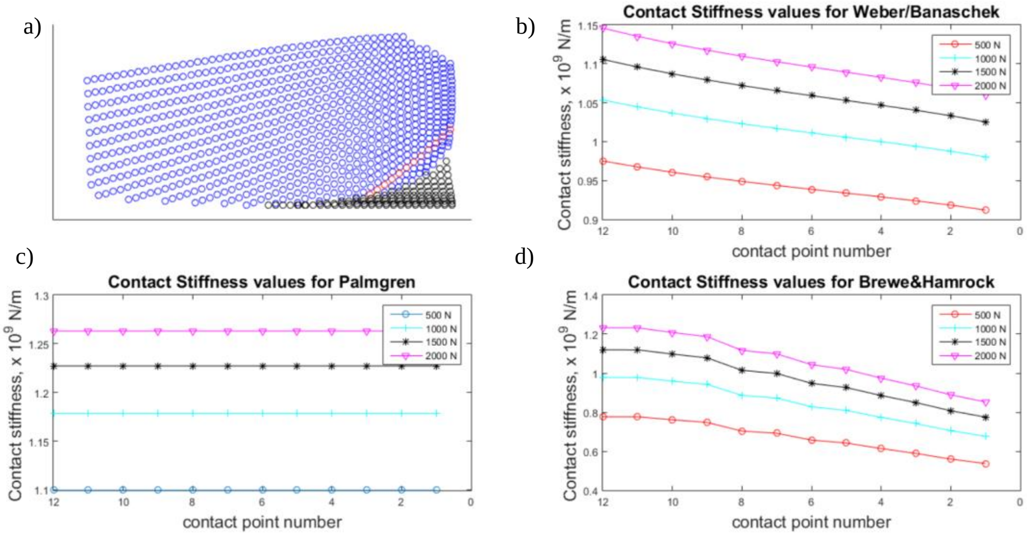

Figure 3-45 Contact stiffness **a)** at the fifth contact line, by **b)** Weber/Banascheck, **c)** Palmgren, **d)** Brewe&Hamrock, for various load levels

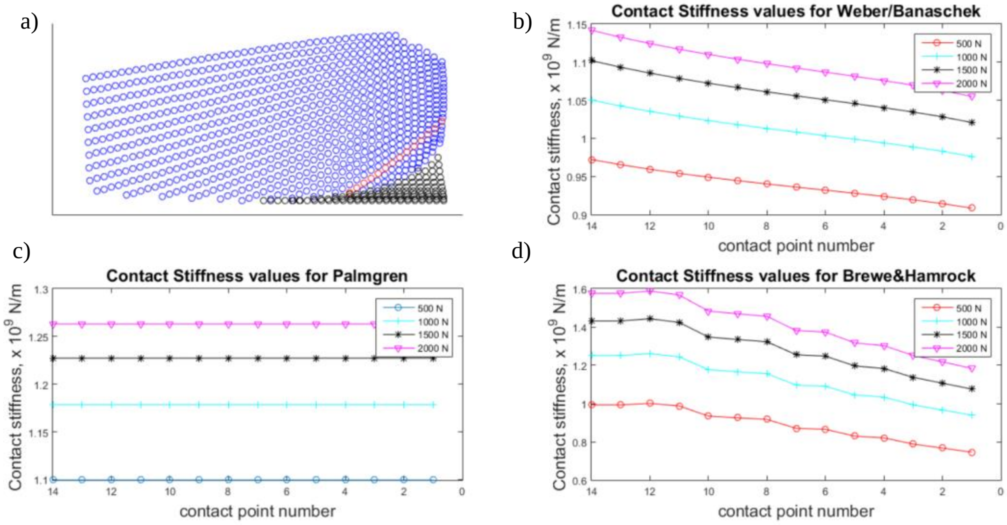

Figure 3-46 Contact stiffness **a)** at the sixth contact line, by **b)** Weber/Banascheck, **c)** Palmgren, **d)** Brewe&Hamrock, for various load levels

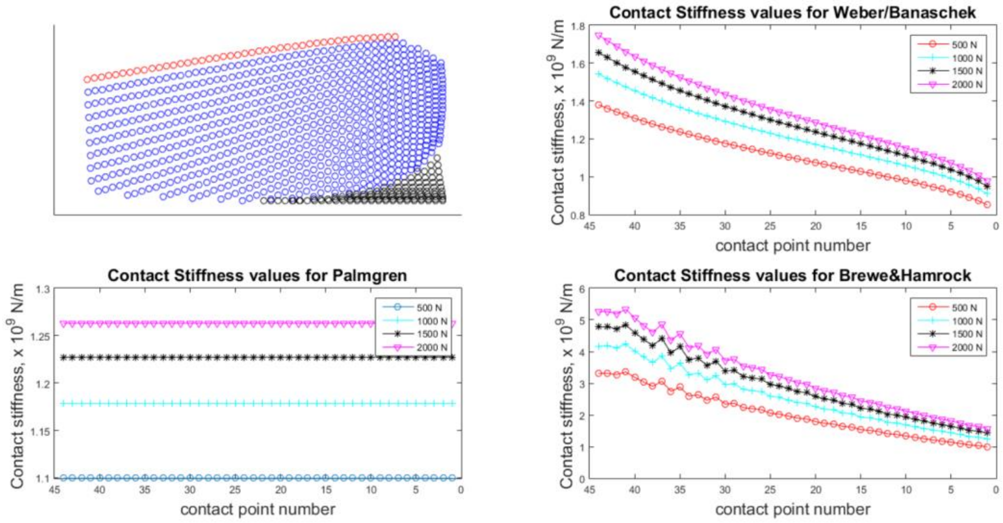

Figure 3-47 Contact stiffness **a)** at the twenty fifth (last) contact line, by **b)** Weber/Banascheck, **c)** Palmgren, **d)** Brewe&Hamrock, for various load levels

3.2 Mesh Stiffness Calculations for a Face-Gear and Spur-Pinion

3.2.1 Introduction

In this study, for the mesh stiffness calculations of the face-gears, semi-analytic FSM (Finite Strip Method) is utilized. The face-gear and the spur gear teeth are discretized through FSM using Mindlin Plate Theory. As shape functions of the finite strip elements, B3-splines are utilized for the longitudinal length of a strip element, and 4-noded simple polynomials are utilized along the short length of the strip element.

The thickness along the face-width and also along the profile direction is generally varied with a linear function for the defined strip element. In this study, the mentioned thickness values along both dimensions are approximated via NURBS (Non-Uniform Rational B-Splines) functions [71], as mentioned in the previous chapter. By this method, the tooth of the face-gear is defined as a surface in space, which provides a continuous thickness variation within the finite strip element. The analytical model is validated via finite element analysis.

Figure 3-48 shows a typical face-gear tooth surface with its fillet, discretized into eight finite strip elements. First, the point cloud is generated for the face-gear tooth's surface, as depicted in Figure 3-48-a. Then, the boundaries of the tooth are calculated. The boundaries of the tooth are shown in Figure 3-48-b and Figure 3-48-c, with and without the generated point cloud, respectively. The tooth is discretized into several elements, as shown in Figure 3-48-d and Figure 3-48-e. Finally, the stiffness matrix and the load vector for each discretized element are calculated to be assembled in a global stiffness matrix and in a global load vector.

The face gear tooth has a significant fillet at the base of part of the tooth. Therefore, the fillet of the face-gear is also included in the FSM element, however compliance due to foundation is not taken into account. The bending contribution is calculated through Finite Strip Method (FSM) whereas the contact contribution is not taken into account. In addition, the face gear has a different cross section at each point along the face width, and a single cross-section model cannot hold for the entire face width. Therefore, the face-gear will be sliced into several parts through its face width, their compliances will be calculated separately and finally they will be averaged to get an averaged stiffness value along the contact lines. The thickness of the tooth also is varied in the element formulation. In other words, each strip element has a variant thickness value. A typical face-gear tooth modelled with 8 finite strip elements along the profile direction, and with seven B3 spline-functions along the tooth profile direction is depicted in Figure 3-49.

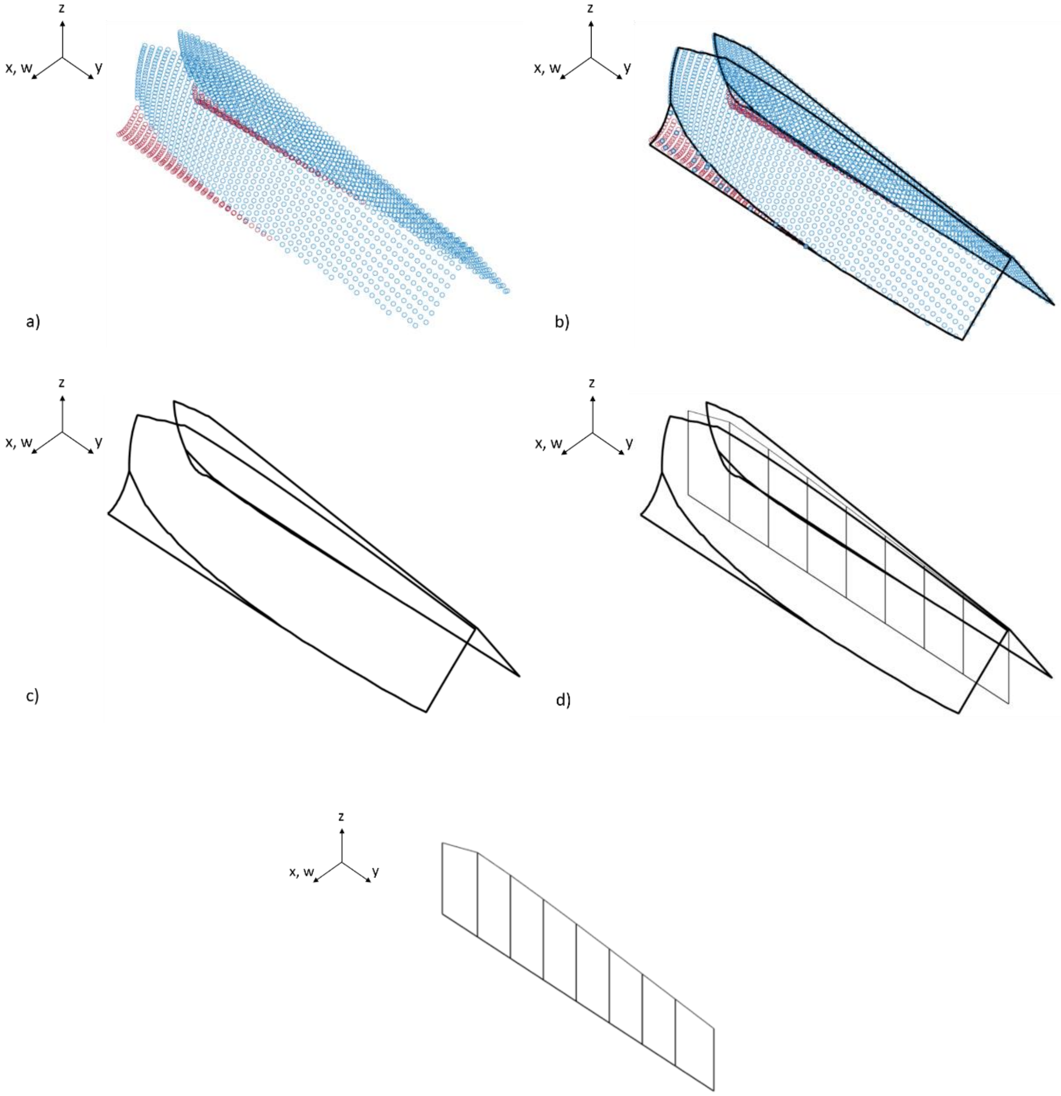

Figure 3-48 a) Generated point cloud for the face-gear tooth profile and its fillet surface, **b)** the boundaries of the tooth with the point cloud, **c)** the boundaries of the tooth **d)** the discretized tooth into eight strip elements, **e)** the resulted finite strip elements

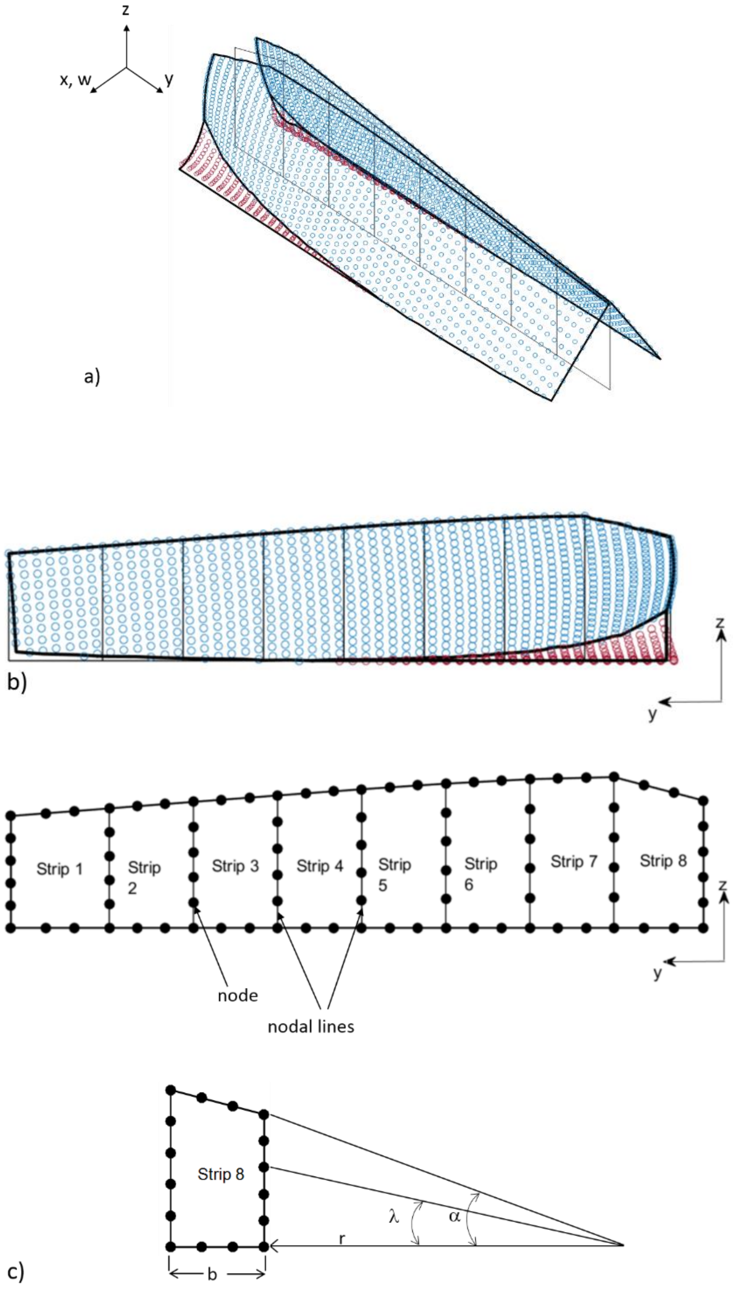
z
x, w
y
a)
b)
z
y
Strip 1
Strip 2
Strip 3
Strip 4
Strip 5
Strip 6
Strip 7
Strip 8
z
y
node
nodal lines
Strip 8
λ
α
r
b
c)

Figure 3-49 a) A typical curved finite strip discretization, isometric view, **b)** view in yz plane, **c)** the grids, six nodes along the profile direction (utilizing 7 cubic B3-spline functions) and four-noded element formulation along the face-width direction

3.2.2 Application of Finite Strip Method to Mindlin Plate Theory with Cubic B-Splines

The formulation utilized for the FSM discretization of Mindlin Plate by cubic B-spline is given below. For a finite strip element with n nodes, the resulted displacement vector is defined as [96,112–114],

$$\boldsymbol{\delta} = \sum_{m=1}^{R}\sum_{i=1}^{n} \boldsymbol{\Lambda}_i^m \begin{bmatrix} w_i^m \\ \theta_{xi}^m \\ \theta_{yi}^m \end{bmatrix} \tag{3-9}$$

where the vector $\boldsymbol{\delta}$ is given as,

$$\boldsymbol{\delta} = \begin{bmatrix} w & \theta_x & \theta_x \end{bmatrix}^T \tag{3-10}$$

and the shape function matrix $\boldsymbol{\Lambda}_i^m$ is for the mth harmonic of the ith node and given as

$$\boldsymbol{\Lambda}_i^m = \begin{bmatrix} \mathrm{N}_i\mathrm{S} & 0 & 0 \\ 0 & \mathrm{N}_i\mathrm{S} & 0 \\ 0 & 0 & \mathrm{N}_i\mathrm{S} \end{bmatrix}. \tag{3-11}$$

The generalized strain vector for a straight strip element is defined as,

$$\boldsymbol{\varepsilon} = \left[-\frac{\partial \theta_x}{\partial x}, -\frac{\partial \theta_\lambda}{\partial y}, -\left(\frac{\partial \theta_x}{\partial y} + \frac{\partial \theta_y}{\partial x} \right), \frac{\partial w}{\partial x} - \theta_x, \frac{\partial w}{\partial y} - \theta_y \right]^T \tag{3-12}$$

and for a curved strip element it is defined as,

$$\boldsymbol{\varepsilon} = \left[\frac{\partial \theta_r}{\partial r}, -\frac{1}{r}\left(\theta + \frac{\partial \theta_\lambda}{\partial \lambda} \right), -\frac{1}{r}\left(\frac{\partial \theta_r}{\partial \lambda} + r\frac{\partial \theta_\lambda}{\partial r} - \theta_\lambda \right), \frac{\partial w}{\partial r} - \theta_r, \frac{1}{r}\frac{\partial w}{\partial \lambda} - \theta_\lambda \right]^T \tag{3-13}$$

The stiffness matrix corresponding to the mth harmonic of the ith nodal line and the nth harmonic of the jth nodal line is calculated as,

$$k_{i,j}^{m,n} = \int\int \left[\mathbf{B}_i^m\right]^T \left[\mathbf{D}\right] \left[\mathbf{B}_i^m\right] dxdy \tag{3-14}$$

where the strain matrix $\mathbf{B}_i^m$ for the mth harmonic of the ith nodal lines is defined as,

$$\left[\mathbf{B}_i^m\right] = \begin{pmatrix} 0 & -\frac{\partial \mathrm{N}_i}{\partial y}\mathrm{S}_m & 0 \\ 0 & 0 & -\mathrm{N}_i \frac{\partial \mathrm{S}_m}{\partial z} \\ 0 & -\mathrm{N}_i \frac{\partial \mathrm{S}_m}{\partial z} & -\frac{\partial \mathrm{N}_i}{\partial y}\mathrm{S}_m \\ \frac{\partial \mathrm{N}_i}{\partial y}\mathrm{S}_m & -\mathrm{N}_i\mathrm{S}_m & 0 \\ \mathrm{N}_i \frac{\partial \mathrm{S}_m}{\partial z} & 0 & \text{-}\mathrm{N}_i\mathrm{S}_m \end{pmatrix} \tag{3-15}$$

Similarly, the stiffness matrix for a curved finite strip element is given as,

$$k_{i,j}^{m,n} = \int\int \left[\mathbf{B}_i^m\right]^T [\mathbf{D}] \left[\mathbf{B}_i^m\right] r d\lambda dr \tag{3-16}$$

and the corresponding strain matrix $\mathbf{B}_i^m$ for the mth harmonic of the ith nodal lines is given as,

$$\left[\mathbf{B}_i^m\right] = \begin{pmatrix} 0 & -\frac{\partial \mathrm{N}_i}{\partial r}\mathrm{S} & 0 \\ 0 & -\frac{\mathrm{N}_i\mathrm{S}}{r} & -\mathrm{N}_i\mathrm{Sd} \\ 0 & -\frac{\mathrm{N}_i\mathrm{Sd}}{r} & -\frac{\partial \mathrm{N}_i}{\partial r}\mathrm{S} + \frac{\mathrm{N}_i}{r}\mathrm{S} \\ \frac{\partial \mathrm{N}_i}{\partial r}\mathrm{S} & -\mathrm{N}_i\mathrm{S} & 0 \\ \mathrm{N}_i\mathrm{Sd} & 0 & \text{-}\mathrm{N}_i\mathrm{S} \end{pmatrix}. \tag{3-17}$$

The utilized four-noded shape functions, which are defined along the face-width direction of the tooth, are expressed with the following equations and they are plotted for a length *b* in Figure 3-50.

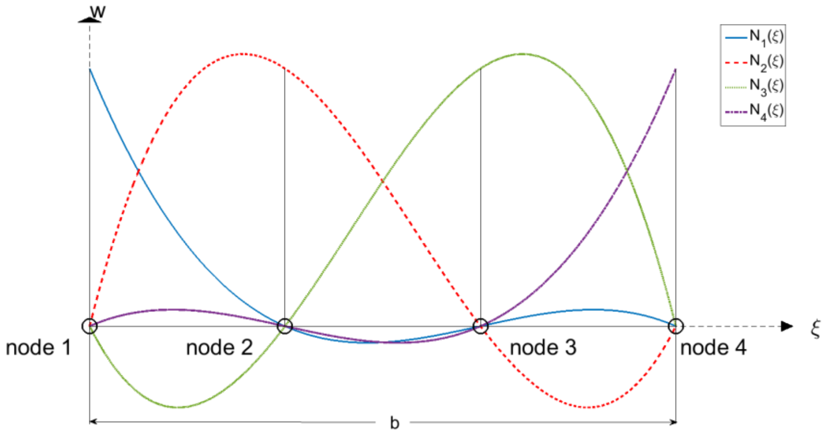

Figure 3-50 The four-noded polynomial shape functions of the finite strip element for the face-width direction of the tooth

The elasticity matrix **D** is defined as,

$$\mathbf{D} = \frac{Et}{24(1+\upsilon)} \begin{bmatrix} 2t^2/(1-\upsilon) & 2\upsilon t^2/(1-\upsilon) & 0 & 0 & 0 \\ 2\upsilon t^2/(1-\upsilon) & 2t^2/(1-\upsilon) & 0 & 0 & 0 \\ 0 & 0 & t^2 & 0 & 0 \\ 0 & 0 & 0 & 12/\alpha & 0 \\ 0 & 0 & 0 & 0 & 12/\alpha \end{bmatrix} \tag{3-18}$$

where α may be taken as 6/5 for rectangular cross section [97]. The force vector for the mth harmonic of the ith nodal line for a straight finite strip element can be defined as

$$\mathbf{f}_i^m = \int\int \mathbf{S}_i^m \cdot q \cdot dxdy \tag{3-19}$$

and similarly, for a curved strip element, the force vector can be defined as

$$\mathbf{f}_i^m = \int\int \mathbf{f}_i^m \cdot q \cdot r d\lambda dr \tag{3-20}$$

where *q* specifies the transverse force.

The utilized cubic B3-spline with equally placed sections, which is defined with the following formula, is plotted for a length *a* is given in Figure 3-51.

$$S_i = \left\{ \begin{array}{c} 0 \\ (\mathrm{z} - (\mathrm{i} - 2)\,\mathrm{h})^3 \\ h^3 + 3h^2(\mathrm{z} - (i-1)h) + 3h(\mathrm{z} - (i-1)h^3 - 3(z-(i-1)h)^3 \\ h^3 + 3h^2((i+1)h - z) + 3h((i+1)h - z)^2 - 3((i+1)h - z)^3 \\ ((\mathrm{i}+2)\,\mathrm{h} - z)^3 \\ 0 \end{array} \quad \text{for} \quad \begin{array}{c} z < (\mathrm{i}-2)\,\mathrm{h} \\ (i-2)h \leq h < (i-1)h \\ (i-1)h \leq< ih \\ ih \leq z < (\mathrm{i}+1)\,\mathrm{h} \\ (i+1)h \leq z \leq (i+2)h \\ (i+2)h < z \end{array} \right\} \tag{3-21}$$

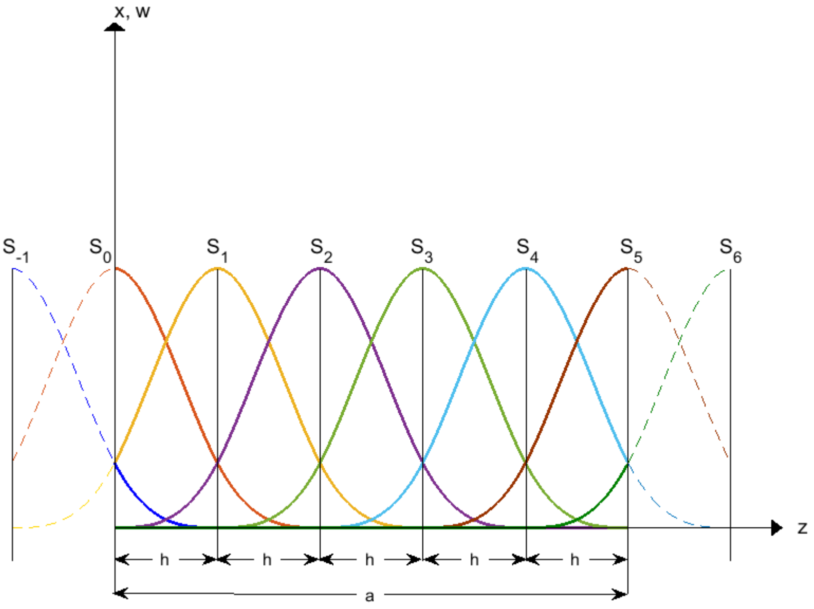

Figure 3-51 The cubic B3-spline functions for equally spaced sections along the length *a*

The tooth is assumed to be clamped from its bottom-land, which specifies that all three degree of freedoms are set to zero at the specified location $\left(w=0,\quad \theta_x=0,\quad \theta_y=0\right)$. In order to satisfy this boundary condition, the cubic-splines curves are modified as,

$$\begin{aligned} &S_{-1}=0 \\ &S_0=S_0-4S_{-1} \\ &S_1=S_1-S_{-1} \end{aligned} \tag{3-22}$$

which gives the new series as in Figure 3-52.

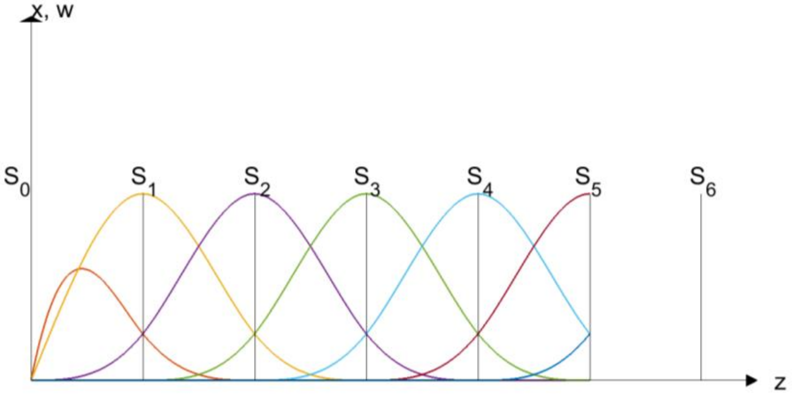

Figure 3-52 The utilized cubic B3-spline functions for the strip element along the cantilevered side to free side of the toot (profile direction)

3.2.3 Combining the stiffnesses of the meshing pairs

Figure 3-53 shows one pair of meshing face-gear and spur-pinion pair at a time instant. A unit load is applied to all contact points on a specific contact line and a compliance matrix is constructed for the specified time instant. The mesh stiffness for that time instant, as depicted in Figure 3-54, is calculated.

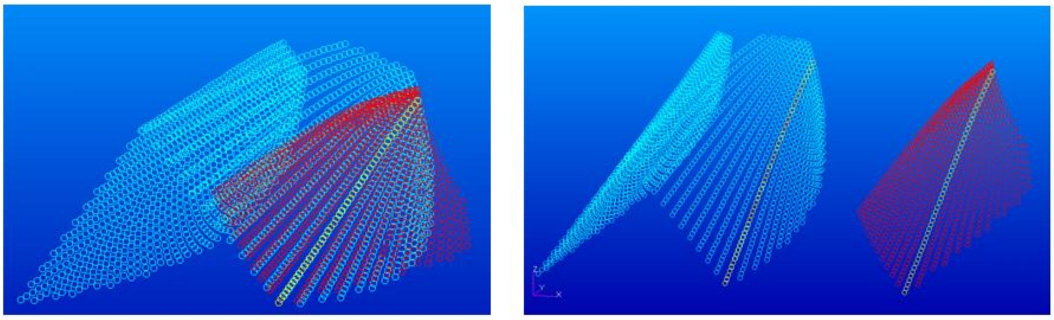

Figure 3-53 Meshed surfaces of a face-gear and its shaper at a time along a contact line **a)** at the meshing position **b)** a separated view of the case in a)

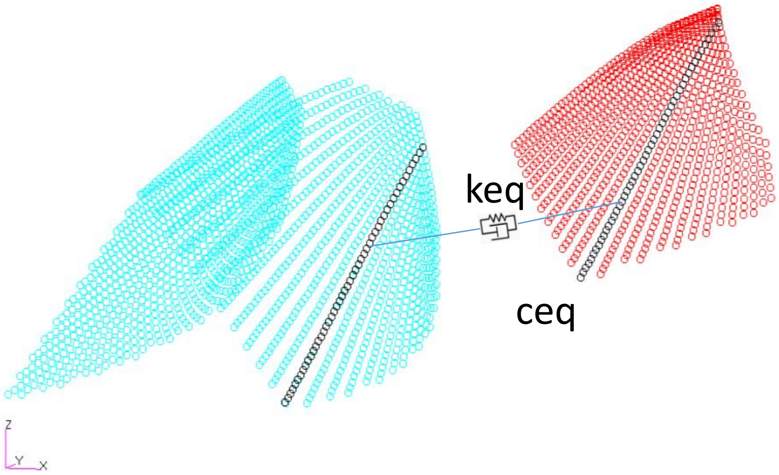

Figure 3-54 Averaged stiffness along the contact line

In the application of the face-gears, contact ratio is greater than 2. This means that there exist time periods when three pairs come to contact at the same time. Figure 3-55 shows a time instant at which three meshing pairs exist. The mesh stiffness has to be calculated with the appropriate combination of them. For this, the time instants where two pairs or three pairs are in contact have to be calculated.

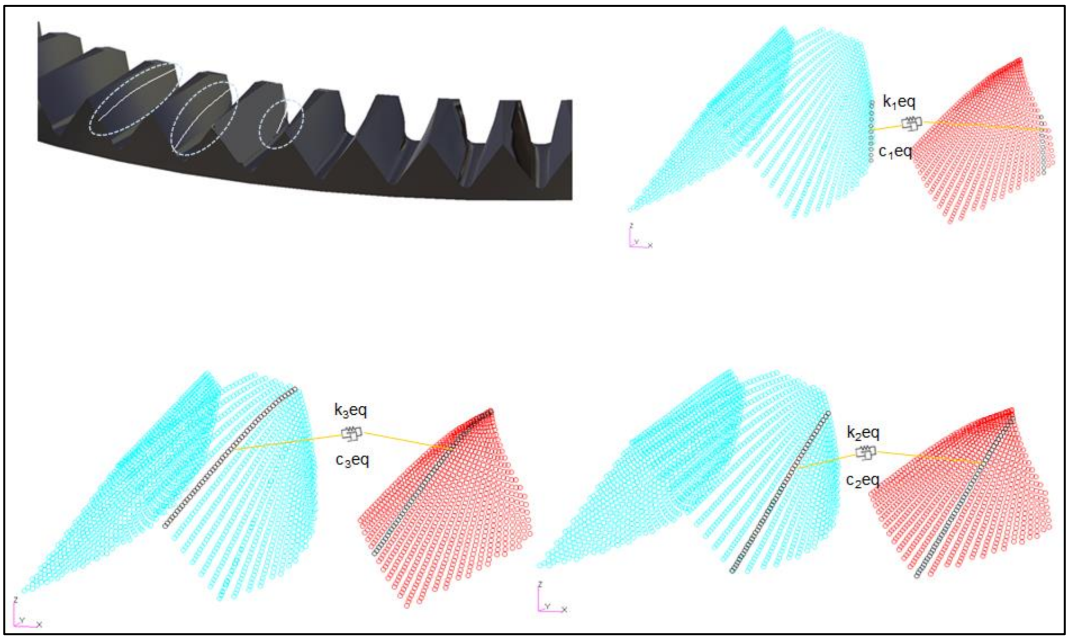

Figure 3-55 Face-gear tooth pairs in contact

The Figure 3-56 to Figure 3-61 demonstrate the instances where two or three Tooth Pairs (TP) make contact. The input parameters for this case study are given below:

Table 3-4 Input parameters

Parameter	Spur Pinion	Face Gear
Number of teeth	23	103
Module (mm)	3.175	
Pressure angle (˚)	20	
Shaft angle (˚)	90	

Figure 3-56 demonstrates the instant where TP 1 makes first contact while TP -1 and TP 0 are already in contact. This case is named as *Case [-1 0 1]*, and rotation angle is read as ϕ_0=0.4826 radians.

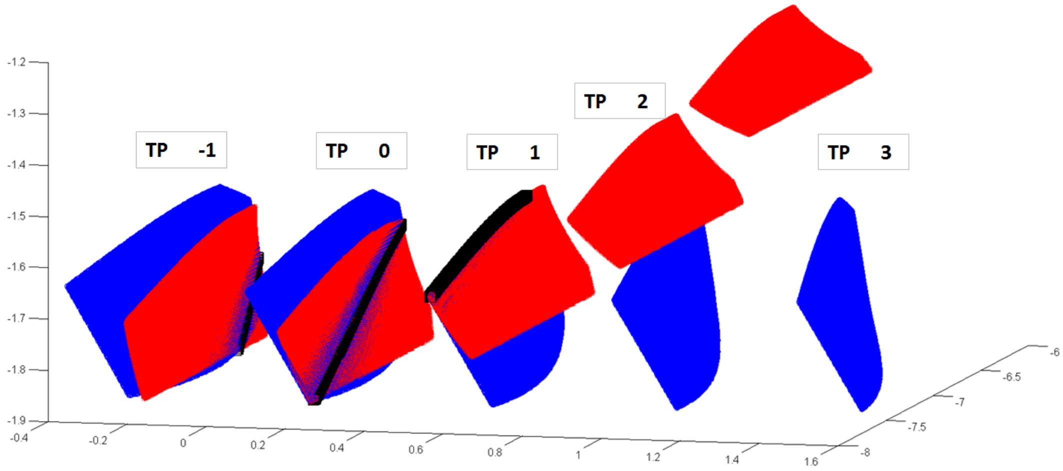

Figure 3-56 Tooth pairs -1, 0 and 1 are in contact, *Case [-1 0 1]*

Figure 3-57 demonstrates the instant where TP -1 just leaves the contact area while TP 0 and TP 1 are already in contact. This case is named as *Case [0 1]*, and rotation angle is read as ϕ_1=0.3466 radians.

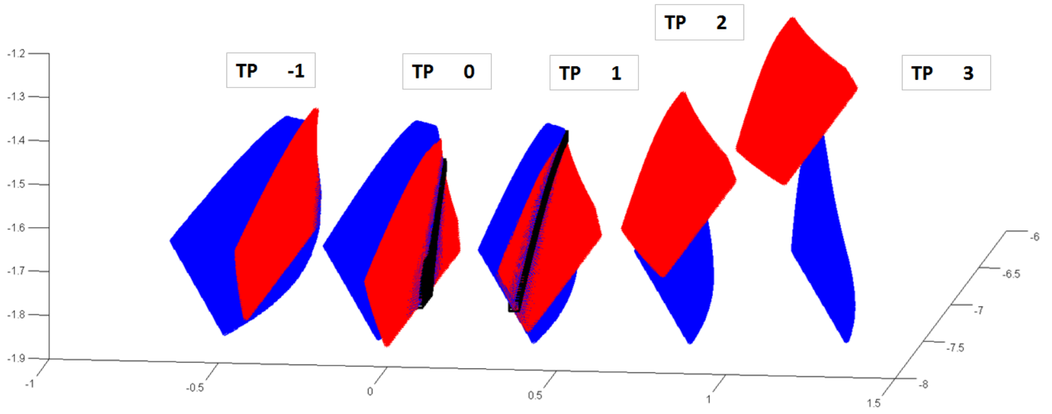

Figure 3-57 Tooth pairs 0 and 1 are in contact, *Case [0 1]*

Figure 3-58 demonstrates the instant where TP 2 makes first contact while TP 0 and TP 1 are already in contact. This case is named as *Case [0 1 2]* and rotation angle is read as v_2=0.2516 radians.

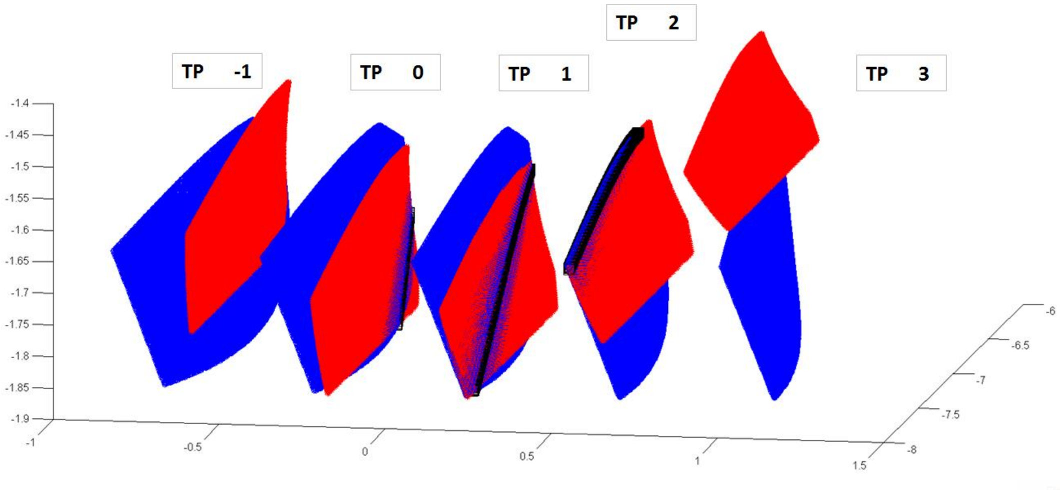

Figure 3-58 Tooth pairs 0, 1 and 2 are in contact, *Case [0 1 2]*

Figure 3-59 demonstrates the instant where TP 0 first leaves the contact area while TP 1 and TP 2 are already in contact. This case is named as *Case [1 2]*, and rotation angle is read as ϕ_3=0.1046 radians.

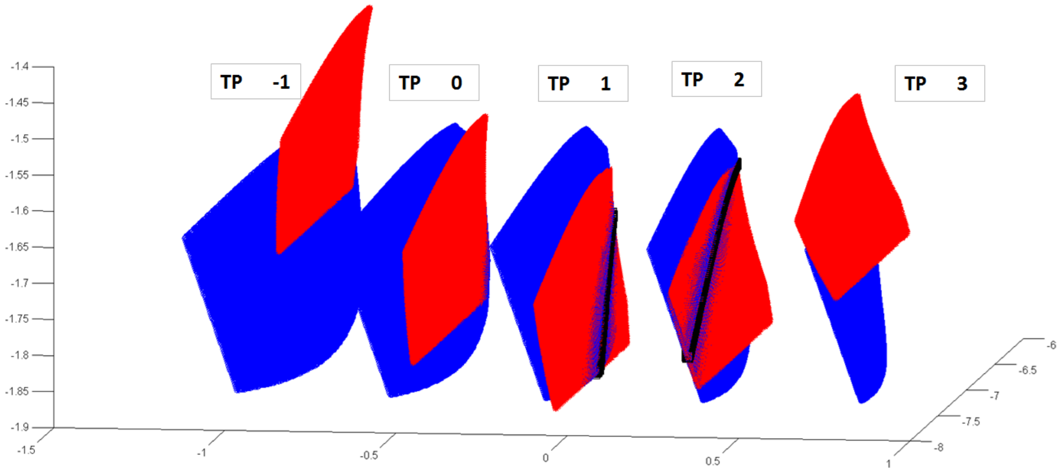

Figure 3-59 Tooth pairs 1 and 2 are in contact, *Case [1 2]*

Figure 3-60 demonstrates the instant where TP 3 makes first contact while TP 1 and TP 2 are already in contact. This case is named as *Case [1 2 3]*, and rotation angle is read as ϕ_4=0.0176 radians.

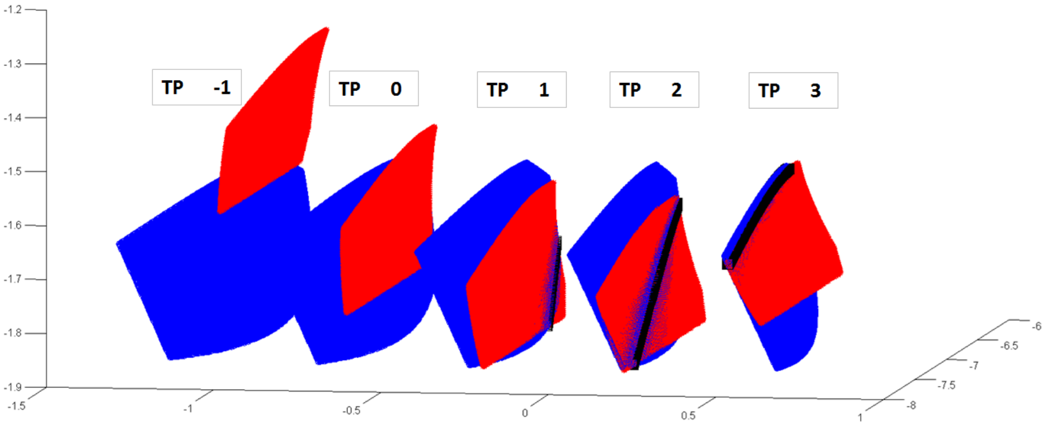
TP -1
TP 0
TP 1
TP 2
TP 3
-1.2
-1.3
-1.4
-1.5
-1.6
-1.7
-1.8
-1.9
-1.5
-1
-0.5
0
0.5
1
-8
-7.5
-7
-6.5
-6

Figure 3-60 Tooth pairs 1, 2 and 3 are in contact, *Case [1 2 3]*

And finally, Figure 3-61 demonstrates the instant where TP 1 first leaves the contact area while TP 2 and TP 3 are already in contact. This case is named as *Case [2 3]* and rotation angle is read as ϕ_s=-0.1124 radians.

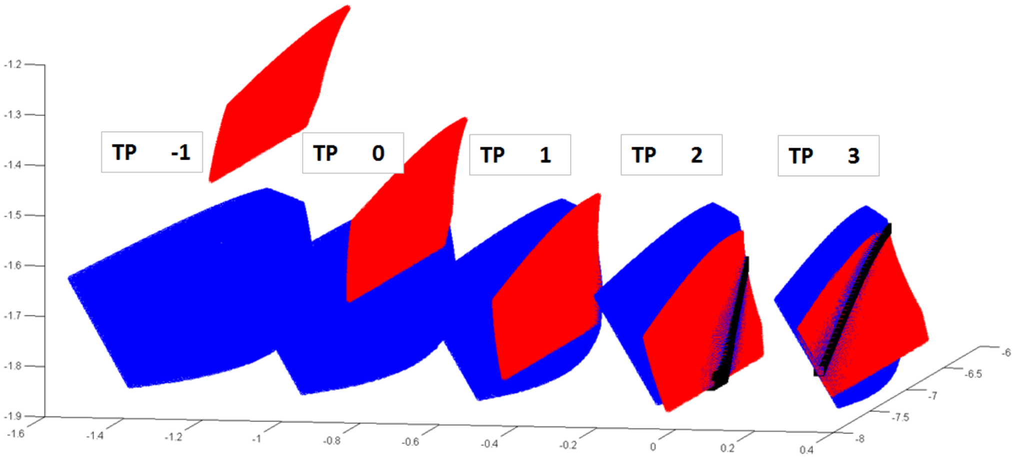
TP -1
TP 0
TP 1
TP 2
TP 3
-1.2
-1.3
-1.4
-1.5
-1.6
-1.7
-1.8
-1.9
-1.6
-1.4
-1.2
-1
-0.8
-0.6
-0.4
-0.2
0
0.2
0.4
-8
-7.5
-7
-6.5
-6

Figure 3-61 Tooth pairs 1 and 2 are in contact, *Case [1 2]*

The rotation angle values in Table 3-5, specifies the instances when tooth pairs make contact for the first time and lose contact from their pairs for the first time. The difference between the values of ϕ_6 and ϕ_1 specifies the period of the variation of mesh stiffness for the tooth pair (TP 1), which is $\phi_1 - \phi_6 = 0.5950$ radians. Setting $\phi_1 = 0$, and knowing that $\alpha_1 - \alpha_6 = 0.5950$ radians corresponds to 25 contact lines, the contact line correspondents for each six time instants are calculated accordingly.

Table 3-5 Rotation angles and corresponding time instants for TP1

Time instant	*i*	ϕ_i(rad)	$\phi_1 - \phi_i$(rad)	*Contact line correspondent*
case [-1 0 1]	1	0.4826	0	1
case [0 1]	2	0.3466	0.136	6.71
case [0 1 2]	3	0.2516	0.231	10.70
case [1 2]	4	0.1046	0.378	16.88
case [1 2 3]	5	0.0176	0.465	20.53
case [2 3]	6	-0.1124	0.595	26

Table 3-6 summarizes the instants that tooth pairs mesh or lose contact in terms of contact lines; for the current case, 25 contact lines are taken into account. *"0"* denotes the instant when toot pair makes contact, *"25"* denotes the time when tooth pair loses contact, and other intermediate values portrays the location of the contact on the tooth surface accordingly, in terms of the available contact lines.

Table 3-6 Instants when the tooth pairs mesh or lose contact

	TP 1	TP 0	TP 1	TP 2	TP 3
case [-1 0 1]	19.2	9.11	1		
case [0 1]	26	15.8	6.7		
case [0 1 2]		19.8	10.7	1	
case [1 2]		26	16.8	7.17	
case [1 2 3]			20.5	10.8	1
case [2 3]			26	16.2	6.4

Figure 3-62 gives the resulting mesh stiffness of the gear pair specified in Table 3-4.

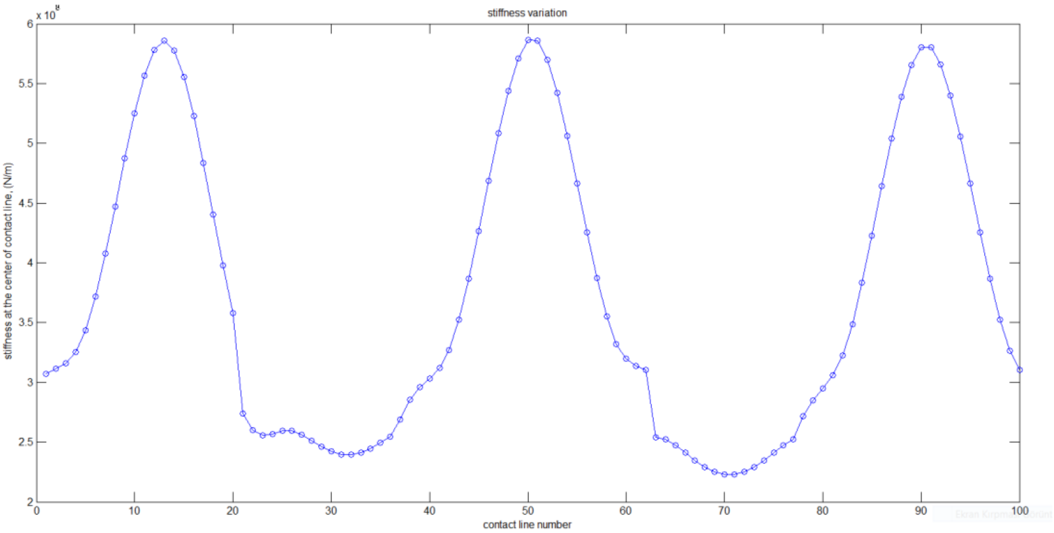

Figure 3-62 Total Mesh stiffness

3.2.4 Determining the Appropriate Strip Elements

Application of a point force creates local singularity, and the deformation of the application point brings significant error. Refining the mesh size also worsens the situation. For the bending contribution of the displacement of a contact point on tooth surface, in 3D FE model, the deflection of the point on the opposite side of the tooth is taken into account. The following tooth surface is generated through the developed Matlab code and exported to Abaqus FE package software.

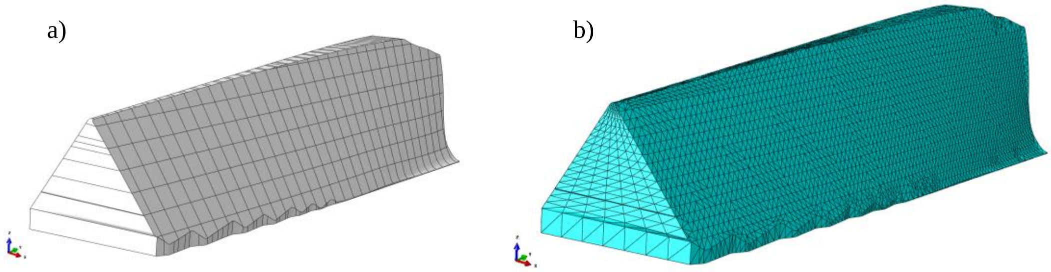

Figure 3-63 a) Generated tooth geometry, **b)** 3D FE model in ABAQUS

The generated tooth is discretized with 3D finite element type of C3D10 of Abaqus. The generated number of nodes is 200614, and the created number of elements is 137970. The point load is applied at the pointing side (outer side) of the tooth, as seen in Figure 3-64 and at the inner side of the tooth, as seen in Figure 3-65.

The deformation due to bending is sought, but due to nature of the point load this value cannot be read from the obtained result at the application point.

The same tooth is discretized using 4, 5, 8, 12, 16, 23, and 44 finite strip elements, and the point force is applied at the same location. The deformation is taken at the nodal point that corresponds to the application point and the nearby nodal line within the same element. These deformation values are averaged, and the resulting values are plotted below. As the number of the strip elements is increased, the resulting value converges to the value obtained from the 3D Abaqus FE model, as shown Figure 3-64 and Figure 3-65. Two arbitrarily loaded case studies are performed:

- Case-1: A unit load is applied at the depicted location in Figure 3-64.
- Case-2: A unit load is applied, at the depicted location in Figure 3-65.

Table 3-7 and Table 3-8 summarize the comparison of the result obtained by 3D Abaqus model discretized with 137970 C3D10 elements formed by 200614 nodes, with those obtained by using the 1D FSM model discretized with 44 strip elements with 133 nodes. The error for Case-1 is around 0.2 %, whereas the error for Case-2 is around 9.8%. These results clearly show the power of FSM method.

Table 3-7 Comparison of FSM results with 3D FEM ABAQUS results, Case-1

	Deformation (mm)
Abaqus Software	9.7145*10^-5
FSM with 4 strips	3.6557
FSM with 5 strips	4.3555
FSM with 8 strips	5.4632
FSM with 12 strips	8.1888
FSM with 16 strips	9.7400
FSM with 23 strips	9.7383
FSM with 44 strips	9.7333

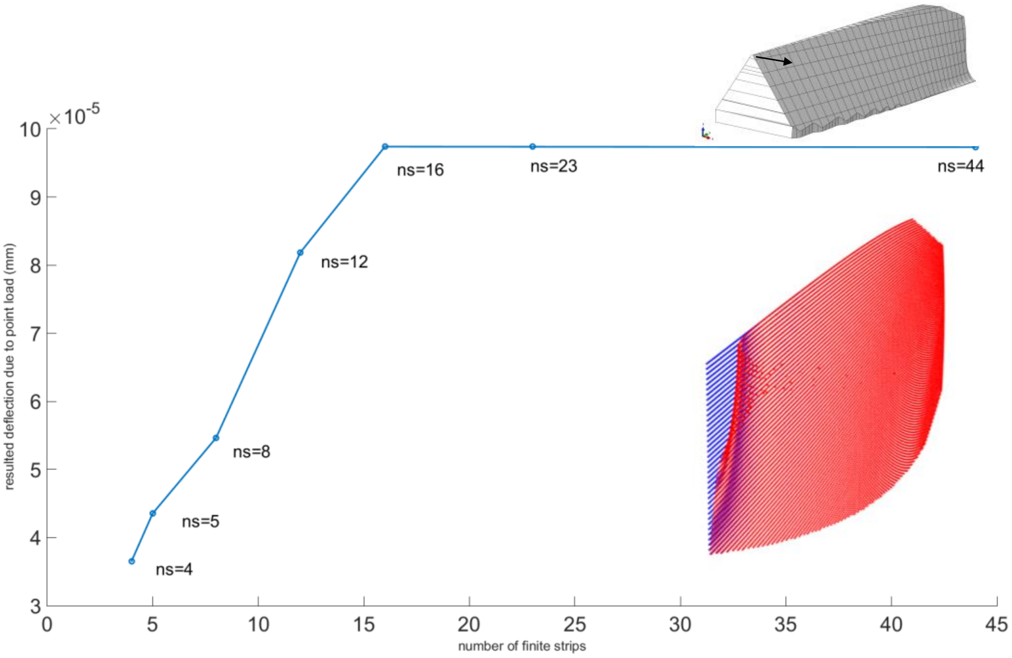

Figure 3-64 Averaged deformation vs number of finite strip elements, Case-1

Table 3-8 Comparison of FSM results with 3D FEM ABAQUS results, Case-2

	Deformation (mm)
Abaqus Software	1.1754x10^-5
FSM with 4 strips	1.1187x10^-5
FSM with 5 strips	1.1604x10^-5
FSM with 8 strips	1.2292x10^-5
FSM with 12 strips	1.2605x10^-5
FSM with 16 strips	1.2744x10^-5
FSM with 23 strips	1.2849x10^-5
FSM with 44 strips	1.2849x10^-5

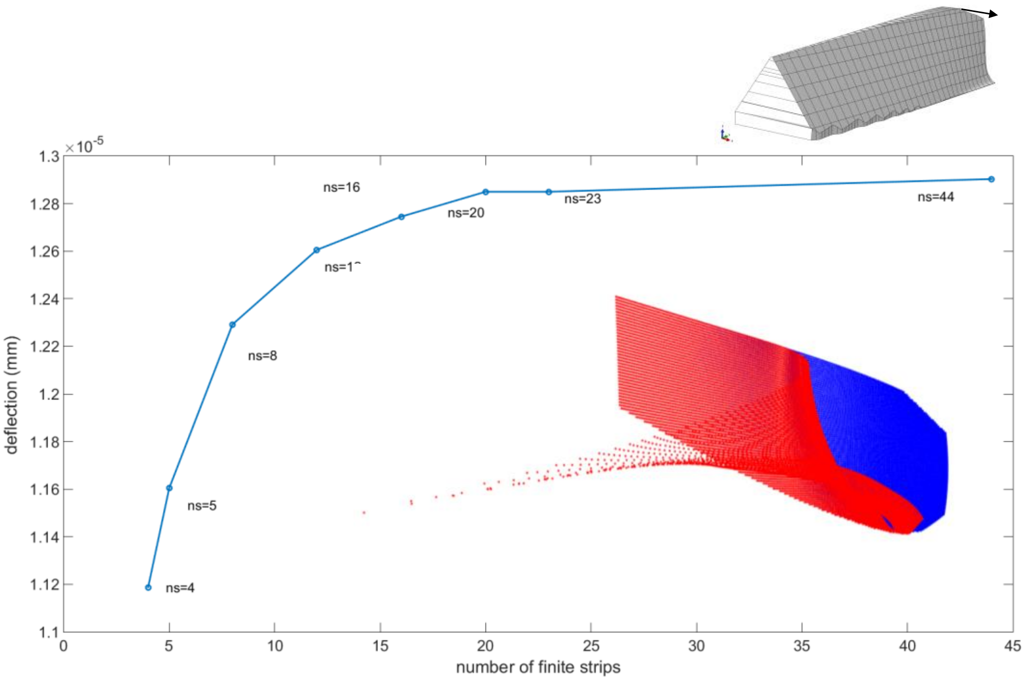

Figure 3-65 Averaged deformation vs number of finite strip elements, Case-2

CHAPTER 4

MATHEMATICAL MODELS AND DYNAMIC ANALYSIS OF FACE-GEARS

4.1 Non-linear Dynamic Model for a Split-Torque Face-Gear Drive System

A non-linear dynamic model of the multi-mesh face-gear split-torque drive system shown in Figure 1-15 is developed. Here, the dynamic model is a lumped mass system consisting of five pinions and two face gears. The system has seven rotational degrees of freedom with all rigid gear bodies. This system has two inputs, two outputs, and three idler gears. The mesh stiffness is established by FSM utilizing the actual spur pinion and face-gear tooth geometries presented in [27]. The enveloping procedure for the surface generation of a face-gear, the mesh stiffness calculation procedure, and the dynamic analysis procedure are depicted in Figure 4-2.

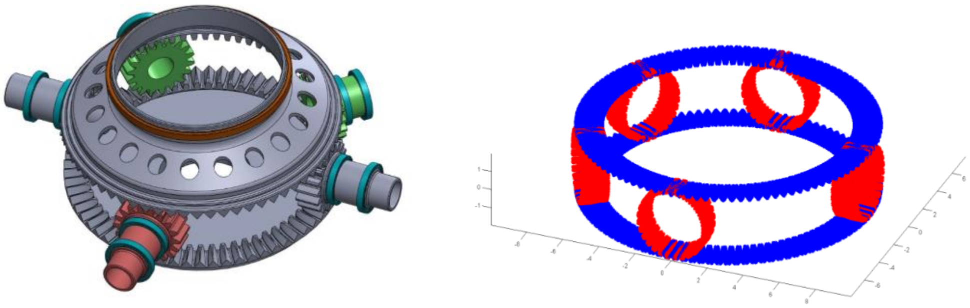

Figure 4-1 a) Example 3D model **b)** Produced tooth geometries

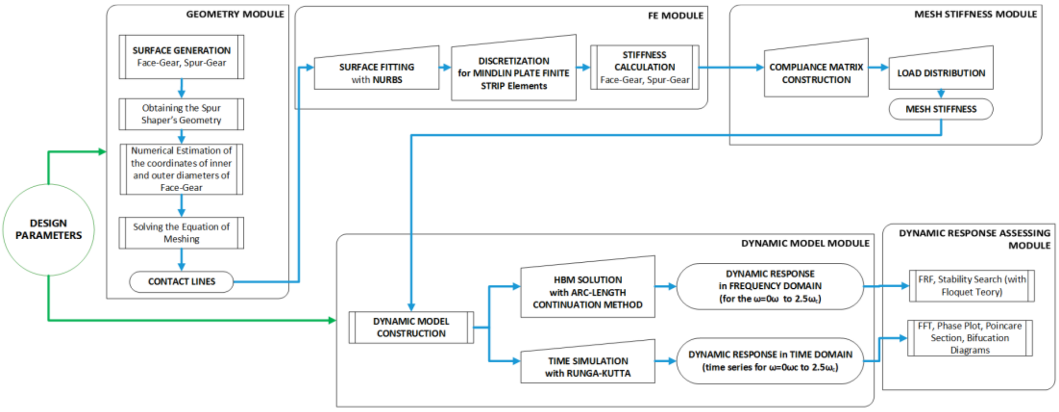
GEOMETRY MODULE
SURFACE GENERATION Face-Gear, Spur-Gear
Obtaining the Spur Shaper's Geometry
Numerical Estimation of the coordinates of inner and outer diameters of Face-Gear
Solving the Equation of Meshing
CONTACT LINES
DESIGN PARAMETERS
FE MODULE
SURFACE FITTING with NURBS
DISCRETIZATION for MINDLIN PLATE FINITE STRIP Elements
STIFFNESS CALCULATION Face-Gear, Spur-Gear
MESH STIFFNESS MODULE
COMPLIANCE MATRIX CONSTRUCTION
LOAD DISTRIBUTION
MESH STIFFNESS
DYNAMIC MODEL MODULE
DYNAMIC MODEL CONSTRUCTION
HBM SOLUTION with ARC-LENGTH CONTINUATION METHOD
TIME SIMULATION with RUNGA-KUTTA
DYNAMIC RESPONSE in FREQUENCY DOMAIN (for the ω=0ω to 2.5ω꜀)
DYNAMIC RESPONSE in TIME DOMAIN (time series for ω=0ωc to 2.5ω꜀)
DYNAMIC RESPONSE ASSESSING MODULE
FRF, Stability Search (with Floquet Teory)
FFT, Phase Plot, Poincare Section, Bifucation Diagrams

Figure 4-2 Flow diagram for the dynamic analysis of the drive system

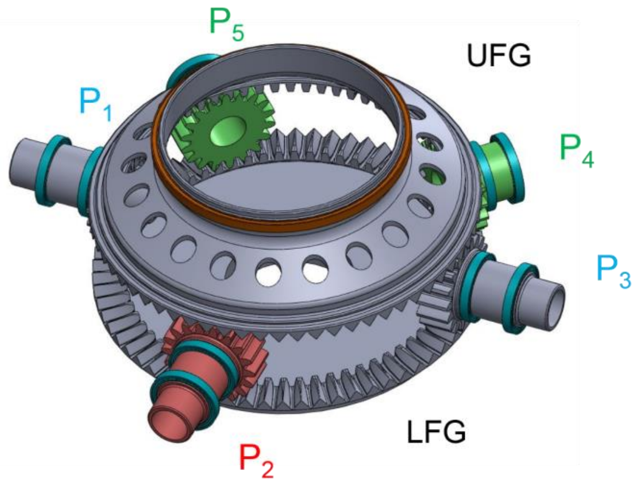
P5
UFG
P1
P4
P3
LFG
P2

Figure 4-3 Split-torque face-gear drive system

The split-torque system consists of one Upper Face Gear (UFG) as output and one Lower Face-Gear (LFG) as an idler. Between them, there exist five pinions, two of which are inputs (P_1, P_3), one is output (P_2), and the remaining two are idler pinions (P_4, P_5), as shown in Figure 4-3.

In this transmission system, P_1 and P_3 may be considered as the input of the drive system, and power input from these pinions is split and then transmitted to UFG and

LFG. UFG is connected to the main output shaft, while LFG serves as an idler in the torque transfer path. Similarly, P_2 is the pinion connecting to the secondary output shaft, which collects torque from UFG and LFG, and drives the secondary output shaft. LFG collects the split torques from P_1 and P_3. Then, it transmits some portions to $P_{2,}$ and some portions directly to UFG through the idler pinions P_4 and P_5, as shown in Figure 4-4.

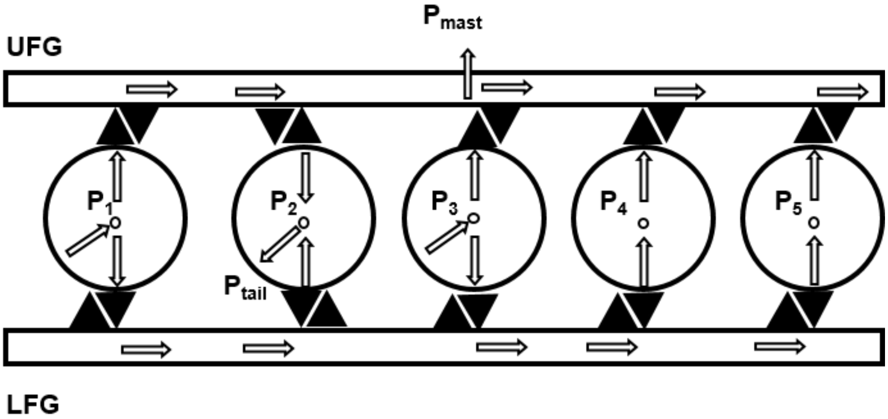

Figure 4-4 Power flow of the split-torque system

4.1.1 Mathematical Model

The developed torsional dynamic model for the given system is depicted in Figure 4-5. The dynamic model of a split-torque face-gear drive system resembles a planetary gear system, as studied in [115–118].

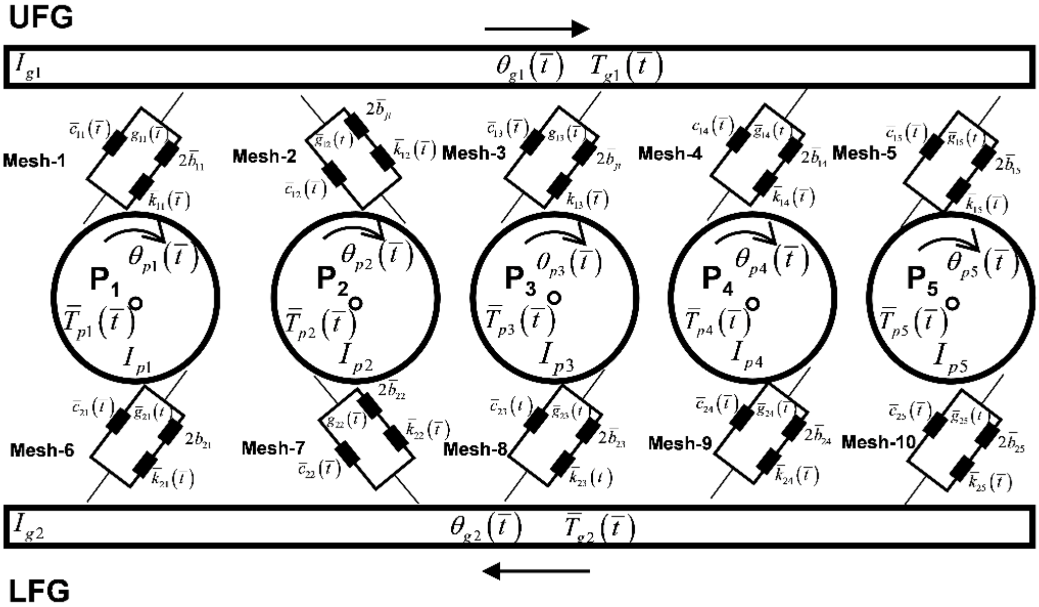
UFG
I_{g1}
$\theta_{g1}(\bar{t})$ $T_{g1}(\bar{t})$
Mesh-1
Mesh-2
Mesh-3
Mesh-4
Mesh-5
$\bar{c}_{11}(\bar{t})$ $g_{11}(\bar{t})$ $2\bar{b}_{11}$ $\bar{k}_{11}(\bar{t})$
$2\bar{b}_{ji}$ $\bar{g}_{12}(\bar{t})$ $\bar{k}_{12}(\bar{t})$ $\bar{c}_{12}(\bar{t})$
$\bar{c}_{13}(\bar{t})$ $g_{13}(\bar{t})$ $2\bar{b}_{ji}$ $\bar{k}_{13}(\bar{t})$
$c_{14}(\bar{t})$ $\bar{g}_{14}(\bar{t})$ $2\bar{b}_{14}$ $\bar{k}_{14}(\bar{t})$
$c_{15}(\bar{t})$ $\bar{g}_{15}(\bar{t})$ $2\bar{b}_{15}$ $\bar{k}_{15}(\bar{t})$
P_1 $\theta_{p1}(\bar{t})$ $\bar{T}_{p1}(\bar{t})$ I_{p1}
P_2 $\theta_{p2}(\bar{t})$ $\bar{T}_{p2}(\bar{t})$ I_{p2}
P_3 $\theta_{p3}(\bar{t})$ $\bar{T}_{p3}(\bar{t})$ I_{p3}
P_4 $\theta_{p4}(\bar{t})$ $\bar{T}_{p4}(\bar{t})$ I_{p4}
P_5 $\theta_{p5}(\bar{t})$ $\bar{T}_{p5}(\bar{t})$ I_{p5}
$\bar{c}_{21}(\bar{t})$ $\bar{g}_{21}(\bar{t})$ $2\bar{b}_{21}$ $\bar{k}_{21}(\bar{t})$
$2\bar{b}_{22}$ $\bar{g}_{22}(\bar{t})$ $\bar{k}_{22}(\bar{t})$ $\bar{c}_{22}(\bar{t})$
$\bar{c}_{23}(\bar{t})$ $\bar{g}_{23}(\bar{t})$ $2\bar{b}_{23}$ $\bar{k}_{23}(\bar{t})$
$\bar{c}_{24}(\bar{t})$ $\bar{g}_{24}(\bar{t})$ $2\bar{b}_{24}$ $\bar{k}_{24}(\bar{t})$
$\bar{c}_{25}(\bar{t})$ $\bar{g}_{25}(\bar{t})$ $2\bar{b}_{25}$ $\bar{k}_{25}(\bar{t})$
Mesh-6
Mesh-7
Mesh-8
Mesh-9
Mesh-10
I_{g2}
$\theta_{g2}(\bar{t})$ $\bar{T}_{g2}(\bar{t})$
LFG

Figure 4-5 Dynamic model for the split-torque system

The equations of motion of the non-linear model may be given as follows:

For face-gears 1 and 2 (jth gear),

$$I_{gj}\ddot{\theta}_{gj}(\bar{t})+\sum_{i=1}^{5}\bar{\lambda}_{gji}(\bar{t})\left\{\bar{c}_{ji}(\bar{t})\dot{\bar{p}}_{ji}(\bar{t})+\bar{k}_{ji}(\bar{t})\bar{g}\left(\bar{p}_{ji}(\bar{t})\right)\right\}=\bar{T}_{gj}(\bar{t}),\ j=1,2 \tag{4-1}$$

For pinions 1 to 5 (ith pinion),

$$I_{pi}\ddot{\theta}_{pi}(\bar{t})+\sum_{j=1}^{2}\bar{\lambda}_{pji}(\bar{t})\left\{\bar{c}_{ji}(\bar{t})\dot{\bar{p}}_{ji}(\bar{t})+\bar{k}_{ji}(\bar{t})g\left(\bar{p}_{ji}(\bar{t})\right)\right\}=\bar{T}_{pi}(\bar{t}),i=1..5 \tag{4-2}$$

where I_{pi} and I_{gi} are the mass moment of inertias of the pinions and the gears, respectively; $\bar{T}_{pi}(\bar{t})$ and $\bar{T}_{gj}(\bar{t})$ are the torque loads on the pinions and face gears, respectively; $\bar{c}_{ji}(\bar{t})$ is the time-variant mesh damping between jth gear and ith pinion; $\bar{k}_{ji}(\bar{t})$ is the time-variant mesh stiffness between jth gear and ^{ith} pinion;

$\bar{\lambda}_{gji}\left(\bar{t}\right)$ and $\bar{\lambda}_{pji}\left(\bar{t}\right)$ are the directional rotational radii of the ith pinion and the jth face-gear, respectively.

Since the constructed system is a pure rotational system, only the rotational displacements are taken into account; therefore, the directional rotational radii are expressed as,

$$\begin{aligned}\bar{\lambda}_{pi}\left(\bar{t}\right)&=\vec{n}_{pi}\left(\bar{t}\right)\cdot(\vec{\varepsilon}_{pi}\times\vec{r}_{pi}\left(\bar{t}\right)),\\ \bar{\lambda}_{gi}\left(\bar{t}\right)&=\vec{n}_{gi}\left(\bar{t}\right)\cdot(\vec{\varepsilon}_{gj}\times\vec{r}_{gi}\left(\bar{t}\right))\end{aligned} \tag{4-3}$$

where $\vec{n}_{pi}\left(\bar{t}\right)$ and $\vec{n}_{gj}\left(\bar{t}\right)$ are the unit normal vectors of the mesh point of the ith pinion and jth face gear, respectively; $\vec{r}_{pi}\left(\bar{t}\right)$ and $\vec{r}_{gj}\left(\bar{t}\right)$ are the position vectors of the mesh point, $\vec{\varepsilon}_{pi}$ and $\vec{\varepsilon}_{gj}$ are the unit vectors along the ith pinion and jth the face-gear rotational axis, respectively.

The expression for the dynamic transmission error (DTE) between the ith pinion and the jth face-gear is:

$$\bar{\delta}_{ji}(\bar{t})=\lambda_{pji}(\bar{t})\,\theta_{pi}\left(\bar{t}\right)+\lambda_{gji}(\bar{t})\,\theta_{gi}\left(\bar{t}\right)\text{ as } i=1..5 \text{ and } j=1,2 \tag{4-4}$$

The gear mesh displacement between the ith pinion and the jth face-gear is:

$$\bar{p}_{ji}\left(\bar{t}\right)=\bar{\delta}_{ji}(t)+\bar{\mathrm{e}}_{\mathrm{ji}}(\mathrm{t})\text{ as } i=1..5 \text{ and } j=1,2 \tag{4-5}$$

where $\bar{e}_{ji}(t)$ is the static transmission error (STE) between the ith pinion and the jth face-gear due to geometrical errors of the gear teeth profile. The gear mesh displacement combines STE and DTE.

The piecewise-linear displacement function between the ith pinion ad the jth face-gear is,

$$\bar{g}_{ji}(\bar{t})=\begin{cases}\bar{p}_{ji}(\bar{t})-\bar{b}_{ji} & \bar{p}_{ji}(\bar{t})>\bar{b}_{ji}\\ 0 & \left|\bar{p}_{ji}(\bar{t})\right|<\bar{b}_{ji}\\ \bar{p}_{ji}(\bar{t})+\bar{b}_{ji} & \bar{p}_{ji}(\bar{t})<-\bar{b}_{ji}\end{cases} \tag{4-6}$$

where $2\bar{b}_{ji}$ is the total gear backlash between the ith pinion and the jth face-gear.

Equations (4-1) and (4-2) are non-dimensionalized by utilizing a characteristic frequency ω_c and a characteristic length b_c by imposing the following equations;

$$p_{ji}(t)=\frac{\bar{p}_{ji}(\bar{t})}{b_c}\quad \lambda_{pji}(t)=\frac{\bar{\lambda}_{pji}(t)}{bc}\quad e_{ji}(t)=\frac{\bar{e}_{ji}(\bar{t})}{b_c}\quad b_{ji}=\frac{\bar{b}_{ji}}{b_c} \tag{4-7}$$

$$\bar{t}=\frac{t}{\omega_c}\quad \frac{d\bar{t}}{dt}=\frac{1}{\omega_c}\quad \frac{d^2\bar{t}}{dt^2}=\frac{1}{\omega_c{}^2} \tag{4-8}$$

Using equations (4-7) and (4-8), with the chain rule, $\dot{p}_{ji}(t)$ may be calculated as,

$$\dot{p}_{ji}(t)=\frac{dp_{ji}(\bar{t})}{d\bar{t}}\frac{d\bar{t}}{dt}=\frac{d}{d\bar{t}}\left(\frac{\bar{p}_{ji}(\bar{t})}{b_c}\right)\frac{1}{\omega_c}=\frac{d\bar{p}_{ji}(\bar{t})}{d\bar{t}}\frac{1}{b_c\omega_c} \tag{4-9}$$

So, $\dot{\bar{p}}_{ji}\left(\bar{t}\right)$ is expressed as:

$$\dot{\bar{p}}_{ji}\left(\bar{t}\right) = \bar{p}_{ji}\left(t\right)\frac{1}{\omega_c} = b_c\omega_c\dot{p}_{ji}\left(t\right) \tag{4-10}$$

Also, stiffness and damping terms are re-written as the product of their mean values and time-variant parts as:

$$\bar{k}_{ji}\left(\bar{t}\right) = \bar{k}m_{ji}k_{ji}\left(t\right),\ \bar{c}_{ji}\left(\bar{t}\right) = \bar{c}m_{ji}c_{ji}\left(t\right) \tag{4-11}$$

where $\bar{k}m_{ji}$ and $\bar{c}m_{ji}$ are the mean, $k_{ji}\left(t\right)$ and $c_{ji}\left(t\right)$ are the time-variant parts of the stiffness and damping terms, respectively. Also, using the definition of $\bar{b}_{ji}$ given in Equation (4-7), Equation (4-6) is nondimensionalized as:

$$g_{ji}\left(t\right) = \begin{cases} p_{ji}\left(t\right) - b_{ji} & p_{ji}\left(t\right) > b_{ji} \\ 0 & \left|p_{ji}\left(t\right)\right| < b_{ji} \\ p_{ji}\left(t\right) + b_{ji} & \bar{p}_{ji}\left(t\right) < -b_{ji} \end{cases} \tag{4-12}$$

Finally, using the definition given in Equation (4-8), $\dot{\theta}_{gj}\left(t\right)$ may be expressed as;

$$\dot{\theta}_{gj}\left(t\right) = \dot{\theta}_{gj}\left(\bar{t}\right)\frac{dt}{d\bar{t}} = \dot{\theta}_{gj}\left(\bar{t}\right)\frac{1}{\omega_c} \tag{4-13}$$

so, $\dot{\theta}_{gj}\left(\bar{t}\right)$ and $\ddot{\theta}_{gj}\left(\bar{t}\right)$ may be expressed as,

$$\dot{\theta}_{gj}\left(\bar{t}\right)=\omega_c\dot{\theta}_{gj}\left(t\right),\ \ddot{\theta}_{gj}\left(\bar{t}\right)=\omega_c{}^2\ddot{\theta}_{gj}\left(t\right) \qquad (4\text{-}14)$$

Substituting the parameters given in Equations through (4-7)-(4-11), Equations (4-1) and (4-2) become nondimensionalized as,

$$\ddot{\theta}_{gj}\left(t\right)+\sum_{i=1}^{5}\left\{2\omega_{gji}\left(t\right)\zeta_{ji}(\mathrm{t})\ \dot{p}_{ji}\left(t\right)+\omega_{gji}\left(t\right)^2 k_{ji}\left(t\right)g_{ji}\left(t\right)\right\}=f_{g\,j}\left(t\right),\ j=1,2 \qquad (4\text{-}15)$$

$$\ddot{\theta}_{pi}\left(\bar{t}\right)+\sum_{j=1}^{2}\left\{2\omega_{pji}\left(t\right)\zeta_{pji}(\mathrm{t})\ \dot{p}_{ji}\left(t\right)+\omega_{pji}\left(t\right)^2 k_{ji}\left(t\right)g_{ji}\left(t\right)\right\}=f_{pi}\left(t\right),i=1..5 \qquad (4\text{-}16)$$

where,

$$f_{g\,j}\left(t\right)=\frac{\bar{T}_{gj}\left(\bar{t}\right)}{\omega_c{}^2 I_{gj}},\quad f_{p\,j}\left(t\right)=\frac{\bar{T}_{pi}\left(\bar{t}\right)}{\omega_c{}^2 I_{pi}} \qquad (4\text{-}17)$$

$$\zeta_{gji}(\mathrm{t})=\frac{\bar{\lambda}_{gji}\left(t\right)\bar{c}_{ji}\left(t\right)b_c\omega_c}{\omega_c{}^2 I_{gj}\,2\omega_{ji}\left(t\right)},\ \zeta_{pji}(\mathrm{t})=\frac{\bar{\lambda}_{pji}\left(\bar{t}\right)\bar{c}_{ji}\left(\bar{t}\right)b_c\omega_c}{\omega_c{}^2 I_{pi}\,2\omega_{pji}\left(t\right)} \qquad (4\text{-}18)$$

$$\omega_{gji}\left(t\right)=\left(\frac{\bar{\lambda}_{gji}\left(\bar{t}\right)}{\omega_c{}^2 I_{gj}}\bar{k}m_{ji}b_c\right)^{\frac{1}{2}},\ \omega_{pji}\left(t\right)=\frac{\bar{\lambda}_{pji}\left(\bar{t}\right)\bar{k}m_{ji}b_c}{\omega_c{}^2 I_{pi}} \qquad (4\text{-}19)$$

4.1.2 Mesh Phasing

There are ten meshing locations between the pinions and the face gears, as shown in Figure 4-5. Mesh-1 is taken as the reference meshing position. Concerning this meshing location, appropriate phase differences are imposed on all remaining meshes according to their gear-set arrangement type, whether a split-torque or an idler arrangement.

The STE for all specified mesh locations is defined as,

$$e_{ji}(t) = \sum_{r=1}^{NE} E_r^{ji} \sin\left(r\Omega t + r\Theta_{ji}\right) \tag{4-20}$$

where E_r^{ji} and Θ_{ji} are the rth harmonic amplitude and the phase difference of the mesh between the ith pinion and the jth face-gear. All gears are assumed to be identical. Therefore, no additional phase is introduced into Equation (4-20), for the sake of simplicity. Hence, the only phase between any two meshing locations is the Θ_{ji} term in Equation (4-20).

There are two types of gear-set arrangements, which are classified according to the imposed loading condition [118]. At the first arrangement, given in Figure 4-6, Gear 2 (G_2) is the input, Gear 1 (G_1) and Gear 3 (G_3) are the outputs. This is known as the split-torque arrangement. At the second case, G_3 (output) is driven by G_1 (input) through G_2 (idler), which is named as the idler arrangement.

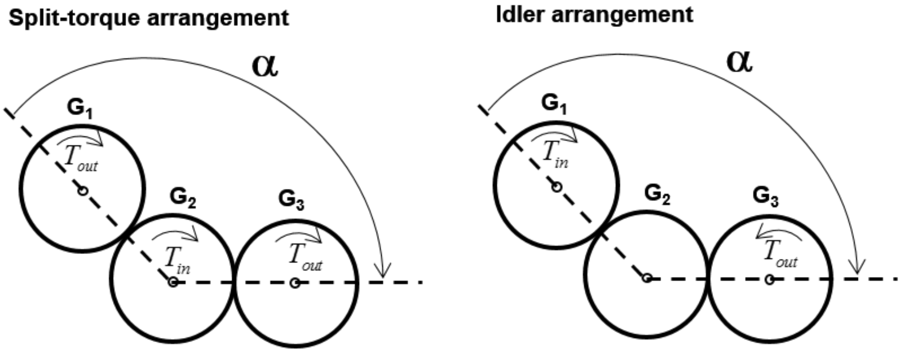
Split-torque arrangement
Idler arrangement
α
α
G₁
G₂
G₃
G₁
G₂
G₃
T_{out}
T_{in}
T_{out}
T_{in}
T_{out}

Figure 4-6 Split-torque and idler arrangements

For the split-torque system, the following phase difference relations are utilized for the phasing between pinion-gear engagements, according to their arrangement types, discussed above;

$$\Theta_{1i} = N_g\left(\alpha_{i-1} + \gamma\right),\ i = 1..5 \tag{4-21}$$

$$\Theta_{2i} = N_p\left(\pi + \gamma\right), i = 1..5 \tag{4-22}$$

where N_g is the face-gear number of teeth, N_p is the spur pinion tooth number, as tabulated in Table 4-1. α is the angle between the lines connecting the centers of the meshing gears. γ is specified as:

$$\gamma = \begin{cases} 0,\ \text{split-torque arrangement} \\ \pi/2,\ \textit{idler arrangement} \end{cases} \tag{4-23}$$

The orientations of all gears are arranged with respect to P_1, as shown in Figure 4-7. The orientation of the pinions and corresponding phase differences are tabulated in Table 4-1.

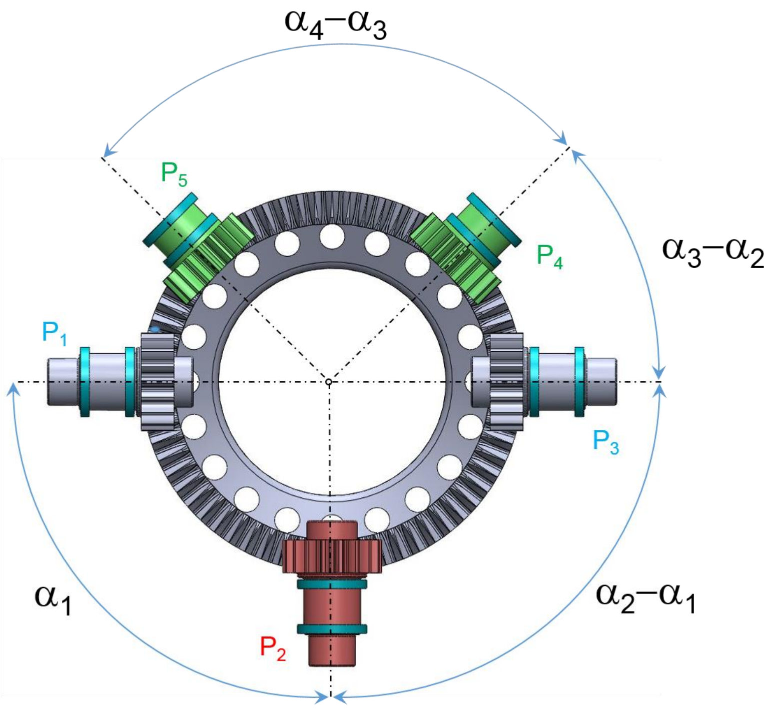
$\alpha_4-\alpha_3$
P_5
P_4
$\alpha_3-\alpha_2$
P_1
P_3
α_1
$\alpha_2-\alpha_1$
P_2

Figure 4-7 Orientation of the pinions on the face-gear

Table 4-1 Phase differences between the meshes

Mesh	Mesh location	Middle gear teeth number	Orientation angle (α)	Mesh phase difference (Θ_{ji})	Arrangement type (between the ith mesh and the reference mesh)
Mesh-1	UFG and P_1	N_g	0	0	reference mesh
Mesh-2	UFG and P_2	N_g	α_1	$N_2*\alpha_1+\pi$	idler
Mesh-3	UFG and P_3	N_g	α_2	$N_2*\alpha_2+0$	split torque
Mesh-4	UFG and P_4	N_g	α_3	$N_2*\alpha_3+\pi$	idler
Mesh-5	UFG and P_5	N_g	α_4	$N_2*\alpha_4+\pi$	idler
Mesh-6	P_1 and LFG	N_p	π	$N_1*\pi+ \Theta_{11}$	split torque
Mesh-7	P_2 and LFG	N_p	π	$N_1*\pi+\Theta_{12}$	split torque
Mesh-8	P_3 and LFG	N_p	π	$N_1*\pi+\Theta_{13}$	split torque
Mesh-9	P_4 and LFG	N_p	π	$N_1*\pi +\Theta_{14}$	split torque
Mesh-10	P_5 and LFG	N_p	π	$N_1*\pi+\Theta_{15}$	split torque

The calculated phases for each mesh location also apply to the corresponding mesh stiffness, where they are taken out of phase at the related meshing location. Thus, the mesh stiffness equation for all specified mesh locations is defined as,

$$k_{ji}\left(t\right)=1+\sum_{r=1}^{NK}\mathrm{K}_r^{ji}\sin\left(r\Omega t+r\Theta_{ji}+\pi\right) \tag{4-24}$$

where K_r^{ji} and Θ_{ji} are the rth harmonic amplitude and the phase difference of the mesh between the ith pinion and the jth face-gear.

4.1.3 Effect of Directional Rotational Radius

Directional rotational radius is calculated at each contact point of the meshing teeth. It specifies the moment arm of the distributed force due to the applied total torque of the pinion and the gear. It has time-varying characteristics when the surface geometry is complex, as in bevel or hypoid gears [119]. Tang et al. [120] studied the effect of this parameter on the dynamic response of the system. However, both analytical and numerical calculations reveal that the directional rotational radii for a face-gear and a mating spur-pinion do not vary with time. Equation (4-3) shows this parameter as time-variant for a general case. However, it is not taken as time-variant throughout the dynamic analysis. The analytical calculations are performed with the Mathematica package program and are given in Appendix F. The obtained expressions for $\bar{\lambda}_{pi}\left(\bar{t}\right)$ and $\bar{\lambda}_{gi}\left(\bar{t}\right)$ are,

$$\bar{\lambda}_{pi}\left(\bar{t}\right)=r_{bs} \tag{4-25}$$

$$\bar{\lambda}_{gi}\left(\bar{t}\right)=-r_{bs}\cos\left(\gamma_m\right)-\cos\left(\phi_s+\theta_{os}+\theta_s\right)\sin\left(\gamma_m\right)u_s \tag{4-26}$$

where θ_{os} is the parameter that specifies the tooth spacing, and may be given as

$$\theta_{os} = \frac{\pi}{2N_s} - inv(\alpha_0) \tag{4-27}$$

where u_s and θ_s are the generalized coordinates that specify the shaper involute tooth profile, α_0 is the pressure angle and N_s is the tooth number of the spur-shaper. The curvilinear coordinate u_s is parallel to the z_s direction of the fixed cartesian coordinate shown in Figure 4-8, and θ_s is the rolling angle.

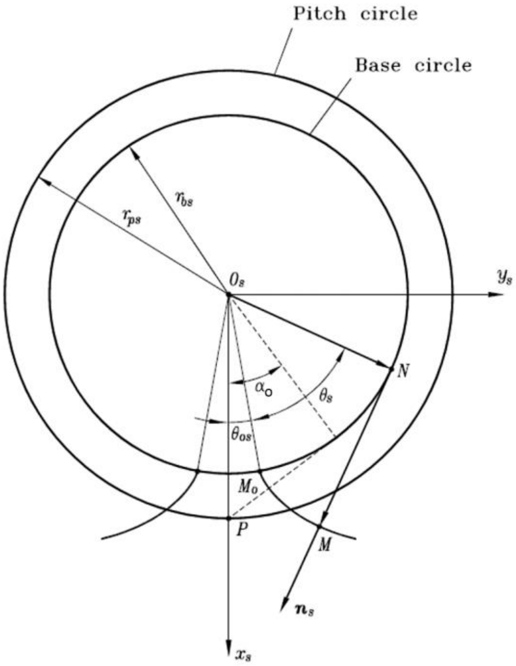

Figure 4-8 Involute profile of the shaper

As specified in Chapter 2, for the conjugate action of tooth profiles (that is to say, surface normal at the point of contact is perpendicular to the sliding velocity between the two meshing surfaces at all time instants), the *equation of meshing* should be satisfied,

$$0 = r_{bs}\left(1 - m_{s/g}\cos\left(\gamma_m\right)\right) - u_s m_{s/g}\sin\left(\gamma_m\right)\cos\left(\phi_s + \theta_{os} + \theta_s\right) \quad (4\text{-}28)$$

Taking $\cos\left(\phi_s + \theta_{os} + \theta_s\right)$ from Equation (4-25) and inserting it into Equation (4-26) yields,

$$\bar{\lambda}_{gi} = -r_{bs}\cos\left(\gamma_m\right) - \frac{r_{bs}\left(1 - m_{s/g}\cos\left(\gamma_m\right)\right)}{u_s m_{s/g}\sin\left(\gamma_m\right)}\sin\left(\gamma_m\right)u_s \quad (4\text{-}29)$$

which simplifies to

$$\bar{\lambda}_{gi} = \frac{r_{bs}}{m_{s/g}} = r_{bs}\cdot\frac{N_g}{N_s} \quad (4\text{-}30)$$

Equations (26) and (4-29) give the directional rotational radius for the spur and the face-gear, respectively. As it can easily be seen, they do not have any time-varying components. $\bar{\lambda}_{gi}$ is equal to the product of the base circle radius of the spur pinion and the reduction ratio.

4.1.4 Solution Method

The non-linear equations of motion are solved by using the Harmonic Balance Method (HBM) together with Arc-Length Continuation Method [121] in obtaining the periodic steady-state response of the system in the frequency domain. The results are compared with the time simulation results obtained with Runga Kutta numerical solution method. The STE and the mesh stiffness are expressed with only the first harmonics terms. The torque values are assumed to be constant.

For seeking the solution by HBM in conjunction with the Arc-Length Continuation Method, similar to the harmonic expressions for the mesh stiffness and STE as in

Equations (4-20) and (4-24), the time and displacement varying parameters of the system (i.e. mesh damping, rotational dofs of the disks, DTE, gear mesh displacement) are also expressed as in the following form

$$\chi_{ji}\left(t\right)=\mathrm{X}_0^{ji}+\sum_{r=1}^{N\mathrm{X}}\left(\mathrm{X}_{2r}^{ji}\cos\left(r\Omega t\right)+\mathrm{X}_{2r+1}^{ji}\sin\left(r\Omega t\right)\right) \tag{4-31}$$

where $\chi_{ji}\left(t\right)$ represents any of these parameters between the ith pinion and the jth face-gear, X_0^{ji} is the bias term, X_{2r}^{ji} and X_{2r+1}^{ji} are the coefficients of sine and cosine terms of the rth harmonic, respectively.

The RMS value of the gear mesh displacement is plotted with respect to dimensionless frequency. The RMS of gear mesh displacement between the jth face-gear and ith pinion is calculated as,

$$p_{ji}^{(rms)}=\left\{\sum_{r=1}^{R}\left[\mathrm{P}_{ji2r}\right]^2+\left[\mathrm{P}_{ji2r+1}\right]^2\right\}^{1/2} \tag{4-32}$$

where P_{ji2r} and P_{ji2r} are the Fourier coefficients of the rth harmonic of $p_{ji}\left(t\right)$.

4.2 Non-linear Dynamic Model For A Face-Gear and Spur Pinion Pair

When *i* and *j* are set to 1 in Equations (4-15) and (4-16), the formulation for a face-gear and a spur pinion pair is obtained. Figure 4-9 shows the dynamic model of the pair model. Re-writing the mentioned equations for *i=1* and *j=1* yield,

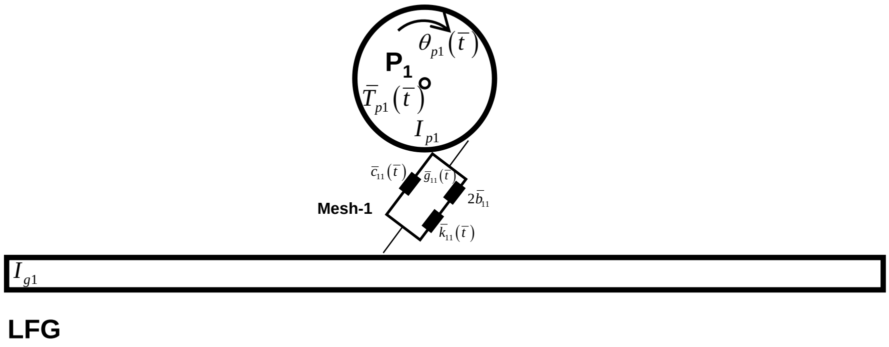
$\theta_{p1}(\bar{t})$
P1
$\bar{T}_{p1}(\bar{t})$
I_{p1}
$\bar{c}_{11}(\bar{t})$
$\bar{g}_{11}(\bar{t})$
$2\bar{b}_{11}$
Mesh-1
$\bar{k}_{11}(\bar{t})$
I_{g1}
LFG

Figure 4-9 Dynamic model for a pair of face-gear and a spur-pinion

$$\ddot{\theta}_{g1}(t)+\left\{2\omega_{g11}(t)\zeta_{11}(\mathrm{t})\,\dot{p}_{11}(t)+\omega_{g11}(t)^2\,k_{11}(t)\,g_{11}(t)\right\}=f_{g1}(t) \tag{4-33}$$

$$\ddot{\theta}_{p1}(\bar{t})+\left\{2\omega_{p11}(t)\zeta_{p11}(\mathrm{t})\,\dot{p}_{11}(t)+\omega_{p11}(t)^2\,k_{11}(t)\,g_{11}(t)\right\}=f_{p1}(t) \tag{4-34}$$

where,

$$f_{g1}(t)=\frac{\bar{T}_{g1}(\bar{t})}{\omega_c{}^2 I_{g1}},\quad f_{p1}(t)=\frac{\bar{T}_{p1}(\bar{t})}{\omega_c{}^2 I_{p1}} \tag{4-35}$$

$$\zeta_{g11}(\mathrm{t})=\frac{\bar{\lambda}_{g11}(t)\bar{c}_{11}(t)b_c\omega_c}{\omega_c{}^2 I_{g1}2\omega_{11}(t)},\ \zeta_{p11}(\mathrm{t})=\frac{\bar{\lambda}_{p11}(\bar{t})\bar{c}_{11}(\bar{t})b_c\omega_c}{\omega_c{}^2 I_{p1}2\omega_{p11}(t)} \tag{4-36}$$

$$\omega_{g11}(t)=\left(\frac{\bar{\lambda}_{g1}(\bar{t})}{\omega_c{}^2 I_{g1}}\bar{k}m_{11}b_c\right)^{\frac{1}{2}},\ \omega_{p11}(t)=\frac{\bar{\lambda}_{p11}(\bar{t})\bar{k}m_{11}b_c}{\omega_c{}^2 I_{p1}} \tag{4-37}$$

The parameters specified in Equations (4-3) through (4-14) are also valid for the face-gear spur-pinion pair case, i.e., when *i=1* and *j=1*.

CHAPTER 5

PARAMETRIC STUDIES

5.1 Case Studies for a Pair of Face-Gear and Pinion

The non-linear equation of motion is solved together with the Harmonic Balance Method (HBM) and Arc-Length Continuation Method [121] for the periodic steady-state response of the system in the frequency domain. The results are compared with the time simulation results obtained with Runga-Kutta numerical method. The STE and the mesh stiffness variations are expressed with only their first harmonics terms. The torque values are assumed to be constant. The input parameter list for the four cases is given in Table 5-1.

Using the SDOF system of the gear pair, some parametric studies are performed to seek the effect of backlash and the applied torque.

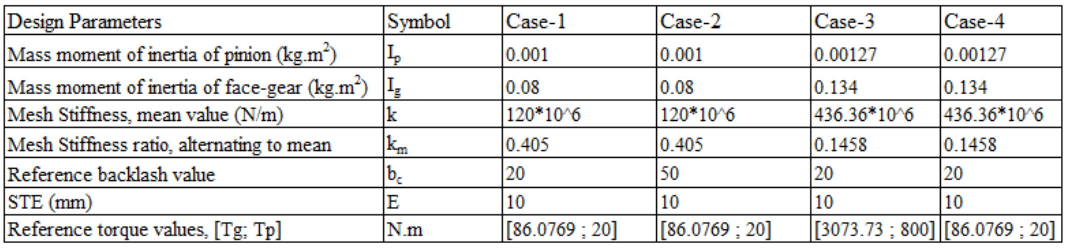

Design Parameters	Symbol	Case-1	Case-2	Case-3	Case-4
Mass moment of inertia of pinion (kg.m^2)	I_p	0.001	0.001	0.00127	0.00127
Mass moment of inertia of face-gear (kg.m^2)	I_g	0.08	0.08	0.134	0.134
Mesh Stiffness, mean value (N/m)	k	120*10^6	120*10^6	436.36*10^6	436.36*10^6
Mesh Stiffness ratio, alternating to mean	k_m	0.405	0.405	0.1458	0.1458
Reference backlash value	b_c	20	50	20	20
STE (mm)	E	10	10	10	10
Reference torque values, [Tg; Tp]	N.m	[86.0769 ; 20]	[86.0769 ; 20]	[3073.73 ; 800]	[86.0769 ; 20]

Table 5-1 Parameters of the gear pair

5.1.1 Effect of Backlash

Case-1

RMS values of the gear mesh displacement between the face-gear and the pinion for several backlash values are shown in Figure 5-1, for Case-1. The solution is obtained with Harmonic Balance Method (HBM) coupled with Arc-Length Continuation Method utilizing three harmonics. The nonlinearity in the SDOF system is the backlash value between the gear teeth. Firstly, the backlash value is set to zero (or the backlash nonlinearity is not taken into account), and the Linear Time Variant (LTV) version of the system with the parameters given in Table 5-1 is obtained. Figure 5-1 shows this LTV version of Case-1.

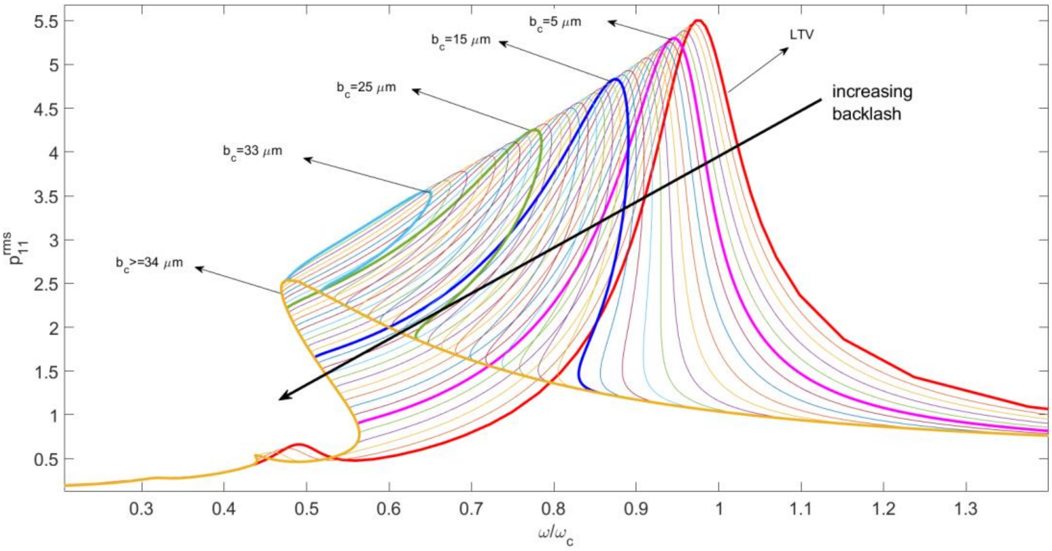

Figure 5-1 Comparison of the RMS values of the response (gear mesh displacement between face-gear and the pinion) for Case-1, increasing backlash from b_c =5 μm to 200 μm, frequency range ω=0.01ω_c to ω=1.4ω_c

Then the effect of the backlash value on the response of the system is investigated. The backlash value is varied from 1 μm to 200 μm (in the increasing arrow direction), as depicted in Figure 5-1, for the specified torque values. The response for the LTV shows no signs of hardening or softening spring effect, as expected. However, with $b_c=1\ \mu m$ to $b_c=34\ \mu m$, both hardening and softening effects are observed for each b_c values.

Figure 5-2 shows the same results given in Figure 5-1, but for only 5 μm, 15 μm, 25 μm, 33 μm, 34 μm and the values larger than 34 μm together with the LTV system response. The softening spring (separation and single sided impact) and then hardening spring (separation and double-sided impact) effect is clearly depicted in Figure 5-2, for the b_c values less than 34 μm. However, for $b_c \geq 34\ \mu m$, hardening effect disappears. This is due to fact that, the deflection of the tooth is not enough to cover the clearance specified by the total backlash value, $2b_c$.

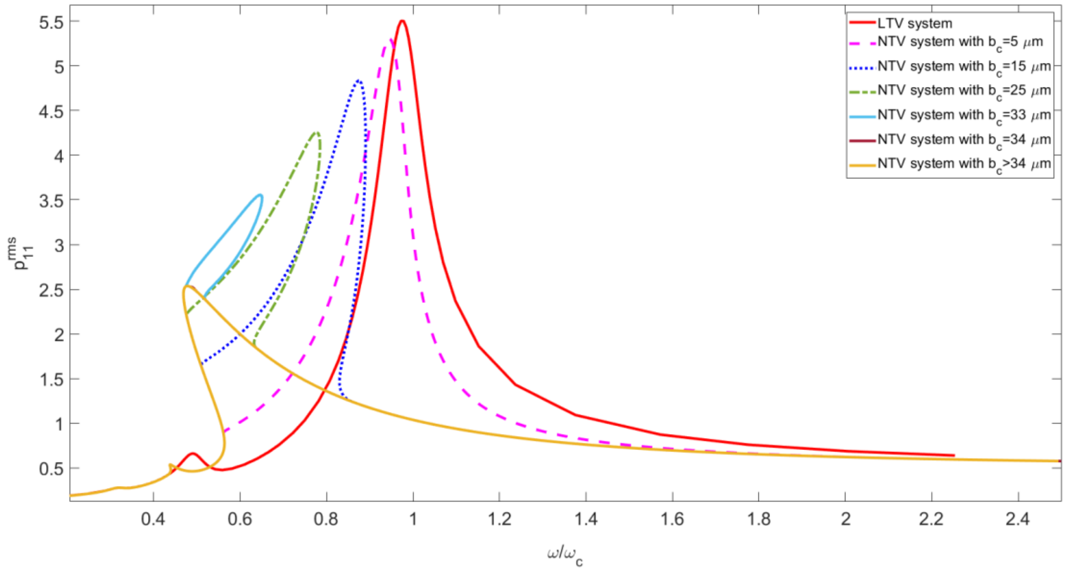

Figure 5-2 Comparison of the RMS values of the response (gear mesh displacement between face-gear and the pinion) for Case-1, for the backlash values b_c =5, 15, 25, 33 μm and 34 μm, frequency range $\omega=0.01\omega_c$ to $\omega=2.5\omega_c$

It can easily be observed that the RMS of the gear mesh displacement values for the specified frequency range are the same for the backlash values 34 μm to 200 μm. This depicts that increasing the backlash beyond 34 μm does not change the system's dynamic response, for the specified static torque values. The hardening spring effect vanishes at a b_c value between 33 μm and 34 μm.

Case-2

The system in Case-2 is the same as the system given in Case-1, but only the reference backlash value is different, as depicted in Table 5-1. The RMS values of the gear mesh displacement between the face-gear and the pinion for several backlash values are depicted in Figure 5-3, for Case-2. Figure 5-3 demonstrates the effect of increasing the backlash value from 1 μm to 200 μm (in the arrow direction) on the system's response. The results for 10, 15, 20, 25, 33, 44 μm and 200 μm are plotted together with the LTV system response. For the LTV system, the clearance is set to zero, as mentioned in the previous case. The response of the system is the same for the backlash values 34 μm to 200 μm, which means increasing the backlash beyond 34 μm does not change the system's dynamic characteristics.

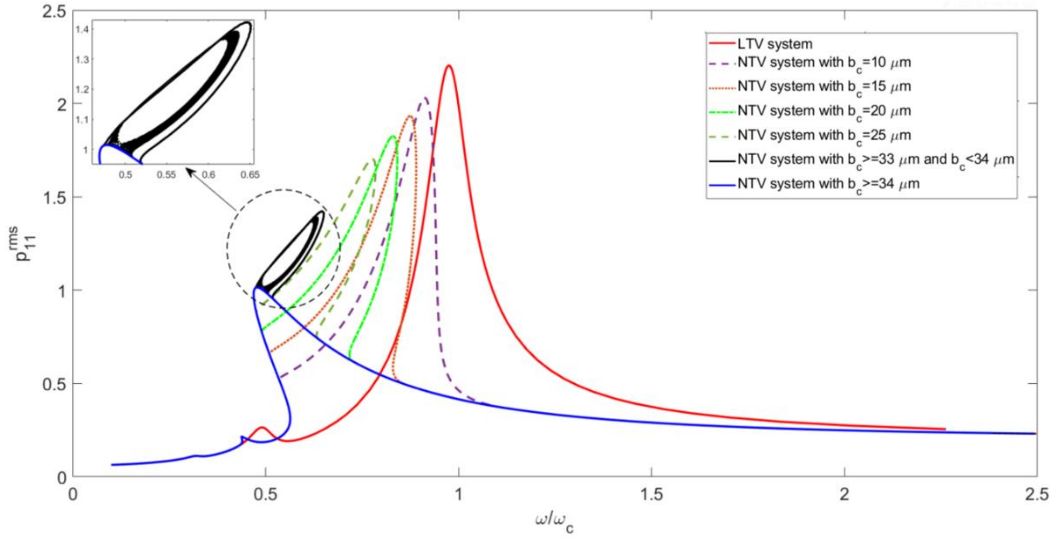

Figure 5-3 Comparison of the RMS values of the response (gear mesh displacement between face-gear and the pinion) for Case-2, for the backlash values b_c =10, 15, 20, 25, 33 μm and for all values between 34 μm and 200 μm, frequency range ω=0.01ω_c to ω=2.5ω_c

The transition between the double-sided and single-sided impacts occurs between the backlash values of 33 μm and 34 μm. Figure 5-3 also shows the system's response for several backlash values between 33μm and 34μm. The transition happens in the circled area; as backlash increases from 33 μm to 34 μm, the bulge closes and disappears when backlash equals 34 μm.

Case 3

The RMS values of the gear mesh displacement between the face-gear and the pinion for several backlash values are plotted for Case-3 in Figure 5-4.

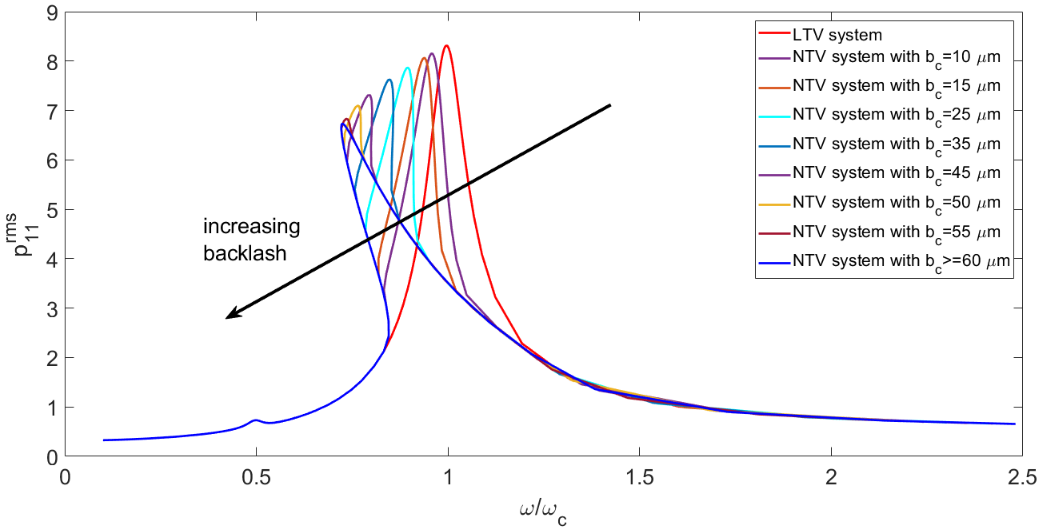

Figure 5-4 Comparison of the RMS values of the response (gear mesh displacement between face-gear and the pinion) for Case-3, for the backlash values b_c =10, 15, 25, 35, 45, 50, 55 μm and for all values between and 60 μm and 200 μm, frequency range ω=0.01ω_c to ω=2.5ω_c

This figure demonstrates the effect of increasing the backlash value from 1 μm to 200 μm (in the arrow direction) on the system's response. Figure 5-4 shows the results for 10 μm, 15 μm, 25 μm, 35 μm, 45 μm, 60 μm and 200 μm together with the LTV system response. It can easily be seen that the results are the same for the backlash values 60 μm to 200 μm. Hence, the backlash does not change the system's dynamic response after 60 μm.

Case-4

The same system given in Case-3 with a reduced static torque value is considered in Case-4. The RMS values of the response between the face-gear and the pinion for several backlash values are calculated. The solution is obtained with the harmonic balance method (HBM) utilizing three harmonics.

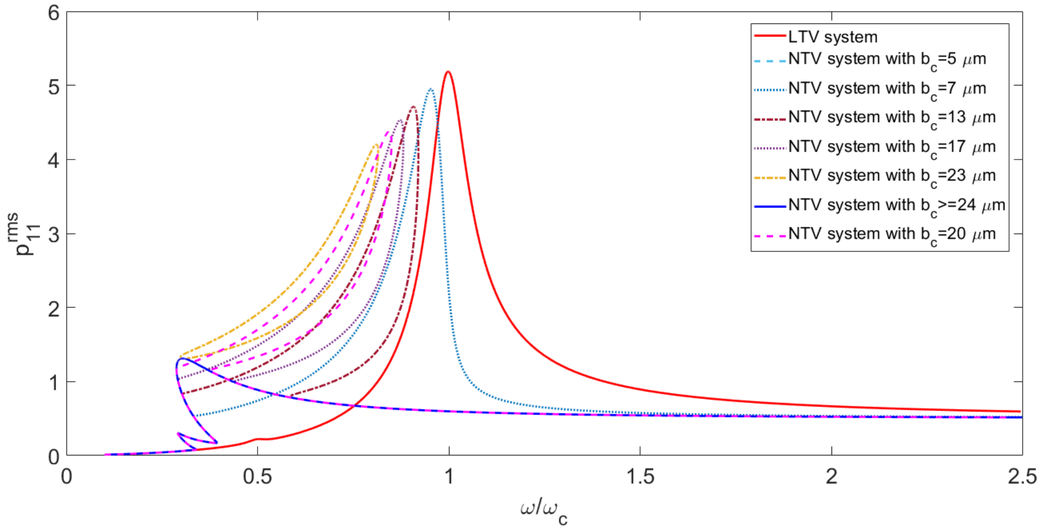

Figure 5-5 Comparison of the RMS values of the response (gear mesh displacement between face-gear and the pinion) for Case-4, for the backlash values b_c =5 μm, 7 μm, 13 μm, 17 μm, 23 μm, and for all values between and 24 μm and 200 μm, frequency range ω=0.01ω_c to ω=2.5ω_c

Figure 5-5 demonstrates the effect of increasing the backlash value from 1 μm to 200 μm (in the arrow direction) on the system's response. The results for 5, 7, 13, 17, 23, 24 μm, and 200 μm, together with the LTV system response are given in Figure 5-5. The results are the same for the backlash values 24 μm to 200 μm. Increasing the backlash after the value of 24 μm, does not change the system characteristics.

Comparing the results in Case-3 and Case-4 shows that the response levels in Case-3 are higher than the levels in Case-4. This is an expected result due to high static torque values. In Case-3, the transition from double-sided impact to single-sided impact occurs around the backlash value of 60 μm. In Case-4, this value is calculated to be around 24 μm, as given in Figure 5-4 and Figure 5-5. The static torque applied in Case-3 causes enough deflection to cover the clearance; therefore, double-sided tooth impact can be seen up to 60 μm backlash value. In Case-4, on the other hand, the torque value is less than the torque in Case-3. Therefore, enough deflection for the double-sided impact is not created, and the amount of clearance avoids the double-sided impact. The system characteristics cannot be altered by increasing the backlash value beyond 24 μm.

5.1.2 Effect of Static Torque

Figure 5-6 and Figure 5-7 show the response between the face-gear and the pinion for several torque values, for the system given in Case-4. The effect of increasing torque value is investigated with the torque values from T_g=1.0 T to 100 T (in the arrow direction), where T is a reference torque value. The results for 1.0 T, 10 T, 20 T, 30 T, 40 T, 50 T, 60 T, 70 T, 80 T, 90 T, and 100 T are given in Figure 5-7.

Figure 5-6 shows the results for only 1.0 T, 20 T, 50T, 70T, and 100T. As the torque value increases, the amplitude of the response, at which the softening (single-sided impact) and hardening (double-sided impact) starts, increases, as depicted in the figure. This phenomenon occurs due to the static deflection caused by the applied torque values. As it is increased, a large amplitude of the dynamic response is needed to separate the tooth. The given backlash value is not large enough to avoid double-sided impact; hence, both single and double-sided impacts occur at each torque level, as shown in Figure 5-6 and Figure 5-7.

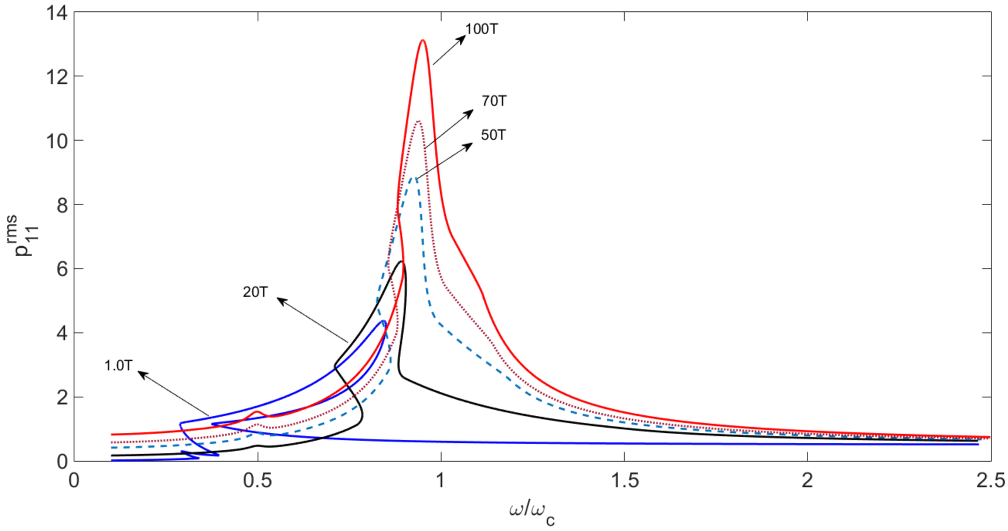

Figure 5-6 Comparison of the RMS values of the response (gear mesh displacement between face-gear and the pinion) for Case-4, increasing reference torque values for b_c =20 μm, frequency range ω=0.01ω_c to ω=2.5ω_c

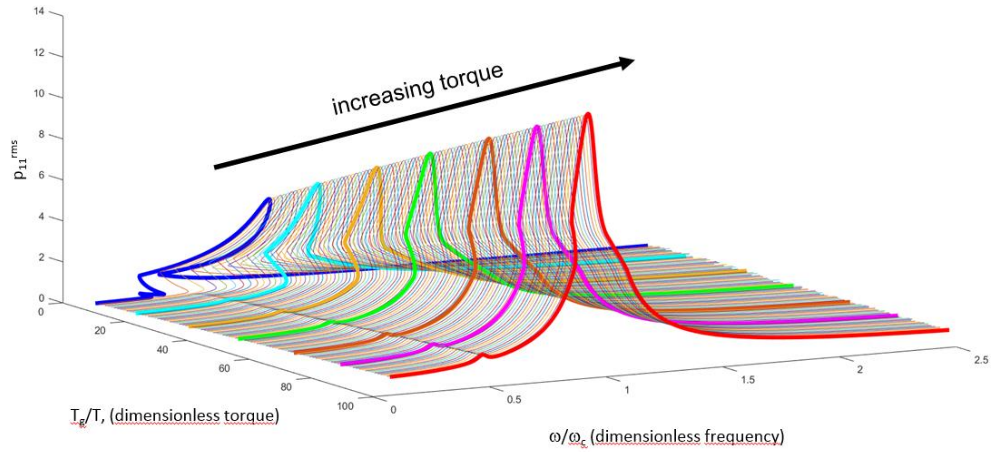

Figure 5-7 Comparison of the RMS values of the response (gear mesh displacement between face-gear and the pinion) for Case-4, increasing reference torque values from 1.00 T to 100 T, for b_c =20 μm, frequency range ω=0.01ω_c to ω=2.5ω_c

5.1.3 Effect of Damping and Static Torque on Subharmonic Response

For the system Case-1 given in Table 5-1, the existence of the subharmonic is investigated for different damping and static torque values. The damping coefficient is varied between 1600 N.s/m to 3250 N.s/m, and its effect on the gear mesh displacement is investigated.

In a geared system, damping can be affected by many parameters such as structural, viscous characteristics, frictional and bearing losses, and churning losses. In this section, the details of the damping physics are not investigated. A reasonable approximation of the damping values is made. The damping values are taken as varying between 1600 N.s/m and 3250 N.s/m, which correspond to viscous damping ratios of 0.038 and 0.076, respectively, being consistent with the values frequently used in literature, [122–124]. The gear mesh displacement between the face-gear and the pinion is calculated by HBM using five super-harmonics together with ½ subharmonic. The results are compared with the time simulation results obtained with Runga-Kutta numerical method for the damping value of 1600 N.s/m.

Figure 5-8 shows the effect of damping on the subharmonic peaks observed around the frequency range $\omega=1.5\omega_c$ and $\omega=2.1\omega_c$. The response curves are plotted for several damping values. For the damping values of 1600 N.s/m and 1800 N.s/m, the dynamic response curves do not form a closed curve at the specified frequency range. However, beginning from the value 2400 N.s/m, the dynamic response curve forms a closed curve. As the damping is increased, the size of this curve becomes smaller.

A similar result is obtained by varying the applied torque value. The applied torque is increased for the same system, and the response curves are obtained. Figure 5-9 gives the gear mesh displacement for several torque values. As depicted in the figure, the closed curves for the subharmonic resonance peaks tend to vanish as the applied torque increases.

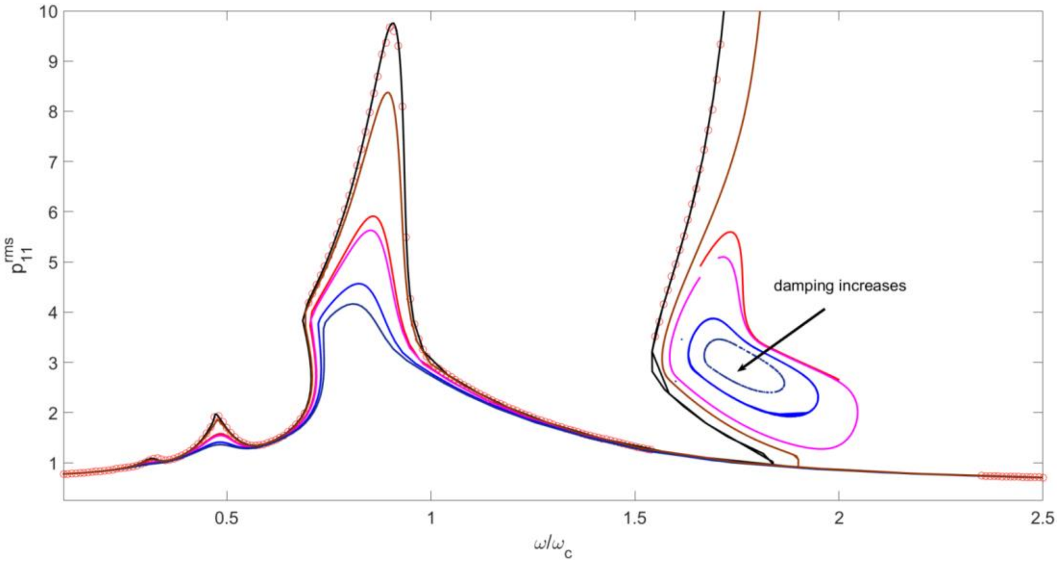

Figure 5-8 Comparison of the RMS values of the response (gear mesh displacement between face-gear and the pinion) for the damping values, 1600 N.s/m time simulation (o), 1600 N.s/m HBM solution (–), 1800 N.s/m HBM solution (–), 2400 N.s/m HBM solution (–), 2500 N.s/m HBM solution (–), 3000 N.s/m HBM solution (–), 3250 N.s/m HBM solution (–),for the frequency range $\omega=0.1\omega_c$ to $\omega=2.5\omega_c$

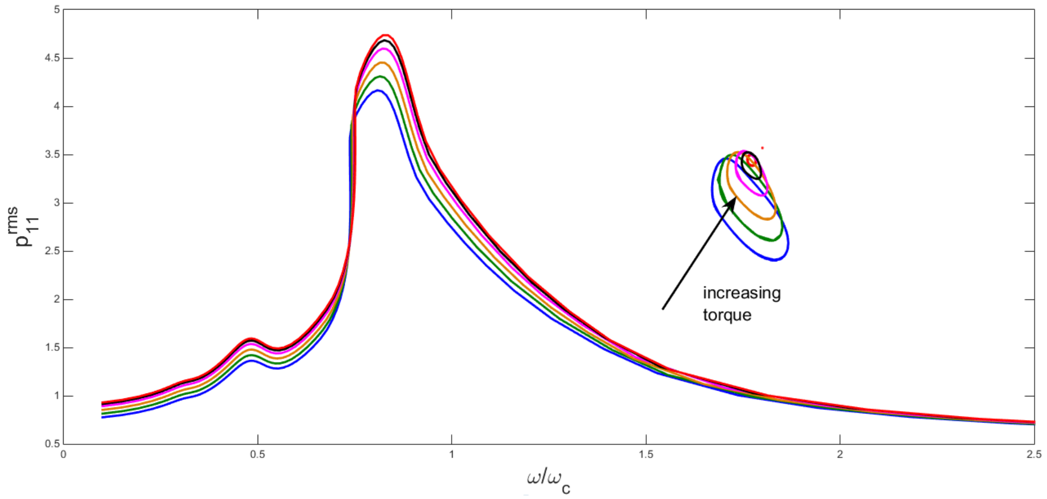

Figure 5-9 Comparison of the RMS values of the response (gear mesh displacement between face-gear and the pinion) for the torque values, T_g=1.00T (–), T_g=1.05T (–), T_g=1.10T (–), T_g=1.15T (–), T_g=1.18T (–), T_g=1.20(–), for the frequency range $\omega=0.1\omega_c$ to $\omega=2.5\omega_c$

5.2 Case Studies for Split-Torque Face-Gear Drive System

5.2.1 Effect of Orientation Angle Pattern

The non-linear equations of motion are solved together with the Harmonic Balance Method (HBM) and Arc-Length Continuation Method [121] for the periodic steady-state response of the system in the frequency domain. The results are compared with the time simulation results obtained with Runga-Kutta numerical method.

Table 5-2 Parameters of the system

Parameter	**Symbol**	**Value**
Number of teeth, face-gear	N_g	103
Number of teeth, spur-gear	N_p	23
Module (mm)	m_n	3.175
Pressure angle (°)	a_c	20
Moment of inertia, jth face-gear (kg.m^2)	I_{gj}	0.1392
Moment of inertia, ith spur-gear (kg.m^2)	I_{pi}	0.0300
Total Gear Backlash, between the ith pinion and jth face-gear (μm)	$2b_{ji}$	80
Input power (kW)	T_{p3}, T_{p5}	750
Secondary output power (kW)	T_{p2}	250
Primary output power (kW)	T_{g1}	1250
Mean value of the mesh stiffness (N/m)	$\bar{k}m_{ji}$	4.5x10^8
Mean value of the mesh damping (N.s/m)	$\bar{c}m_{ji}$	3000
STE, for all mesh locations	E_1^{ji}	0.075

The STE and the mesh stiffness variations are expressed with only their first harmonics terms. The torque values are assumed to be constant. The input parameters for this case study are listed in Table 5-2.

For seeking the solution by HBM in conjunction with the Arc-Length Continuation Method, similar to the harmonic expressions for the mesh stiffness and STE as in Equations (4-20) and (4-24), the time and displacement varying parameters of the system (i.e., mesh damping, rotational dofs of the disks, DTE, gear mesh displacement) are also expressed as in the following form

$$\chi_{ji}\left(t\right)=\mathrm{X}_0^{ji}+\sum_{r=1}^{N\mathrm{X}}\left(\mathrm{X}_{2r}^{ji}\cos\left(r\Omega t\right)+\mathrm{X}_{2r+1}^{ji}\sin\left(r\Omega t\right)\right) \tag{5-1}$$

where $\chi_{ji}\left(t\right)$ represents any of these parameters between the ith pinion and the jth face-gear, X_0^{ji} is the bias term, X_{2r}^{ji} and X_{2r+1}^{ji} are the coefficients of sine and cosine terms of the rth harmonic, respectively.

The RMS value of the gear mesh displacement is plotted with respect to dimensionless frequency. The RMS value of gear mesh displacement between the jth face-gear and ith pinion is calculated as,

$$p_{ji}^{(rms)}=\left\{\sum_{r=1}^{R}\left[\mathrm{P}_{ji2r}\right]^2+\left[\mathrm{P}_{ji2r+1}\right]^2\right\}^{1/2} \tag{5-2}$$

where P_{ji2r} and P_{ji2r} are the Fourier coefficients of the rth harmonic of $p_{ji}\left(t\right)$.

Due to the non-linear nature of the system, the response may include many harmonic and sub-harmonic components. To further clarify, an example case study is presented below for a system defined in Table 5-2, where input pinion orientation angles of P_1 and P_3 are 45° with respect to P_2 axis, while idler pinions P_4 and P_5 are at 30° with respect to P_2 axis. In order to evaluate the level of accuracy of the HBM solution, the harmonic content is firstly investigated with 3-harmonics in this numerical case study. The RMS values of the gear mesh displacements at ten meshing positions generated by HBM and the time simulation results are shown in Figure 5-10 for comparison. While comparing the results with the time simulation results, particularly at specific frequency ranges, it can be observed that the 3-harmonic HBM solution becomes insufficient to express the exact solution. For these frequency ranges, the harmonic content of the solution is altered to comprise some sub-harmonic content. Solving this highly non-linear case becomes computationally too expensive for parametric studies. Hence, reasonable approximations are made for accurate and meaningful evaluations.

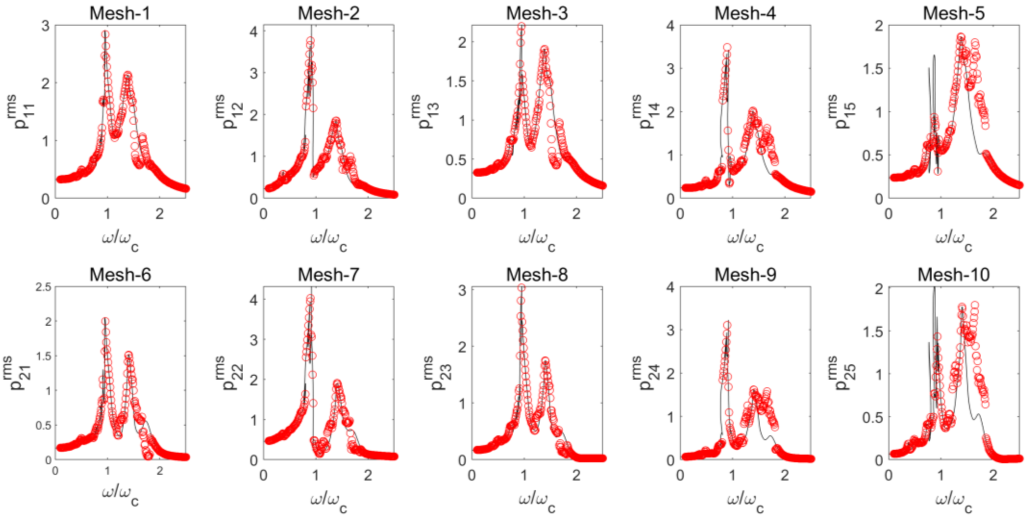

Figure 5-10 Comparison of RMS value of the gear mesh displacements at ten meshing locations, 3-harmonic HBM (—), and time simulation (o)

For simplicity, to seek the effect of the orientation pattern of the pinions among the face gears, only the response at the Mesh-10 is explained here. Figure 5-11 demonstrates the RMS value of the response between the LFG and the idler pinion P_5. HBM solution and time simulation are given in the same plot. As shown in the figure, the 3-harmonics HBM solution fits well with the time simulation results. However, particularly between $\omega=1.0\ \omega_c$ and $\omega=2.0\ \omega_c$, the response differs from the time simulation results at some frequency values due to the sub-harmonic content of the system response. This phenomenon is typical because the drive system has non-linear mesh stiffnesses varying both with displacement and time. With a specific phase, as discussed in the following section, these sub-harmonics may be excited about a given frequency range. To evaluate this phenomenon, the frequency content of the system's dynamic response is assumed to have 1/2 sub-harmonic together with the fundamental harmonic. The obtained solution between the frequencies ω =1.02 ω_c and ω=1.92 ω_c, is shown in Figure 5-11. A large portion of the time data within the specified frequency range is approximated pretty accurately with the given HBM solution.

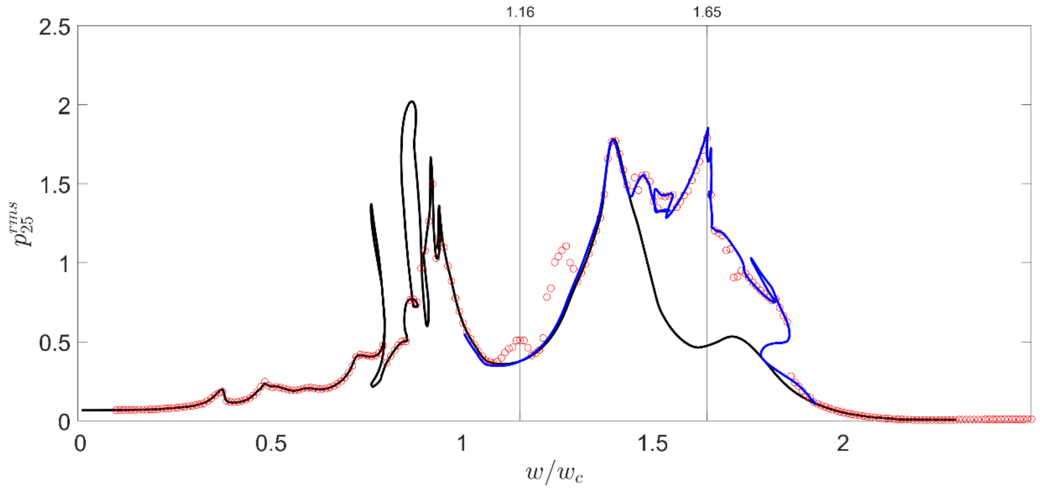

Figure 5-11 Comparison of the RMS values of the response (gear mesh displacement between lower face gear and one of the idler pinions), 3-harmonic HBM (—), 1-harmonic HBM with ½ sub-harmonic solution (—) between 1.00 ω_c and 1.92 ω_c, and the time simulation results (o)

At $\omega=1.65\ \omega_c$, the time series and the power spectrum at the specified frequency are presented in Figure 5-12, along with phase projection and Poincare map. Here, phase projection shows the gear mesh displacement and the time derivative of the gear mesh displacement, while the Poincare map presents the phase projection at discrete time values $t_i=t_0+k(2\pi\omega/\omega_c)$, where $t_0=0$, $i=0,1,2,\ldots$). The power spectrum shows that the gear mesh displacement between the idler pinion and the UFG comprises two main frequencies; the fundamental frequency and ½ sub-harmonic. As shown in Figure 5-12-d, two points on Poincare map indicate that the dynamic response is a period-2 motion. Phase projection shows a closed orbit, which indicates a periodic motion. It does not cross itself because ½ sub-harmonic content of the response is dominant, as depicted in the power spectrum. Thus, the given HBM solution fits well with the time data; since the frequency content is consistent with the assumed HBM solution.

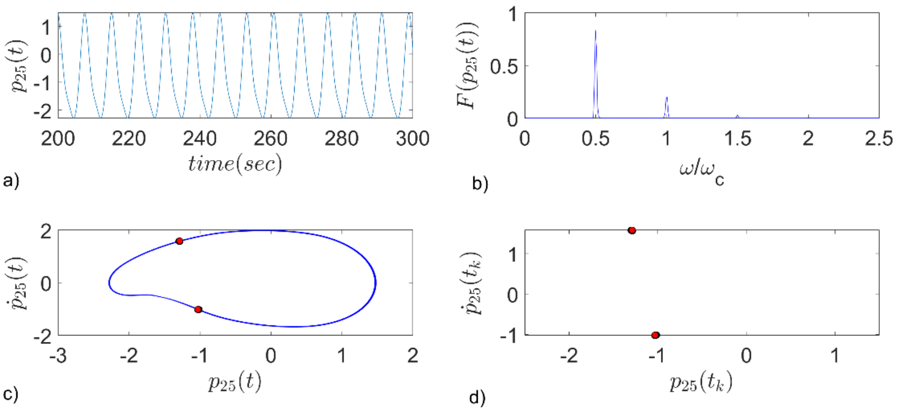

Figure 5-12 (a) Time series **(b)** power spectrum, **(c)** Phase projection, **(d)** Poincare section, at $\omega=1.65\ \omega_c$

Similarly, at $\omega=1.16\ \omega_c$, as seen from the power spectrum of the time series given in Figure 5-13, the frequency content seems to be rich in 1/4, 2/4, ¾, 5/4, 6/4, and 7/4 sub-harmonics, while assumed HBM solution contains of only ½ sub-harmonic and the fundamental harmonic. Therefore, seeking a solution with the fundamental harmonic and ½ sub-harmonic is not enough to approximate the exact solution around those frequencies. Besides, the Poincare map of the steady-state portion of the time simulation forms a smooth curve with many points, indicating that the dynamic response may be a quasiperiodic motion [125,126]. Hence, it is difficult to approximate the exact solution by HBM with these many sub-harmonic frequency contents.

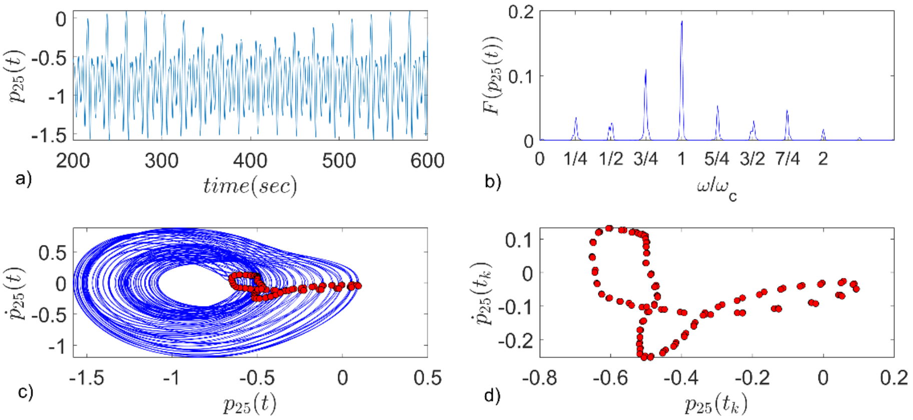

Figure 5-13 (a) Time series **(b)** power spectrum, **(c)** Phase projection, **(d)** Poincare section, at ω=1.16 ω_c

The parametric study is performed to seek the effect of orientation angle pattern which dictates mesh phasing among pinions on the system's dynamic response. Here, 2 sets of 3 different configurations are solved with HBM utilizing 3-harmonics for $\omega=0$ and ω=2.5ω_c and utilizing ½ sub-harmonic for ω=1.4ω_c and ω=2.5ω_c, reducing the computational time drastically compared to the time simulation. In the first set (Set-1), the idler pinions P_4 and P_5 are set at 90° with respect to each other (at 45° with respect to P_2), while the input pinions P_1 and P_3 are set at 45° (Case-1), by 60° (Case-2) and by 90° (Case-3) with respect to P_2. In the second set (Set-2), the idler pinions P_4 and P_5 are set at 60° with respect to each other (at 30° with respect to P_2), while the input pinions P_1 and P_3 are set at 45° (Case-4), by 60° (Case-5) and by 90°

(Case-6) with respect to P_2. The basic orientations of the gears are presented in Figure 5-13.

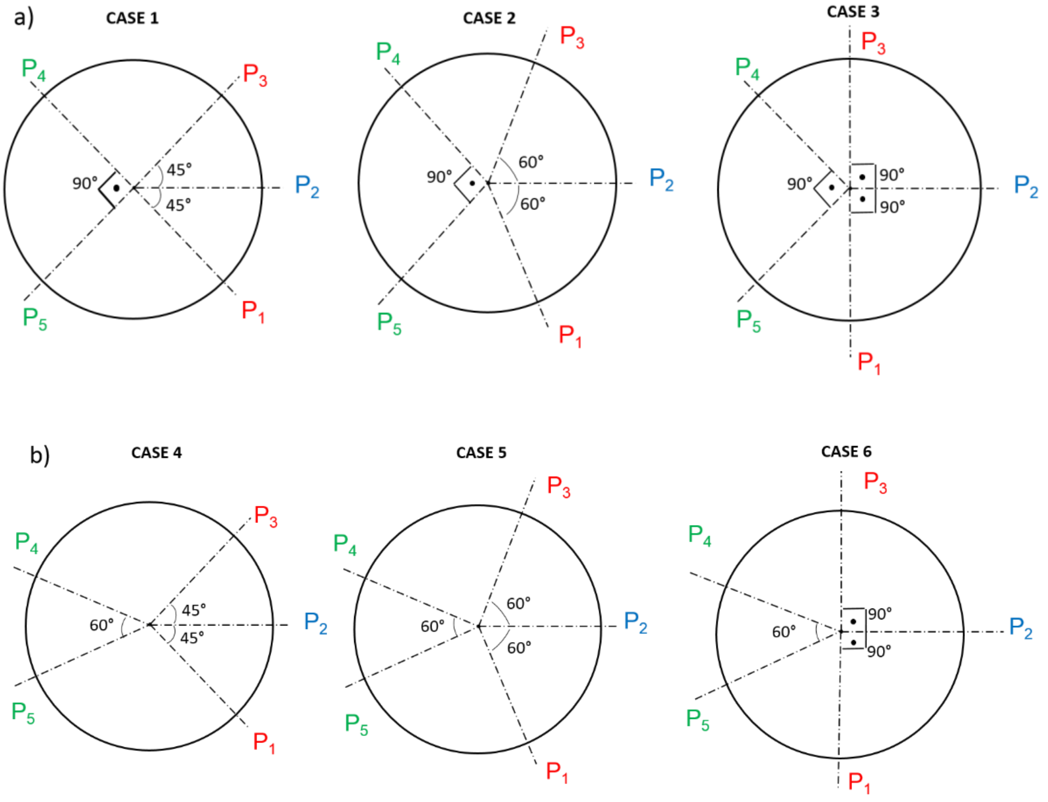
a)
CASE 1
P4
P3
90°
45°
45°
P2
P5
P1
CASE 2
P4
P3
90°
60°
60°
P2
P5
P1
CASE 3
P4
P3
90°
90°
90°
P2
P5
P1
b)
CASE 4
P4
P3
60°
45°
45°
P2
P5
P1
CASE 5
P4
P3
60°
60°
60°
P2
P5
P1
CASE 6
P4
P3
60°
90°
90°
P2
P5
P1

Figure 5-14 Visual representation of the Case Study Sets, **a)** Set-1 of the parametric study, **b)** Set-2 of the parametric study

Table 5-3 Orientation angles of the pinions

CASE	α_1	α_2	α_3	α_4
1	45°	90°	180°	270°
2	60°	120°	195°	285°
3	90°	180°	225°	315°
4	45°	90°	195°	255°
5	60°	120°	210°	270°
6	90°	180°	240°	300°

The orientation angles of the six cases are summarized in Table 5-3. HBM results for Set-1 are presented in Figure 5-15. Non-linear behavior is observed as single-sided and double-sided tooth impacts with the given system parameters for all three cases around ω=0.74 ω_c and ω=0.89 ω_c. As can be seen, Case-3 has the lowest response amplitude when compared with the other two cases between the dimensionless frequencies ω=1.2ω_c and ω=2.5ω_c. Time-varying mesh stiffness leads to the parametric excitation which reveals itself as super-harmonic resonance peaks at ω=0.37 ω_c and ω=0.47ω_c. Unlike the previous two configurations, in Case-3, no subharmonic motions are observed. However, Case-3 gives the maximum amplitude around ω=0.89ω_c.

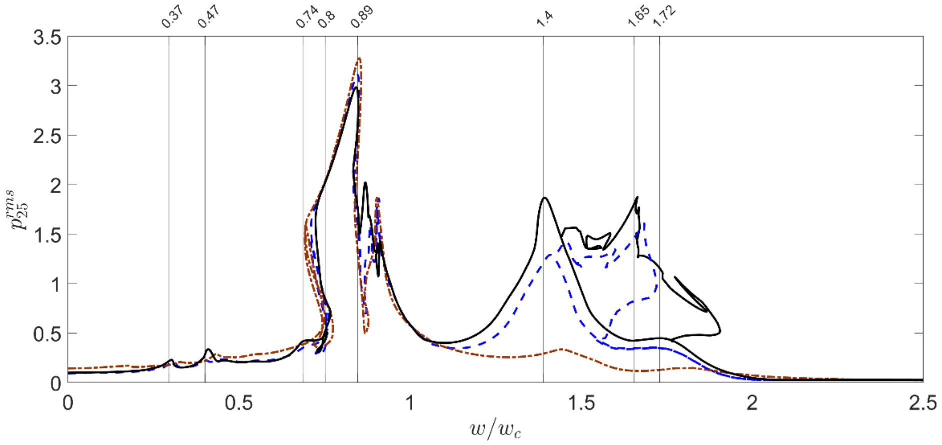

Figure 5-15 The RMS values of the gear mesh displacement between LFG and P5 for Set-1; (—) Case-1, (---) Case-2, (–·–) Case-3

Similarly, Figure 5-16 demonstrates the RMS value of the response between the LFG and one of the idler pinions (P_5) for Set-2 (Case-4, 5, and 6) for comparison. Case-6 depicts no subharmonic motions, while the other two cases clearly show subharmonic resonance peaks between ω=1.4ω_c and ω=2.3ω_c. At ω=0.38ω_c and ω=0.5ω_c, super-harmonic resonance peaks are observed due to parametric excitation. Case-6 gives the maximum amplitude around ω=0.89ω_c.

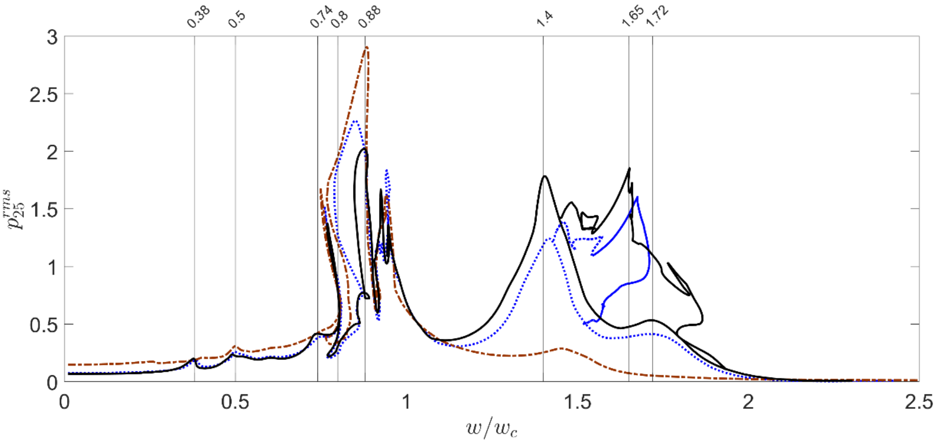

Figure 5-16 The RMS values of the gear mesh displacement between LFG and P5 for Set-2; (—) Case-4, (---) Case-5, (–·–) Case-6

As seen in Figure 5-15 and Figure 5-16, the response levels for Case-3 and Case-6 are the lowest among all six cases for the specified frequency range ω=1.0ω_c and ω=2.5ω_c.

In Case-3 and Case-6, the sub-harmonics around ω=1.5 ω_c vanish due to the feasible orientation of the pinions compared to the other cases. These feasible orientations enable proper phase differences between the non-linear teeth meshing parameters. Therefore, with the proper phase differences, sub-harmonic resonance does not occur. However, since the meshing parameters (stiffness, damping) vary with displacement and time, proper phase differences can only be calculated with a comprehensive parametric non-linear analysis of a given drive system.

The phase values at the meshing locations are prescribed in Table 3. As an example, in Case-1 and 4, the non-linear restoring and damping forces at Mesh-1 are in phase with the forces at Mesh-4, and forces at Mesh-3 are in phase with the forces at Mesh-5.

Therefore, considering Mesh-10 as an example, the phase at which the torque is split from P_3 to LFG becomes exactly equal to the phase at which the torque is transferred from LFG to UFG through the pinion P_5.

Also, the phase at which the torque is split to UFG or LFG through the input pinion P_1 becomes exactly equal to the phase at which the energy is being dissipated during the torque transfer through P_5 at Mesh-5 and Mesh-10.

With these proper phase differences, the drive system achieves a steady-state motion, and the nonlinearity limits the amplitude to a finite value whose frequency is exactly one-half the frequency of the excitation [127]. Therefore, a sub-harmonic motion is observed.

On the other hand, in Case-3 and 6, the phase at which the torque is transferred from any of the input pinions to LFG is not exactly equal to the phase at which the torque is transferred from P_5 to UFG. Therefore, a sub-harmonic resonance does not occur.

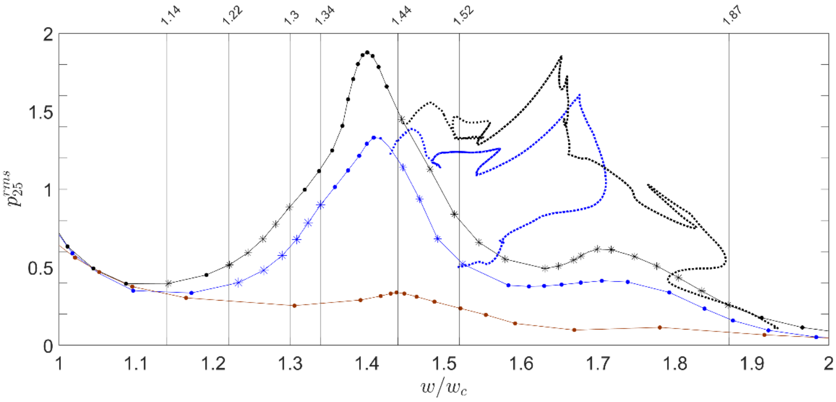

Figure 5-17 The RMS values of gear mesh displacement between LFG and P_5 for Set-2, the regions of unstable points between ω=1.0ω_c and ω=2.4ω_c; Case-4, (—) 3-harmonic HBM, (···) 1-harmonic HBM with ½ sub-harmonic; Case-5 (—) 3-harmonic HBM, (···) 1-harmonic HBM with ½ sub-harmonic; Case-6 (—) 3-harmonic HBM, (···) 1-harmonic HBM with ½ sub-harmonic, (·) stable solution, (*) unstable solution

Here, a numerical Floquet Theory [21,22] approach is used to substantiate the stability of the drive system through the obtained HBM solution. This approach easily depicts the regions where the sub-harmonic resonance occurs. Then, this phenomenon may be avoided with a proper orientation of the pinions. Figure 5-17 focuses on the response obtained for the Set-2 between ω=1.0ω_c and ω=2.0ω_c with only 3-harmonics. It demonstrates the regions on the frequency axis where the drive system has at least one positive eigenvalue, making it unstable. These regions are also consistent with the HBM solution obtained with ½ sub-harmonic. Case-4 and Case-5 have unstable points for the prescribed frequency range, whereas, for Case-6, these points become stable.

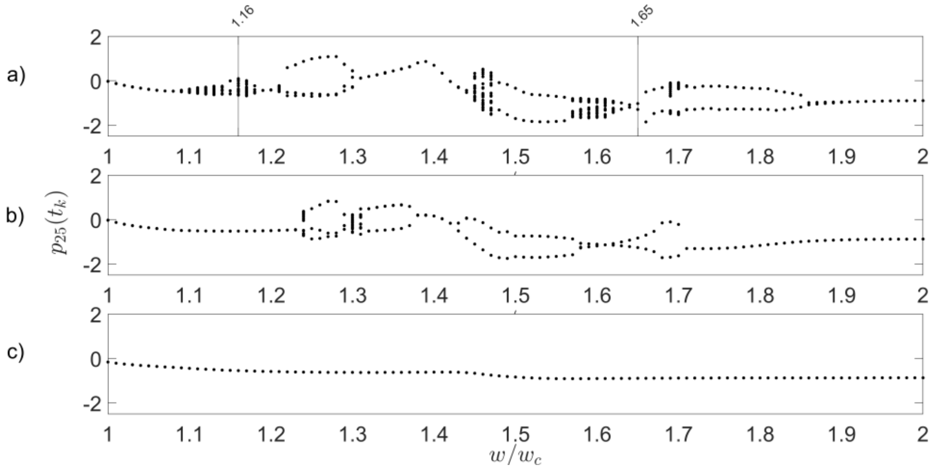

Figure 5-18 Bifurcation diagrams for the RMS values of gear mesh displacement between LFG and P_5 for Set-2, a) Case-4, b) Case-5, c) Case-6

In order to validate the results, the bifurcation diagrams for the specified drive systems in Set-2 are generated by cascading the Poincare sections taken from the time simulation data obtained for all excitation frequencies in the range ω=1.0ω_c and ω=2.0ω_c and shown in Figure 5-18. To concentrate on the pure steady state conditions, the time simulation between 125 to 250 cycles is considered in this investigation. As depicted in Figure 5-18, Case-4 and Case-5 have several regions of period-2, period-3, period-4 motion. The diagram also reveals quasiperiodic or chaotic regions for some frequency ranges, depicted with many points. However, Case-6 has only period-1 motion in the given frequency range. For Case-4, the diagram reveals many points for $\omega=1.16\ \omega_c$ and only two points for $\omega=1.65\omega_c$, as shown in Figure 5-12 and Figure 5-13.

In some cases, not using sub-harmonics in the HBM solution gives misleading results. On the other hand, utilizing sub-harmonics and super harmonics together in the HBM solution increases the computational time. The regions of sub-harmonic resonances, on the other hand, are located and defined by the Floquet Theory as unstable regions in the system response. Hence, even if ½ sub-harmonic is omitted to reduce the computational time, the HBM results with 3-harmonics coupled with the Floquet Theory may be utilized to locate and then avoid these sub-harmonic resonances in the system response.

5.2.2 Effect of Time-Variant Parameters

5.2.3 Effect of Power Values and Torque-Split Amounts

A split-torque system utilized in high-torque applications such as helicopter and marine transmission systems is given in Chapter 1. Transmitting the torque through several paths brings many advantages to the system. Several methods were mentioned in Chapter 1 for providing an even torque split between the split branches. One of the popular methods was the quill shaft method, which introduced additional torsional flexibility between the connected gears.

The developed model in this study is a split-torque system, as depicted in Figure 4-4. Power coming from two input pinions is divided into two paths, upper face-gear (UFG) and lower face-gear (LFG). The power directed to LFG is again re-collected at the UFG through the idler gears. The load transmitted by the idlers to the UFG is the portion of input torque transmitted from the input pinions to the LFG and then to the idlers.

Shaft compliance plays an essential role in the torsional dynamics of the drive systems. This chapter introduces torsional flexibility to the input pinions P_1 and P_3, which simulates a quill shaft.

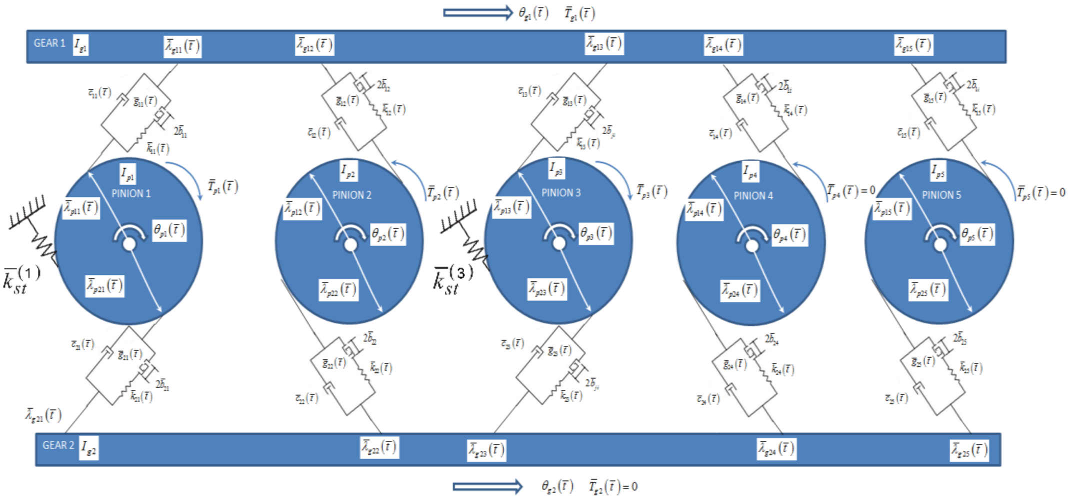
$\theta_{g1}(\bar{t})$ $\bar{T}_{g1}(\bar{t})$
GEAR 1 I_{g1}
$\bar{\lambda}_{g11}(\bar{t})$
$\bar{\lambda}_{g12}(\bar{t})$
$\bar{\lambda}_{g13}(\bar{t})$
$\bar{\lambda}_{g14}(\bar{t})$
$\bar{\lambda}_{g15}(\bar{t})$
PINION 1 I_{p1}
PINION 2 I_{p2}
PINION 3 I_{p3}
PINION 4 I_{p4}
PINION 5 I_{p5}
$\bar{T}_{p1}(\bar{t})$
$\bar{T}_{p2}(\bar{t})$
$\bar{T}_{p3}(\bar{t})$
$\bar{T}_{p4}(\bar{t})=0$
$\bar{T}_{p5}(\bar{t})=0$
$\theta_{p1}(\bar{t})$
$\theta_{p2}(\bar{t})$
$\theta_{p3}(\bar{t})$
$\theta_{p4}(\bar{t})$
$\theta_{p5}(\bar{t})$
$\bar{k}_{st}^{(1)}$
$\bar{k}_{st}^{(3)}$
GEAR 2 I_{g2}
$\bar{\lambda}_{g21}(\bar{t})$
$\bar{\lambda}_{g22}(\bar{t})$
$\bar{\lambda}_{g23}(\bar{t})$
$\bar{\lambda}_{g24}(\bar{t})$
$\bar{\lambda}_{g25}(\bar{t})$
$\theta_{g2}(\bar{t})$ $\bar{T}_{g2}(\bar{t})=0$

Figure 5-19 Modified dynamic model of the split-torque face-gear drive system

The equations of motion for the developed torsional dynamic model were given through Equations (4-1) and (4-2) in Chapter 4. Re-writing Equation (4-1) here for UFG and LFG in Figure 5-19 yields,

$$I_{gj}\ddot{\theta}_{gj}(\bar{t})+\sum_{i=1}^{5}\bar{\lambda}_{gji}(\bar{t})\left\{\bar{c}_{ji}(\bar{t})\dot{\bar{p}}_{ji}(\bar{t})+\bar{k}_{ji}(\bar{t})\bar{g}\left(\bar{p}_{ji}(\bar{t})\right)\right\}=\bar{T}_{gj}(\bar{t}), \tag{5-3}$$

where $j=1..2$.

By introducing the quill shafts as torsional springs at the input pinions and modifying the Equation (4-2) only for the input pinions yields,

$$I_{pi}\ddot{\theta}_{pi}\left(\bar{t}\right)+\sum_{j=1}^{2}\bar{\lambda}_{pji}\left(\bar{t}\right)\left\{\bar{c}_{ji}\left(\bar{t}\right)\dot{\bar{p}}_{ji}\left(\bar{t}\right)+\bar{k}_{ji}\left(\bar{t}\right)\bar{g}\left(\bar{p}_{ji}\left(\bar{t}\right)\right)\right\}+\bar{k}_{st}{}^{i}\theta_{pi}\left(\bar{t}\right)=\bar{T}_{pi}\left(\bar{t}\right), \quad (5\text{-}4)$$

where $i=1,3$.

Finally, re-writing the Equation (4.2) here for the idler pinions gives

$$I_{pi}\ddot{\theta}_{pi}\left(\bar{t}\right)+\sum_{j=1}^{2}\bar{\lambda}_{pji}\left(\bar{t}\right)\left\{\bar{c}_{ji}\left(\bar{t}\right)\dot{\bar{p}}_{ji}\left(\bar{t}\right)+\bar{k}_{ji}\left(\bar{t}\right)\bar{g}\left(\bar{p}_{ji}\left(\bar{t}\right)\right)\right\}=\bar{T}_{pi}\left(\bar{t}\right), \quad (5\text{-}5)$$

where $i=2,4,5$.

At any time instant, the fraction of the torque transmitted to the UFG through the ith pinion's mesh is defined as,

$$UTS^{i}=\frac{W_{tpu}{}^{i}}{W_{tpu}{}^{i}+W_{tpl}{}^{i}}, \quad (5\text{-}6)$$

where UTS^{i} is the Upper Torque Split, LTS^{i} is Lower Torque Split, $W_{tpu}{}^{i}$ is tangential load transmitted at ith pinion to UFG, $W_{tpl}{}^{i}$ is the tangential load transmitted at ith pinion to LFG, at any time instant, as depicted in Figure 5-20.

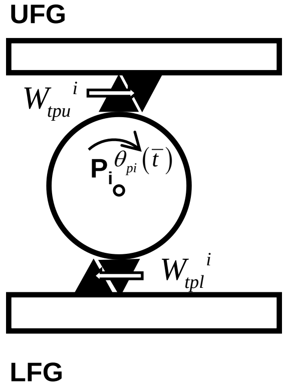

Figure 5-20 W_{tpu}^{i} and W_{tpl}^{i} at the ith pinion

The fraction of torque transmitted to the LFG through the ith pinion's mesh is defined with the following formula,

$$LTS^{i} = 1 - UTS^{i} \tag{5-7}$$

The system specified as Case-1 in Chapter 1.2.1 is solved for calculating torque-split ratios. When the flotation is not permitted, the pinion's torque split ratios become as depicted in Figure 5-21.

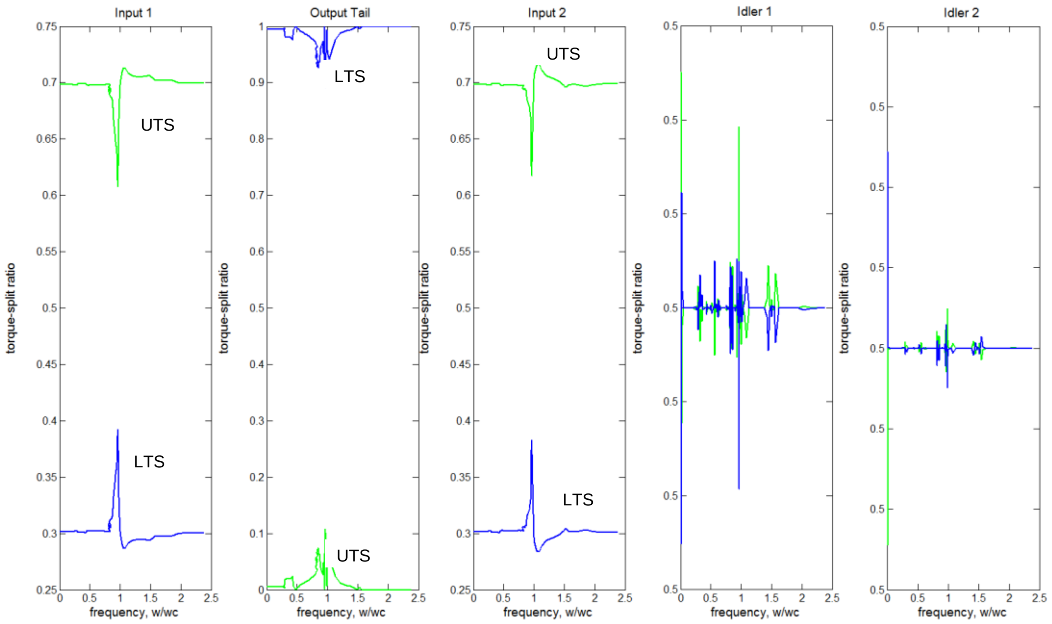

Figure 5-21 Torque split ratios for the pinions in the face-gear drive system

Away from the resonant frequency, 70 percent of the input torque is directly transmitted to UFG, and around 30 percent of the input torque is transmitted to LFG through the input pinions P_1 and P_3.

Around the resonant frequency, the torque sharing approaches 60 percent through UFG and 40 percent through LFG.

The output pinion P_2 collects most of its torque from the LFG around the resonant frequency. This ratio becomes at most 89 percent through LFG and 11 percent through UFG.

On the other hand, idler pinions P_4 and P_5 transmit all the power from LFG to UFG. Hence, a torque-split ratio of 50 percent is achieved.

In order to simulate the floating pinion case, the support stiffness values for the input pinions are altered with the scale factors SF=1.0, SF=0.5, SF=0.1, SF=0.05, and SF=0.01 with respect to the mesh stiffness value, where the mesh stiffness value is assumed to be 1.0.

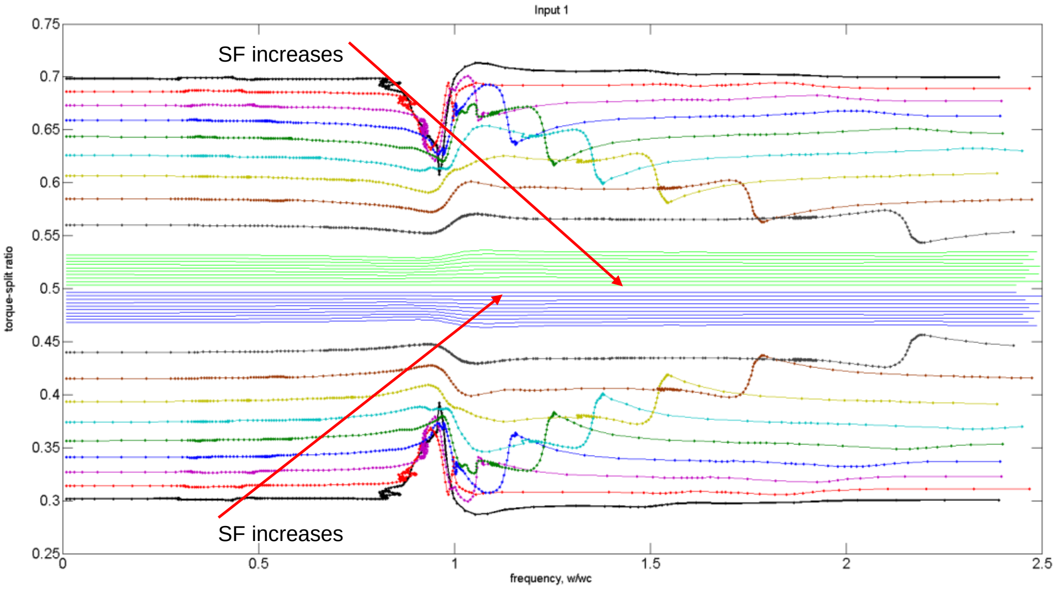

Figure 5-22 Torque split ratios for the input pinion P_1

Figure 5-22 and Figure 5-23 show the torque split ratios of the input pinions P_1 and P_3, respectively. The split ratios are plotted for several SF values. By the reduction in SF, the floating action of the input pinions is allowed. As SF is reduced, an even torque split is achieved. The torque split ratios UTS and LTS for each input pinion approach to *0.5*, which denotes the even torque split. In Figure 5-22 and Figure 5-23, when SF=0.01, UTS and LTS values become 0.503 and 0.496, respectively, where the torque split ratios differ less than 1%.

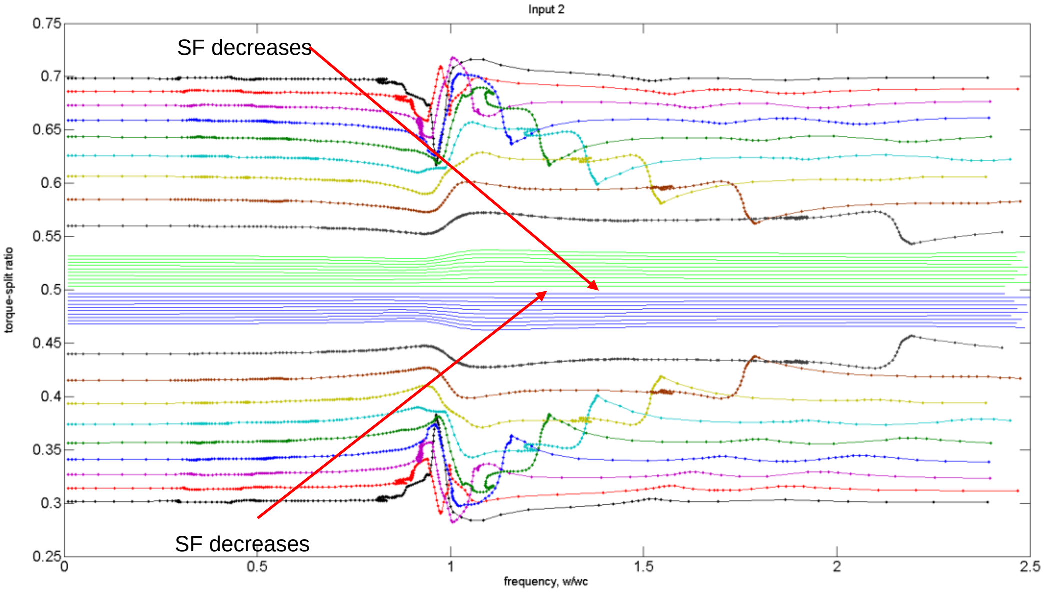

Figure 5-23 Torque split ratios for the input pinion P_3

Figure 5-24 shows the torque split ratios for the output pinion P_2. For this pinion, LTS is calculated to be 0.8 while LTS is calculated to be 0.2 for SF=0.01. Even torque split for this pinion is not intended since P_2 is connected to a low torque consuming drive train such as a helicopter tail gearbox. Compared with the input pinions, the torque level is lower than P_1 and P_3. Therefore, the strength of the output gear is not critical to have 80 percent of the load from LFG and 20 percent from UFG. In this study, all five pinions' macro geometry is assumed to be identical. However, the face-width of the output pinion P_2 may be reduced to achieve an appropriate torsional stiffness for an even torque split ratio at the UFG and LFG.

Finally, the idlers take power from LFG and transmit it to UFG. Therefore, the torque-split ratio remains 0.5 throughout all investigated frequencies for both UTS and LTS. Figure 5-25 shows the UTS and LTS values for the idler pinions P_4 and P_5.

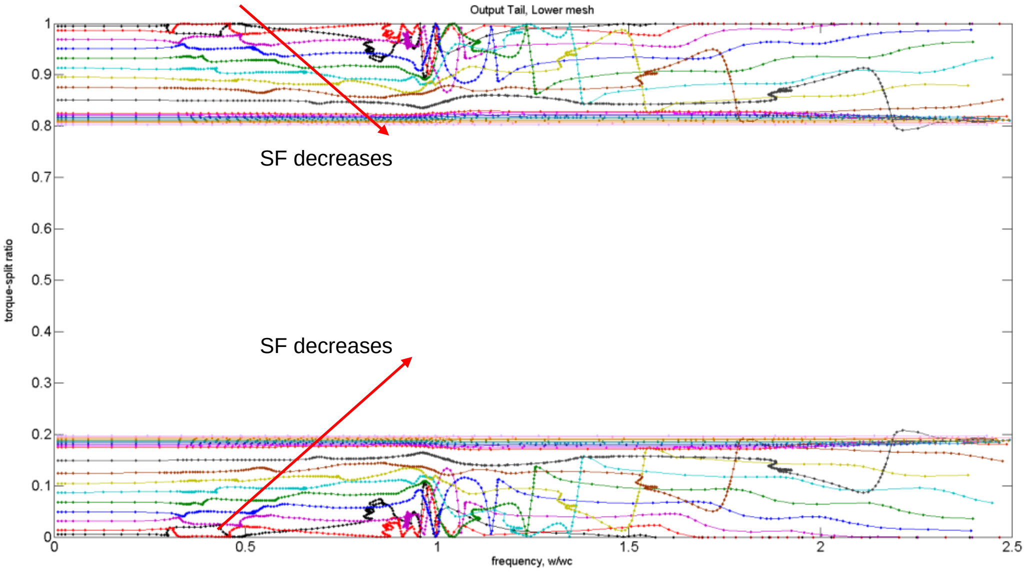

Figure 5-24 Torque split ratio for the output pinion P_2

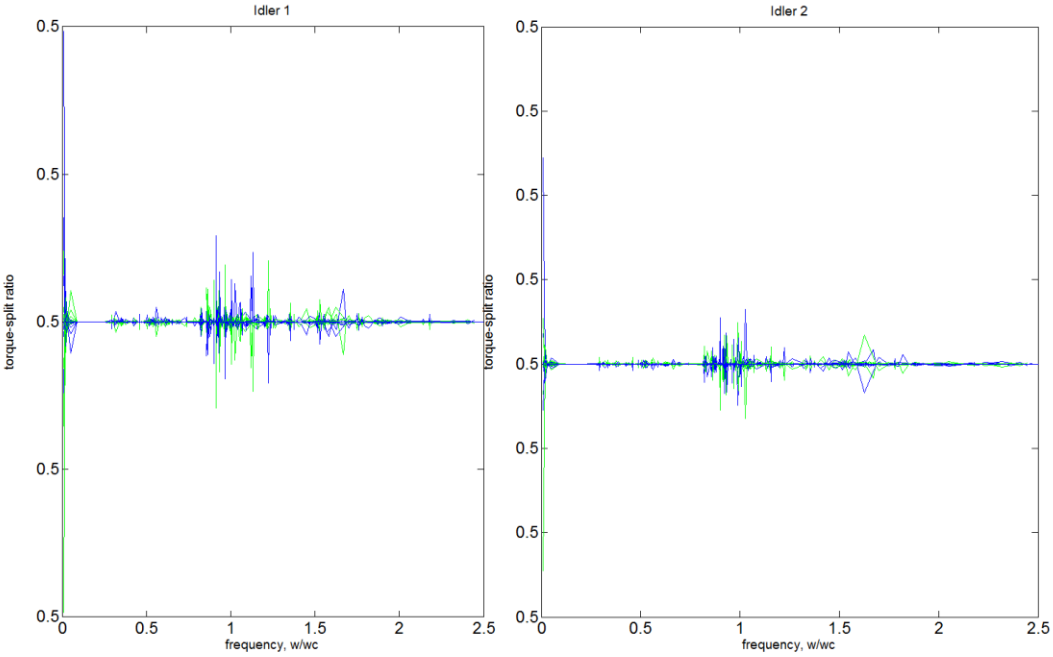

Figure 5-25 Torque split ratios for the idler pinion P_4 and P_5

Figure 5-26 shows the achieved torque split ratios before and after introducing an additional torque stiffness for simulating the quill shaft connected to the input pinions P_1 and P_3.

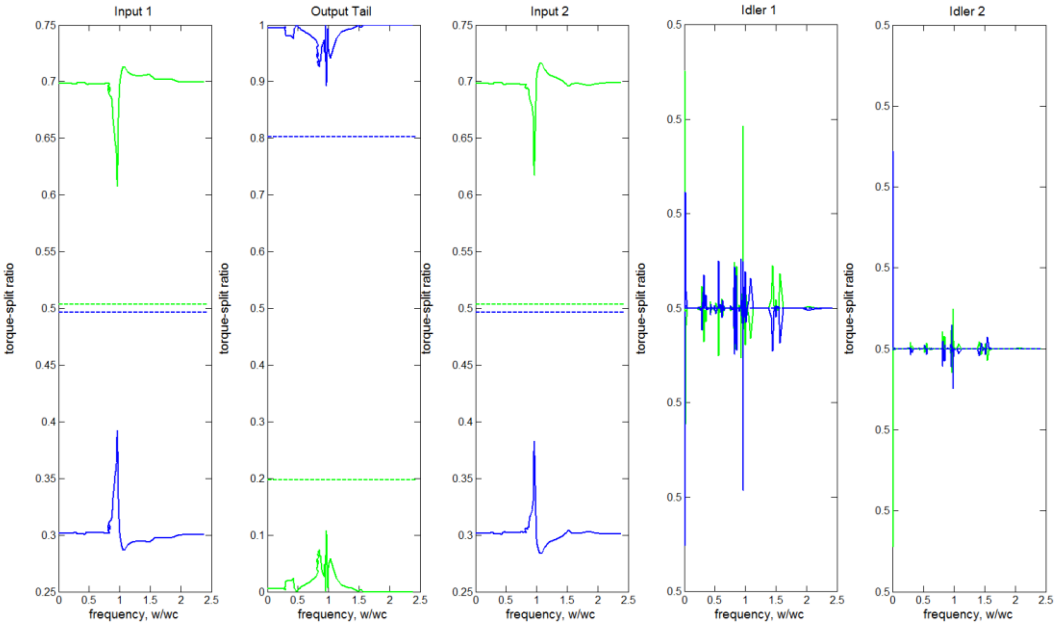

Figure 5-26 Achieved torque split ratios for the specified system

.

CHAPTER 6

CONCLUSION AND FUTURE WORK

6.1 Summary & Conclusion

In this thesis it is aimed to develop a torsional non-linear dynamic model for a multi-mesh involute spur pinion-driven face-gear split-torque drive system which utilizes the exact face-gear tooth geometries employing the theory of gearing and differential geometry. For this purpose, a lumped mass system consisting of five pinions and two face gears was constructed. The system has seven rotational degrees of freedom. All pinion and gear blanks are assumed to be rigid disks. The constructed split-torque model includes two inputs, two outputs, and three idler gears. The model includes clearance-type nonlinearity for backlash. The non-linear time-variant equations of motions are solved with HBM coupled with the Arc-Length Continuation Method to obtain the system's periodic steady-state response. HBM results are compared with direct numerical integration solutions to validate the accuracy.

The developed model may be considered as a second-stage reduction to the main transmission system and then may be connected to a planetary gear set at the third stage for the final reduction. Before that, there may be two nose gear-boxes as the first stages. According to engine speed, the face-gear system can also be used as the Main Gear Box (MGB) of a helicopter with or without planetary.

In order to reduce the computational time during the parametric studies, the HBM with Arc-Length Continuation Method is utilized with 3-harmonics and ½ sub-harmonic. The comparison of the frequency domain solution obtained with the direct numerical integration results shows that, except for some frequency ranges where several sub-harmonic resonances are excited simultaneously, the method gives exact results. Numerical Floquet Theory is applied to validate the system's stability obtained by three harmonics HBM solutions. Bifurcation diagrams for the specified frequency ranges are generated by cascaded Poincare Sections established from time domain simulations.

Macro geometry of the face-gear surface is generated by transforming the tooth profile of a spur gear shaper into the face-gear tooth profile by simulating the machine tool motions. Mesh stiffness is calculated via the finite strip method. Unloaded tooth contact analysis is performed without any profile or face-width modifications on the tooth surface. The generated tool is also capable of calculating the transmission error with these modifications.

Several methods have been investigated for the mesh stiffness calculations, namely, Thin Slice Method (1-D), Rayleigh-Ritz Method (1.5D), Finite Strip Method (1.5D), Finite Prism Method (2.5D), and Quasi-Prism Method (2.5D). The results are compared with the ones obtained from MSC Patran-Nastran and Abaqus models. The Finite Strip Method (FSM) is selected to calculate the mesh stiffness due to its feasible adaptation for parametric studies. Mindlin Plate Theory is used for the tooth model. As mentioned above, the tooth is discretized using Finite Strip Method, and since FSM utilizes simple polynomials along the face-width direction and adjusted B3 spline curves (according to cantilevered boundary condition) along the tooth profile, the discretization is performed as if the tooth is a 1D element. Hence, the element formulation, the connectivity of the elements, and the solving process become simpler than a 2D or 3D finite elements. The NURBS curves fit the surfaces of both the face-gear and the spur gear. This surface fit approximation generates a variable thickness finite strip element. Generally, constant thickness finite strip element is utilized for discretization. In order to achieve an acceptable level of accuracy, the element number has to be increased. However, even with a small number of elements, accurate results are obtained with a variable thickness element.

A dynamic model for a face-gear and spur-gear pair is developed, and some parametric studies are performed. The effect of backlash, the static torque, and the damping on the gear mesh displacement are investigated. The hardening and softening stiffness effects are demonstrated for several backlash and torque levels. It is observed that the hardening stiffness effect disappears at a specific backlash value, and only softening stiffness effect remains. This phenomenon happens because the resulting amplitude of the dynamic response becomes insufficient to cover the resulting deflection due to the applied static torque and the imposed backlash clearance. This phenomenon also dictates that the system characteristics cannot be altered by increasing the backlash beyond some specific value. The effect of damping on the dynamic response is also sought. For some specific damping ratios, subharmonic resonance peaks and closed curves (islands) are observed for a frequency range. As the damping ratio increases, these closed curves become smaller and smaller and then vanish. The same phenomenon is also observed for some static torque values. As the static torque is increased, these closed curves of subharmonic response become smaller and finally vanish.

A dynamic model for a multi-mesh split-torque face-gear drive system is constructed, and some parametric studies are performed to search the effect of orientation angle pattern (mesh phasing among pinions) and power values (or static torque values).

The effects of mesh phasing on the system response are studied with the established fully coupled comprehensive mathematical models of face-gear tooth geometry, mesh stiffness, and non-linear dynamics. In this investigation, the mesh phasing defines the position of one tooth pair relative to the other pairs in contact in a mesh cycle. It is observed that, by altering the pinion positions, the drive system's response characteristics are significantly changed. For instance, when the input pinions are positioned at 180° angles to each other, the subharmonic resonance peaks around $\omega=1.4\omega_c$ and $\omega=1.72\omega_c$ vanish. Around the fundamental harmonic, the gear mesh displacement increases as expected. In cases where the idler pinions are positioned at 60° angles, the response levels decrease around the fundamental harmonic, compared to the cases where they are positioned at 90° angles. Thus, it is evident that achieving proper phase differences between the meshing teeth by altering pinion positions is a critical design parameter in the preliminary design phase of the split-torque face-gear drive systems from dynamics perspective. The presented non-linear dynamic model enables to carry out various parametric studies while capturing the mesh stiffness from the face-gear tooth geometry.

Achieving an even torque-split ratio between the upper and the lower face gears through the input pinions is investigated. For this purpose, the floating pinion case is implemented as a shaft torsional spring, and then several cases for different support stiffness values have been studied. As expected, the floating pinion achieves the even torque split case for the input pinions. On the other hand, uneven torque split may also be an intended design feature, according to system demands.

There is an AGMA standard for epicyclic (planetary) gear trains. The main design topics are well established and well defined in this standard. Thus, a designer utilizes and chooses the critical design parameters from various parameters, i.e., tooth geometry, sufficient backlash and pressure angle requirement, meshing requirements, arrangements of the sun, ring, and planet gears, and load sharing ratio among the gears. Currently, there is no standard (AGMA, ISO, DIN) for the face-gear or split-torque face-gear drive systems. Hence, some of the critical design parameters, i.e., position of idler gears, position of input gears, shaft compliance, are investigated to be utilized in the system's preliminary and detailed design phases. The potential design parameters (such as pressure angle, shaft angle, number of teeth etc.) may also be utilized for the same purpose.

In summary, this thesis proposes a physics and theory of gearing based evaluation method of face-gear drives without relying on any commercial FEA software packages by establishing accurate tooth and mesh stiffness calculations utilized in non-linear dynamics of single-pair mesh and split-torque configurations.

6.2 Future Work

The torsional dynamic model can be extended to include the coupling between axial and the radial degrees of freedom of the face-gear and pinion with the shaft and bearing. Furthermore, the face-gear and the spur pinion webs can be modelled as deformable bodies with Kirchoff or Mindlin Plate Theory. Their contribution can also be added to the gear tooth deflection as a foundation effect.

A more detailed STE function is recommended to be developed from the related gear macro and micro geometries. A new DTE function should be modeled and investigated based on the proposed STE.

The mesh damping in the model can be improved to include the frictional, bearing, and churning losses. The structural and viscous characteristics can be investigated by proper tests, and then the results can be implemented in the model developed in this thesis.

Finally, the validation of the developed models with tests can be conducted starting from linear and non-linear dynamic cases. The preparation of the test benches in the laboratory environment is very critical. Hence, they should be dynamically well isolated from the test specimen. Three vital points in the establishment of a proper test stand should be paid attention to; i) the design and production of the test bench; ii) the design and production of the test specimen by which the predicted non-linear effects are to be observed, and finally; iii) the test execution. The test specimen should be accurate enough to avoid all disturbances affecting the test data to be compared with the analytical model.

REFERENCES

[1] Bill, R., C., 1990, Advanced Rotorcraft Transmission Program, NASA Technical Memorandum No: 103276.

[2] Kish, G., K., 1993, Sikorsky Aircraft Advanced Rotorcraft Transmission (ART) Program, Final Report.

[3] Ames, E. C., and Henry, Z. S., 2000, “Advanced Rotorcraft Transmission II – Demonstrator Design,” American Helicopter Society 56th Annual Forum, Virginia Beach, Virginia.

[4] Litvin, F. L., Wang, J.-C., Bossler, R. B., Chen, Y.-J., Heath, G., and Lewicki, D. G., 1994, “Application of Face-Gear Drives in Helicopter Transmissions,” Journal of Mechanical Design, Transactions of the ASME, 116(September 1994), pp. 672–676.

[5] Heath, G. F., Filler, R. R., and Tan, J., 2002, Development of Face Gear Technology for Industrial and Aerospace Power Transmission.

[6] Grendel H.F., 1996, “Cylkro Gears: An Alternative in Mechanical Power Transmission, Gear Technology – The Journal of Gear Manufacturing,” Gear Technology – The Journal of Gear Manufacturing, 13(3), pp. 26–31.

[7] Basstein, G., 2000, “Calculation, Manufacturing and Applications of Cylkro Angular Face Gear Transmissions,” Troy (Detroit).

[8] Litvin, F. L., Fuentes, A., Zanzi, C., and Pontiggia, M., 2002, “Design, Generation, and Stress Analysis of Two Versions of Geometry of Face-Gear Drives,” Mechanism and Machine Theory, 37(10), pp. 1179–1211.

[9] Stadtfeld H., 2010, “Coniface Face Gear Cutting and Grinding,” Gear Technology– The Journal of Gear Manufacturing.

[10] He S., Gmirya Y., Mowka F., Meyer B.W., A. E. C., “Trade Study on Different Gear Reduction Ratios of the 5100 HP RDS-21 Demonstrator Gear Box,” AHS 62nd Annual Forum, Phoenix, AZ.

[11] Ron Gilbert R., Craig G., Filler R., Hamilton W., Hawkins J., Higman J., G. W., “3400 HP Apache Block III Improved Drive System,” AHS 64th Annual Forum, Montreal, Canada.

[12] Litvin F.L. , Wang J.-C., Bossler R.B. Jr., Chen Y.-J.D., Heath G., Lewicki D.G., 1992, “Face-Gear Drives: Design, Analysis, and Testing for Helicopter Transmission Applications,” AGMA 1992 Fall Technical Meeting, Baltimore, Maryland,.

[13] Litvin, F L, F. A., 2004, Gear Geometry and Applied Theory, Cambridge University Press.

[14] Litvin, F. L. , Zhang, Y., and Wang, J. C., Bossler, R.B., Chen, Y. J. D., 1992, “Design and Geometry of Face-Gear Drives,” Journal of Mechanical Design, 114(4), pp. 642–647.

[15] Litvin, F.L., Egelja, A., Tan, J., Chen, D.Y.D, Heath, G., 2000, “Handbook on Face Gear Drives With a Spur Involute Pinion”, NASA/CR-2000-209909.

[16] Litvin, F. L., Fuentes, A., Zanzi, C., Pontiggia, M., and Handschuh, R. F., 2002, “Face-Gear Drive with Spur Involute Pinion : Geometry , Generation by a Worm , Stress Analysis”, Comput. Methods Appl. Mech. Engrg., 191, pp. 2785–2813.

[17] Handschuh, R. F., Lewicki, D. G., Heath, G. F., and Bossler, R. B., 1996, “Experimental Evaluation of Face Gears for Aerospace Drive System Applications,” American Society of Mechanical Engineers, Design Engineering Division (Publication) DE, 88, pp. 581–588.

[18] Heath, G. F., Slaughter, S. C., Morris, M. T., Fetty, J., Lewicki, D. G., and Fisher, D. J., 2009, “Face Gear Development under the Rotorcraft Drive

System for the 21 St Century Program," American Helicopter Society 65th Annual Forum, Grapevine, Texas.

[19] Guingand, M., de Vaujany, J.-P., and Jacquin, C.-Y., 2005, "Quasi-Static Analysis of a Face Gear under Torque," Computer Methods in Applied Mechanics and Engineering, 194(39–41), pp. 4301–4318.

[20] Wang, Y.-Z., Wu, C.-H., Gong, K., Wang, S., Zhao, X.-F., and Lv, Q.-J., 2012, "Loaded Tooth Contact Analysis of Orthogonal Face-Gear Drives," Proceedings of the Institution of Mechanical Engineers, Part C: Journal of Mechanical Engineering Science, 226(9), pp. 2309–2319.

[21] Peng, M., DeSmidt, H., Saribay, Z. B., and Smith, E. C., 2011, "Parametric Instability of Face-Gear Drives with a Spur Pinion," Annual Forum Proceedings - AHS International, 4, pp. 2478–2488.

[22] Peng, M., DeSmidt, H. A., and Zhao, J., 2015, "Parametric Instability of Face-Gear Drives Meshing with Multiple Spur Pinions," Journal of Mechanical Design, Transactions of the ASME, 137(12), pp. 1–9.

[23] Hu, Z., Tang, J., Chen, S., and Lei, D., 2013, "Effect of Mesh Stiffness on the Dynamic Response of Face Gear Transmission System," Journal of Mechanical Design, 135(July), pp. 1–7.

[24] Chen, S., Tang, J., Chen, W., Hu, Z., and Cao, M., 2014, "Nonlinear Dynamic Characteristic of a Face Gear Drive with Effect of Modification," Meccanica, 49(5), pp. 1023–1037.

[25] Jinyuan, T., Hu, Z., Chen, S., and Lei, D., 2013, "Effects of Directional Rotation Radius and Transmission Error on the Dynamic Characteristics of Face Gear Transmission System," Proceedings of the Institution of Mechanical Engineers, Part C: Journal of Mechanical Engineering Science, 228(7), pp. 1108–1118.

[26] Hu, Z., Tang, J., Chen, S., and Sheng, Z., 2015, “Coupled Translation-Rotation Vibration and Dynamic Analysis of Face Geared Rotor System,” Journal of Sound and Vibration, 351(January 2018), pp. 282–298.

[27] Aydoğan, M., Ö., Sarıbay, Z., B., Özgüven, H., N., 2017, “Dynamic Modelling of Split-Torque Face-Gear Drive Systems,” IDETC2017, Cleveland, Ohio, USA.

[28] Zhao, N., Li, W., Hu, T., Guo, H., Zhou, R., and Peng, Y., 2018, “Quasistatic Load Sharing Behaviours of Concentric Torque-Split Face Gear Transmission with Flexible Face Gear,” Mathematical Problems in Engineering, 2018.

[29] Feng, G., Xie, Z., and Zhou, M., 2019, “Geometric Design and Analysis of Face-Gear Drive with Involute Helical Pinion,” Mechanism and Machine Theory, 134, pp. 169–196.

[30] Ambarisha, V. K., and Parker, R. G., 2007, “Nonlinear Dynamics of Planetary Gears Using Analytical and Finite Element Models,” Journal of Sound and Vibration, 302(3), pp. 577–595.

[31] Liu, L., and Zhang, J., 2019, “Meshing Characteristics of a Sphere–Face Gear Pair with Variable Shaft Angle,” Advances in Mechanical Engineering, 11(6), pp. 1–10.

[32] Dong, J., Tang, J., and Hu, Z., 2019, “Investigation of Assembly, Power Direction and Load Sharing in Concentric Face Gear Split-Torque Transmission System,” Meccanica, 54(15), pp. 2485–2506.

[33] Dong, J., Tang, J., Hu, Z., and Wang, Y., 2020, “A Semi-Analytical Method of Time-Varying Mesh Stiffness in Concentric Face Gear Split-Torque Transmission System,” Journal of Mechanical Science and Technology, 34(2), pp. 589–602.

[34] Li, W., and Zhao, N., 2020, "Nonlinear Dynamic Characteristics of Face Gear Pair for Helicopter," Vibroengineering Procedia, 30, pp. 140–145.

[35] Segade-Robleda, A., Vilan-Vilan, J. A., Lopez-Lago, M., and Casarejos-Ruiz, E., 2012, "Split Torque Gearboxes: Requirements, Performance and Applications," Mechanical Engineering, pp. 56–74.

[36] GMIRYA, Y., 2006, "MULTI-FLOW REDUCER FOR ROTORCRAFT," Russia, RU-2402710.

[37] GMIRYA, Y., 2013, "MULTI-PATH ROTARY WING AIRCRAFT GEARBOX," Germany, EP-2005-03.

[38] Krantz, T. L., Rashidi, M., and Kish, J. G., 1994, "Split Torque Transmission Load Sharing," Proceedings of the Institution of Mechanical Engineers, Part G: Journal of Aerospace Engineering, 208(2), pp. 137–148.

[39] White, G., 1998, "Design Study of a Split-Torque Helicopter Transmission," Proceedings of the Institution of Mechanical Engineers, Part G: Journal of Aerospace Engineering, 212(2), pp. 117–123.

[40] Gmirya, Y., He, S., and Buzel, G., 2009, "LOAD SHARING TEST OF THE CH-53K SPLIT-TORQUE MAIN GEARBOX," American Helicopter Society, 65th Annual Forum(Grapevine, Texas), p. 10.

[41] Palcic, P. X., He, S., Gmirya, Y., and Leigh, L., 2017, "THE ROAD TO FIRST FLIGHT: DEVELOPMENT OF THE CH-53K DRIVE SYSTEM," (September).

[42] Krantz, T. L., 1996, "A Method to Analyze and Optimize the Load Sharing of Split-Path Transmissions," American Society of Mechanical Engineers, Design Engineering Division (Publication) DE, 88, pp. 227–237.

[43] Krantz, T. L., 1994, "Dynamics of a Split Torque Helicopter Transmission," NASA TM-106410, (NASA Lewis Research Center).

[44] Krantz, L., Delgado, R., Diego, S., and Army, U. S., 1996, “Experimental Transmission Study of Split-Path Load Sharing,” NASA TM-107202, (NASA Lewis Research Center).

[45] Lewicki, David G, Robert R . Filler, G. F. . H. and S. C. . S., 2002, “Torque Splitting by a Concentric Face Gear Transmission,” American Helicopter Society 58th Annual Forum, Montreal, Canada.

[46] Heath, G. F., Filler, R. R., and Tan, J., 2002, “Development of Face Gear Technology for Industrial and Aerospace Power Transmission,” NASA-CR-22002-211320, (Glenn Research Center).

[47] Chun, H., Filler, R., and Tan, J., 2006, “Analytical Determination of Load Distribution in a Statically Indeterminate Face Gear Transmission,” AHS 62nd Annual Forum, Phoenix, AZ.

[48] Hansen, B. D., 2009, “RDS-21 Demonstrator Gearbox Testing,” American Helicopter Society 65th Annual Forum, Grapevine, Texas.

[49] He, S., Gmirya, Y., Mowka, F., Meyer, B. W., and Ames, E. C., 2006, “Trade Study on Different Gear Reduction Ratios of the 5100 HP RDS-21 Demonstrator Gearbox,” American Helicopter Society 62nd Annual Forum, Phoenix, AZ.

[50] Roberto, P., and Sergio, T., 1998, “Face-Gear Transmission Assembly with Floating Pinions,” Italy, EP-0971155.

[51] Litvin, F. L., Wang, J.-C., Bossler, R. B., Chen, Y.-J. D., and Heath, G., 1991, “Application of Face-Gear Drives in Helicopter Transmissions,” NASA Technical Memorandum 105655.

[52] Litvin, F. L., Gonzalez-perez, I., Fuentes, A., Vecchiato, D., Hansen, B. D., and Binney, D., 2005, “Design, Generation and Stress Analysis of Face-Gear Drive with Helical Pinion,” 194, pp. 3870–3901.

[53] Litvin, F. L., Nava, A., Fan, Q., Fuentes, A., 2002, "New Geometry of Worm Face Gear Drives With Conical and Cylindrical Simulation of Meshing , Worms : Generation , and Stress Analysis", NASA/CR-2202-211895, ARL-CR-0511.

[54] Litvin, F. L., 2002, "Face-Gear Drive with Spur Involute Pinion: Geometry, Generation by a Worm, Stress Analysis", NASA/CR-2002-211362, ARL-CR-491.

[55] Litvin, F. L., Gonzalez-Perez, I., Fuentes, A., Vecchiato, D., Hansen, B. D., and Binney, D., 2005, "Design, Generation and Stress Analysis of Face-Gear Drive with Helical Pinion," Computer Methods in Applied Mechanics and Engineering, 194(36–38), pp. 3870–3901.

[56] Saribay, Z. B., 2009, "Analytical Investigation of the Pericyclic Variable-Speed Transmission System for Helicopter Main-Gearbox," The Pennsylvania State University.

[57] Buckingham, E., 1963, Analytical Mechanics of Gears, Dover Publications, Mineola, New York.

[58] Dudley D. W., 1984, "Handbook of Practical Gear Design, McGraw-Hill Inc, New York.

[59] "Extracted from AGMA 203.03, Fine-Pitch on-Center Face Gears for 20-Degree Involute Spur Pinions, with the Permission of the Publisher, the American Gear Manufacturers Association, 1500 King Street, Suite 201, Alexandria, Virginia 22314."

[60] Guingand M., Remond D., Vaujany J.P., 2008, "Face Gear Width Prediction Using the DOE Method," Journal of Mechanical Design, 130.

[61] Drago R.J., 1988, Fundamentals of Gear Design, Butterwoths, Stoneham, MA.

[62] Zimmer, H., W., 1968, Verzahnungen 1 Stirnrader Mit Geraden Und Schragen Zahnen, Springer-Verlag.

[63] Dooner, D., B., 2012, Kinematic Geometry of Gearing, John Wiley & Sons.

[64] Guingand M., de Vaujany J.P., Icard Y., 2005, "Analysis of Optimization of the Loaded Meshing of Face Gears," Journal of Mechanical Design - Transactions of the ASME, 127(4), pp. 135–143.

[65] Litvin, F. L., Zhang, Y., Wang, J.-C., Bossler, R. B., and Chen, Y.-J. D., 1992, "Design and Geometry of Face-Gear Drives," Journal of Mechanical Design, 114(4), pp. 642–647.

[66] Guingand, M., de Vaujany, J.-P., and Jacquin, C.-Y., 2005, "Quasi-Static Analysis of a Face Gear under Torque," Computer Methods in Applied Mechanics and Engineering, 194(39–41), pp. 4301–4318.

[67] Litvin, F. L., Fuentes, a, Demenego, a, Vecchiato, D., and Fan, Q., 2001, "New Developments in the Design and Generation of Gear Drives," Proceedings of the Institution of Mechanical Engineers, Part C: Journal of Mechanical Engineering Science, 215(7), pp. 747–757.

[68] Litvin, F. L., Fuentes, A., and Howkins, M., 2001, "Design , Generation and TCA of New Type of Asymmetric Face-Gear Drive with Modified Geometry," 190.

[69] Zanzi, C., and Pedrero, J. I., 2005, "Application of Modified Geometry of Face Gear Drive," Computer Methods in Applied Mechanics and Engineering, 194(27–29), pp. 3047–3066.

[70] Litvin, F. L., Fuentes, A., Fan, Q., and Handschuh, R. F., 2002, "Computerized Design, Simulation of Meshing, and Contact and Stress Analysis of Face-Milled Formate Generated Spiral Bevel Gears," Mechanism and Machine Theory, 37(5), pp. 441–459.

[71] Hughes, T. J. R., Cottrell, J. a., and Bazilevs, Y., 2005, "Isogeometric Analysis: CAD, Finite Elements, NURBS, Exact Geometry and Mesh Refinement,"

Computer Methods in Applied Mechanics and Engineering, 194(39–41), pp. 4135–4195.

[72] Cheng, Q., Yang, G., and Lu, J., 2013, “An Analysis of Gear Based on Isogeometric Analysis,” (1), pp. 17–22.

[73] Wellauer, E. J., and Seireg, A., 1960, “Bending Strength of Gear Teeth by Cantilever-Plate Theory,” Journal of Manufacturing Science and Engineering, Transactions of the ASME, 82(3), pp. 213–220.

[74] Peng, M., 2012, “Parametric Instability Investigation and Stability Based Design for Transmission Systems Containing Face-Gear Drives,” The Pennsylvania State University.

[75] Cornell, R. W., and Westervelt, W. W., 1977, “Dynamic Tooth Loads and Stressing for High Contact Ratio Spur Gears.,” American Society of Mechanical Engineers (Paper), 100(77-DET-101).

[76] Cornell, R. W., 2010, “Compliance and Stress Sensitivity of Spur Gear Teeth,” Journal of Mechanical Design, 103(2), p. 447.

[77] Pintz, A., Kasuba, R., 1983, “Dynamic Effects of Internal Spur Gear Drives”, NASA Contractor Report 3692.

[78] Lin, H.H., Liou, C. H., 1998, “‘Parametric Study of Spur Gear Dynamics’, NASA/CR-1998-20659,” (January).

[79] Yoon, K. Y., and Rao, S. S., 1996, “Dynamic Load Analysis of Spur Gears Using a Nevi/Tooth Profile,” Journal of Mechanical Design, Transactions of the ASME, 118(1), pp. 1–6.

[80] Harianto, J., and Houser, D. R., 2007, “Detc2007-34655 Topographies for Noise and Stress Minimization Over a Broad,” Mechanical Engineering, pp. 1–15.

[81] Lin, H.H., Huston, R. L., 1986, "'Dynamic Loading on Parallel Shaft Gears', NASA Report No: 179473," Contractor, (July 1986), p. 79.

[82] Stegemiller, M. E., and Houser, D. R., 1993, "A Three-Dimensional Analysis of the Base Flexibility of Gear Teeth," Journal of Mechanical Design, Transactions of the ASME, 115, pp. 186–192.

[83] O'Donnell, W. J., 1963, "Stresses and Deflections in Built-in Beams," Journal of Manufacturing Science and Engineering, Transactions of the ASME, 85(3), pp. 265–272.

[84] Matusz, J. M., O'donnell, W. J., and Erdlac, R. J., 1969, "Local Flexibility Coefficients for the Built-in Ends of Beams and Plates," Journal of Manufacturing Science and Engineering, Transactions of the ASME, 91(3), pp. 607–612.

[85] Weber, C., 1949, "The Deformations of Loaded Gears and the Effect on Their Load-Carrying Capacity", British Dept. of Scientific and Industrial Research, Report No. 3.

[86] Harianto, J. and Houser, D., R., 2007, "A Methodology for Obtaining Optimum Gear Tooth Micro-Topographies for Noise and Stress Minimization over a Broad Operating Torque Range," Proceedings of the ASME 2007 International Design Engineering Technical Conferences & Computers and Information in Engineering Conference IDETC/CIE 2007.

[87] Yoon, K. Y., Rao, S. S., 1996, "Dynamic Load Analysis of Spur Gears Using a New Tooth Profile," ASME Journal of Mechanical Design, 118(1).

[88] 2002, "Load Distribution Program Manual."

[89] Yakubek, David, 1984, "Plate Bending and Finite Element Analysis of Spur and Helical Gear Tooth Deflections," The Ohio State University.

[90] Yau, E., 1987, "Analysis of Shear Effect on Gear Tooth Deflections Using the Rayleigh-Ritz Energy Method," MSc. Thesis, The Ohio State University.

[91] Wright, S., 2001, “Face-Gear Contact Analysis Program Development Using the Thin Slice Method,” MSc Thesis, The Ohio State University.

[92] Christo T. Christov, L. B. P., “Comparison of Some Variants of the Finite Strip Method for Analysis of Complex Shell Structures.”

[93] Mawenya, A. S., Daviesi, J. D., Element, B., Formulation, S., and Finite, T. H. E., 1974, “Finite Strip Analysis of Plate Bending Including Transverse Shear Effects,” 9(c), pp. 175–180.

[94] Fan, S. C., and Partnership, H. A., 1983, “Analysis of Shallow Shells by Spline Finite Strip Method,” 5.

[95] Friedrich, and Richard, 2000, “Finite Strip Method: 30 Years A Bibliography (1968-1998),” Engineering Computations, 17(1), pp. 92–111.

[96] Gosselin, C., Gagnon, P., and Cloutier, L., 2014, “Accurate Tooth Stiffness of Spiral Bevel Gear Teeth by the Finite Strip Method,” 120(December 1998), pp. 599–605.

[97] Oñate, E., Suarez, B., 1983, “A Comparison of the Linear, Quadratic and Cubic Mindlin Strip Elements for the Analysis of Thick and Thin Plates,” Computers & Structures, 17(3), pp. 427–439.

[98] Guingand, M., de Vaujany, J. P., and Icard, Y., 2004, “Fast Three-Dimensional Quasi-Static Analysis of Helical Gears Using the Finite Prism Method,” Journal of Mechanical Design, 126(6), p. 1082.

[99] Oñate, E., 2013, Structural Analysis with the Finite Element Method Linear Statics Volume 2. Beams, Plates and Shells, Springer.

[100] Oñate, E., 2013, “Structural Analysis with the Finite Element Method Linear Statics Volume 2. Beams, Plates and Shells,” Springer, pp. 675–728.

[101] Al-ghabsha, A. T. S., 2006, “Dynamic Analysis of Bridges Subjected To Moving Vehicles,” Al-Rafidain Engineering, 14(July 2005), pp. 34–50.

[102] Chong, K. P., Tham, L. G., and Cheung, Y. G., 1982, “Thermal Behavior of Formed Sandwich Plate by Finite-Prism-Strip Method,” Computers & Structures, 15(3), pp. 321–324.

[103] Elgadir, A. B. D., “Static Analysis of Plates and Bridges Using Finite Prism Method.”

[104] Li, Z., and Szyniszewski, S., 2013, “Finite Prism Elastic Buckling Analysis and Application in Steel Foam Sandwich Members,” Proceedings of the Annual Stability Research Council, (2012), pp. 1–15.

[105] Too, J., and Zeinkiewicz, O., 1972, “The Finite Prism in Analysis of Thick Simply Supported Bridge Boxes.,” ICE Proceedings, 53(2), pp. 147–172.

[106] Wong, C. C. K., and Vardy, A. N. D. A. E., 1985, “Finite Prism Analysis of Plates and Shells,” International Journal for Numerical Methods in Engineering, 2(February 1984), pp. 529–541.

[107] Zienkiewicz, O. C., and Taylor, R. L., 2005, “Semi-Analytical Finite Element Processes – Use of Orthogonal Functions and ‘ Finite Strip ’ Methods,” The Finite Element Method for Solid and Structural Mechanics, Elsevier Butterworth-Heinemann, pp. 498–516.

[108] Vijayakar, S. M., Busby, H. R., and Houser, D. R., 1987, “Finite Element Analysis of Quasi-Prismatic Bodies Using Chebyshev Polynomials,” International Journal for Numerical Methods in Engineering, 24(8), pp. 1461–1477.

[109] Vijayakar, S. M., 1987, “Finite Element Analysis of Quasi-Prismatic Bodies with Application to Gears, Phd Dissertation,” The Ohio State University.

[110] Hoffman, R. M., Kinzel, G. L., and Grandhi, R. V., 2004, “Nonlinear Elastic-Plastic Analysis Using the Modified Finite Quasi-Prism Element,” Finite Elements in Analysis and Design, 40(4), pp. 449–460.

[111] Stegemiller, M., 1986, “The Effects of Base Flexibility on Thick Beams and Plates Used in Gear Tooth Deflection Models.”

[112] Gosselin, C., Gagnon, P., and Cloutier, L., 1998, “Accurate Tooth Stiffness of Spiral Bevel Gear Teeth by the Finite Strip Method,” Journal of Mechanical Design, 120(4), pp. 599–605.

[113] Cheung, Y., K., 1976, Finite Strip Method in Structural Analysis, Pergamon Press.

[114] Cheung, Y., K., Tham, L., G., 1998, Finite Strip Method, CRC Press LCC.

[115] Cooley, C. G., and Parker, R. G., 2014, “A Review of Planetary and Epicyclic Gear Dynamics and Vibrations Research,” Applied Mechanics Reviews, 66(4), p. 040804.

[116] Al-shyyab, a, and Kahraman, a, 2007, “A Non-Linear Dynamic Model for Planetary Gear Sets,” Proceedings of the Institution of Mechanical Engineers, Part K: Journal of Multi-body Dynamics, 221(4), pp. 567–576.

[117] Al-Shyyab, A., Alwidyan, K., Jawarneh, A., and Tlilan, H., 2009, “Non-Linear Dynamic Behaviour of Compound Planetary Gear Trains: Model Formulation and Semi-Analytical Solution,” Proceedings of the Institution of Mechanical Engineers, Part K: Journal of Multi-body Dynamics, 223(3), pp. 199–210.

[118] Kahraman, A., 1994, “Dynamic Analysis of a Multi-Mesh Helical Gear Train,” Journal of Mechanical Design, 116(SEPTEMBER 1994), pp. 706–712.

[119] Zhiheng, F., Shilong, W., Teik, C., L., Tao, P., 2011, “Enhanced Friction Model for High-Speed Right-Angle Gear Dynamics,” Journal of Mechanical Science and Technology, 25(11).

[120] Tang, J., Hu, Z., Chen, S., and Lei, D., 2014, “Effects of Directional Rotation Radius and Transmission Error on the Dynamic Characteristics of Face Gear Transmission System,” Proceedings of the Institution of Mechanical Engineers, Part C: Journal of Mechanical Engineering Science, 228(7), pp. 1108–1118.

[121] Ferreira, J., V., and Serpa, A., L., “Application of the Arc-Length Method in Nonlinear Frequency Response,” Journal of Sound and Vibration, 284(1–2), pp. 133–149.

[122] Kahraman, A., “On the Response of a Preloaded Mechanical Oscillator with a Clearance: Period-Doubling and Chaos,” Nonlinear Dynamics, 3(1992), pp. 183–198.

[123] Blankenship, G., W., and Kahraman, A., “Steady State Forced Response of a Mechanical Oscillator with Combined Parametric Excitation and Clearance Type Non-Linearity,” Journal of Sound and Vibration, 185(5), pp. 743–765.

[124] Al-shyyab, A., and Kahraman, A., 2005, “Non-Linear Dynamic Analysis of a Multi-Meshgear Train Usin Multi-Term Harmonic Balance Method: Period-One Motions,” Journal of Sound and Vibration, 284(1–2), pp. 151–172.

[125] Dai, Liming, 2008, Nonlinear Dynamics of Piecewise Constant Systems and Implementation of Piecewise Constant Arguments, Singapore.

[126] Moon, F. C., 1987, Chaotic Vibrations : An Introduction for Applied Scientists and Engineers, John Wiley & Sons, New York.

[127] Hartog, J. P. Den, 1985, Mechanical Vibrations, Dover Publications, New York.

[128] Reedy, J., N., 2002, Energy Principles and Methods In Applied Mechanics, John Wiley&Sons.

[129] Reedy, J., N., 2006, An Introduction to Nonlinear Finite Elements, Oxford University Press.

[130] Nayfeh, A., H., 2004, Linear and Nonlinear Structural Mechanics, John Wiley & Sons.

[131] Ribeiro, P. , Petyt, M., 1999, “Nonlinear Vibration of Plates by the Hierarchical Finite Element and Continuation Methods,” International Journal of Mechanical Sciences, 41(4–5), pp. 437–459.

[132] Ribeiro, P., 2005, “Nonlinear Vibrations of Simply-Supported Plates by the p-Version Finite Element Method,” Finite Elements In Analysis and Design, 41(Issues 9–10), pp. 911–924.

[133] Young, W. C., 1989, Roark’s Formulas for Stress & Strain. 4.

[134] Palmgren, A., 2008, Ball and Roller Bearing Grease, S.H. Burbank & Co., Inc.

[135] Laskin, I., Orcutt, F. K., and Shipley, E. E., 1968, “Analysis of Noise Generated By UH-1 Helicopter Transmission,” USAAVLABS Technical Report 68-41, U.S. Army Aviation Materiel Laboratories, 6(2), p. 320.

[136] Weber, Constantin / Banaschek, K., 1953, “Formänderung Und Profilrücknahme Bei Gerad- Und Schrägverzahnten Rädern,” Schriftenreihe Antriebstechnik, 11.

[137] Brewe, D., D., Hamrock, B., 1976, “Simplified Solution for Point Contact Deformation between Two Elastic Solids.”

[138] Hamrock, B., J., Dowson, D., 1976, “Isothermal Elastohydrodynamic Lubrication of Point Contacts Part I—Theoretical Formulation,” Transactions of ASME.

[139] Hamrock, B., J., Dowson, D., 1976, “Isothermal Elastohydrodynamic Lubrication of Point Contacts Part II—Ellipticity Parameter Results,” Transactions of ASME.

[140] Hamrock, B., J., Dowson, D., 1977, “Isothermal Elastohydrodynamic Lubrication of Point Contacts Part III—Fully Flooded Results,” Transactions of ASME.

[141] Hamrock, B., J., Dowson, D., 1977, “Isothermal Elastohydrodynamic Lubrication of Point Contacts Part IV—Starvation Results,” Transactions of ASME.

[142] Mathur, D. M., Smith, E. C., DeSmidt, H., and Bill, R., 2016, “Load Distribution and Mesh Stiffness Analysis of an Internal External Bevel Gear Pair in a Pericyclic Drive,” American Helicopter Society International, West Palm, Florida, USA.

APPENDICES

A. NURBS Approximation

NURBS curves are generally given by [72],

$$C(u) = \frac{\sum_{i=1}^{n} N_{i,p}(u) w_i P_i}{\sum_{i=1}^{n} N_{i,p}(u) w_i} \tag{A-1}$$

NURBS surfaces are generally given by,

$$S(u_{1,} u_2) = \frac{\sum_{i=1}^{n}\sum_{j=1}^{m} N_{i,p}(u_1) N_{j,q}(u_2) w_{i,j} P_{i,j}}{\sum_{i=1}^{n}\sum_{j=1}^{m} N_{i,p}(u_1) N_{j,q}(u_2) w_{i,j}} \tag{A-2}$$

For the NURBS curve formulation, assume that $\{Q_k\}$ is a given set of points, or point cloud; then,

$$Q_k = C(\bar{u}_k) = \sum_{i=1}^{n} N_{i,p}(\bar{u}_k) w_i P_i \tag{A-3}$$

where k=1,2,3,…n.

Equation (A-3) has to be calculated for every data point in order to solve for the coefficients P$_i$, where

$$\bar{u}_n = 1, \quad for \quad k = 1 \tag{A-4}$$

$$\bar{u}_1 = 0, \quad for \quad k = n \tag{A-5}$$

$$\bar{u}_k = \bar{u}_{k-1} + \frac{|Q_k - Q_{k-1}|}{d} \quad for \quad k = 2,3,...n-1 \tag{A-6}$$

where $d = \sum_{k=1}^{n} |Q_k - Q_{k-1}|$.

NURBS basis functions are given as, for p=0,

$$N_{i,p}(u) = \begin{cases} 1, u_i \le u \le u_{i+1} \\ 0, otherwise \end{cases} \tag{A-7}$$

and for $p \ge 1$,

$$N_{i,p}(u) = \frac{u - u_i}{u_{i+p} - u_i} N_{i,p-1}(u) + \frac{u_{i+p+1} - u}{u_{i+p-1} - u_{i+1}} N_{i+1,p-1}(u) \tag{A-8}$$

where,

$$u_1 = \ldots u_{p+1} = 0 \tag{A-9}$$

$$u_{m-p} = \ldots u_m = 1 \tag{A-10}$$

$$u_{j+p} = \frac{1}{p} \sum_{i=j}^{j+p+1} \bar{u}_k \,,\; j = 2,3,\ldots n-p. \tag{A-11}$$

Here, n is the number of control points, p is the degree of the NURBS basis function, m is the number of values in the knot vector and specified as,

$$m = n + p + 1. \tag{A-12}$$

B. Thin Slice Method

The following formulation is utilized for the bending compliance calculation for a slice of TSM element [81].

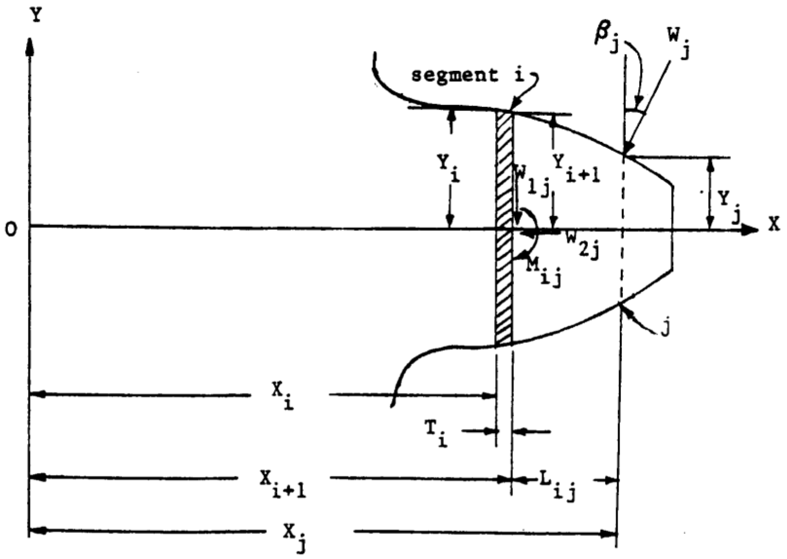

Figure B-1 A slice for an involute profile

Bending Deflection of the ith segment due to forcing at j^th^ position of a slice:

$$q^{w}{}_{i,j} = \frac{W_j \cos\left(\beta_j\right)}{3EI_i} \cdot \left(T_i\right)^3 + \frac{W_j \cos\left(\beta_j\right)}{2EI_i} \cdot \left(T_i\right)^2 L_{i,j} \tag{B-1}$$

where W_j is the applied force, β_j is the angle of the force with the vertical axis, T_i is thickness of the ith segment, E is the Young's modulus, I_i is the area moment of inertia of the ith segment, $L_{i,j}$ is the distance between the ith segment and the jth load application point.

Bending Deflection due to moments:

$$q^{M}{}_{i,j}=\frac{W_j\left(L_{i,j}\cdot\cos\left(\beta_j\right)-Y_j\cdot\sin\left(\beta_j\right)\right)}{2EI_i}\cdot\left(T_i\right)^2+\frac{W_j\left(L_{i,j}\cdot\cos\left(\beta_j\right)-Y_j\cdot\sin\left(\beta_j\right)\right)}{EI_i}\cdot T_iL_{i,j} \tag{B-2}$$

Shear Deformation:

$$q^{s}{}_{i,j}=\frac{2.4\left(1+\upsilon\right)W_jT_i\cos\left(\beta_j\right)}{EA_i} \tag{B-3}$$

Axial Compression:

$$q^{c}{}_{i,j}=\frac{W_jT_i\sin\left(\beta_j\right)}{EA_i} \tag{B-4}$$

Total Deformation:

$$q^{T}{}_{i,j}=\left(q^{w}{}_{i,j}+q^{M}{}_{i,j}+q^{s}{}_{i,j}\right)\cdot\cos\left(\beta_j\right)+q^{c}{}_{i,j}\cdot\sin\left(\beta_j\right) \tag{B-5}$$

C. Rayleigh-Ritz Approximation

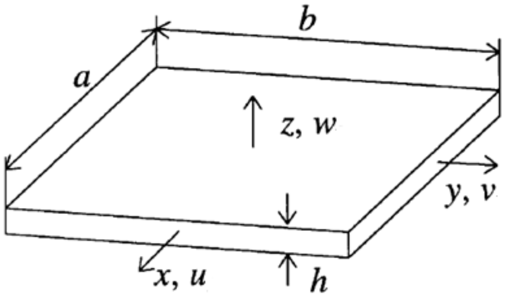

Figure C-1 A slice for an involute profile

Let the following parameters are defined as,

- *w* is the transverse deflection of the plate
- *u* is the stretching deflection along x axis
- *v* is the stretching deflection along y axis
- *h* is the thickness of the plate
- *E* is the modulus of elasticity of the isotropic plate material
- *a* is the length of the plate
- *b* is the width of the plate
- υ is the Poisson's ratio

Formulation For a Kirchoff Plate [128]:

The virtual strain energy of the plate can be expressed as,

$$\delta U = \iint\limits_{A} \int_{-h/2}^{h/2} \left(\sigma_{xx}\delta\varepsilon_{xx} + \sigma_{yy}\delta\varepsilon_{yy} + 2\sigma_{xy}\delta\varepsilon_{xy} \right) dzdxdy \qquad \text{(C-1)}$$

The potential energy due to virtual loads, such as pressure loading over plate surface, can be expressed in variational form as,

$$\delta V = \iint_A q(x, y, t) \cdot \delta w \cdot dxdy \tag{C-2}$$

Since the total potential energy functional is [128],

$$\delta \Pi = \delta U + \delta V = 0 \tag{C-3}$$

then, it can be expressed as,

$$\delta \Pi = \iint_A \int_{\frac{-h}{2}}^{\frac{h}{2}} (\sigma_{xx}\delta\varepsilon_{xx} + \sigma_{yy}\delta\varepsilon_{yy} + 2\sigma_{xy}\delta\varepsilon_{xy}) dzdxdy - \iint_A q(x, y, t) \cdot \delta wdxdy \tag{C-4}$$

The Von-Karman strains of the plate may be defined as [128–132],

$$\begin{aligned} \varepsilon_{yy} &= v_y + \frac{1}{2} w_y{}^2 - zw_{yy} \\ \varepsilon_{xx} &= u_x + \frac{1}{2} w_x{}^2 - zw_{xx} \\ \varepsilon_{xy} &= u_y + v_x + w_x w_y - 2zw_{xy} \end{aligned} \tag{C-5}$$

Setting the strains in transverse directions zero yields,

$$\varepsilon_{zz} = \varepsilon_{xz} = \varepsilon_{yz} = 0 \tag{C-6}$$

Taking the variations of the strain expressions yield,

$$\delta\varepsilon_{xx} = \delta u_x + w_x \delta w_x - z\delta w_{xx} \tag{C-7}$$

$$\varepsilon_{yy} = \delta v_y + w_y \delta w_y - z\delta w_{yy} \tag{C-8}$$

$$\delta\varepsilon_{xy} = \delta u_y + \delta v_x + w_x \delta w_y + w_y \delta w_x - 2z\delta w_{xy} \tag{C-9}$$

Substituting the strain variations into the virtual potential energy expression yields,

$$\delta V = \iint_A \Big[N_{xx}(\delta u_x + w_x \delta w_x) + N_{yy}(\delta v_y + w_y \delta w_y) \tag{C-10}$$

$$+ N_{xy}(\delta u_y + \delta v_x + w_x \delta w_y + w_y \delta w_x) - M_{xx}\delta w_{xx} - M_{yy}\delta w_{yy} - 2M_{xy}\delta w_{xy} \Big] dxdy$$

The terms N_{xx}, N_{yy} and N_{xy}, *namely the membrane forces*, are generated during the out of plane deflection of the plate. As the plates deflects, these terms become dominant, with the strain formulas given below,

$$N_{xx} = \frac{Eh}{12(1-\upsilon^2)}(u_x + \frac{1}{2}w_x{}^2 + \upsilon(u_y + \frac{1}{2}w_y{}^2))$$

$$N_{yy} = \frac{Eh}{12(1-\upsilon^2)}(\upsilon(u_x + \frac{1}{2}w_x{}^2) + u_y + \frac{1}{2}w_y{}^2) \tag{C-11}$$

$$N_{xy} = \frac{h}{2}G(u_y + v_x + w_x w_y)$$

Also, M_{xx}, M_{yy}, M_{yz} are defined as,

$$M_{xx} = -\frac{Eh^3}{12(1-\upsilon^2)}(w_{xx} + \upsilon w_{yy})$$

$$M_{yy} = -\frac{Eh^3}{12(1-\upsilon^2)}(\upsilon w_{xx} + w_{yy}) \tag{C-12}$$

$$M_{xy} = -\frac{Eh^3}{12(1+\upsilon)}(w_{xy})$$

It is assumed that, during the deflection of the plate, no transverse shear develops. Therefore, the term N_{xy} is assumed to be zero (Kirchoff plate model where shear energy is considered to be negligible). Also, it is assumed that, ux and vy are equal to zero. This final assumption also denotes imposing δu_x and δv_y are equal to zero. After these assumptions, dropping the neglected terms, the virtual potential energy expression becomes;

$$\delta V = \iint_A \Big(N_{xx}\left(w_x \delta w_x\right) + N_{yy}\left(w_y \delta w_y\right) - M_{xx}\delta w_{xx} - M_{yy}\delta w_{yy} - 2M_{xy}\delta w_{xy} \Big) dxdy \tag{C-13}$$

and, similarly, after dropping the neglected terms, N_{xx} and N_{yy} become,

$$N_{xx} = \frac{Eh}{12(1-\upsilon^2)}\left(\frac{1}{2}w_x{}^2 + \upsilon\frac{1}{2}w_y{}^2\right) \tag{C-14}$$

$$N_{yy} = \frac{Eh}{12(1-\upsilon^2)}\left(\upsilon\frac{1}{2}w_x{}^2 + \frac{1}{2}w_y{}^2\right) \tag{C-15}$$

Inserting Equations (C-12), (C-14) and (C-15) into the virtual potential energy expression given in Equation (C-13) yields

$$\begin{aligned}\delta V = \iint_A \Bigg[& \frac{Eh}{12(1-\upsilon^2)}\left(\frac{1}{2}w_x{}^2 + \upsilon\frac{1}{2}w_y{}^2\right)(w_x \delta w_x) \\ & + \frac{Eh}{12(1-\upsilon^2)}\left(\upsilon\frac{1}{2}w_x{}^2 + \frac{1}{2}w_y{}^2\right)(w_y \delta w_y) \\ & - - \frac{Eh^3}{12(1-\upsilon^2)}(w_{xx} + \upsilon w_{yy})\delta w_{xx} \\ & - - \frac{Eh^3}{12(1-\upsilon^2)}(\upsilon w_{xx} + w_{yy})\delta w_{yy} \\ & - - \frac{Eh^3}{12(1+\upsilon)}(w_{xy})\delta w_{xy} \Bigg] dxdy\end{aligned} \tag{C-16}$$

Since,

$$D = \frac{Eh^3}{12(1-\upsilon^2)} \tag{C-17}$$

then, Equation (C-16) may be re-written as,

$$\begin{aligned}\delta V = D\iint_A \Big[& (\frac{1}{2}w_x{}^2 + \upsilon\frac{1}{2}w_y{}^2)(w_x \delta w_x) \\ & +(\upsilon\frac{1}{2}w_x{}^2 + \frac{1}{2}w_y{}^2)(w_y \delta w_y) \\ & +(w_{xx} + \upsilon w_{yy})\delta w_{xx} \\ & +(\upsilon w_{xx} + w_{yy})\delta w_{yy} \\ & +2(1-\upsilon)(w_{xy})\delta w_{xy} \Big] dxdy\end{aligned} \tag{C-18}$$

Here it may be stated that the interested plate is classified as thick plate rather that thin plate, so terms N_{xx}, N_{yy} and N_{xy}, the membrane forces, can be eliminated from the equations. Assuming a solution in the form,

$$w(x,y) = \sum_{i=1}^{N}\sum_{j=1}^{M} c_{i,j} X_i(x) Y_j(y) \tag{C-19}$$

yields,

$$
\begin{aligned}
R_{pq,ij} = D\int_0^a\int_0^b \Bigg[& \frac{d^2X_i}{dx^2}Y_j \frac{d^2X_p}{dx^2}Y_q + 2(1-\upsilon)\frac{dX_i}{dx}\frac{dY_j}{dy}\frac{dX_p}{dx}\frac{dY_q}{dy} \\
& +\upsilon\left(X_i \frac{d^2Y_j}{dy^2}\frac{d^2X_p}{dx^2}Y_q + \frac{d^2X_i}{dx^2}Y_j X_p \frac{d^2Y_q}{dy^2}\right) \\
& + X_i \frac{d^2Y_j}{dy^2} X_p \frac{d^2Y_q}{dy^2}\Bigg] dxdy
\end{aligned}
\tag{C-20}
$$

where *N* and *M* represent the utilized shape functions along longitudinal and transverse axis, respectively. The forcing matrix is written as,

$$
Q_{ij} = \int_0^a\int_0^b \left(f \cdot X(x,i)\cdot Y(y,j)\cdot dxdy\right),
\tag{C-21}
$$

where,

$$
\begin{aligned}
& Q_{ij} = \int_0^a\int_0^b \left(f \cdot X(x,i)\cdot Y(y,j)\cdot dxdy\right), \text{ for pressure load} \\
& Q_{ij} = \int_0^a\int_0^b \left(f \cdot X(x_0,i)\cdot Y(\mathrm{y}_0,j)\cdot dxdy\right), \text{ for a point load at } (x_0, y_0) \\
& Q_{ij} = Y(\mathrm{y}_0, j)\int_0^a \frac{f}{2} X(x,i))\cdot dx, \text{ for a distributed load along x axis at } (x, y_0) \\
& Q_{ij} = X(x_0, i)\int_0^b \frac{f}{2} Y(\mathrm{y}, \mathrm{j})\cdot dx, \text{ for a distributed load along y axis at } (x_0, y)
\end{aligned}
\tag{C-22}
$$

D. Finite Prism Method and Quasi-Prism Method

The following formulation is utilized for the Element formulation of a Finite Prism Method. as detailed in references [99,113,114].

8-noded isoparametric element is utilized for the formulation of a FPM element.

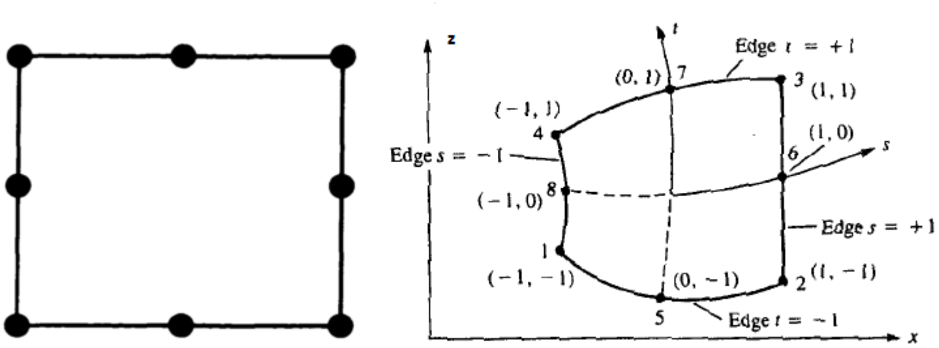
z
t
Edge t = +1
(0, 1)
7
3
(1, 1)
(−1, 1)
4
(1, 0)
s
6
Edge s = −1
8
(−1, 0)
Edge s = +1
1
(−1, −1)
(0, −1)
2
(1, −1)
5
Edge t = −1
x

Figure D-1 8-noded isoparametric element

The shape functions are used to interpolate the coordinates from the nodal coordinates as [99,113,114];

$$\mathrm{x} = \sum_{m=1}^{8} C_k(\xi,\eta)x_k$$

$$\mathrm{z} = \sum_{m=1}^{8} C_k(\xi,\eta)z_k \qquad \text{D-1}$$

where the shape functions can be written as,

$$
\begin{aligned}
C_1(\xi,\eta) &= 1/4\ (1-\xi)\ (1-\eta)\ (-\xi-\eta-1)\\
C_2(\xi,\eta) &= 1/4\ (1+\xi)\ (1-\eta)\ (\xi-\eta-1)\\
C_3(\xi,\eta) &= 1/4\ (1+\xi)\ (1+\eta)\ (\xi+\eta-1)\\
C_4(\xi,\eta) &= 1/4\ (1-\xi)\ (1+\eta)\ (-\xi+\eta-1)\\
C_5(\xi,\eta) &= 1/2\ (1-\eta)\ (1+\xi)\ (1-\xi)\\
C_6(\xi,\eta) &= 1/2\ (1+\xi)\ (1+\eta)\ (1-\eta)\\
C_7(\xi,\eta) &= 1/2\ (1+\eta)\ (1+\xi)\ (1-\xi)\\
C_8(\xi,\eta) &= 1/2\ (1-\xi)\ (1+\eta)\ (1-\eta)
\end{aligned}
\tag{D-2}
$$

For simply support end conditions, $u = w = \frac{\partial v}{\partial y} = 0$ at y=0 and y=b; the following displacement functions are assumed,

$$
\begin{aligned}
\mathrm{u} &= \sum_{m=1}^{r}\sum_{k=1}^{8} C_k u_{km} sin(k_m y)\\
\mathrm{y} &= \sum_{m=1}^{r}\sum_{k=1}^{8} C_k v_{km} cos(k_m y)\\
\mathrm{w} &= \sum_{m=1}^{r}\sum_{k=1}^{8} C_k w_{km} sin(k_m y)
\end{aligned}
\tag{D-3}
$$

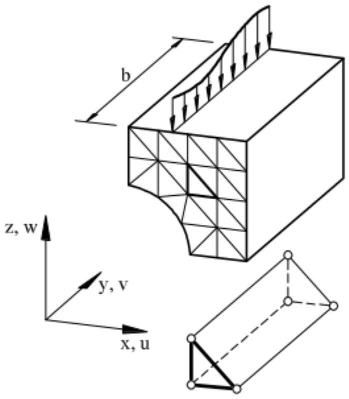

Figure D-2 A general prism to be modelled with FPM

The stiffness matrix is calculated as

$$[\mathrm{K}_{ij}]_{mn} = \int [B_i]_m{}^T [D] [B_j]_m dV \qquad \text{D-4}$$

where material matrix is given as

$$[D] = \frac{E}{(1-\nu^2)} \begin{bmatrix} (1-\nu) & 0 & 0 & 0 & 0 & 0 \\ 0 & (1-\nu) & 0 & 0 & 0 & 0 \\ 0 & 0 & (1-\nu) & 0 & 0 & 0 \\ 0 & 0 & 0 & (1/2-\nu) & 0 & 0 \\ 0 & 0 & 0 & 0 & (1/2-\nu) & 0 \\ 0 & 0 & 0 & 0 & 0 & (1/2-\nu) \end{bmatrix} \qquad \text{D-5}$$

and strain displacement relation may be expressed as,

$$[B_i]_m = \begin{bmatrix} \frac{dC_i(x,z)}{dx}\sin(k_m y) & 0 & 0 \\ 0 & -C_i(x,z)k_m\sin(k_m y) & 0 \\ 0 & 0 & \frac{dC_i(x,z)}{dz}\sin(k_m y) \\ -C_i(x,z)k_m\cos(k_m y) & \frac{dC_i(x,z)}{dx}\cos(k_m y) & 0 \\ 0 & \frac{dC_i(x,z)}{dx}\cos(k_m y) & -C_i(x,z)k_m\cos(k_m y) \\ \frac{dC_i(x,z)}{dx}\sin(k_m y) & 0 & \frac{dC_i(x,z)}{dz}\sin(k_m y) \end{bmatrix} \tag{D-6}$$

where the derivatives of the shape functions may be calculated by applying the chain rule as

$$\begin{aligned} \frac{\partial C_i}{\partial \xi} &= \frac{\partial C_i}{\partial x}\frac{\partial x}{\partial \xi} + \frac{\partial C_i}{\partial z}\frac{\partial z}{\partial \xi} \\ \frac{\partial C_i}{\partial \eta} &= \frac{\partial C_i}{\partial x}\frac{\partial x}{\partial \eta} + \frac{\partial C_i}{\partial z}\frac{\partial z}{\partial \eta} \end{aligned} \tag{D-7}$$

Writing in matrix form yields,

$$\begin{Bmatrix} \frac{\partial C_i}{\partial \xi} \\ \frac{\partial C_i}{\partial \eta} \end{Bmatrix} = \begin{bmatrix} \frac{\partial x}{\partial \xi} & \frac{\partial z}{\partial \xi} \\ \frac{\partial x}{\partial \eta} & \frac{\partial z}{\partial \eta} \end{bmatrix} \begin{Bmatrix} \frac{\partial C_i}{\partial x} \\ \frac{\partial C_i}{\partial z} \end{Bmatrix} = [J] \begin{Bmatrix} \frac{\partial C_i}{\partial x} \\ \frac{\partial C_i}{\partial z} \end{Bmatrix} \tag{D-8}$$

where J is referred to as the Jacobian matrix. Utilizing the Equation (D-1), Jacobian can be written as,

$$[J] = \begin{bmatrix} \frac{\partial x}{\partial \xi} & \frac{\partial z}{\partial \xi} \\ \frac{\partial x}{\partial \eta} & \frac{\partial z}{\partial \eta} \end{bmatrix} = \sum_{k=1}^{8} \begin{bmatrix} \frac{\partial C_i}{\partial \xi} x_k & \frac{\partial C_i}{\partial \xi} z_k \\ \frac{\partial C_i}{\partial \eta} x_k & \frac{\partial C_i}{\partial \eta} z_k \end{bmatrix} \qquad \text{D-9}$$

and for a 8-noded element, this yields,

$$= \begin{bmatrix} \frac{\partial C_1}{\partial \xi} & \frac{\partial C_2}{\partial \xi} & \frac{\partial C_3}{\partial \xi} & \frac{\partial C_4}{\partial \xi} & \frac{\partial C_5}{\partial \xi} & \frac{\partial C_6}{\partial \xi} & \frac{\partial C_7}{\partial \xi} & \frac{\partial C_8}{\partial \xi} \\ \frac{\partial C_1}{\partial \eta} & \frac{\partial C_2}{\partial \eta} & \frac{\partial C_3}{\partial \eta} & \frac{\partial C_4}{\partial \eta} & \frac{\partial C_5}{\partial \eta} & \frac{\partial C_6}{\partial \eta} & \frac{\partial C_7}{\partial \eta} & \frac{\partial C_8}{\partial \eta} \end{bmatrix} \begin{bmatrix} x_1 & z_1 \\ x_2 & z_2 \\ x_3 & z_3 \\ x_4 & z_4 \\ x_5 & z_5 \\ x_6 & z_6 \\ x_7 & z_7 \\ x_8 & z_8 \end{bmatrix} \qquad \text{D-10}$$

Finally, the global derivatives can be expressed as

$$\begin{Bmatrix} \frac{\partial C_i}{\partial x} \\ \frac{\partial C_i}{\partial z} \end{Bmatrix} = [J]^{-1} \begin{Bmatrix} \frac{\partial C_i}{\partial \xi} \\ \frac{\partial C_i}{\partial \eta} \end{Bmatrix} \qquad \text{D-11}$$

and the area of the defined element can be re-written as

$$dxdz = \det(J) d\xi d\eta \qquad \text{D-12}$$

substituting Equation (D-12) into Equation (D-4) yields,

$$[\mathrm{K}_{ij}]_{mn} = \int_{0}^{a}\int_{-1}^{+1}\int_{-1}^{+1}[B_i]_m{}^T[D][B_j]_n \det(J)\,d\xi d\eta dy \qquad \text{D-13}$$

The following formulation is utilized for element formulation of a Finite-Quasi Prism Element. Details can be found in references [109,110].

The displacement functions is written as

$$\mathrm{u}(\xi,\eta,\zeta) = \sum_{i=1}^{nod}\sum_{j=0}^{cho} u_{ij}C_i(\xi,\eta)T_j(\zeta)$$

$$\mathrm{v}(\xi,\eta,\zeta) = \sum_{i=1}^{nod}\sum_{j=0}^{cho} v_{ij}C_i(\xi,\eta)T_j(\zeta) \qquad \text{D-14}$$

$$\mathrm{w}(\xi,\eta,\zeta) = \sum_{i=1}^{nod}\sum_{j=0}^{cho} w_{ij}C_i(\xi,\eta)T_j(\zeta)$$

where, nod is the number of the nodes, and cho is the order of the utilized Chebyshev function. The shape functions are used to interpolate the coordinates from the nodal coordinates as

$$\mathrm{x}(\xi,\eta,\zeta) = \sum_{i=1}^{nod}\sum_{j=0}^{cho} x_{ij}C_i(\xi,\eta)T_j(\zeta) \qquad \text{D-15}$$

$$\mathrm{y}(\xi,\eta,\zeta) = \sum_{i=1}^{nod}\sum_{j=0}^{cho} y_{ij}C_i(\xi,\eta)T_j(\zeta)$$

$$\mathrm{z}(\xi,\eta,\zeta) = \sum_{i=1}^{nod}\sum_{j=0}^{cho} z_{ij}C_i(\xi,\eta)T_j(\zeta)$$

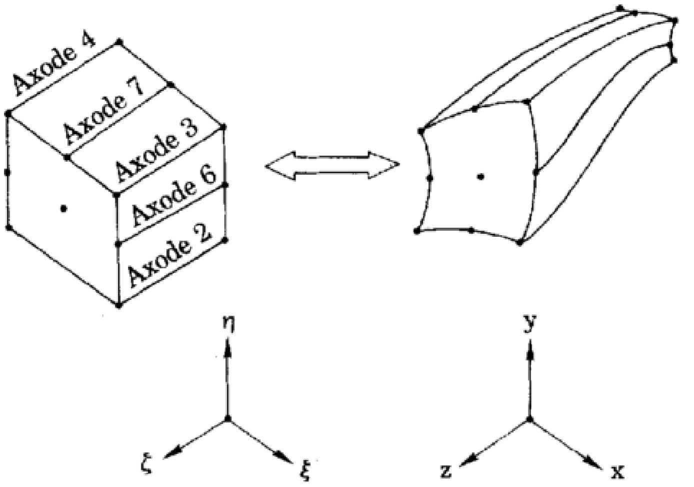

Figure D-3 Mapping from pyhsical system to element in natural coordinate system

8-noded iso-parametric element is selected for the xy plane and therefore same shape functions are assumed, as already given in Equation (D-2). For the longitudinal axis, however, modified Chebyshev polynomials are utilized.

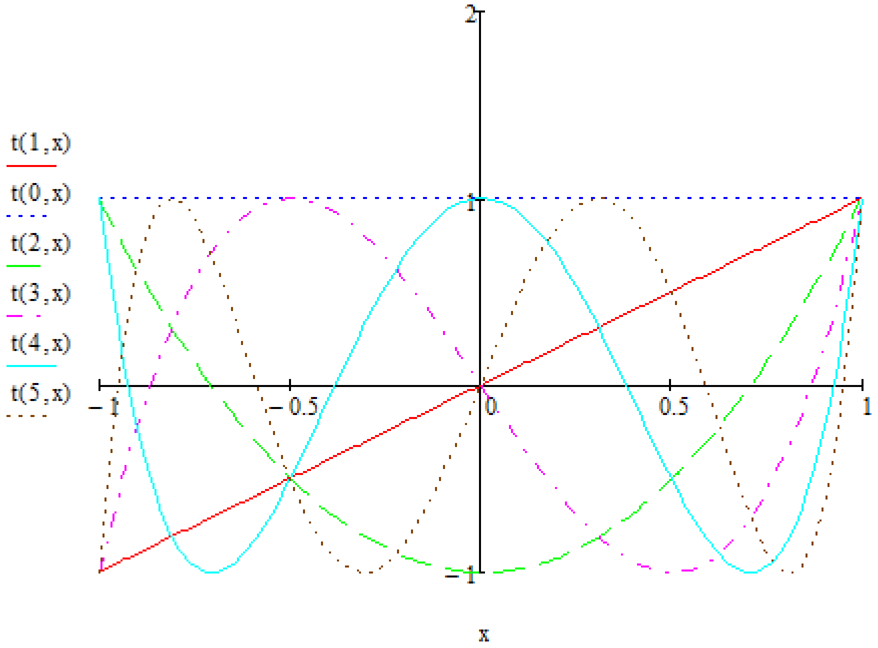

Figure D-4 Chebyshev functions

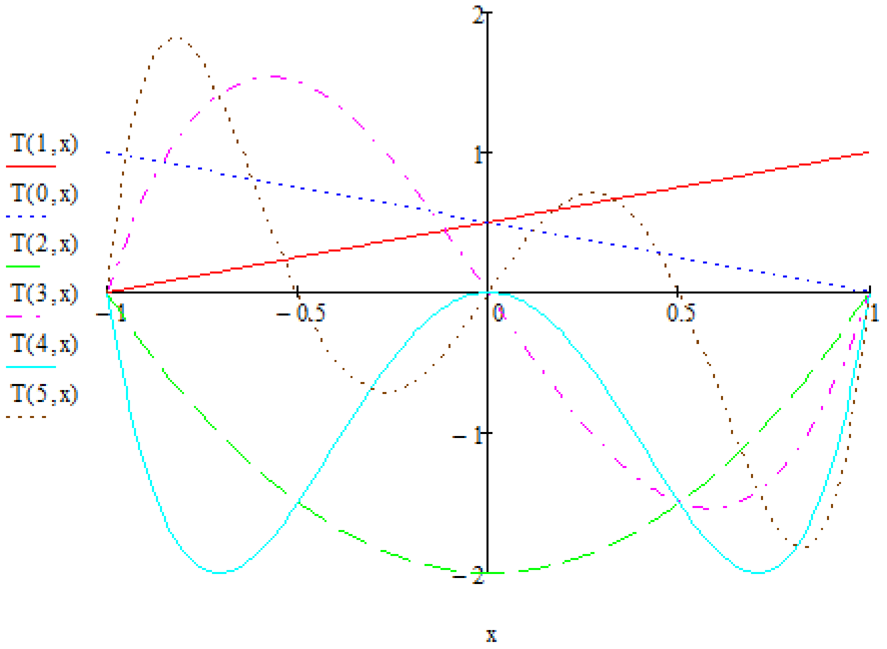

Figure D-5 Modified Chebyshev functions

Along each node at the xy plane, towards the end of the longitudinal axis z, curve fit is performed for all three dimensions x, y, z with Chebyshev polynomials. By performing this, the prism is cut for sections in order to seek the variation along the prism axis. So, the variation in coordinates x, y, z is formulated as follows

$$\mathrm{x}(\xi,\eta,\zeta)=\sum_{j=0}^{cho} x_{km}T_m(\zeta)$$

$$\mathrm{y}(\xi,\eta,\zeta)=\sum_{j=0}^{cho} y_{km}T_m(\zeta) \qquad \text{D-16}$$

$$\mathrm{z}(\xi,\eta,\zeta)=\sum_{j=0}^{cho} z_{km}T_m(\zeta)$$

The total shape functions definition for a 3D node becomes,

$$[N_{im}] = \begin{bmatrix} C_i(\xi,\eta)T_m(\zeta) & 0 & 0 \\ 0 & C_i(\xi,\eta)T_m(\zeta) & 0 \\ 0 & 0 & C_i(\xi,\eta)T_m(\zeta) \end{bmatrix}. \qquad \text{D-17}$$

Strain matrix can be expressed as

$$\left[B_i\right]_m = \begin{bmatrix} \frac{\partial(C_i\left(x,y\right)T_m(z))}{\partial x} & 0 & 0 \\ 0 & \frac{\partial(C_i\left(x,y\right)T_m(z))}{\partial y} & 0 \\ 0 & 0 & \frac{\partial(C_i\left(x,y\right)T_m(z))}{\partial z} \\ 0 & \frac{\partial(C_i\left(x,y\right)T_m(z))}{\partial z} & \frac{\partial(C_i\left(x,y\right)T_m(z))}{\partial y} \\ \frac{\partial(C_i\left(x,y\right)T_m(z))}{\partial z} & 0 & \frac{\partial(C_i\left(x,y\right)T_m(z))}{\partial x} \\ \frac{\partial(C_i\left(x,y\right)T_m(z))}{\partial x} & \frac{\partial(C_i\left(x,y\right)T_m(z))}{\partial x} & 0 \end{bmatrix} \tag{D-18}$$

The stiffness matrix can be calculated as

$$\left[\mathrm{K}_{ij}\right]_{mn} = \int_{-1}^{+1}\int_{-1}^{+1}\int_{-1}^{+1} [B_i]_m{}^T [D] \left[B_j\right]_n \det(J)\, d\xi d\eta d\,\zeta \tag{D-19}$$

E. Contact Stiffness Methods

Hertz's Equation:

Hertz's deflection formula specified for two cylinders in contact is given as follows [133]

$$C_c = \frac{2(1-\upsilon^2)}{fE\pi}\left(\frac{2}{3} + \ln\left(\frac{2D_1}{b}\right) + \ln\left(\frac{2D_2}{b}\right)\right) \tag{E-1}$$

$$b = 1.6\sqrt{\frac{2P(1-\upsilon^2)\,\mathrm{D}_1 D_2}{fE(\mathrm{D}_1 + D_2)}} \tag{E-2}$$

where,

- b is the half contact width,
- f facewidth
- E modulus of elasticity
- υ poisson's ratio
- P contact force
- D_1 diameter of the first gear
- D_2 diameter of the second gear

Conry's Equation:

Conry's equation represents a linear expression for the Hertzian contact deflection [111]. The deflection is given as

$$\delta_c = 7.96 \frac{(1-\upsilon^2)}{fE} \tag{E-3}$$

and the compliance is calculated as,

$$C_c = 7.96 \frac{(1-\upsilon^2)\mathrm{P}}{fE} \tag{E-4}$$

where

- f facewidth
- E modulus of elasticity
- υ poisson's ratio
- P contact force

Cornell's Equation:

Cornell's equation does not take into account the contact width, location of the contact point, and the magnitude of the applied load [76]. The deflection is given as

$$\delta_c = 4.55 \frac{(1-\upsilon^2)\mathrm{P}}{fE} \tag{E-5}$$

and then the compliance can be calculated as

$$C_c = 4.55 \frac{(1-\upsilon^2)}{fE} \qquad \text{(E-6)}$$

where

- f facewidth
- E modulus of elasticity
- υ poisson's ratio
- P contact force

Palmgren's Equation:

Palmgren's semi-empirical equation was developed for contacting cylinders in roller bearings [134]. It is further modified to the following form [135], and the compliance is obtained as

$$C_c = \frac{1.37}{E^{0.9} f^{0.8} P^{0.1}} \qquad \text{(E-7)}$$

where

- f facewidth
- E modulus of elasticity
- P contact force

This equation does not need any iteration loop for the contact force. It is independent of the location of the contact force along the tooth surface.

Weber's Equation:

Weber proposed a closed form approach for the calculation of the contact deflection of the two gear teeth [136]. The equation for the deflection when the both gears are of the same material is written as

$$\delta_c = \frac{4(1-\upsilon^2)\,\mathrm{P}}{fE\pi}\left(\ln\left(\frac{2\sqrt{h_1 h_2}}{b}\right) - \frac{\upsilon}{2(1-\upsilon)}\right) \tag{E-8}$$

The compliance can be calculated as

$$C_c = \frac{4(1-\upsilon^2)}{fE\pi}\left(\ln\left(\frac{2\sqrt{h_1 h_2}}{b}\right) - \frac{\upsilon}{2(1-\upsilon)}\right) \tag{E-9}$$

A

nd the half contact width b can be expressed as

$$b = \sqrt{\frac{8P(1-\upsilon^2)R_1 R_2}{fE\pi\left(R_1 + R_2\right)}} \tag{E-10}$$

and the other necessary calculations are listed as follows

$$
\begin{aligned}
r_1 &= R_1 \sin(\phi_L) = R_{B1} \tan(\phi_L) \\
r_2 &= R_2 \sin(\phi_L) = R_{B2} \tan(\phi_L) \\
h_1 &= 1/2\, h_{L_1} \big/ \cos(\phi'_{L_1}) \\
h_2 &= 1/2\, h_{L_2} \big/ \cos(\phi'_{L_2}) \\
\phi'_{L_1} &= \phi_{L_1} - \alpha_1 \\
\phi'_{L_2} &= \phi_{L_1} - \alpha_2 \\
\phi_{L_1} &= \phi_{L_2} = \phi_L
\end{aligned}
\tag{E-11}
$$

where

- f facewidth
- E modulus of elasticity
- υ poisson's ratio
- P contact force
- h_{L_1} thickness of the gear 1 at the contact point
- h_{L_2} thickness of the gear 2 at the contact point
- h_1 distance from contact point to the center line of the gear 1
- h_2 distance from contact point to the center line of the gear 1
- R_1 radius of curvature at the contact point, gear 1
- R_2 radius of curvature at the contact point, gear 2

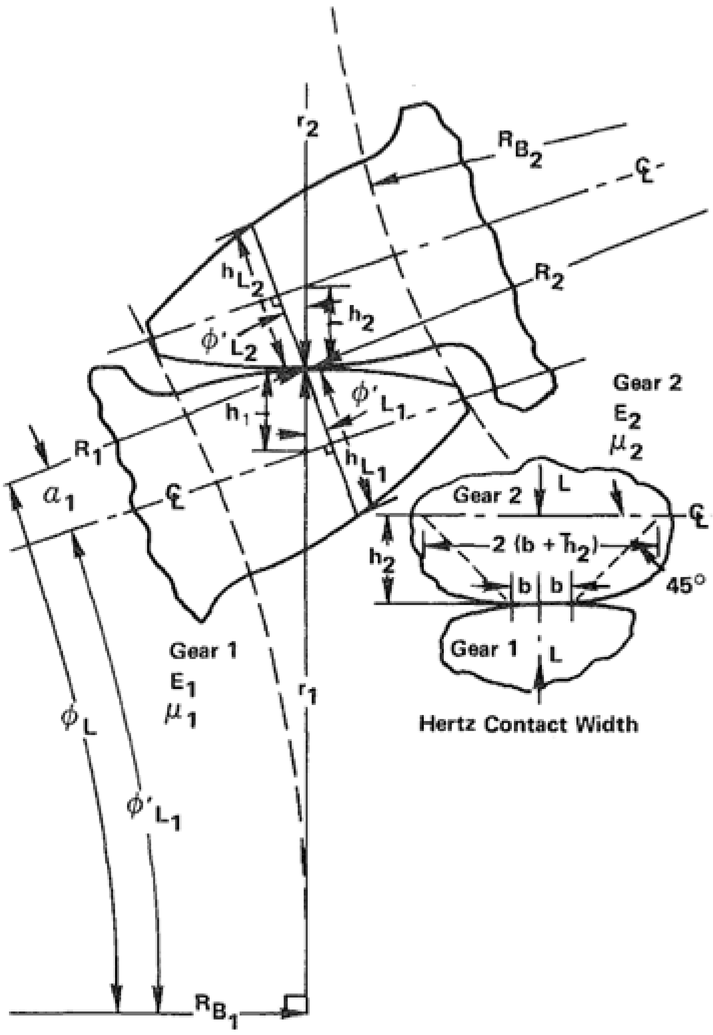
r2
RB2
℄
R2
hL2
h2
φ'L2
φ'L1
h1
hL1
R1
a1
℄
Gear 2
E2
μ2
Gear 2
L
℄
2 (b + h2)
h2
b
b
45°
Gear 1
L
Hertz Contact Width
Gear 1
E1
μ1
r1
φL
φ'L1
RB1

Figure E-1 Two gears in contact [75]

This formula is developed particularly for gear teeth that are in contact, therefore it is more accurate than the previous formulas. But, the calculation of this deflection needs the load at the specified contact point to be calculated first, and therefore it increases computational effort.

Brewe&Hamrock's Equation:

The classical Hertz solution for two elastic bodies in contact requires complex integral calculations. This equation, however, presents a simplified formula for calculating the Hertzian contact deflection in two elliptically shaped elastic solids that are in point contact. The ellipticity and the complete elliptic integrals of the first and second kind are expressed as a function of radius of curvature in the principal x-plane and y-plane [137–142]:

$$\delta_c = \left[\frac{9F^2\Gamma^3}{2\pi^2 k^2 \varepsilon R} \left(\frac{1-\upsilon^2}{E} \right)^2 \right]^{1/3} \tag{E-12}$$

and

$$\varepsilon = 1.0003 + \frac{0.5968}{R_y / R_x} \tag{E-13}$$

$$\Gamma = 1.5277 + 0.6023 \ln \frac{R_y}{R_x} \tag{E-14}$$

$$\frac{1}{R} = \frac{1}{R_x} + \frac{1}{R_y} \tag{E-15}$$

$$\frac{1}{R_x} = \frac{1}{r_{1x}} + \frac{1}{r_{2y}} \tag{E-16}$$

where

- r_{1x}, r_{1y} principal radii of gear 1

- r_{2x}, r_{2y} principal radii of gear 2
- E modulus of elasticity
- υ poisson's ratio
- R_x effective radius of curvature in the principal x-plane
- R_y effective radius of curvature in the principal y-plane
- R curvature sum
- ε complete elliptic integral of the first kind expression by method of least squares
- Γ complete elliptic integral of the first kind expression by method of least squares
- k ellipticity (ratio of semimajor to semiminor axis) expression by method of least squares

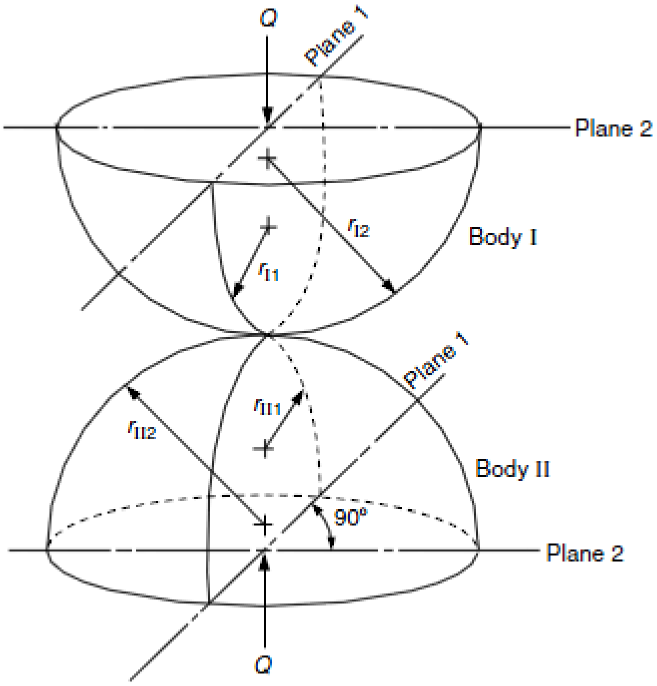
Q
Plane 1
Plane 2
r_{I2}
Body I
r_{I1}
Plane 1
r_{II1}
r_{II2}
Body II
90°
Plane 2
Q

Figure E-2 two elliptically shaped elastic solids in contact, [137–142]

F. Mathematica Symbolic Code for The Directional Rotational Radius

```
(*SHAPER SURFACE and SURFACE NORMAL*)
rs[us,θs]:={rbs*(Sin[θos+θs]-θsCos[θos+θs]),-
rbs*(Cos[θos+θs]+θs*Sin[θos+θs]),us};
ns[us,θs]:=Cross[D[rs[us,θs],θs],D[rs[us,θs],us]]*1/(rbs *θs);

(*PINION SURFACE and SURFACE NORMAL*)
r1[u1,θ1]:={rb1*(Sin[θo+θ1]-θ1Cos[θo+θ1]),-
rb1*(Cos[θo+θ1]+θ1*Sin[θo+θ1]),u1};
n1[u1,θ1]:=Cross[D[r1[u1,θ1],θ1],D[r1[u1,θ1],u1]]*1/(rb1*θ1);

(*TRANSFORMATION MATRIX for the PINION NORMAL*)
Lf1[ϕ1]:={{Cos[ϕ1], -Sin[ϕ1],0},{Sin[ϕ1],Cos[ϕ1],0},{0,0,1}};

(*ROTATED SURFACE NORMAL for THE PINION*)
nf1[θ1,ϕ1]:=Simplify[MatrixForm[Lf1[ϕ1].n1[u1,θ1]]];

(*TRANSFORMATION MATRIX for the rotation around z axis*)
Tz[ϕ_]:={{Cos[ϕ], -Sin[ϕ],0},{Sin[ϕ],Cos[ϕ],0},{0,0,1}};

(*TRANSFORMATION MATRIX for the rotation around x axis*)
Tx[ϕ_]:={{1,0,0},{0,Cos[ϕ], -Sin[ϕ]},{0,Sin[ϕ],Cos[ϕ]}};

(*TRANSFORMATION MATRIX for the rotation of FACE-GEAR*)
Mf2[ϕ2p_]:=MatrixForm[{{Cos[ϕ2p], -
Sin[ϕ2p],0},{Sin[ϕ2p],Cos[ϕ2p],0},{0,0,1}}];

(*TRANSFORMATION MATRIX for SHAPER to FACE_GEAR*)
M2s[ϕ2]:=MatrixForm[Tz[-ϕ2].Tx[γm].Tz[ϕs]];

(*ROTATED PINION SURFACE *)
rf1[u1,θ1,ϕ1]:=Lf1[ϕ1].r1[u1,θ1];

(*GENERATED FACE-GEAR SURFACE*)
r2[θs,ϕs]:=M2s[ϕ2].rs[us,θs];

(*ROTATED FACE-GEAR SURFACE*)
rf2[ϕ2p,θs,ϕs]:=Mf2[ϕ2p_].r2[θs,ϕs];

(*TRANSFORMATION MATRIX of SURFACE NORMAL for SHAPER to
FACE-GEAR*)
L2s[ϕ2]:=M2s[ϕ2];

(*TRANSFORMATION MATRIX for the rotation of SURFACE NORMAL
of FACE-GEAR*)
```

```
Lf2[ϕ2p]={{Cos[ϕ2p], -
Sin[ϕ2p],0},{Sin[ϕ2p],Cos[ϕ2p],0},{0,0,1}};

(**)
Simplify[MatrixForm[Lf2[ϕ2p].n2[θs,ϕs]]];
(**)
n2[θs,ϕs]:=L2s[ϕ2].ns[us,θs];
(**)
nf2[ϕ2p,θs,ϕs]:=Simplify[MatrixForm[Lf2[ϕ2p].n2[θs,ϕs]]];
(**)
Mf2[ϕ2p].M2s[ϕ2].rs[us,θs];

(*Subscript[θ, os]=π/(2*Subscript[N, s])-(tan[Subscript[α,
s]]-Subscript[α, s])
Subscript[θ, o]=π/(2*Subscript[N, 1])-(tan[Subscript[α, 1]]-
Subscript[α, 1])*)

(*UNIT NORMAL VECTOR ALONG ROTATING AXIS*)
nj={0,0,1};

(*DIRECTIONAL ROTATIONAL RADIUS FOR THE SPUR GEAR (OR
SHAPER)*)
(*-----------------------------------------------------------
--*)
λp=Simplify[MatrixForm[ns[us,θs].(nj□rs[us,θs])]];
λp
 -rbs

 (*DIRECTIONAL ROTATIONAL RADIUS FOR THE FACE GEAR*)
(*-----------------------------------------------------------
--*)
 λg=Simplify[MatrixForm[n2[θs,ϕs].(nj□r2[θs,ϕs])]]
 (_{
   {Cos[ϕ2] Cos[ϕs]+Cos[γm] Sin[ϕ2] Sin[ϕs], Cos[γm] Cos[ϕs]
Sin[ϕ2]-Cos[ϕ2] Sin[ϕs], -Sin[γm] Sin[ϕ2]},
   {-Cos[ϕs] Sin[ϕ2]+Cos[γm] Cos[ϕ2] Sin[ϕs], Cos[γm] Cos[ϕ2]
Cos[ϕs]+Sin[ϕ2] Sin[ϕs], -Cos[ϕ2] Sin[γm]},
   {Sin[γm] Sin[ϕs], Cos[ϕs] Sin[γm], Cos[γm]}
  }_).{-Cos[θos+θs],-Sin[θos+θs],0}.{0,0,1}□((_{
      {Cos[ϕ2] Cos[ϕs]+Cos[γm] Sin[ϕ2] Sin[ϕs], Cos[γm]
Cos[ϕs] Sin[ϕ2]-Cos[ϕ2] Sin[ϕs], -Sin[γm] Sin[ϕ2]},
      {-Cos[ϕs] Sin[ϕ2]+Cos[γm] Cos[ϕ2] Sin[ϕs], Cos[γm]
Cos[ϕ2] Cos[ϕs]+Sin[ϕ2] Sin[ϕs], -Cos[ϕ2] Sin[γm]},
      {Sin[γm] Sin[ϕs], Cos[ϕs] Sin[γm], Cos[γm]}
     }_).{rbs (Sin[θos+θs]-Cos[θos+θs] θs),-rbs
(Cos[θos+θs]+Sin[θos+θs] θs),us})
```

```
 λg
  =Simplify[(_{
      {Cos[ϕ2] Cos[ϕs]+Cos[γm] Sin[ϕ2] Sin[ϕs], Cos[γm]
Cos[ϕs] Sin[ϕ2]-Cos[ϕ2] Sin[ϕs], -Sin[γm] Sin[ϕ2]},
      {-Cos[ϕs] Sin[ϕ2]+Cos[γm] Cos[ϕ2] Sin[ϕs], Cos[γm]
Cos[ϕ2] Cos[ϕs]+Sin[ϕ2] Sin[ϕs], -Cos[ϕ2] Sin[γm]},
      {Sin[γm] Sin[ϕs], Cos[ϕs] Sin[γm], Cos[γm]}
     }_).{-Cos[θos+θs],-Sin[θos+θs],0}.{0,0,1}□((_{
         {Cos[ϕ2] Cos[ϕs]+Cos[γm] Sin[ϕ2] Sin[ϕs], Cos[γm]
Cos[ϕs] Sin[ϕ2]-Cos[ϕ2] Sin[ϕs], -Sin[γm] Sin[ϕ2]},
         {-Cos[ϕs] Sin[ϕ2]+Cos[γm] Cos[ϕ2] Sin[ϕs], Cos[γm]
Cos[ϕ2] Cos[ϕs]+Sin[ϕ2] Sin[ϕs], -Cos[ϕ2] Sin[γm]},
         {Sin[γm] Sin[ϕs], Cos[ϕs] Sin[γm], Cos[γm]}
        }_).{rbs (Sin[θos+θs]-Cos[θos+θs] θs),-rbs
(Cos[θos+θs]+Sin[θos+θs] θs),uₛ})];
 λg

 -rbs Cos[γm]-Cos[θos+θs+ϕs] Sin[γm] uₛ
```

G. Dynamic Modelling of Split-Torque Face-Gear Drive Systems

ASME IDETC-2017, Extended Abstract

Proceedings of the ASME 2017 International Design Engineering Technical Conferences &
Computers and Information in Engineering Conference
IDETC2017
August 6-9, 2017, Cleveland, Ohio, USA

DETC2017-68498

DYNAMIC MODELLING OF SPLIT-TORQUE FACE-GEAR DRIVE SYSTEMS

Mustafa Ozgur Aydogan
Turkish Aerospace Industries,
Ankara/Turkey
Dep. of Mechanical Engineering,
Middle East Technical University
Ankara / Turkey

Zihni Burcay Saribay
Turkish Aerospace Industries,
Ankara/Turkey

H. Nevzat Özgüven
Fellow ASME
Dep. of Mechanical Engineering,
Middle East Technical University
Ankara / Turkey
Contact: ozguven@metu.edu.tr

INTRODUCTION

A face-gear drive consists of a spur or helical pinion meshing with a face-gear. They are utilized to transmit torque between intersecting shafts and reduce the weight of transmission by incorporating load sharing and torque-split capabilities [1-2].

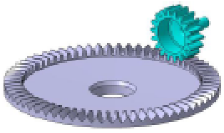

Fig. 1 A face-gear with a spur pinion

They were generally used for low power applications. However, the demands for weight and noise reduction of the rotorcraft transmissions make the researchers to investigate the face-gear drives. The interest in the application of face-gear drives in the high power helicopter transmissions has begun with ART (Advanced Rotorcraft Transmission) program [3]. The results were promising and therefore motivated the researchers to further investigate the face-gear transmission systems for the helicopters. Two lightweight helicopter transmission examples (shown in Fig. 2) utilizing face-gear drives are presented in [4-5].

The advantages of the face-gear drive systems are listed as reduced sensitivity of bearing contact to gear misalignment, reduced level of noise due to very low level of transmission error, more favorable power transfer from one tooth to another and favorable assembly inaccuracy tolerances compared to the spiral bevel gears [1].

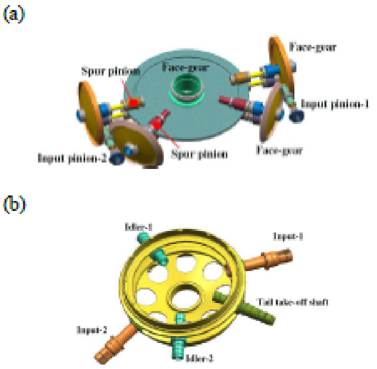

Fig. 2 (a) RDS-21 Demonstrator Gearbox [4] (b) Apache Block III [5]

Several researchers have studied face-gears; Litvin et al. generated surface of a face-gear by simulating the machine tool motions [6], also studied tooth contact and bending stress analyses using finite element method (FEM) [7,8]; Heath et al. performed experiments on tooth contact performances and failure modes of face-gears [9], conducted split torque tests on a 250 hp face gear transmission with 2 inputs 2 idlers system [2], and also performed tests to seek face-gear surface fatigue characteristics [10].

In the literature, there is limited number of studies on dynamic modelling of face gear drive systems. Chen et al. studied the effect of profile modification and mesh stiffness variation on the dynamic behavior of face-gears [11, 12]. Tang et al. studied the effect of variation of directional rotational radius on face-gear dynamics [13]. However, in all these studies a pair of face-gear with a single pinion was considered. However, dynamic analysis of a face-gear drive system resembles to a planetary gear system, which is well studied [14-17].

MATHEMATICAL MODEL

In this study the nonlinear dynamic model of a multi-mesh involute spur pinion driven face-gear split-torque drive system is developed. A lumped mass system consisting of five pinions and two face-gears is constructed. The system has seven rotational degrees of freedom. All pinion and gear blanks are assumed to be rigid disks. The constructed split-torque model consists of two inputs, two outputs and three idler gears. The mesh parameters, i.e. mesh stiffness, directional rotational radius and mesh damping have time varying characteristics. The model includes clearance-type nonlinearity for backlash.

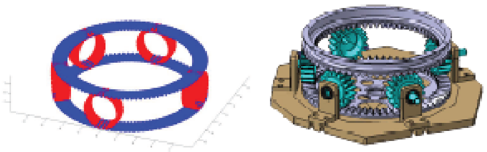

Fig. 3 Model of the split-torque face-gear drive system: Point cloud and CAD model

The developed torsional dynamic model of the system is shown in Fig. 4.

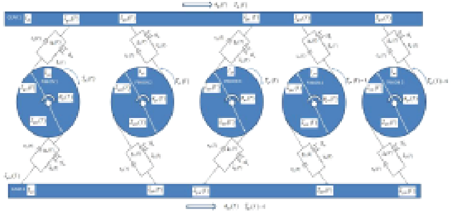

Fig. 4 Lumped mass model of the system

Face-gear geometry is generated as a point cloud by transforming the spur gear (shaper) tooth profile into face-gear tooth profile by simulating the machine tool motions. Then, the surface is approximated via NURBS (Non-Uniform Rational B-Splines) functions [18, 19]. This enables a continuous thickness variation within the strip element along the face width and also along the profile directions. From this extracted geometry, the stiffness of the face-gear is calculated via Finite Strip Method (FSM), which is a numerical method that compares favorably with FEM in terms of run-time, storage of stiffness and load matrices and the result outputs [20, 21].

SOLUTION AND RESULTS

The nonlinear equations of motion are solved with Harmonic Balance Method (HBM) in order to obtain the periodic steady state response of the system. The accuracy of the results are compared with the direct numerical integration solutions (comparison of the results with HBM solution and time simulation are given in Fig. 5).

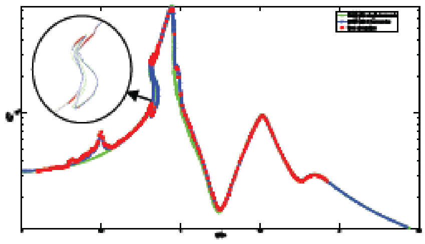

Fig. 5 Rms value of dynamic transmission error (between lower face gear and one of idler pinions), single harmonic HBM (-), two harmonics HBM (-), and time simulation (o)

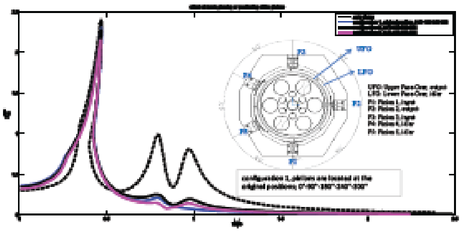

Fig. 6 The effect of mesh phasing on dynamic transmission error (between upper face gear and output pinion)

To the best of the authors' knowledge, this is the first study on the development of a nonlinear dynamic model for a multi-mesh face-gear split-torque system. The current work is focused on the study of the effects of several parameters (mesh phasing, mesh stiffness, backlash and power values or static torque values etc.) on the system response. As an example, the effect of mesh phasing on the total dynamic transmission error between upper face-gear and the output pinion is demonstrated in Fig. 6. The results may provide guidance in the preliminary design of such gear systems, in micro geometry modifications and therefore in the manufacturing machine settings.

Copyright © 2017 by ASME

REFERENCES

[1] Litvin, F. L., Wang, J.-C., Bossler, R. B., Chen, Y.-J., Heath, G., and Lewicki, D. G., 1994, “Application of Face-Gear Drives in Helicopter Transmissions,” J. Mech. Des. Trans. ASME, 116 (September 1994), pp. 672–676.

[2] Heath, G F., Filler, R. R., and Tan, J., 2002, “Development of Face Gear Technology for Industrial and Aerospace Power Transmission", NASA CR—2002-211320, ARL–CR–0485, 1L18211–FR–01001, May, 2002.

[3] Bill, R.C., “Advanced Rotorcraft Transmission Program, NASA-TM-103276”, 46th Annual American Helicopter Society Forum, Washington, D.C., May 21, 1990.

[4] He S., Gmirya Y., Mowka F., Meyer B.W., Ames E.C., “Trade Study on Different Gear Reduction Ratios of the 5100 HP RDS-21 Demonstrator Gear Box,” AHS 62nd Annual Forum, Phoenix, AZ, May 9-11, 2006.

[5] Ron Gilbert R., Craig G., Filler R., Hamilton W., Hawkins J.,Higman J., Green W., “3400 HP Apache Block III Improved Drive System,” AHS 64th Annual Forum, Montreal, Canada, April 29 – MAY 1, 2008.

[6] Litvin, F. L., Bossler, R. B., Chen, Y.J.D., Zhang Y., Wang, J.-C., “Design and Geometry of Face-Gear Drives”, J. Mech. Des. 114(4), 642-647, 1992.

[7] Litvin, F.L., Fuentes, A., Zanzi, C., Pontiggia, M., “Design, Generation, and Stress Analysis of Two Versions of Geometry of Face-Gear Drives”, Mechanism and Machine Theory, Vol. 37, Iss. 10, October, 2002, pp. 1179-1211.

[8] Litvin, F. L., Fuentes, A., Zanzi, C., Pontiggia, M., Handschuh, R.F., Face-Gear Drive with Spur Involute Pinion: Geometry, Generation by a Worm, Stress Analysis, Computer Methods in Applied Mechanics and Engineering, Vol. 191, Iss. 25-26, April, 2002, pp. 2785-2813.

[9] Heath, F., Diego, S., Handschuh, R. F., Lewicki, D. G, and Heath, G. F., 1996, “Experimental Evaluation Aerospace Drive System of Face Gears for Applications”, NASA Technical Memorandum 107227, ARL Technical Report 1109, September, 1996.

[10] Heath, G. F., Slaughter, S. C., Morris, M. T., Fetty, J., Lewicki, D. G., and Fisher, D. J., “Face Gear Development under the Rotorcraft Drive System for the 21 st Century Program”, AHS 65th Annual Forum, Grapevine, Texas, May 27-29, 2009.

[11] Chen, S., Tang, J., Chen, W., Hu, Z., Cao, M., “Nonlinear dynamic characteristic of a face gear drive with effect of modification”, Meccanica, vol. 49, no. 5, pp. 1023–1037, 2014.

[12] Hu, Z., Tang, J., Chen, S., Lei, D., “Effect of Mesh Stiffness on the Dynamic Response of Face Gear Transmission System,” J. Mech. Des., vol. 135, no. July, pp. 1–7, 2013.

[13] Jinyuan, T., Hu, Z., Chen, S., Lei, D., “Effects of directional rotation radius and transmission error on the dynamic characteristics of face gear transmission system,” Proc. Inst. Mech. Eng. Part C J. Mech. Eng. Sci., vol. 0, no. 0, pp. 1–11, 2013.

[14] Cooley, C. G., Parker, R. G., “A Review of Planetary and Epicyclic Gear Dynamics and Vibrations Research,” Appl. Mech. Rev., vol. 66, no. 4, p. 040804, 2014.

[15] Al-shyyab, A., Kahraman A., “A non-linear dynamic model for planetary gear sets,” Proc. Inst. Mech. Eng. Part K J. Multi-body Dyn., vol. 221, no. 4, pp. 567–576, 2007.

[16] Al-shyyab, A., Alwidyan, K., Jawarneh, A., Tlilan, H. “Non-linear dynamic behavior of compound planetary gear trains: model formulation and semi-analytical solution,” Proc. Inst. Mech. Eng. Part K J. Multi-body Dyn., vol. 223, no. 3, pp. 199–210, 2009.

[17] Kahraman A., “Dynamic Analysis of a Multi-Mesh Helical Gear Train,” J. Mech. Des., vol. 116, no. SEPTEMBER 1994, pp. 706–712, 1994.

[18] Hughes, T. J. R., Cottrell, J. A., Bazilevs, Y., “Isogeometric analysis: CAD, finite elements, NURBS, exact geometry and mesh refinement,” Comput. Methods Appl. Mech. Eng., vol. 194, no. 39–41, pp. 4135–4195, 2005.

[19] Cheng, Q., Yang, G., Lu, J., “An Analysis of Gear Based on Isogeometric Analysis,” no. 1, pp. 17–22, 2013

[20] Friedrich, R., “Finite strip method: 30 years, A Bibliography 1968-1998”, Engineering Computations, Vol. 17, No 1, pp. 92-111, 2000.

[21] Gosselin, C., Gagnon, P., Cloutier, L., “Accurate Tooth Stiffness of Spiral Bevel Gear Teeth by the Finite Strip Method”, vol. 120, pp. 599–605, 1998.

[22] Litvin, F. L., Fuentes, A., Demenego, A., Vecchiato, D., Fan, Q., “New developments in the design and generation of gear drives,” Proc. Inst. Mech. Eng. Part C J. Mech. Eng. Sci., vol. 215, no. 7, pp. 747–757, Jan. 2001.

CURRICULUM VITAE

Surname, Name : Aydoğan, Mustafa Özgür
Date and Place of Birth : 12-April-1977, Ordu
Phone : +905334842011
E-mail : moaydogan@gmail.com

EDUCATION

Degree	Institution	Year of Graduation
MS	METU Mechanical Engineering	2003
BS	METU Mechanical Engineering	2000
High School	Ordu Anadolu High School, Ordu	1995

WORK EXPERIENCE

Year	Place	Enrollment
2006-Present	Türk Havacılık ve Uzay Sanayi	Senior Tech. Des. Engineer
2005-2006	Enkapower Plants	Maintenance Engineer
2000-2004	METU	Teaching Assistant

FOREIGN LANGUAGES

Good English, Intermediate German

PUBLICATIONS

1. Aydoğan, M. Ö., Sarıbay, Z. B., Özgüven, H. Nevzat, Dynamic Modelling of Split-Torque Face-Gear Drive Systems, Proceedings of the ASME 2017 International Design Engineering Technical Conferences & Computers and Information in Engineering Conference IDETC2017, Cleveland, Ohio, USA · Aug 9, 2017.

2. Pehlivanoğlu, Y., Aydoğan, M., Ö., Sabuncuoğlu, B., Mesh stiffness of micro-spur gears by finite element formulations based on modified couple stress theory, Microsystem Technologies, May 15, 2020.